

# Stability of hydrate assemblages and properties of cementitious systems with higher alumina content

Présentée le 11 juin 2021

Faculté des sciences et techniques de l'ingénieur  
Laboratoire des matériaux de construction  
Programme doctoral en science et génie des matériaux

pour l'obtention du grade de Docteur ès Sciences

par

**Natechanok CHITVORANUND**

Acceptée sur proposition du jury

Dr Y. Leterrier, président du jury  
Prof. K. Scrivener, Dr B. Lothenbach, directrices de thèse  
Prof. M. Aranda, rapporteur  
Prof. T. Matschei, rapporteur  
Prof. R. Flatt, rapporteur

# Acknowledgements

This thesis would not be completed without the support and help from many people during these four years of my PhD which is a challenging step of my life.

First of all, I would like to acknowledge Prof. Karen Scrivener for this great opportunity to work in LMC. It is beyond my dream that I could work and learn with her. Thank you for all of her frank comments that made me improve myself and overcome my limits. She always helps and guides me to achieve my goal. It was a great pleasure to work with you for four years.

Special thanks to my co-adviser, Barbara Lothenbach, who has always supported me even before my PhD. Thank you for her kindness, her incredible guidance and her patience. She made me feel amazed every time she showed me some GEMs tricks and always solved the problems in one minute like magic.

I would like to thank the jury members for the time, discussions and comments on this thesis: Prof. Robert Flatt, Prof. Thomas Matschei and Prof. Miguel Aranda.

I am thankful for the nanocem consortium for the financial support during these four years. In particular, I would like to thank the members of Core Project 16 for the comments and very useful advice: Prof. Jørgen Skibsted, Mohsen Ben Haha, Patrick Julian, Duncan Herfort, and Marios Katsiotis. I would like to thank Marie-Alix Dalang-Secrétan for all the administrative work.

It is really a pleasure for me to work at Empa. I would like to express my gratitude to all the staff and friends at Empa. Special thanks to Frank Winnefeld for his supports and saying “never give up”, Luigi Brunetti for pore solution, Boris Ingold for clinker synthesis, Josef Kaufmann for the PSD advice, Beat Münch for fruitful discussions on image analysis, Roman Loser for the office, Andreas Leeman for the mapping advice, Alexander German for the XRD analysis. I had an incredible time every time I went to Empa with all my “Empa’s friends”: Ellina, Alessio, Enia, Sonia, Malene, Nikolajs, Andrea, Biwan, Zhengua, Yiru, Lina.

To the LMC crews and all the LMC guests, thanks for making this lab so special. I had so much fun with you guys. Thanks to Julien for the astronomy course, Alex for the crazy stuff and tax refund, Viola for the vodka, Lili for NMR and chemical shrinkage, Aurélie for the hike, Elise for the polishing tips, Yu Yan for nice photos, Shiyu for the weekend work, Mariana for giving my fourth name “Anita”, Aslam for some nice lunch, Sreejith for making the belite, Tanvi for her lively smile, Josh for her kind. For the last gen of LMC crew, thanks for a good memory: Andrea for being so active and full of energy (like me a few years ago), Sarra for her care, Maya for the cup cake recipe, Alex P. for the night life, Monisha for the vegan cake, Gabie for Thanksgiving Day, Ziga for his drunk voice, Masood for the help on visa application. Lunch time is also my favorite (before COVID) because of you guys: Khalil for eating my food nah, Silas for creating this group nah, Franco for his bloody jokes, his crimes, his cooking, his beverages (coffee + alcohols) etc. nah. I am grateful to a dream team postdoc: Xuerun for the training, William for the chloride ingress and nice discussions about life, Diana for the XRD analysis and many helps and Fabien for very nice discussions and ideas. My gratitude also to the support staff in the lab: the secretary team - Maude, Mirabella, Anne-Sandra - thank you for making my life easier on the administrative tasks, the technical support team – Lionel, Jean, Antonio, Paul, Nathan, Maxim and Noah – thanks for a lot of helps and funny jokes and the IT support team – John – for saving my wrist. I wouldn’t work happily with-



## Acknowledgements

---

out my incredible officemates (before COVID): Solène for establishing Kee Mao Gang, (Mama) Mahsa for her nice soul, Qiao for his encouragement. All of you made me feel so happy to be in the lab.

Thanks to all the students for their contributions. My gratitude goes to Edgar, Eric, Claire, Yutong, Shreyas, François, Léa and Julien.

I would also like to thank for all of the supports from my friends both for work and life: Hadi for lifting me up, Hamed for his calm, Frank B. for his incredible mind and supports on CSA part, Arnaud for belite synthesis advice and a hiking trip, Pawel for alpine hiking tips, Aleksandra for your kindness. Very special thanks to Chang's family (Pure, Samuel, Joshua and Jasmine) for food support and making me feel like home, P' Mink + P' Ji for all of their help on how to survive in Lausanne, Morn and Pomme for their support and their deep listening. Thanks to Thai-Lausannois for a great time: P' Wynn, Tar, Bank, Noom, Arm, Ice, P'Kiat, Pat and Fai (from Bern). I would like to thank all of the supports from Thailand: my relatives, Aj. Tare + Aj. Gib, SRI boses and friends (especially everyone in แก๊งปลาซ่า), MS34 friends (Morn, Chy, Wicky, Bird and June), MS master group (P'Jay, Baifern, P' Moo, Nui, Kui), CUD39 friends (especially the three doctors: Jenette, Thun, Phing) and all the friends who visited me in Lausanne.

Finally, I wouldn't come this far without my family who always supported me, encouraged me and believed in me. Thank you to my parents who taught me to be "me". They showed me how to be a fighter in difficult circumstances. I would also like to thank my brother (Arm) and my sister (Emmie) who always listen to me and give me the power when I feel down. They both have taken huge responsibilities and let me persue my dream. A million thanks to Fabien for the great support in "everything" and lots of positive energy during this tough time.

Thanks to everyone who made this chapter of my life beautiful.

Lausanne, le 30 avril 2021

Natechanok Chitvoranund (Erng, Anna, Anita)

# Abstract

Two low CO<sub>2</sub> cement systems are investigated: one made with the use of supplementary cementitious materials (SCMs) (metakaolin and limestone) and the other an alternative binder, calcium sulfoaluminate cement (CSA). These two low CO<sub>2</sub> cements contain a similar higher alumina content compared to Portland cement (PC), but they have contrasting chemical hydration reactions. It leads to the changes in phase assemblage, microstructure and properties. There have been previous studies on these materials separately mainly at room temperature. But here we make a systematic comparison looking at several temperatures and relating the phase assemblages and microstructure to strength and transport properties.

Temperature has a strong influence on the aluminate phases such as ettringite, monosulfate and strätlingite. Thermodynamic modelling with the current CEMDATA database was used over a wide range of realistic curing temperatures. It is a good tool to predict phase assemblages in the equilibrium state, especially for qualitative predictions. The accuracy of the characterization methods is an important factor to obtain the best inputs. Accurate measurement of the degree of reaction of amorphous phases such as metakaolin is challenging. Another issue is to obtain a realistic composition of the C-A-S-H phase.

A more homogeneous microstructure was observed in the metakaolin blends compared to the PC reference and the CSA system. It improves the transport properties. However, the higher alumina content of the blended systems seems to inhibit the hydration of belite, resulting in a lower compressive strength, especially for the CSA system at early age.

The correlations between the hydration, microstructure and properties were explored with various techniques. For the Portland based systems, the combined water fraction correlates well with the compressive strength despite some deviation in the blended systems. However, this concept does not appear to relate well to strength for the CSA system. The mini-migration method can be used to determine the resistance of chloride, especially in the PC systems. A simple method of effective conductivity can be applied as a rough indicator. The transport properties in the CSA system are more difficult to measure with accelerated methods.

## Keywords

Metakaolin, limestone, calcium sulfoaluminate cement, temperature, phase assemblage, thermodynamic modelling, hydration, microstructure, compressive strength, chloride ingress.

# Résumé

Deux systèmes de ciment à faible teneur en CO<sub>2</sub> sont étudiés : le premier utilise des matériaux cimentaires supplémentaires (SCM) (métakaolin et calcaire) et le second un clinker alternatif : un ciment sulfo-alumineux (CSA). Ces deux ciments à faible teneur en CO<sub>2</sub> contiennent une composition en alumine supérieure à celle du ciment Portland (PC), mais ils ont différentes réactions d'hydratation chimiques. Cela conduit à des changements d'assemblage de phase, de microstructure et de propriétés. Les études précédentes ont étudié ces matériaux séparément, principalement à température ambiante. Dans cette étude, nous faisons une comparaison systématique en examinant plusieurs températures et en reliant les assemblages de phases et la microstructure aux propriétés de transport et de durabilité.

La température a une forte influence sur les phases aluminates telles que l'ettringite, le monosulfate et la strätlingite. La modélisation thermodynamique avec la base de données CEMDATA a été utilisée sur une large gamme de températures de cure réalistes. C'est un bon outil pour prédire les assemblages de phases à l'équilibre, en particulier pour les prédictions qualitatives. La précision des méthodes de caractérisation est un facteur important pour obtenir les meilleures entrées des simulations. Une mesure précise du degré de réaction des phases amorphes telles que le métakaolin est difficile. Un autre problème est d'obtenir une composition réaliste de la phase C-A-S-H.

Une microstructure plus homogène a été observée dans les mélanges de métakaolin par rapport à la référence du ciment Portland et au système CSA. Il améliore les propriétés de transport. Cependant, la teneur plus élevée en alumine des systèmes mélangés semble inhiber l'hydratation de la bélite, entraînant une diminution de la résistance à la compression, en particulier pour le système CSA à un âge précoce.

Les corrélations entre l'hydratation, la microstructure et les propriétés ont été explorées avec diverses techniques. Pour les systèmes à base de ciment Portland, la fraction d'eau combinée (combined water fraction) est bien corrélée à la résistance à la compression malgré des écarts dans les systèmes mélangés. Cependant, ce concept ne semble pas expliquer la solidité du système CSA. La méthode de mini-migration peut être utilisée pour déterminer la résistance aux chlorures, en particulier dans les systèmes PC. La mesure de la conductivité effective peut être appliquée comme indicateur approximatif. Les propriétés de transport dans le système CSA sont plus difficiles à mesurer avec des méthodes accélérées.

## Mots-clés

Métakaolin, calcaire, ciment sulfo-alumineux, température, assemblage de phase, modélisation thermodynamique, hydratation, microstructure, résistance à la compression, résistance aux chlorures.

# Contents

<b>Acknowledgements</b> .....	<b>v</b>
<b>Abstract</b> .....	<b>vii</b>
<b>Keywords</b> .....	<b>vii</b>
<b>Résumé</b> .....	<b>viii</b>
<b>Mots-clés</b> .....	<b>viii</b>
<b>List of Figures</b> .....	<b>xiii</b>
<b>List of Tables</b> .....	<b>xviii</b>
<b>Chapter 1 Introduction</b> .....	<b>19</b>
1.1 Background of the thesis.....	20
1.2 Objectives of the thesis.....	21
1.3 Research approach and the content of the thesis .....	21
1.4 References.....	24
<b>Chapter 2 Materials preparation</b> .....	<b>27</b>
2.1 Portland cement (PC) system.....	28
2.1.1 Commercial cement.....	28
2.1.2 Sulfate optimization.....	30
2.2 Calcium sulfoaluminate system (CSA).....	32
2.2.1 Clinker synthesis .....	32
2.2.2 Mayenite adjustment.....	34
2.3 Characterization of raw materials.....	36
2.4 References.....	40
<b>Chapter 3 Phase assemblages of the PC systems</b> .....	<b>41</b>
3.1 Introduction .....	43
3.2 Materials and methods.....	43
3.2.1 Raw materials .....	43
3.2.2 Preparation of cement pastes and hydration stoppage .....	44

3.2.3	Selective dissolution .....	45
3.2.4	Methods of analysis .....	45
3.3	Results and discussion.....	48
3.3.1	Reaction of anhydrous phases.....	48
3.3.2	Comparison of phase assemblages based on experimental data and thermodynamic modelling .....	52
3.3.3	Strätlingite formation .....	56
3.3.4	Siliceous hydrogarnet .....	61
3.3.5	Hydrotalcite formation .....	64
3.3.6	The ettringite – monosulfate balance 60°C .....	65
3.3.7	Why is hemicarbonat observed ? .....	66
3.4	Conclusions .....	67
3.5	References.....	68
3.6	Appendix .....	71
<b>Chapter 4</b>	<b>Phase assemblages of the CSA system.....</b>	<b>73</b>
4.1	Introduction .....	75
4.2	Materials and methods .....	76
4.2.1	Raw materials and mixture design.....	76
4.2.2	Raw materials characterization .....	76
4.2.3	Preparation of cement pastes.....	77
4.2.4	Methods.....	77
4.3	Results and discussion.....	79
4.3.1	Reaction of belite and ye’elimite in BY cement paste .....	79
4.3.2	Comparison of phase assemblages between experimental data at 90d and thermodynamic modelling .....	80
4.3.3	Identification of C-S-H formation.....	81
4.3.4	Formation of siliceous hydrogarnet at 60°C .....	85
4.3.5	Quantification and validation of AFm formation in BY cement.....	86
4.4	Conclusions .....	89
4.5	References.....	90
4.6	Appendix .....	93
<b>Chapter 5</b>	<b>Hydration, microstructure and compressive strength.....</b>	<b>95</b>
5.1	Introduction .....	97
5.2	Materials and methods .....	98

5.2.1	Raw materials .....	98
5.2.2	Mix design and hydration stoppage.....	99
5.2.3	Methods of analysis .....	100
5.3	Results.....	102
5.3.1	Hydration kinetics .....	102
5.3.2	Hydration .....	105
5.3.3	Microstructure and porosity at 90d.....	110
5.3.4	Compressive strength .....	115
5.4	Discussion.....	117
5.4.1	Degree of hydration of belite in CSA.....	117
5.4.2	Correlation between degree of hydration and compressive strength .....	117
5.4.3	Correlation between porosity VS compressive strength .....	119
5.4.4	Correlation between combined water fraction (CWF) and compressive strength.....	120
5.4.5	The contribution of C-S-H to compressive strength in CSA .....	121
5.4.6	Effect of microstructure.....	121
5.5	Conclusions .....	122
5.6	References.....	123
5.7	Appendix .....	126
<b>Chapter 6</b>	<b>Transport properties.....</b>	<b>133</b>
6.1	Introduction .....	135
6.2	Materials and methods .....	136
6.2.1	Raw materials characterization .....	136
6.2.2	Mix design and preparation.....	137
6.2.3	Methods.....	139
6.3	Results.....	144
6.3.1	Chloride penetration depth .....	144
6.3.2	Effective diffusion coefficient ( $D_{eff}$ ).....	147
6.3.3	Effective conductivity ( $\sigma_{eff}$ ) .....	147
6.3.4	Electrical conductivity and ion concentrations of pore solution .....	148
6.3.5	Formation factor and tortuosity .....	151
6.4	Discussion.....	153
6.4.1	Role of $OH^-$ concentrations in the sample .....	153
6.4.2	Effective conductivity in metakaolin blended systems.....	154

6.4.3 Relationship between effective conductivity and $D_{eff}$ .....	154
6.4.4 Relationship between effective conductivity at 180 days, $D_{eff}$ at 28 days and chloride penetration depth.....	155
6.5 Conclusions .....	157
6.6 References.....	158
6.7 Appendix .....	160
<b>Chapter 7 Conclusions and perspectives .....</b>	<b>165</b>
7.1 Accuracy of thermodynamic modelling .....	166
7.2 Portland cement systems.....	166
7.3 Calcium sulfoaluminate system .....	167
7.4 CO <sub>2</sub> emissions.....	168
7.5 Reference .....	170
<b>Appendix A: Belite and ye'elimite clinker .....</b>	<b>172</b>
<b>Appendix B: Effect of mayenite at 60°C .....</b>	<b>177</b>
<b>Appendix C: EDS point analysis of C-(A)-S-H of the PC systems.....</b>	<b>179</b>
<b>Appendix D: Activation energy (Ea).....</b>	<b>181</b>
<b>Appendix E: Bulk diffusion test – AgNO<sub>3</sub> spraying – Chloride penetration depth .....</b>	<b>182</b>
<b>Curriculum Vitae.....</b>	<b>185</b>

# List of Figures

Fig. 1-1 The CaO-Al <sub>2</sub> O <sub>3</sub> -SiO <sub>2</sub> ternary plot in wt.% in the presence of excess phase pore solution, ferrihydrite and possibly calcite modified from [41].....	22
Fig. 2-1 A typical heat flow curve of OPC [2].....	28
Fig. 2-2 Sulfate adjustment on white Portland cement at (a) 20, (b) 40 and (c) 60°C with additional sulfate in (wt.%).....	29
Fig. 2-3 Sulfate adjustment on white Portland cement blended with metakaolin and limestone (WPCMKLS) at (a) 20, (b) 40 and (c) 60°C with additional sulfate. ....	29
Fig. 2-4 Heat of hydration of WPC and LGC without gypsum and with 3% of gypsum at 40°C.....	30
Fig. 2-5 Heat of hydration of LGC, LGCMK and LGCMKLS at temperatures of (a) 20, (b) 40 and (c) 60°C without additional sulfate.....	30
Fig. 2-6 Heat of hydration of LGC, LGCMK and LGCMKLS at temperatures of (a) 20, (b) 40 and (c) 60°C with sulfate optimization. ....	31
Fig. 2-7 A schematic of clinker synthesis adapted from the cylinder method [4].....	33
Fig. 2-8 XRD plot of a laboratory prepared belite-ye'elimite clinker: B = beta-belite, Y = ye'elimite...33	
Fig. 2-9 Heat flow of different BY clinkers containing 0, 0.3, 0.8 and 1.2% free lime (L) with fixed calcium sulfate to ye'elimite ratio of 1:1 and water to binder ratio of 0.6. ....	34
Fig. 2-10 heat flow curves of 3 different BYF industrial cement, where only minor phases and alkalis content are different) at 20°C and w/c ratio of 0.5 [5]. ....	35
Fig. 2-11 Heat flow of different content of mayenite added to BY40.....	36
Fig. 3-1 Comparison of degree of hydration (DoH) of alite and belite calculated by XRD Rietveld quantification and <sup>29</sup> Si-NMR of (a) LGC, (b) LGCMK and (c) LGCMKLS at 90 days of hydration.....	48
Fig. 3-2 Average degree of hydration (DoH) of alite and belite of LGC, LGCMK and LGCMKLS at 90 days of hydration at different temperatures. ....	49
Fig. 3-3 Degree of reaction (DoR) of metakaolin calculated from <sup>29</sup> Si-NMR spectra of LGCMK and LGCMKLS at 90 days of hydration at different temperatures. ....	50
Fig. 3-4 Average C-(A)-S-H composition of the investigated systems at 5, 20, 40 and 60°C analysed by EDS point analysis: A = alite, B = belite, C-(A)-S-H = calcium aluminate silicate hydrates, CH = portlandite, Cc = calcite, E = ettringite and AFm = alumino-ferrite-mono-phase.....	51
Fig. 3-5 Main hydrate phases in XRD patterns of (a) LGC, (b) LGCMK and (c) LGCMKLS cured at different temperatures at 90 days of hydration: E = ettringite, Ms = monosulfate, Hc = hemicarbonate, Mc = monocarbonate, HT = hydrotalcite and Si-HG = Siliceous hydrogarnet.....	53
Fig. 3-6 Comparison of phase assemblages between experimental data at 90 days of hydration and thermodynamic modelling at different temperatures of (a) LGC, (b) LGCMK and (c) LGCMKLS: CH = portlandite, E = ettringite, Mc = monocarbonate, Hc = hemicarbonate, Ms = monosulfate, S = strätlingite, HT = hydrotalcite, Si-HG = siliceous hydrogarnet, MK = metakaolin, Amor = amorphous, Cc = calcite, minor phases = quartz and dolomite.....	55
Fig. 3-7 <sup>27</sup> Al MAS NMR spectra (14.09 T, ν <sub>R</sub> =13.0 kHz) of (a) LGC, (b) LGCMK and (c) LGCMKLS at 90 days of hydration cured at 5, 20, 40 and 60°C: S = strätlingite, E = ettringite. Spinning sidebands are indicated in the first-row spectra by asterisks. The spectra in (a) for the pure LGC are vertically expanded by a factor of three compared to the LGCMK and LGCMKLS blends in (b) and (c).....	57



Fig. 3-8 Atomic ratio plots of Si/Ca and Al/Ca of LGCMK at 90 days of representative points obtained from EDS mapping [22] with the main composition of hydrated phases. The points around the strätlingite composition are selected in red: A = alite, B = belite, MK = metakaolin, CH = portlandite, Cc = calcite, CS = calcium sulfate, E = ettringite and AFm = alumino-ferrite-mono phase. ....58

Fig. 3-9 Overlay mask of the selected points in the ratio plot identified as strätlingite (in red) on BSE images of LGCMK at 90 days cured at 5, 20, 40 and 60°C: CK = anhydrous clinker, CH = portlandite and AFm = alumino-ferrite-mono phase.....58

Fig. 3-10 Atomic ratio plots of Si/Ca and Al/Ca of LGCMKLS at 90 days of representative points obtained from EDS mapping [22] with the main composition of hydrated phases. The points around the strätlingite composition are selected in red: A = alite, B = belite, MK = metakaolin, CH = portlandite, Cc = calcite, CS = calcium sulfate, E = ettringite and AFm = alumino-ferrite-mono phase. ....59

Fig. 3-11 Overlay mask of the selected points in the ratio plot identified as strätlingite (in red) on BSE images of LGCMK at 90 days cured at 5, 20, 40 and 60°C: CK = anhydrous clinker, CH = portlandite and AFm = alumino-ferrite-mono phase.....59

Fig. 3-12 Strätlingite (red) and portlandite (yellow) formation in the microstructure of LGCMK at 90 days of hydration cured at 5 and 20°C: CK = anhydrous clinker, CH = portlandite, S = strätlingite and AFm = alumino-ferrite-mono phase (monsulfate, monocarbonate or hem carbonate) .....60

Fig. 3-13 Siliceous hydrogarnet (HG) of (a) LGC, (b) LGCMK and (c) LGCMKLS at different temperatures after selective dissolution with SAM at the zoomed section of XRD patterns between 15 - 25° (2θ): Si-HG = siliceous hydrogarnet, Q = quartz, S = strätlingite and Cc = calcite.....61

Fig. 3-14. High Fe containing hydrates (in red) in the microstructure of LGCMK at 90 days of hydration cured at 20°C (a) Fe mapping, (b) the ratio plot of Fe/Ca and Si/Ca, (c) the mask in red on BSE image and (d) the ratio plots of (Al+Fe)/Ca and Si/Ca. The composition is close to siliceous hydrogarnet and strätlingite.63

Fig. 3-15. High Fe containing hydrates (in red) in the microstructure of LGCMKLS at 90 days of hydration cured at 20°C (a) Fe mapping, (b) the ratio plot of Fe/Ca and Si/Ca, (c) the mask in red on BSE image and (d) the ratio plots of (Al+Fe)/Ca and Si/Ca. ....63

Fig. 3-16 DTG data at 90 days of hydration indicating hydrated phases of (a) LGC, (b) LGCMK and (c) LGCMKLS: E = ettringite, Hc = hem carbonate, Mc = monocarbonate, Ms = monosulfate, S = strätlingite and CH = portlandite.....64

Fig. 3-17 XRD patterns at the zoomed section of between 5 - 15° (2θ) indicating hydrotalcite-like phase (HT) humps mainly in (a) LGC but not clear evidence on (b) LGCMK and (c) LGCMKLS: E = ettringite, Hc = hem carbonate, Mc = monocarbonate, Ms = monosulfate, AFmss = alumino-ferrite-mono phase solid solution.....65

Fig. 3-18 Comparison of thermodynamic modelling based on different inputs of DoH of anhydrous clinker/DoR of metakaolin: E = ettringite, Ms = monosulfate, Cc = calcite, Si-HG = siliceous hydrogarnet, S = strätlingite, MK = metakaolin, Amor = amorphous.....66

Fig. 4-1. Phase content of anhydrous phases in BY cement paste up to 90 days of hydration obtained by XRD with Rietveld refinement. ....79

Fig. 4-2. Degree of hydration (DoH) of belite, ye'elimite and anhydrite at 90 days of hydration obtained by XRD with Rietveld refinement. ....80

Fig. 4-3. Comparison of phase assemblages at different temperatures between thermodynamic modelling and the experimental data at 90 days: Y = ye'elimite, Anh = anhydrite, D = dolomite, E = ettringite, Ms = total monosulfate, S = strätlingite, AH<sub>3</sub> = aluminium hydroxide, Amor = amorphous and C-S-H = calcium silicate hydrates. ....81

Fig. 4-4. C-S-H humps at different temperatures at the zoomed section of XRD patterns between 2θ 28 - 34°: C-S-H = calcium silicate hydrates, E = ettringite, S = strätlingite, Ms = monosulfate.....82

Fig. 4-5 Microstructure around belite grains at 5 and 60°C with high resolution SEM.....	82
Fig. 4-6. Microstructure of C-S-H at 5 and 60°C with magnification (a, b) 1,000x and (c, d) 10,000x. .	83
Fig. 4-7. Identification of C-S-H formation in BY cement at 5°C (a) BSE image (b) BSE image with C-S-H overlay as detected in (c) Si/Ca – Al/Ca ratio plot and (d) Al/Ca – S/Ca ratio plot. Ideal compositions of relevant phases are added to the ratio plots as guidelines. ....	84
Fig. 4-8. Identification of C-S-H formation in BY cement at 60°C (a) BSE image (b) BSE image with C-S-H overlay as detected in (c) Si/Ca – Al/Ca ratio plot and (d) Al/Ca – S/Ca ratio plot.....	84
Fig. 4-9 Thermodynamic modelling calculations: without Al-containing siliceous hydrogarnet (Al-Si-HG), a restricted amount of Al-Si-HG and freely allowed Al-Si-HG at 60°C compared to experimental data. 85	
Fig. 4-10 Main hydration products at all curing temperatures at the zoomed section of XRD patterns between 2theta 5 - 15°: E = Ettringite, Ms = monosulfate and S = strätlingite.....	86
Fig. 4-11 Main hydration products after 90 days of hydration at all curing temperature analysed by TGA curve. ....	87
Fig. 4-12 Strätlingite intermixed with AFm at different temperatures after 90 days obtained by SEM-EDS mapping at magnification of 2000x. The cross indicates the pure composition of each phase.....	88
Fig. 4-13 . Strätlingite formation (red) in the microstructure at 20°C (a) Si/Ca – Al/Ca ratio plot and (b) BSE image. ....	89
Fig. 4-14 Full scaled XRD patterns of BY cement after 90 days of hydration cured at 5, 20, 40 and 60°C. 93	
Fig. 5-1 Heat flow curves of the investigated system measured at (a) 5, (b) 20, (c) 40 and (d) 60°C.103	
Fig. 5-2 Cumulative heat release of the investigated systems at different temperatures up to 28 days of hydration; (a) LGC, (b) LGCMK, (c) LGCMKLS and (d) CSA.....	104
Fig. 5-3 Comparison of the DoH of the main clinker phase calculated from XRD Rietveld refinement of (a) LGC, (b) LGCMK, (c) LGCMKLS and (d) CSA at different temperatures. The main clinker phases of the PC systems are alite and belite. The main clinker phases of CSA are belite and ye’elimite.....	105
Fig. 5-4 Comparison of XRD patterns of (a) LGC, (b) LGCMK, (c) LGCMKLS and (d) CSA after 1 day of hydration at 5, 20, 40 and 60°C: E = ettringite, CH = Portlandite, Ms = monosulfate, Hc = hemicarbonat, Mc = monocarbonat, Q = Quartz, Cc = calcite, A = alite, B = belite, Y = ye’elimite, Ah = anhydrite, CAH <sub>10</sub> = calcium aluminat hydrates, AH <sub>3</sub> = aluminium hydroxide. ....	106
Fig. 5-5 Comparison of XRD patterns of (a) LGC, (b) LGCMK, (c) LGCMKLS and (d) CSA at 90 days of hydration at 5, 20, 40 and 60°C: E = ettringite, CH = Portlandite, Ms = monosulfate, Hc = hemicarbonat, Mc = monocarbonat, AFm <sub>ss</sub> = solid solution of AFm (SO <sub>3</sub> -OH-CO <sub>3</sub> ), S = strätlingite, Si-HG = siliceous hydrogarnet, Q = Quartz, Cc = calcite, B = belite, Y = ye’elimite, AH <sub>3</sub> = aluminium hydroxide. ....	107
Fig. 5-6 Comparison of the phase assemblages in (a) LGC, (b) LGCMK, (c) LGCMKLS and (d) CSA after 90 days of hydration at different temperatures determined by XRD Rietveld analysis.....	108
Fig. 5-7 Comparison of bound water content at different temperatures in (a) LGC, (b) LGCMK, (c) LGCMKLS and (d) CSA. ....	109
Fig. 5-8 Comparison of the microstructures of LGC at 90 days cured at 5, 20, 40 and 60°C.....	110
Fig. 5-9 Comparison of the microstructures of LGCMK at 90 days cured at 5, 20, 40 and 60°C. ....	111
Fig. 5-10 Comparison of the microstructures of LGCMKLS at 90 days cured at 5, 20, 40 and 60°C. ...	111
Fig. 5-11 Comparison of the microstructures of CSA at 90 days cured at 5, 20, 40 and 60°C.....	112
Fig. 5-12 Comparison of the C-S-H formation around the clinker grains of (a) LGCMK and (b) CSA at 90 days of hydration cured at 60°C.....	113

Fig. 5-13 The BSE image of the microstructure of C-S-H formed in the CSA system at 90 days of hydration cured at 60°C with magnification of (a) 1000x and (b) 3000. ....	113
Fig. 5-14 EDS ratio plot of Si/Ca and Al/Ca from the mapping data of (a) LGCMK and (b) CSA at 20°C. Strätlingite was selected as red with the edxia interface [35]. ....	114
Fig. 5-15 Comparison of strätlingite formation in the microstructure of (a) LGCMK and (b) CSA cured at 20°C. ....	114
Fig. 5-16 MIP porosity of the investigated systems (a) LGC, (b) LGCMK, (c) LGCMKLS and (d) CSA at different curing temperatures at 90 days of hydration. ....	115
Fig. 5-17 The effect of temperature on the compressive strength development of (a) LGC, (b) LGCMK, (c) LGCMKLS and (d) CSA. ....	116
Fig. 5-18 Relation between the formation of $CAH_{10}$ at 5°C and/or $AH_3$ at 20 - 60°C and belite reaction in the CSA system. ....	117
Fig. 5-19 The DoH of clinker of (a) LGC, (b) LGCMK, (c) LGCMKLS and (d) CSA at different curing temperatures. ....	118
Fig. 5-20 Comparison of compressive strength and degree of hydration (DoH) of clinker calculated by XRD Rietveld quantification: (a) LGC, (b) LGCMK, (c) LGCMKLS and (d) CSA. ....	119
Fig. 5-21 Comparison of compressive strength and total porosity measured by MIP at 90 days. ....	120
Fig. 5-22 Comparison of compressive strength and CWF of the investigated systems at different temperatures. ....	121
Fig. 5-23 Comparison of ettringite content at different temperatures of (a) LGC, (b) LGCMK, (c) LGCMKLS and (d) CSA. ....	126
Fig. 5-24 Comparison of monosulfate content at different temperatures of (a) LGC, (b) LGCMK, (c) LGCMKLS and (d) CSA. ....	127
Fig. 5-25 Comparison of strätlingite content at different temperatures of (a) LGCMK, (b) LGCMKLS, and (c) CSA. ....	128
Fig. 5-26 Comparison of portlandite content at different temperatures of (a) LGC, (b) LGCMK and (c) LGCMKLS. ....	128
Fig. 5-27 The concentration of (a) S and (b) Al in the pore solution of the investigated systems at 5, 20, 40 and 60°C. ....	129
Fig. 5-28 Effective saturation indices of hydrate phases in (a) LGC, (b) LGCMK, (c) LGCMKLS and (d) CSA calculated from ion concentration of pore solution at 90 days: CH = portlandite, S = strätlingite, E = ettringite, $AH_3$ = aluminium hydroxide. ....	131
Fig. 5-29 Comparison of combined water fraction (CWF) and compressive strength calculated by TGA: (a) LGC, (b) LGCMK, (c) LGCMKLS and. ....	132
Fig. 6-1 Sample curing for transport property test. ....	138
Fig. 6-2 The sample after applying 0.1N $AgNO_3$ on the surface. The chloride penetration depth (d) was measured at the white and brown boundary. ....	139
Fig. 6-3 Schematic of estimation of the effective chloride diffusion coefficient ( $D_{eff}$ ) from mini-migration test. ....	140
Fig. 6-4 A sample mounted with a plastic ring by silicone. ....	141
Fig. 6-5 The setup of mini-migration test. ....	141

Fig. 6-6 A typical result of the evolution of chloride mass obtained by the chloride titration from the downstream sampling solution as a function of time.....142

Fig. 6-7 Chloride penetration depth cured in a saturated condition for 28 days and exposed in 0.5M NaCl solution at (a) room temperature and (b) the same curing temperature of the investigated systems for 9 months for the PC system and 6 months for the CSA system.....145

Fig. 6-8 The crack samples of the CSA system cured and exposed at 60°C after applied AgNO<sub>3</sub> on the surface of the sample. The area without chloride can be observed in some parts. ....145

Fig. 6-9 Effective diffusion coefficient of the investigated systems cured in the saturated condition at 5, 20, 40 and 60°C for 28 days of hydration. The test was carried out at room temperature for all the sample. 147

Fig. 6-10 Effective conductivity of (a) LGC, (b) LGCMK, (c) LGCMKLS and (d) CSA cured at 5, 20, 40 and 60°C as a function of time. ....148

Fig. 6-11 Pore solution conductivity ( $\sigma_0$ ) as a function of OH<sup>-</sup> concentration of pore solution. ....149

Fig. 6-12 (a) Electrical conductivity and (b) OH<sup>-</sup> concentration of pore solution of LGC, LGCMK, LGCMKLS and CSA cured at different temperatures.....150

Fig. 6-13 (a) Formation factor and (b) inverse formation factor calculated by conductivity. ....152

Fig. 6-14 Tortuosity (defined by Equation 6-7) of the investigated systems at different temperatures.153

Fig. 6-15 The increase of effective conductivity value of CSA cured in 0.3M NaOH compared to pore solution curing measured at 28 days.....154

Fig. 6-16 The relationship between the effective conductivity and the effective diffusion coefficient,  $D_{eff}$ , from the mini migration test of the investigated systems at 28 days.....155

Fig. 6-17 Relationship between (a) the penetration depth (9 months for the PC systems, 6 months for the CSA system) exposed at different temperature and the effective conductivity at 180d and (b) the penetration depth and the effective diffusion coefficient ( $D_{eff}$ ) exposed at room temperature of the investigated systems.....156

Fig. 6-18 Current curves during the mini migration test of (a) LGC, (b) LGCMK, (c) LGCMKLS and (d) CSA systems with two duplicates cured in the saturated condition for 28 days. ....160

Fig. 6-19 Phase assemblages of CSA at 28 days of hydration compared between pore solution curing and 0.3M NaOH curing determined from XRD-Rietveld. ....161

Fig. 6-20 The appearance of the up and down sample surface exposed in (a) 0.3M NaOH, (b) 0.025M NaOH and (c) 0.025M NaOH + 0.01 Al<sub>2</sub>(SO<sub>4</sub>)<sub>3</sub> after mini migration test.....162

Fig. 6-21 The damage of the down surface when the solution 2 and 3 are used. ....163

Fig. 6-22 Comparison of current monitored during the mini migration test: (a) 0.3M NaOH and (b) 0.025M NaOH. ....163

Fig. 7-1 Comparison of the raw materials CO<sub>2</sub> emission to the production of stoichiometric phases as given in [1] to the compressive strength at 90 days. ....169

Fig. 7-2 Comparison of the raw materials CO<sub>2</sub> emission of the investigated systems according to the production of stoichiometric phases as given in [1] to the compressive strength at different temperatures. ....169

## List of Tables

Table 2-1 The composition of binder for sulfate adjustment (in wt%).	31
Table 2-2 Chemical reagents and mix design used for a laboratory prepared belite-ye'elimite clinker.	32
Table 2-3 The composition (wt %) of belite-ye'elimite clinker from different batches	34
Table 2-4 The clinker batch used in the experiment with mayenite optimization.	36
Table 2-5: Chemical composition and particle size value of the raw materials.	37
Table 2-6 Parameters used for particle size distribution analysis.	37
Table 2-7 Phase composition of the raw materials.	38
Table 2-8 Mix designs and chemical composition of the investigated systems.	39
Table 3-1 Elemental and mineral composition and particle sizes of the raw materials.	44
Table 3-2 Cement composition (wt.%) of the investigated systems	44
Table 3-3 Mineralogical references for quantitative Rietveld refinement on XRD patterns (ICSD).	46
Table 3-4: Average C-(A)-S-H composition of the investigated systems at 5, 20, 40 and 60°C analysed by EDS point analysis.	51
Table 3-5 Summary hydrated phase assemblage precipitation in the investigated systems at different temperatures from the experimental observation at 90 days of hydration compared to thermodynamic modelling prediction.	71
Table 4-1: Chemical composition, mineralogy and distribution value of the raw materials.	76
Table 5-1: Chemical composition and particle size value of the raw materials	98
Table 5-2: Phase composition of the raw materials.	99
Table 5-3: Composition of the investigated systems (mass %).	100
Table 5-4: Molar ratio of the main elements in the investigated system	100
Table 5-5: Ion concentrations in the pore solution at 90 days of hydration of the investigated system at 5, 20, 40 and 60°C.	130
Table 6-1: Chemical composition and particle size value of the raw materials	136
Table 6-2: Phase composition of the raw materials.	137
Table 6-3: Composition of the investigated systems (% mass).	138
Table 6-4 The applied voltage (V) of each system for the mini migration test	142
Table 6-5 Chloride penetration depth in the bulk diffusion test of the investigated systems.	146
Table 6-6 The ion concentrations in the pore solution of the PC and CSA systems cured at 5,20, 40 and 60°C at 90 days. OH <sup>-</sup> was estimated by charge balance.	151
Table 6-7 Parameters used in the preliminary study	162
Table 7-1 CO <sub>2</sub> emission and % CO <sub>2</sub> reduction of the investigated system considering only the chemical contribution to CO <sub>2</sub> emission.	168

# Chapter 1 Introduction

## CONTENTS

---

<b>Chapter 1</b>	<b>Introduction .....</b>	<b>19</b>
1.1	Background of the thesis.....	20
1.2	Objectives of the thesis.....	21
1.3	Research approach and the content of the thesis .....	21
1.4	References.....	24

---

## 1.1 Background of the thesis

Concrete is the most used as construction materials because it is cheap and has good performance. The demand for concrete rises every year. The main component of concrete is cement which releases 0.65 to 0.95 tons of CO<sub>2</sub> per one ton produced [1]. There are two main sources of CO<sub>2</sub> in cement production [2]. First (about 60%) is the decomposition of limestone, the main ingredient of the raw meal, to produce clinker. Second is the fuel needed to produce the temperature around 1450°C needed to produce clinker. Most current research on cements is motivated to reduce CO<sub>2</sub> emission from the cement production.

There are two main approaches to lower the CO<sub>2</sub> emissions related to the cement [2]. The first approach is to use supplementary cementitious materials (SCMs). This approach can reduce CO<sub>2</sub> emission by lowering the clinker factor in cement. Replacing clinker with SCMs such as fly ash (low and high Ca fly ash), ground granulated blast furnace slag (GGBFS) and natural or industrial pozzolans to Portland cement is a common practice in the cement industry, but these classic SCMs are in relative short supply compared to the demand for cement [3]. Calcined clay containing metakaolin is one of the promising materials to increase the supply of SCMs because it is very abundant and widely available worldwide [4]. Metakaolin, an amorphous aluminosilicate-rich material, is also more reactive than common SCMs such as fly ash [5]. Finally, the substitution level of metakaolin with limestone can reach 50% with similar mechanical properties to plain Portland cement at 7 days [6].

The other approach to reduce CO<sub>2</sub> emission is to use alternative binders which can reduce the firing temperature and the limestone content in a raw meal. One example of these binders is calcium sulfoaluminate (CSA) cements which contain ye'elimite (C<sub>4</sub>A<sub>3</sub>S̄ or Ca<sub>4</sub>Al<sub>6</sub>O<sub>12</sub>SO<sub>4</sub>) as the main reactive component. There are different types of CSA cement depending on their composition: high ye'elimite and low ye'elimite commonly called BYF (Belite-Ye'elimite-Ferrite). CSA is generally produced with the same process as Portland cement clinker but the firing temperature is about 200°C lower [7]. BYF cements or high belite CSA cement are of interest due to lower cost of raw materials than the high ye'elimite CSA. The CO<sub>2</sub> emission of BYF clinker can be reduced about 30% compared to Portland cement [8].

CSA and OPC blended with metakaolin have higher alumina contents compared to the Portland cement composition. Although the phase compositions of these binders and the hydration kinetics are different [9], the overall chemical composition is similar, so, it might be expected, that the final phase assemblage at complete hydration would be similar [9]. In the PC based system, the reaction of C<sub>3</sub>S starts first, resulting in the precipitation of C-S-H and portlandite. The reaction of metakaolin provides additional C-S-H and AFm phases due to the pozzolanic reaction [10]. When the content of metakaolin is high enough, strätlingite can be observed [11,12]. In the case of CSA, ye'elimite reacts first with sulfate leading to the formation of ettringite, monosulfate and aluminium hydroxide. Monocarbonate, gibbsite or hydrogarnet can be found depending on the presence of minor phases in CSA cement [13]. The reaction of belite is slower, resulting in the formation of strätlingite and C-S-H at later age [13].

These two types of low CO<sub>2</sub> binders with similar chemical composition have been previously investigated by M. Zajac et. al. [9]. The phases formed were ettringite, AFm, C-S-H and strätlingite but the quantities were different depending on the reaction kinetics of anhydrous phases in the binders. The phase assemblages formed in the different systems had a strong influence on the microstructure. The microstructure is only densified when the silicate phase starts to react. This study investigated the hydration and microstructure at room temperature but did not link these to the properties of these two types of low CO<sub>2</sub> binders.

Most previous investigations of low CO<sub>2</sub> binder have been at room temperature but in practice concrete is used in different climates. The hydration of cementitious materials is sensitive to temperature. The hydration rate is decreased at low temperature and enhanced with increasing temperature. The influence of temperature on the hydration of Portland cement [14–19] was well investigated and some studies have been made on blended cements [20–22]. However, the effect of temperature on the hydration of metakaolin blends [23,24] and CSA [25–27] are scarce in

the literature. The sensitivity to temperature is important to verify if a cement can be used reliably in a wide range of conditions.

Thermodynamic modelling is more and more used because it helps to understand the effect of binder composition or temperature on hydrate assemblage [28]. Thermodynamic modelling of hydrate phase assemblages was studied and verified in the real Portland cement system [16,29,30]. However, there are several difficulties to apply thermodynamic modelling to higher alumina systems. Siliceous hydrogarnet, which may form in such systems, is not well crystalline and difficult to detect by XRD or TGA. Thermodynamically incompatible hydrates are often observed co-existing, e.g. strätlingite and portlandite, in the real systems of Portland cement blended with metakaolin [12,31]. For CSA, thermodynamic modelling has also been used to predict the phase assemblages in the studies of BYF cement [13,32,33]. The presence of alumina-containing amorphous phases (i.e. aluminium hydroxide) and metastable phases (i.e.  $\text{CAH}_{10}$ ) are challenging to quantify. The stability of these phases changes as a function of temperature [34], making prediction of phases assemblage thermodynamic modelling difficult.

Good mechanical properties are the first requirement for the construction materials. Several studies have looked at the relation of hydration and microstructure to the compressive strength in the higher alumina system at room temperature [6,31,33,35,36]. However, understanding of the influence of temperature on compressive strength in these systems is still limited [25,37].

Concrete is a construction material used in various environments e.g. in sea water. Therefore, it is important to also study durability. Some studies claimed that higher alumina systems show good performance with respect to chloride resistance [38–40]. However, the effect of temperature on the chloride ingress and a direct comparison between the metakaolin blends and the CSA system have not been reported.

## 1.2 Objectives of the thesis

The general goal of this thesis is to identify the influence of temperature on the hydration and microstructure of two higher alumina systems with similar chemical composition but contrasting reactions, and to link these to the properties and durability performance of the materials. The chemical composition was decided to minimize the iron content to reduce the number of variables and facilitate NMR.

## 1.3 Research approach and the content of the thesis

Portland cement blended with metakaolin and a laboratory produced belite-ye'elimite binder are the higher alumina binders studied in this thesis. The compositions of these two systems were chosen to have a similar chemical composition as seen in the ternary plot in Fig. 1-1. Therefore, differences in phase assemblage comes from the hydration process. The presence of limestone in the metakaolin blends was also investigated. Plain Portland cement was used as a reference system. For the CSA system, BY clinker was produced in the laboratory with no ferrite to be able to compare with the PC systems which aimed to use a low iron content in the system. The main parameter investigated was temperature. Realistic temperature conditions were studied: 5, 20, 40 and 60°C. The water to binder ratio (w/b) was fixed at 0.6 so the hydration was not significantly limited by the space available. It is irrelatively high w/b ratio than used in practice to ensure high degree of hydration can be achieved for the comparison with thermodynamic modelling.





further investigated to identify possible kinetic hindrance phenomena, or the need for improvement in the thermodynamic database.

**Chapter 4** provides the result of phase assemblages of the CSA system. Following the same approach as given in Chapter 3.

**Chapter 5** looks at the kinetics of reaction in the two systems. Phase evolution and bound water were investigated with time as a function of temperature. Various techniques were applied to the two contrasting systems for microstructural characterization. The microstructures of the high alumina system at 90 days are compared, then linked to the hydrate formation in the microstructure. The MIP porosity of the investigated system are also reported in this chapter. The link between compressive strength and the phase assemblage and microstructure. The combined water fraction (CWF) [42] was applied to investigate the correlation between the formation of hydrates and the compressive strength. The degree of hydration of clinker and porosity are also examined to relate with the compressive strength. The effect of microstructure and the contribution of the C-S-H in the CSA to the compressive strength are also discussed.

**Chapter 6** reports the results on the transport properties focusing on the chloride ingress for the investigated system at different temperatures. To be able to understand and explain the chloride ingress in the cement paste, the effective diffusion coefficient obtained from the mini-migration method [38] was compared to the penetration depth from the bulk diffusion test. . The effective conductivity and the ion conductivity were studied to understand the ion transport properties in the cement pastes. The possibilities of applying the techniques which are based on the PC setup to the CSA system is also discussed.

**Chapter 7** summarizes the main findings and provides perspectives for the future work.

## 1.4 References

- [1] N. Müller, J. Harnisch, A blueprint for a climate friendly cement industry, (2008). [https://wwfeu.awsassets.panda.org/downloads/english\\_report\\_lr\\_pdf.pdf](https://wwfeu.awsassets.panda.org/downloads/english_report_lr_pdf.pdf).
- [2] E. Gartner, H. Hirao, A review of alternative approaches to the reduction of CO<sub>2</sub> emissions associated with the manufacture of the binder phase in concrete, *Cem. Concr. Res.* 78 (2015) 126–142. <https://doi.org/10.1016/j.cemconres.2015.04.012>.
- [3] K.L. Scrivener, V.M. John, E.M. Gartner, Eco-efficient cements: Potential economically viable solutions for a low-CO<sub>2</sub> cement-based materials industry, *Cem. Concr. Res.* 114 (2018) 2–26. <https://doi.org/10.1016/j.cemconres.2018.03.015>.
- [4] K. Scrivener, F. Martirena, S. Bishnoi, S. Maity, Calcined clay limestone cements (LC3), *Cem. Concr. Res.* 114 (2018) 49–56. <https://doi.org/10.1016/j.cemconres.2017.08.017>.
- [5] J. Skibsted, R. Snellings, Reactivity of supplementary cementitious materials (SCMs) in cement blends, *Cem. Concr. Res.* 124 (2019) 105799. <https://doi.org/10.1016/j.cemconres.2019.105799>.
- [6] M. Antoni, J. Rossen, F. Martirena, K. Scrivener, Cement substitution by a combination of metakaolin and limestone, *Cem. Concr. Res.* 42 (2012) 1579–1589. <https://doi.org/10.1016/j.cemconres.2012.09.006>.
- [7] M.M. Ali, S. Gopal, S.K. Handoo, Studies on the formation kinetics of calcium sulphoaluminate, *Cem. Concr. Res.* 24 (1994) 715–720. [https://doi.org/10.1016/0008-8846\(94\)90196-1](https://doi.org/10.1016/0008-8846(94)90196-1).
- [8] L. Barcelo, J. Kline, G. Walenta, E. Gartner, Cement and carbon emissions, *Mater. Struct.* 47 (2014) 1055–1065. <https://doi.org/10.1617/s11527-013-0114-5>.
- [9] M. Zajac, S. Hoock, C. Stabler, M. Ben Haha, Effect of hydration kinetics on properties of compositionally similar binders, *Cem. Concr. Res.* 101 (2017) 13–24. <https://doi.org/10.1016/j.cemconres.2017.08.005>.
- [10] B. Lothenbach, K. Scrivener, R.D. Hooton, Supplementary cementitious materials, *Cem. Concr. Res.* 41 (2011) 1244–1256. <https://doi.org/10.1016/j.cemconres.2010.12.001>.
- [11] Z. Dai, T.T. Tran, J. Skibsted, Aluminum Incorporation in the C-S-H Phase of White Portland Cement-Metakaolin Blends Studied by <sup>27</sup>Al and <sup>29</sup>Si MAS NMR Spectroscopy, *J. Am. Ceram. Soc.* 97 (2014) 2662–2671. <https://doi.org/10.1111/jace.13006>.
- [12] W. Kunther, Z. Dai, J. Skibsted, Thermodynamic modeling of hydrated white Portland cement-metakaolin-limestone blends utilizing hydration kinetics from <sup>29</sup>Si MAS NMR spectroscopy, *Cem. Concr. Res.* 86 (2016) 29–41. <https://doi.org/10.1016/j.cemconres.2016.04.012>.
- [13] F. Winnefeld, B. Lothenbach, Hydration of calcium sulfoaluminate cements — Experimental findings and thermodynamic modelling, *Cem. Concr. Res.* 40 (2010) 1239–1247. <https://doi.org/10.1016/j.cemconres.2009.08.014>.
- [14] X. Zhang, Quantitative microstructural characterisation of concrete cured under realistic temperature conditions, 2007.
- [15] B. Lothenbach, F. Winnefeld, C. Alder, E. Wieland, P. Lunk, Effect of temperature on the pore solution, microstructure and hydration products of Portland cement pastes, *Cem. Concr. Res.* 37 (2007) 483–491. <https://doi.org/10.1016/j.cemconres.2006.11.016>.

- [16] B. Lothenbach, T. Matschei, G. Möschner, F.P. Glasser, Thermodynamic modelling of the effect of temperature on the hydration and porosity of Portland cement, *Cem. Concr. Res.* 38 (2008) 1–18. <https://doi.org/10.1016/j.cemconres.2007.08.017>.
- [17] J.I. Escalante-García, J.H. Sharp, Effect of temperature on the hydration of the main clinker phases in portland cements: part i, neat cements, *Cem. Concr. Res.* 28 (1998) 1245–1257. [https://doi.org/10.1016/S0008-8846\(98\)00115-X](https://doi.org/10.1016/S0008-8846(98)00115-X).
- [18] A.M. Gajewicz-Jaromin, P.J. McDonald, A.C.A. Muller, K.L. Scrivener, Influence of curing temperature on cement paste microstructure measured by <sup>1</sup>H NMR relaxometry, *Cem. Concr. Res.* 122 (2019) 147–156. <https://doi.org/10.1016/j.cemconres.2019.05.002>.
- [19] E. Gallucci, X. Zhang, K.L. Scrivener, Effect of temperature on the microstructure of calcium silicate hydrate (C-S-H), *Cem. Concr. Res.* 53 (2013) 185–195. <https://doi.org/10.1016/j.cemconres.2013.06.008>.
- [20] J.I. Escalante-García, J.H. Sharp, Effect of temperature on the hydration of the main clinker phases in portland cements: part ii, blended cements, *Cem. Concr. Res.* 28 (1998) 1259–1274. [https://doi.org/10.1016/S0008-8846\(98\)00107-0](https://doi.org/10.1016/S0008-8846(98)00107-0).
- [21] T. Matschei, F.P. Glasser, Temperature dependence, 0 to 40°C, of the mineralogy of Portland cement paste in the presence of calcium carbonate, *Cem. Concr. Res.* 40 (2010) 763–777. <https://doi.org/10.1016/j.cemconres.2009.11.010>.
- [22] F. Deschner, B. Lothenbach, F. Winnefeld, J. Neubauer, Effect of temperature on the hydration of Portland cement blended with siliceous fly ash, *Cem. Concr. Res.* 52 (2013) 169–181. <https://doi.org/10.1016/j.cemconres.2013.07.006>.
- [23] F. Avet, Effect of temperature on the water content of C-A-S-H in plain Portland and blended cements, *Cem. Concr. Res.* (2020) 6.
- [24] M.F. Rojas, J. Cabrera, The effect of temperature on the hydration rate and stability of the hydration phases of metakaolin–lime–water systems, *Cem. Concr. Res.* 32 (2002) 133–138. [https://doi.org/10.1016/S0008-8846\(01\)00642-1](https://doi.org/10.1016/S0008-8846(01)00642-1).
- [25] P. Wang, N. Li, L. Xu, Hydration evolution and compressive strength of calcium sulphoaluminate cement constantly cured over the temperature range of 0 to 80 °C, *Cem. Concr. Res.* 100 (2017) 203–213. <https://doi.org/10.1016/j.cemconres.2017.05.025>.
- [26] J. Kaufmann, F. Winnefeld, B. Lothenbach, Stability of ettringite in CSA cement at elevated temperatures, *Adv. Cem. Res.* 28 (2016) 251–261. <https://doi.org/10.1680/jadcr.15.00029>.
- [27] L. Xu, S. Liu, N. Li, Y. Peng, K. Wu, P. Wang, Retardation effect of elevated temperature on the setting of calcium sulfoaluminate cement clinker, *Constr. Build. Mater.* 178 (2018) 112–119. <https://doi.org/10.1016/j.conbuildmat.2018.05.061>.
- [28] B. Lothenbach, M. Zajac, Application of thermodynamic modelling to hydrated cements, *Cem. Concr. Res.* 123 (2019) 105779. <https://doi.org/10.1016/j.cemconres.2019.105779>.
- [29] B. Lothenbach, F. Winnefeld, Thermodynamic modelling of the hydration of Portland cement, *Cem. Concr. Res.* 36 (2006) 209–226. <https://doi.org/10.1016/j.cemconres.2005.03.001>.

- [30] B. Lothenbach, D.A. Kulik, T. Matschei, M. Balonis, L. Baquerizo, B. Dilnesa, G.D. Miron, R.J. Myers, Cemdata18: A chemical thermodynamic database for hydrated Portland cements and alkali-activated materials, *Cem. Concr. Res.* 115 (2019) 472–506. <https://doi.org/10.1016/j.cemconres.2018.04.018>.
- [31] M. Zajac, P. Durdzinski, C. Stabler, J. Skocek, D. Nied, M. Ben Haha, Influence of calcium and magnesium carbonates on hydration kinetics, hydrate assemblage and microstructural development of metakaolin containing composite cements, *Cem. Concr. Res.* 106 (2018) 91–102. <https://doi.org/10.1016/j.cemconres.2018.01.008>.
- [32] F. Winnefeld, B. Lothenbach, Phase equilibria in the system  $\text{Ca}_4\text{Al}_6\text{O}_{12}\text{SO}_4 - \text{Ca}_2\text{SiO}_4 - \text{CaSO}_4 - \text{H}_2\text{O}$  referring to the hydration of calcium sulfoaluminate cements, *RILEM Tech. Lett.* (2016) 7.
- [33] M. Zajac, J. Skocek, C. Stabler, F. Bullerjahn, M. Ben Haha, Hydration and performance evolution of belite–ye’elimite–ferrite cement, *Adv. Cem. Res.* 31 (2019) 124–137. <https://doi.org/10.1680/jadcr.18.00110>.
- [34] B. Lothenbach, L. Pelletier-Chaignat, F. Winnefeld, Stability in the system  $\text{CaO}-\text{Al}_2\text{O}_3-\text{H}_2\text{O}$ , *Cem. Concr. Res.* 42 (2012) 1621–1634. <https://doi.org/10.1016/j.cemconres.2012.09.002>.
- [35] J. Skocek, M. Zajac, C. Stabler, M. Ben Haha, Predictive modelling of hydration and mechanical performance of low Ca composite cements: Possibilities and limitations from industrial perspective, *Cem. Concr. Res.* 100 (2017) 68–83. <https://doi.org/10.1016/j.cemconres.2017.05.020>.
- [36] M. Zajac, J. Skocek, S. Adu-Amankwah, L. Black, M. Ben Haha, Impact of microstructure on the performance of composite cements: Why higher total porosity can result in higher strength, *Cem. Concr. Compos.* 90 (2018) 178–192. <https://doi.org/10.1016/j.cemconcomp.2018.03.023>.
- [37] K. Quillin, Performance of belite–sulfoaluminate cements, *Cem. Concr. Res.* 31 (2001) 1341–1349. [https://doi.org/10.1016/S0008-8846\(01\)00543-9](https://doi.org/10.1016/S0008-8846(01)00543-9).
- [38] W. Wilson, F. Georget, K. Scrivener, Unravelling chloride transport/microstructure relationships for blended-cement pastes with the mini-migration method, *Cem. Concr. Res.* 140 (2021) 106264. <https://doi.org/10.1016/j.cemconres.2020.106264>.
- [39] F.P. Glasser, L. Zhang, High-performance cement matrices based on calcium sulfoaluminate–belite compositions, *Cem. Concr. Res.* 31 (2001) 1881–1886. [https://doi.org/10.1016/S0008-8846\(01\)00649-4](https://doi.org/10.1016/S0008-8846(01)00649-4).
- [40] S. Sui, F. Georget, H. Maraghechi, W. Sun, K. Scrivener, Towards a generic approach to durability: Factors affecting chloride transport in binary and ternary cementitious materials, *Cem. Concr. Res.* 124 (2019) 105783. <https://doi.org/10.1016/j.cemconres.2019.105783>.
- [41] K. Scrivener, R. Snellings, B. Lothenbach, eds., *A practical guide to microstructural analysis of cementitious materials*, CRC Press, Boca Raton, 2016.
- [42] V.M. John, M. Quattrone, P.C.R.A. Abrão, F.A. Cardoso, Rethinking cement standards: Opportunities for a better future, *Cem. Concr. Res.* 124 (2019) 105832. <https://doi.org/10.1016/j.cemconres.2019.105832>.

# Chapter 2 Materials preparation

## CONTENTS

---

<b>Chapter 2</b>	<b>Materials preparation.....</b>	<b>27</b>
2.1	Portland cement (PC) system.....	28
2.1.1	Commercial cement.....	28
2.1.2	Sulfate optimization.....	30
2.2	Calcium sulfoaluminate system (CSA).....	32
2.2.1	Clinker synthesis .....	32
2.2.2	Mayenite adjustment.....	34
2.3	Characterization of raw materials.....	36
2.4	References.....	40

---

## 2.1 Portland cement (PC) system

### 2.1.1 Commercial cement

One of the main goals of this project is to study hydration as a function of temperature of higher alumina systems. The studied systems need to react correctly over the temperature range studied. In particular, aluminates hydration must be correctly controlled to occur after the silicate reaction. Sulfate is used in cement to retard the  $C_3A$  reaction so it mainly takes place after the  $C_3S$  reaction and to prevent flash setting [1]. Fig. 2-1 shows a typical calorimetry curve of a Portland cement with a correct level of sulfate addition. The reactions of  $C_3S$  and aluminates are indicated. The first peak is associated with an alite reaction. The second peak is attributed to the aluminate reaction. The third peak corresponds to the formation of AFm phases. However, the temperature modifies the relative extent of reaction of alite and  $C_3A$ . Therefore, the sulfate addition must be corrected for all temperatures.

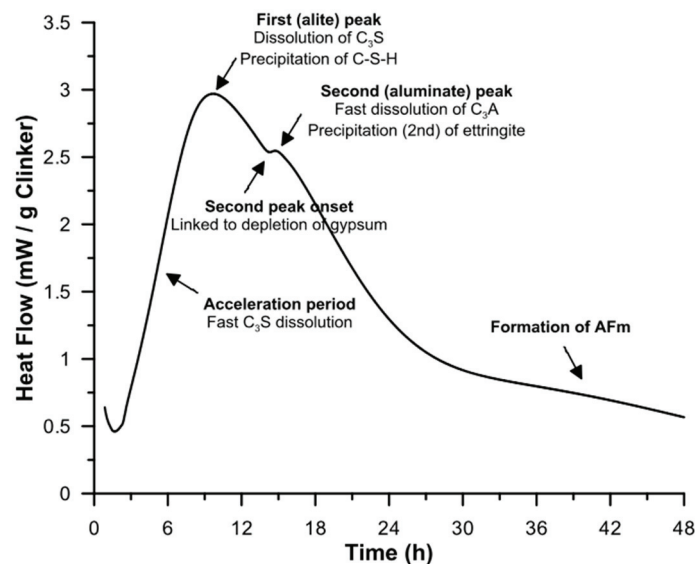


Fig. 2-1 A typical heat flow curve of OPC [2].

Ideally, all system should have a similar  $SO_3$  content at all temperatures in order to be able to compare the thermodynamic calculations easily. The sulfate addition was verified from the heat of hydration obtained by isothermal calorimetry. Initially, the project was designed for White Portland cement (WPC) because the solid-state NMR was planned to quantify the anhydrous reactions, in particular metakaolin [3]. This technique has a better noise to signal ration when the iron content is low. Hence, WPC was used for the initial hydration study during the first year. For sulfate adjustment, a chemical grade gypsum (G) was used in this study. With higher temperatures, there were a lot of problems from undersulfation, as shown in Fig. 2-2. The aluminate reaction is accelerated with increasing temperature. At  $60^\circ C$ , silicate and aluminate peaks are combined even when a high sulfate content was used (5 wt.%). The results show that the reactions of silicate and aluminate cannot be clearly separated at high temperature although more gypsum was added. The problem became worse when WPC was blended with metakaolin and limestone, called WPCMKLS (see Fig. 2-3).

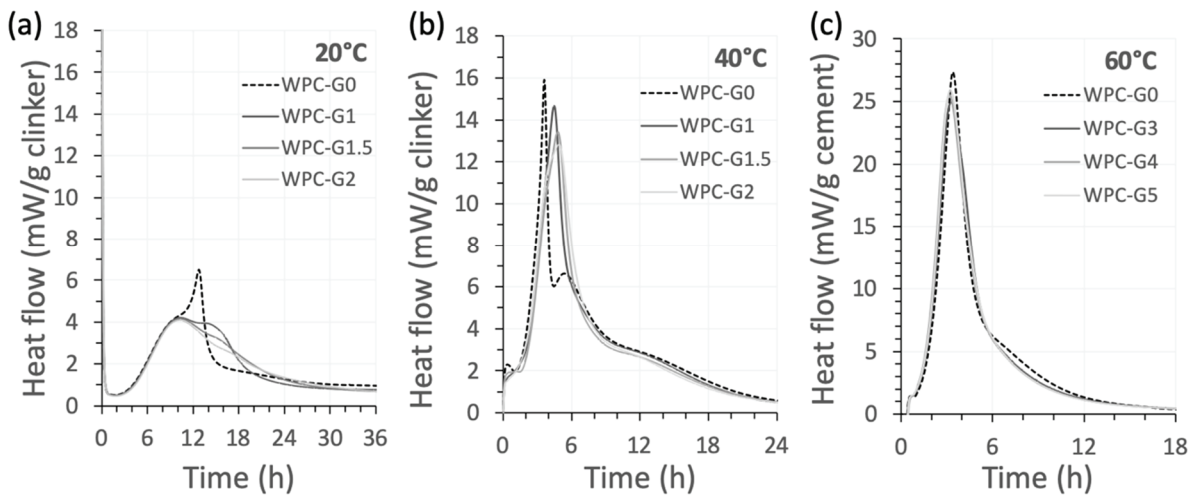


Fig. 2-2 Sulfate adjustment on white Portland cement at (a) 20, (b) 40 and (c) 60°C with additional sulfate in (wt.%)

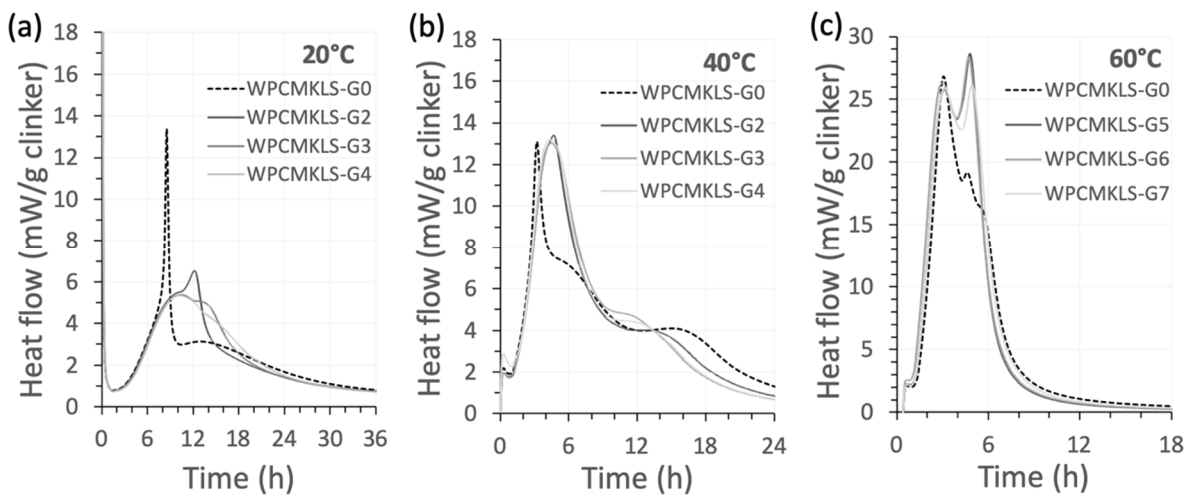


Fig. 2-3 Sulfate adjustment on white Portland cement blended with metakaolin and limestone (WPCMKLS) at (a) 20, (b) 40 and (c) 60°C with additional sulfate.

Therefore, progress was delayed until the focus was switched to a light grey cement (LGC) which is a Portland cement with low iron content (1.2%). LGC seems to be more stable with respect to sulfate addition.

The two types of cements; WPC and LGC, were studied by isothermal calorimetry. Fig. 2-4 shows the comparison of heat of hydration between WPC and LGC at 40°C when 3% of gypsum was added. WPC reacts slightly faster than LGC, but the silicate and aluminate peaks are overlapping, while for LGC it is still possible to separate the two peaks even without additional gypsum. At 40°C, when sulfate is added, the silicate peak is suppressed, while it is slightly enhanced for LGC. Because the hydration of LGC samples was more consistent with temperature, it was chosen as the main OPC-type cement for this project.



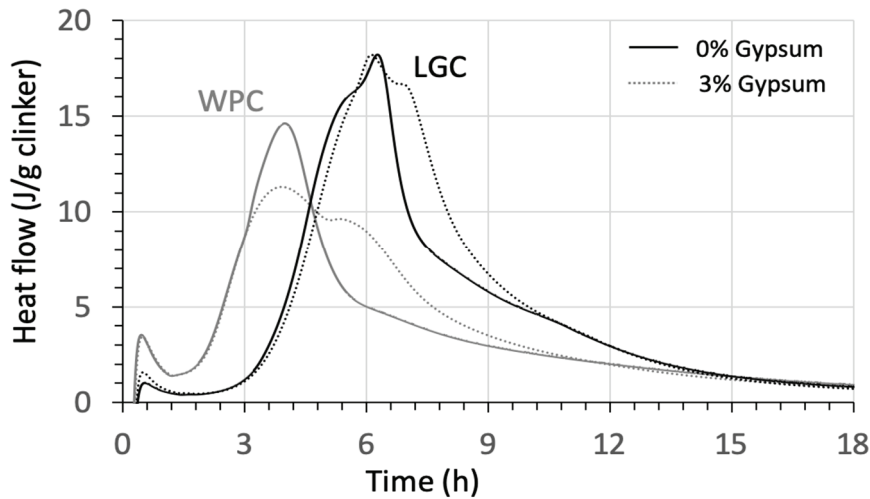


Fig. 2-4 Heat of hydration of WPC and LGC without gypsum and with 3% of gypsum at 40°C

### 2.1.2 Sulfate optimization

The heat flow of LGC as-received, which has optimized sulfate for 20°C and the two blended systems before adjusting the sulfate content at 20, 40 and 60°C are shown in Fig. 2-5. The aluminate peak of the blended systems is strongly increased and it slightly overlaps with the silicate peak when metakaolin (MK) is present. The heat flow curves at high temperature show undersulfation, therefore sulfate optimization is necessary at higher temperatures.

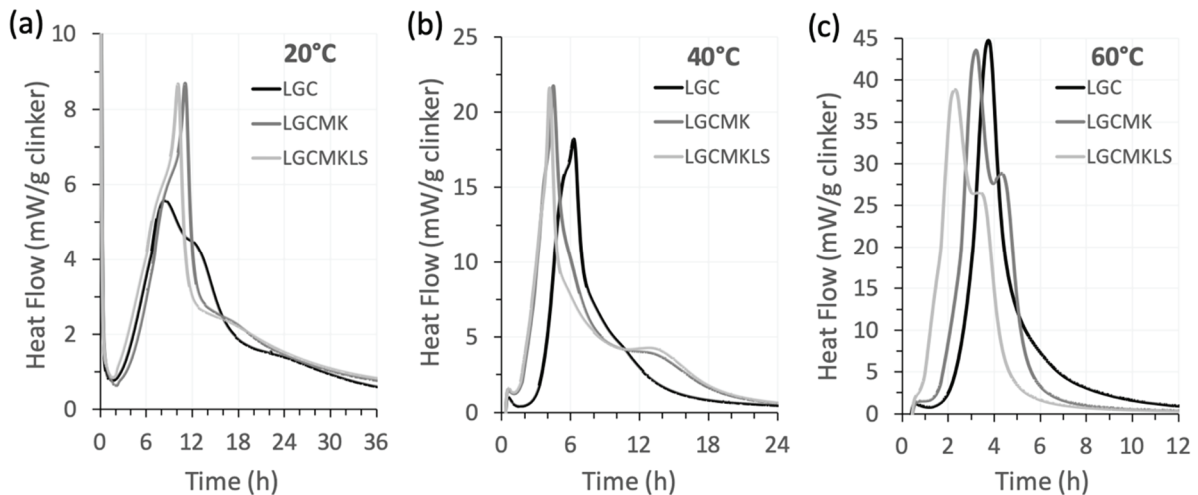


Fig. 2-5 Heat of hydration of LGC, LGCMK and LGCMKLS at temperatures of (a) 20, (b) 40 and (c) 60°C without additional sulfate.

Sulfate adjustment at 20, 40 and 60°C was carried out by using isothermal calorimetry (TAM Air, TA instrument). The composition of binders is shown in Table 2-1. The homogenized binders, deionized water, glass ampoules and caps were equilibrated overnight at the intended curing temperature before mixing. Cement paste was mixed with water to binder ratio of 0.4 by a bench top mixer with 1600 rounds per minute (rpm) for 2 minutes. A small amount of polycarboxylate (PCE) was added to obtain an adequate workability of the cement paste during the mixing. 10 g of paste

were transferred into a glass ampoule, sealed and placed in the calorimeter directly after mixing. Water was used as a reference sample with the same specific heat as the paste in this study.

The optimized gypsum contents in the blends at all temperatures were 3%, 4% and 4% by weight corresponding to the  $\text{SO}_3$  content in the cement of 4.6, 4.4 and 4.1% for LGC, LGCMK and LGCMKLS, respectively. The amount of  $\text{SO}_3$  in the cements for each system that was used in the subsequent studies is as shown in Fig. 2-6.

Table 2-1 The composition of binder for sulfate adjustment (in wt%).

	LGC	Metakaolin	Limestone
LGC	100	0	0
LGCMK	80	20	0
LGCMKLS	70	20	10

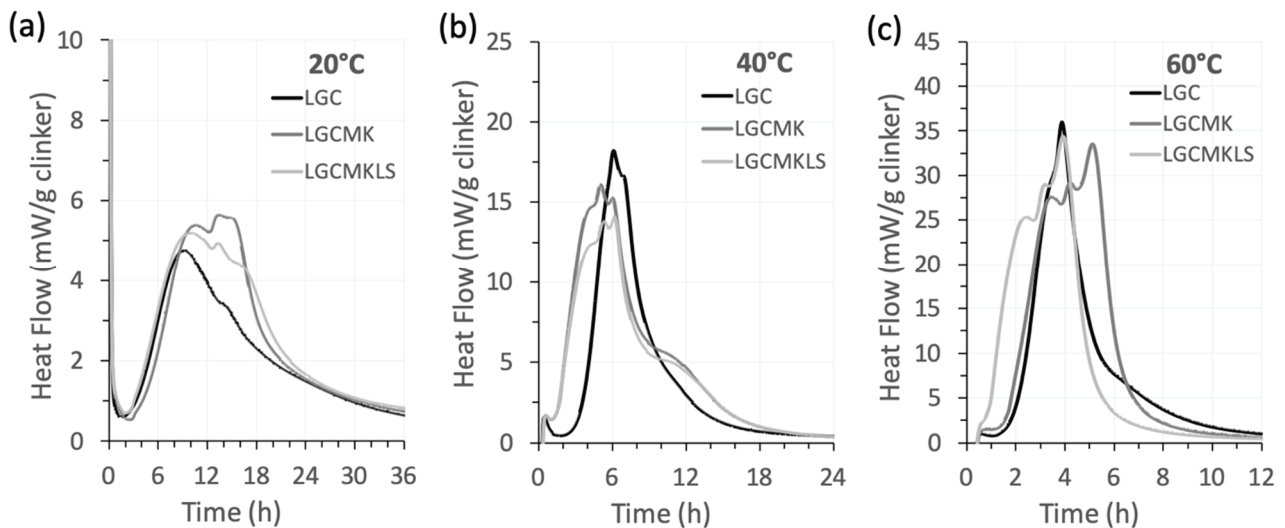


Fig. 2-6 Heat of hydration of LGC, LGCMK and LGCMKLS at temperatures of (a) 20, (b) 40 and (c) 60°C with sulfate optimization.

## 2.2 Calcium sulfoaluminate system (CSA)

The initial goal of this part was to synthesize belite clinker and ye'elimite clinker separately because it was planned to study the belite hydration. Ye'elimite synthesis was accomplished. However, belite synthesis could not be reproduced on a large scale due to a high gamma belite content which is not reactive. The details of clinker synthesis and basic characterization are in Appendix A. The trials of belite clinker synthesis were carried out for two years without success. Therefore, to obtain results before the end of the thesis, it was decided to use a polyphase clinker, easier to synthesize in large quantities.

### 2.2.1 Clinker synthesis

The target of the polyphase clinker was set to obtain 60% of  $\beta$ -belite and 40% of ye'elimite with less than 2% of minor phases such as lime and anhydrite and no alite. The raw materials used for a laboratory prepared belite-ye'elimite (BY) clinker are chemical reagent grade. The composition of the raw meal mix is shown in Table 2-2. The BY clinker was prepared using an adaptation of the cylinder method presented by X. Li et al. [4].

Table 2-2 Chemical reagents and mix design used for a laboratory prepared belite-ye'elimite clinker.

Oxides	Details	Brand	wt%
CaCO <sub>3</sub>	Precipitated low alkali content	VWR Chemicals	61.5
SiO <sub>2</sub>	Silica, fumed powder 0.007 $\mu$ m	ALDRICH	14.4
Al <sub>2</sub> O <sub>3</sub>	Aluminium oxide, anhydrous ( $\gamma$ -alumina)	MERCK	14.5
CaSO <sub>4</sub> .2H <sub>2</sub> O	Calciumsulfate Dihydrate $\geq$ 98%	Carl ROTH	9.6

The chemical reagents were mixed with distilled water with a water to solid ratio of 1:1 in a ceramic jar with ceramic balls. The raw meal was homogenized on a roller mill for 24 hours, then it was separated from the ceramic balls. The wet raw meal was transferred to cardboard cylindrical containers and dried in the oven at 110°C for at least 48 hours before sintering. The dried raw meal cylinders were transferred in platinum or alumina crucibles. The synthesis was carried out at 1300°C with a heating rate of 7°C/min and held at the maximum temperature for 1 hour in a static furnace. Then, the clinker was quenched from 1300°C at room temperature with air flow from an electric fan. The output of this laboratory clinker synthesis is about 500g per batch which corresponds to 3 cylinders of clinker. The schematic of clinker synthesis is shown in Fig. 2-7. Every clinker cylinder was sampled in the middle for the XRD analysis to control the quality of clinker, as shown in Fig. 2-8. The BY clinker was ground in a concentric disc mill in batches of 100 g for 30 seconds twice (60 seconds in total) with 7-10 drops of isopropanol as a grinding aid. The laboratory prepared clinker was ground by a disc mill, resulting in very fine particle size compared to the other raw materials.

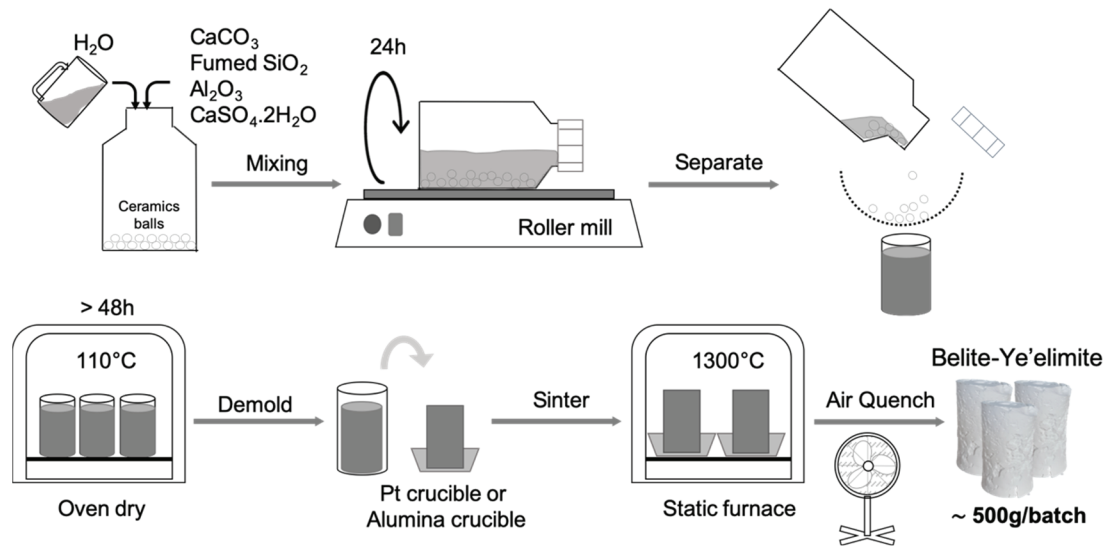


Fig. 2-7 A schematic of clinker synthesis adapted from the cylinder method [4].

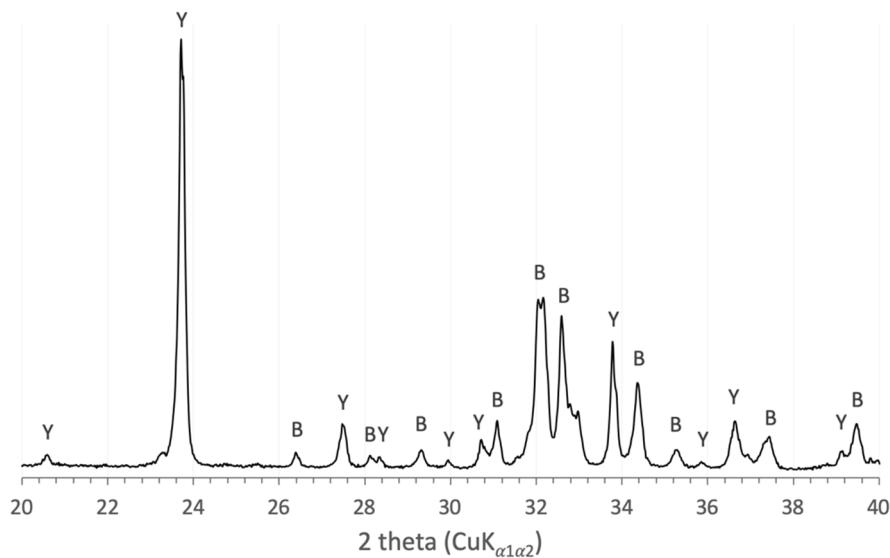


Fig. 2-8 XRD plot of a laboratory prepared belite-ye'elimate clinker: B = beta-belite, Y = ye'elimate.

The clinkers in some batches contain free lime and anhydrite as minor phases less than 1%. Free lime can accelerate the reaction of belite-ye'elimate clinker. However, the reaction is sensitive to the amount of free lime in the clinker, as shown in Fig. 2-9. In addition, it is difficult to control the content of free lime during synthesis to have the right amount for the reactivity. Therefore, free lime needs to be strictly controlled in the clinker less than 0.5%. 5 kg of ground clinker was combined into batches to achieve this target. The composition of belite-ye'elimate clinker from different batches is shown in Table 2-3.

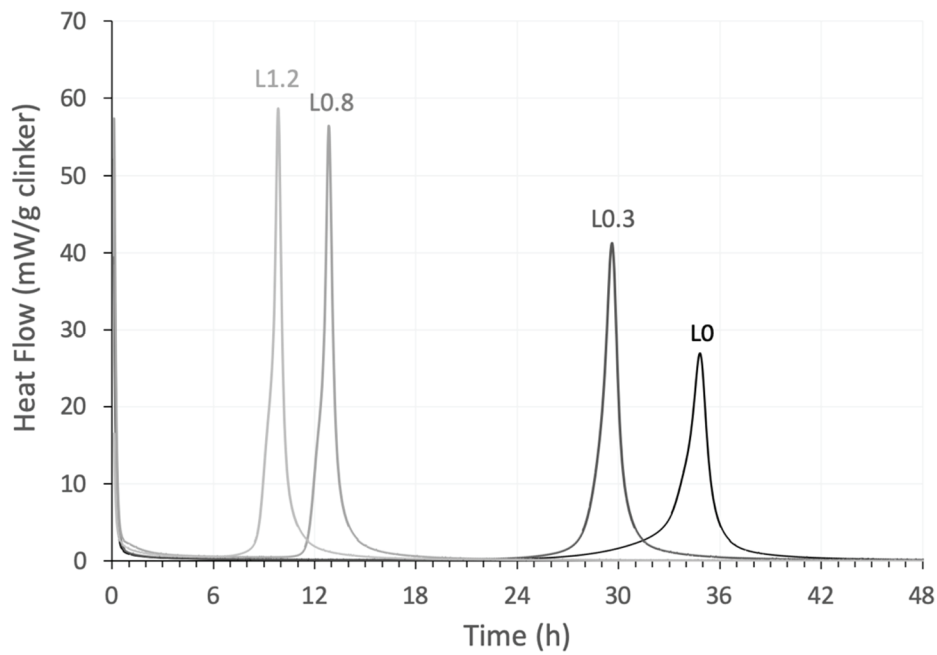


Fig. 2-9 Heat flow of different BY clinkers containing 0, 0.3, 0.8 and 1.2% free lime (L) with fixed calcium sulfate to ye'elimate ratio of 1:1 and water to binder ratio of 0.6.

Table 2-3 The composition (wt %) of belite-ye'elimate clinker from different batches

	Belite	Ye'elimate (orthorhombic)	Ye'elimate (cubic)	Free lime	Anhydrite
Batch 1	60.3	37.0	2.4	0.3	0.0
Batch 2	59.7	34.9	5.2	0.0	0.1
Batch 3	59.5	35.3	5	0.0	0.1
Batch 4	59.6	35.5	4.9	0	0.1

### 2.2.2 Mayenite adjustment

The reactivity and the behaviour of BYF cement is also difficult to control. It can differ from one clinker to another with small changes in the raw materials, as shown in Fig. 2-10 [5]. Therefore, the reactivity control is needed for BY cement to be as close as the commercial cement.

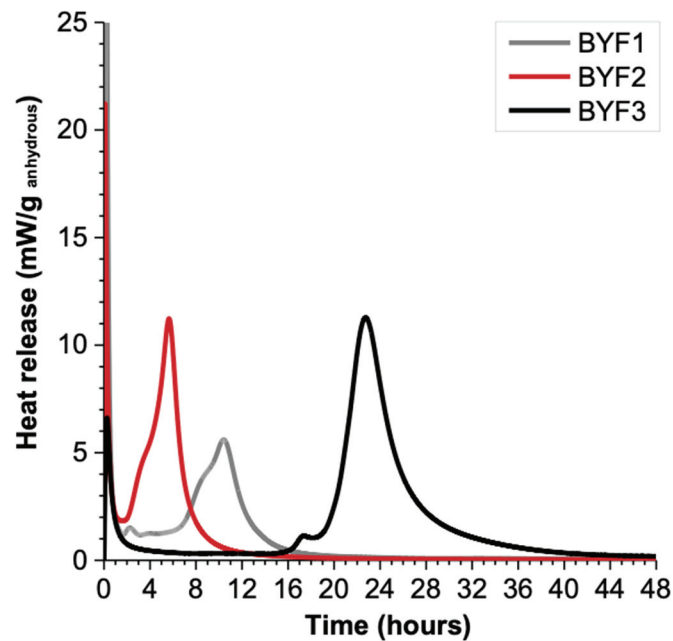


Fig. 2-10 heat flow curves of 3 different BYF industrial cement, where only minor phases and alkalis content are different) at 20°C and w/c ratio of 0.5 [5].

The BY clinker was blended with micro-anhydrite (mAH), which is a reactive anhydrite, at a sulfate to ye'elinite molar ratio of 1:1, called BY40. The water to binder ratio (w/b) of 0.6 was used for mayenite optimization (same as the one used in this study). Mayenite ( $C_{12}A_7$ ), which was synthesized separately following the steps in [6], was provided from HeidelbergCement Technology Center (HTC).

An example of the heat flow curves of BY40 using clinker batch no. 2 at 20°C is shown in Fig. 2-11. Micro-anhydrite retards the reaction of ye'elinite. The main peak starts around 33 hours which is very late compared to the commercial BYF cements in Fig. 2-10. The hydration of ye'elinite is very sensitive to the presence of a small amount of mayenite (MY) [6]. Therefore, a small amount of mayenite is also added in this study to accelerate the hydration. The heat flow of BY40 with 0.5% of mayenite shows the main peak around 10 hours, as shown in Fig. 2-11. Therefore, the reactivity of the different batches of clinker was adjusted by adding mayenite to control the main peak to around 6-12 hours. Different amounts of mayenite were needed in different batches mainly due to the varying free lime content. Each batch of the BY clinker was adjusted with respect to the mayenite content addition by isothermal calorimetry. The list of clinker batches used in each experiment in this study with mayenite optimization is given in Table 2-4.

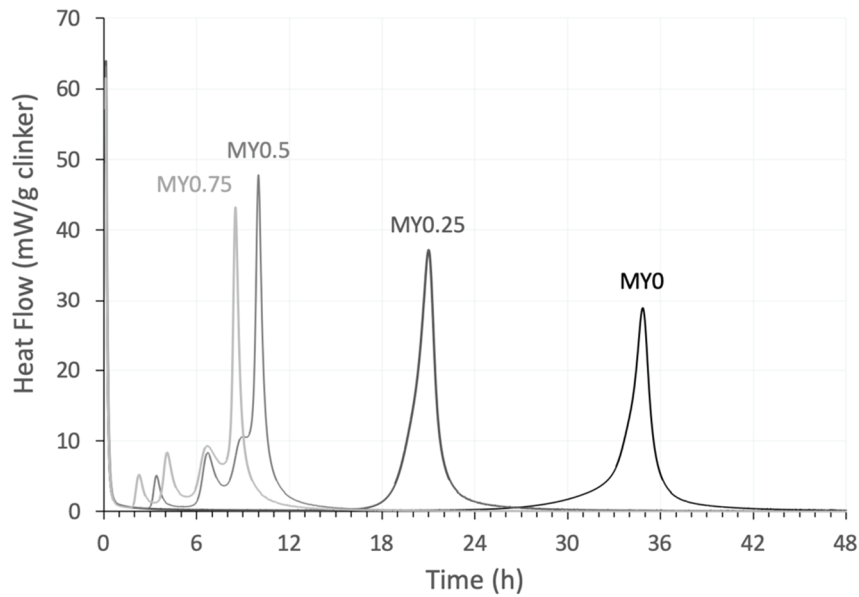


Fig. 2-11 Heat flow of different content of mayenite added to BY40.

Table 2-4 The clinker batch used in the experiment with mayenite optimization.

Batch number	Mayenite (wt.%)	Experiment	Chapter
1	0.25	Hydration study Effective conductivity	4 and 5A 6
2	0.5	Bulk diffusion Isothermal calorimetry	6 5A
3	0.4	Compressive strength	5B
4	0.4	Pore solution Mini migration	5A 6

## 2.3 Characterization of raw materials

The raw materials used in the PC system are light grey cement (LGC), metakaolin (MK, 95% purity from Burgess) and limestone (LS, Durcal 5 from Omya). A laboratory produced BY clinker, anhydrite (natural source) and a synthetic mayenite were used as raw materials in the CSA system. The chemical composition and particle size distribution of raw materials determined by X-Ray fluorescence (XRF) and laser diffraction (Malvern MasterSizer S) are shown in Table 2-5. About 0.1 g of powder was dispersed in isopropanol in small plastic containers. The suspension was stirred and dispersed using an ultrasonic probe for 15 min. After the dispersion, the suspension was transferred to the measuring unit filled with isopropanol until the proper level of the obscuration was reached. The refractive index and imaginary index of the raw materials are shown in Table 2-6.

The phase composition (by XRD/Rietveld) is given in Table 2-7. The phase composition of BY clinker reported in this table is the average value from the 4 batches. The back-loading method was applied to reduce the effects of preferred orientation. The samples were characterized in Bragg-Brentano mode by a X'Pert PANalytical diffractometer with a  $\text{CuK}\alpha$  source with 45 kV and 40 mA. Continuous rotation was applied during the acquisition. Samples were scanned from 2 theta between 5 and 70 degrees for a total duration of 30 minutes. A summarized table of the mix design and the chemical composition of the investigated systems of this study is shown in Table 2-8.

Table 2-5: Chemical composition and particle size value of the raw materials.

<b>PSD</b>	<b>LGC</b>	<b>MK</b>	<b>LS</b>	<b>BY clinker</b>	<b>Anhydrite</b>	<b>MY</b>
Dv,10	1.26	0.54	2.27	0.54	2.7	0.25
Dv,50	8.44	5.13	7.71	4.34	8.41	8.97
Dv,90	24.37	20.17	19.3	15.88	29.88	31.75
<b>XRF (wt.%)</b>						
SiO <sub>2</sub>	22.4	52.0	0.11	18.9	2.5	0.1
Al <sub>2</sub> O <sub>3</sub>	3.8	43.8	0.00	20.9	0.6	50.1
Fe <sub>2</sub> O <sub>3</sub>	1.2	0.3	0.04	0.0	0.3	0.1
CaO	65.6	0.0	56.16	53.1	38.7	47.6
MgO	0.8	0.0	0.15	0.1	1.9	-
SO <sub>3</sub>	3.3	0.1	0.03	6.4	52.2	0.1
K <sub>2</sub> O	0.7	0.1	0.01	-	0.2	-
Na <sub>2</sub> O	0.2	0.3	0.06	0.1	0.1	0.1
TiO <sub>2</sub>	0.2	1.5	0.01	-	-	-
P <sub>2</sub> O <sub>5</sub>	0.1	0.2	0.00	0.0	0.0	0.0
Others	0.0	0.1	0.00	0.0	0.2	0.0
*LOI	1.1	1.5	43.43	0.6	3.4	1.2
Sum	99.6	100.0	100.0	100.0	100.2	99.4

\*LOI = Loss of ignition

Table 2-6 Parameters used for particle size distribution analysis.

	Refractive index	Imaginary index
LGC	1.7	0.1
Metakaolin	1.53	0.001
Limestone	1.6	0.001
BY clinker	1.66	0.001
Mayenite	1.62	0.001
Anhydrite	1.53	0.001



Table 2-7 Phase composition of the raw materials.

XRD (wt.%)	LGC	MK	LS	BY clinker*	Anhydrite	MY
C <sub>3</sub> S	60.6	-	-	-	-	-
C <sub>2</sub> S	21.5	-	-	59.8	-	-
C <sub>3</sub> A	9.1	-	-	-	-	1.9
C <sub>4</sub> AF	1.4	-	-	-	-	-
C <sub>4</sub> A <sub>3</sub> \$	-	-	-	35.7	-	-
C <sub>12</sub> A <sub>7</sub>	-	-	-	-	-	97.5
CA	-	-	-	-	-	0.6
Dolomite	-	-	-	-	6.9	-
Free lime	-	-	-	0.1	-	-
Portlandite	-	-	-	-	0.1	-
Calcite	1.5	-	99	-	-	-
Dolomite	0.7	-	0.7	-	-	-
Gypsum	0.2	-	-	-	2.5	-
Anhydrite	4.7	-	-	0.1	77.7	-
Quartz	0.3	-	0.3	-	2.3	-
Metakaolin	-	94.2	-	-	1.2	-
Rutile	-	-	-	-	8.5	-
Anatase	-	1.2	-	-	0.7	-
Mullite	-	4.6	-	-	-	-
Muscovite	-	-	-	-	-	-
Cristobalite	-	-	-	-	-	-
Sum	100.0	100.0	100.0	100	99.9	100.0

\*Average phase composition from 4 batches of BY clinker given in Table 2-3.

Table 2-8 Mix designs and chemical composition of the investigated systems.

Mix design	LGC	LGCMK	LGCMKLS	CSA
LGC	97	76	66	-
MK	0	20	20	-
LS	0	0	10	-
GS	3	4	4	-
BY clinker	-	-	-	89.2
Anhydrite	-	-	-	10.6
Mayenite	-	-	-	0.25
XRF (wt.%)				
SiO <sub>2</sub>	21.8	27.4	25.2	17.3
Al <sub>2</sub> O <sub>3</sub>	3.7	11.7	11.3	18.6
Fe <sub>2</sub> O <sub>3</sub>	1.2	1.0	0.9	0.1
CaO	64.6	51.2	50.1	52.1
MgO	0.7	0.6	0.5	0.3
SO <sub>3</sub>	4.6	4.4	4.1	11.2
Na <sub>2</sub> O	0.2	0.2	0.2	0.1
K <sub>2</sub> O	0.7	0.6	0.5	0.0
TiO <sub>2</sub>	0.2	0.5	0.4	0.0
P <sub>2</sub> O <sub>5</sub>	0.1	0.1	0.1	0.0
MnO	0.0	0.0	0.0	0.0
SrO	0.0	0.0	0.0	0.0
Cr <sub>2</sub> O <sub>3</sub>	0.0	0.0	0.0	0.0
ZnO	0.0	0.0	0.0	0.0
LOI*	1.7	1.9	6.1	0.9
SUM	99.6	99.7	99.5	100.6

\*LOI = Loss of ignition

## 2.4 References

- [1] W. Lerch, The influence of gypsum on the hydration and properties of Portland cement pastes, *Am Soc Test Mater J.* 12 (1946) 1–41.
- [2] F. Zunino, K. Scrivener, The influence of the filler effect on the sulfate requirement of blended cements, *Cem. Concr. Res.* 126 (2019) 105918. <https://doi.org/10.1016/j.cemconres.2019.105918>.
- [3] W. Kunther, Z. Dai, J. Skibsted, Thermodynamic modeling of hydrated white Portland cement–metakaolin–limestone blends utilizing hydration kinetics from <sup>29</sup>Si MAS NMR spectroscopy, *Cem. Concr. Res.* 86 (2016) 29–41. <https://doi.org/10.1016/j.cemconres.2016.04.012>.
- [4] X. Li, A. Ouzia, K. Scrivener, Laboratory synthesis of C3S on the kilogram scale, *Cem. Concr. Res.* 108 (2018) 201–207. <https://doi.org/10.1016/j.cemconres.2018.03.019>.
- [5] M. Ben Haha, F. Winnefeld, A. Pisch, Advances in understanding ye’elinite-rich cements, *Cem. Concr. Res.* 123 (2019) 105778. <https://doi.org/10.1016/j.cemconres.2019.105778>.
- [6] F. Bullerjahn, M. Zajac, M. Ben Haha, K.L. Scrivener, Factors influencing the hydration kinetics of ye’elinite; effect of mayenite, *Cem. Concr. Res.* 116 (2019) 113–119. <https://doi.org/10.1016/j.cemconres.2018.10.026>.

# Chapter 3 Phase assemblages of the PC systems

**Note:** This chapter is based on an article in preparation for submission to a peer reviewed journal.

Contribution of the doctoral candidate: Writing of the first manuscript draft, experimental design, conduction of the experiment and thermodynamic modelling.

## Abstract

The influence of metakaolin on phase assemblages compared with Portland cement within a temperature range of 5 to 60°C is investigated. This study focuses on a comparison between thermodynamic modelling and experimental data from combined techniques at 90 days of hydration. In general, temperature accelerates the reactivity of anhydrous phases, but low reactivity of belite is found in the blended systems. An overall good agreement between experimental data and thermodynamic modelling on qualitative data is observed with some discrepancies which are further investigated. The Al incorporation in the C-S-H is higher when metakaolin is present and it increases with increasing temperature. Various AFm types and solid-solutions can be observed depending on the temperature. Strätlingite is more stable at low temperature in metakaolin blends, but significantly less strätlingite is observed when limestone is present in the ternary system. Iron present is observed to be in siliceous hydrogarnet and possibly also into the strätlingite structure, for the blended system at low temperature as indicated by SEM-EDS mapping together with image analysis.

**Keywords:** Blended cement, Metakaolin, Limestone, Hydration, Phase assemblages, Thermodynamic modelling, temperature.

## CONTENTS

---

<b>Chapter 3</b>	<b>Phase assemblages of the PC systems .....</b>	<b>41</b>
3.1	Introduction .....	43
3.2	Materials and methods .....	43
3.2.1	Raw materials .....	43
3.2.2	Preparation of cement pastes and hydration stoppage .....	44
3.2.3	Selective dissolution .....	45
3.2.4	Methods of analysis .....	45
3.3	Results and discussion.....	48
3.3.1	Reaction of anhydrous phases.....	48
3.3.2	Comparison of phase assemblages based on experimental data and thermodynamic modelling .....	52
3.3.3	Strätlingite formation .....	56
3.3.4	Siliceous hydrogarnet .....	61
3.3.5	Hydrotalcite formation .....	64
3.3.6	The ettringite – monosulfate balance 60°C .....	65
3.3.7	Why is hemicarbonat observed ? .....	66
3.4	Conclusions .....	67
3.5	References.....	68
3.6	Appendix .....	71

---

## 3.1 Introduction

Supplementary cementitious materials (SCMs) are widely used in the cement industry for environmental and economic purposes [1]. Calcined clays, containing metakaolin as a main component, is a promising material for a sustainable cement and received more interest [2]. Metakaolin is considered as a pozzolanic material. The presence of metakaolin in cement increases the Al and Si when compared to Portland cement and therefore the final phase assemblage changes. The reaction of metakaolin leads to the formation of additional C-S-H with higher Al/Si ratio and monosulfate [1,3,4]. Strätlingite formation is strongly dependent on the degree of hydration of metakaolin and the type of AFm, sulfate or carbonate anions [3,5]. The presence of limestone in Portland cement generally stabilizes monocarbonate and hemiacarbonate instead of monosulfate, preventing the transformation of ettringite into monosulfate [6].

High temperatures can accelerate the reaction of clinker and SCMs [7]. It also modifies the stability of the hydrates [7,8]. The main temperature effect in Portland cement is on the calcium aluminate hydrates [6,7,9]. Monosulfate becomes more stable than ettringite at elevated temperature [7]. Ettringite can form a solid solution with carbonates ( $\text{CO}_3\text{-AFt}$ ) at low temperature [9], while monocarbonate becomes less stable at high temperature [7].

Previous studies have focused on the study of the effect of temperature on Portland cement and blended cements with SCMs, such as slag, fly ash and limestone [7,9–11], but little data are available for temperature effect in metakaolin blends [4]. Available studies on the Portland cement blended with metakaolin focus on ambient temperature [3,5,12]. The aim of this study is to identify the hydrated phases in Portland cement blended with metakaolin in the temperature range of 5 to 60°C from the experimental data and thermodynamic modelling of equilibrium stage. The change of phase assemblages is investigated by XRD, TGA, solid-state NMR, SEM-EDS and image analysis. The differences between experimental data and thermodynamic modelling are further investigated to identify possible kinetic hindrance phenomena, which could lead to further changes in the long term.

## 3.2 Materials and methods

### 3.2.1 Raw materials

Commercial Light grey cement (LGC), a high grade metakaolin (MK), commercial limestone (LS) and a chemical grade of gypsum were used as raw materials. LGC is a Portland cement CEM I 52.5 R with low iron content. The chemical composition, mineralogical and particle size value of these materials were determined by X-Ray fluorescence (XRF), X-ray diffraction (XRD) and laser diffraction (Malvern MasterSizer S), as shown in Table 3-1. The mineralogy of raw materials was determined by Rietveld XRD with a back-loading method. The detailed parameters will be discussed in section 2.4.1. Samples were scanned from 5 and 70 degrees  $2\theta$  for a total duration of 30 minutes. For particle size distribution measurement, the powder approximately 0.1 g was mixed in the isopropanol. The suspension was stirred and placed in an ultrasonic probe for 15 minutes, then transferred to the measuring unit filled with isopropanol until reaching the proper level of obscuration. The optical model was set following the recommendation given in [13].

Table 3-1 Elemental and mineral composition and particle sizes of the raw materials.

PSD	LGC	Metakaolin	Limestone	XRD (wt.%)	LGC	Metakaolin	Limestone
D <sub>v,10</sub>	1.26	0.54	2.27	C <sub>3</sub> S	60.6	-	-
D <sub>v,50</sub>	8.44	5.13	7.71	C <sub>2</sub> S	21.5	-	-
D <sub>v,90</sub>	24.37	20.17	19.3	C <sub>3</sub> A	9.1	-	-
XRF (wt.%)				C <sub>4</sub> AF	1.4	-	-
SiO <sub>2</sub>	22.4	52.0	0.11	Calcite	1.5	-	99
Al <sub>2</sub> O <sub>3</sub>	3.8	43.8	0.00	Dolomite	0.7	-	0.7
Fe <sub>2</sub> O <sub>3</sub>	1.2	0.3	0.04	Gypsum	0.2	-	-
CaO	65.6	0.0	56.16	Anhydrite	4.7	-	-
MgO	0.8	0.0	0.15	Quartz	0.3	-	0.3
SO <sub>3</sub>	3.3	0.1	0.03	Metakaolin	-	94.2	-
K <sub>2</sub> O	0.7	0.1	0.01	Anatase	-	1.2	-
Na <sub>2</sub> O	0.2	0.3	0.06	Mullite	-	4.6	-
TiO <sub>2</sub>	0.2	1.5	0.01				
P <sub>2</sub> O <sub>5</sub>	0.1	0.2	0.00				
Others	0.0	0.1	0.00				
*LOI	1.1	1.5	43.43				
Sum	99.6	100.0	100.0		100.0	100.0	100.0

\*LOI = Loss of ignition

### 3.2.2 Preparation of cement pastes and hydration stoppage

The composition of the investigated system in this study is given in Table 3-2. Sulfate adjustment [14] was carried out up to 3 days by isothermal calorimetry. A small amount of gypsum was added to the systems to control the hydration kinetics and obtain a similar range of SO<sub>3</sub> content at all temperatures (see Chapter 2).

Table 3-2 Cement composition (wt.%) of the investigated systems

System	LGC	Metakaolin	Limestone	Gypsum	SO <sub>3</sub> *
LGC	97	0	0	3	4.6
LGCMK	76	20	0	4	4.4
LGCMKLS	66	20	10	4	4.1

\* Total SO<sub>3</sub> in gypsum and cement

The binders were equilibrated overnight with at the curing temperature before mixing. The dry powders were blended with a laboratory benchtop mixer at 1200 rpm for 1 minute and a small amount of admixture, polycarboxylate (PCE), was added into the distilled water before mixing for controlling the workability of the cement paste. Cement pastes were blended with a water to binder ratio (w/b) of 0.6, in order to compare with the CSA system, by the mixer at 1600 rpm for 2 minutes. The samples were cast in a 50 ml polypropylene container under sealed condition with a few drops

of distilled water on top of the paste. The samples were stored in the controlled temperature at 5, 20, 40 and 60°C for 90 days.

Hydration was stopped by solvent exchange method as prescribed in [13]. The cement pastes were cut on a benchtop by a circular saw with water-cooling. The fresh slices of 2-3 mm thickness were immersed in the isopropanol for one week. The isopropanol was changed at 1, 3 and 7 days. The sample was placed in a plastic bag with a hole and dried in a desiccator under light vacuum at least 7 days before the analysis.

### 3.2.3 Selective dissolution

Selective dissolution [15] is a method that can dissolve major phases from the cement paste. As a result, the minor phases in the residue can be identified by XRD. A salicylic acid with methanol (SAM) extraction was applied in this study to dissolve alite, belite, portlandite, C-S-H, AFt and AFm phases. The residue of siliceous hydrogarnet and hydrotalcite can be detected. The experiment method was adapted from [16]. A mixture of 600 ml of methanol and 40g of salicylic acid was stirred on a magnetic stirrer. Then, 10 g of the sample after stopping hydration were added into the mixture. The suspension was stirred for 2 – 3 h, then settled for about 30 min. The suspension was filtered with vacuum using 0.45 $\mu$ m nylon filters, washed with methanol and dried at 90°C for 45 – 60 min. The residue was analysed by XRD.

### 3.2.4 Methods of analysis

X-ray diffraction was conducted by a PANalytical X'per Pro diffractometer using  $\text{CuK}_{\alpha 1\alpha 2}$  source. The X-ray tube worked at 45 kV and 40 mA ( $\lambda = 1.54 \text{ \AA}$ ) and the Bragg-Brentano configuration included a fixed diverge slit of  $1/2^\circ$ , a Soller slit of 0.04 rad and mask of 15 mm. The patterns were recorded between 5 and  $70^\circ$  ( $2\theta$ ) using a step size of  $0.017^\circ$ . The total duration of the analysis for the powder sample and the fresh disc are 30 min and 15 min, respectively. Rutile was used as an external standard to quantify the amorphous content in the cement paste. The quantitative phase assemblages were carried out by using Rietveld refinement method with the High Score Plus software, using the reference pattern presented in Table 3-3. The structure of monosulfate 14 ( $\text{Ms}_{14}$ ) for XRD Rietveld refinement is modified from kuzelite crystal structure (ICSD-100138) [17] with refined lattice parameters of  $a \sim 5.75 \pm 0.01 \text{ \AA}$  and  $c \sim 28.4 - 28.6 \text{ \AA}$ . The structure of solid solution of AFm ( $\text{AFm}_{ss}$ ) is modified from hemicarbonatite structure with refined lattice parameters of  $a \sim 5.776 \pm 0.01 \text{ \AA}$  and  $c \sim 50.8 \pm 0.1 \text{ \AA}$ . It is considered as hemicarbonatite in the quantification. The partial or no known crystal structure (PONKCS) approach is used to estimate the C-S-H and metakaolin background. The experimental errors of XRD were estimated on the quantified amount of alite and belite on 90 days samples analysed with two replicates. The error limits of the XRD Rietveld quantification is around 2% mass.



Table 3-3 Mineralogical references for quantitative Rietveld refinement on XRD patterns (ICSD).

	ICSD		ICSD
C <sub>3</sub> S	94742	Ettringite	155395
C <sub>2</sub> S	81096	Monosulfate-14	100138
C <sub>3</sub> A	1841	Monosulfate-12	100138
C <sub>4</sub> AF	9197	AFm <sub>SS</sub>	263124
Gypsum	151692	Hemicarbonate	263124
Anhydrite	28546	Monocarbonate	59327
Calcite	73446	Strätlingite	69413
Dolomite	66333	Si-Katoite	1720177
Portlandite	202220	Quartz	174
CSH crystalline	1028762		

The quantification done on fresh discs of cement paste is normalized to 100 g of anhydrous using the water to binder ratio (w/b) expressed in Equation 3-1.

$$\text{Equation 3-1: } W_{i,\text{rescaled}} = W_{i,\text{Rietveld}} \times \left(1 + \frac{w}{b}\right)$$

where  $W_i$  is weight percent.

The degree of hydration (DoH) of anhydrous phases at time  $t$  was calculated from the mass fraction of reacted to initial amount. The formula for the calculation is given in Equation 3-2.

$$\text{Equation 3-2: } \text{DoH } (\%)_t = \left(\frac{W_0 - W_t}{W_0}\right) \times 100$$

where  $W_0$  is initial amount,  $W_t$  is the amount at time  $t$ .

A small piece of the dried sample was polished on every side of the surface to remove the carbonated area before being gently grinded in a ceramic mortar. About 50 mg of sample powder was placed in a 150  $\mu\text{L}$  alumina crucible with a lid, then was analysed by TGA (Mettler Toledo TGA/SDTA 851 instrument) from 30°C to 1000°C with the rate of 10°C/min and under 30 ml/min  $\text{N}_2$  gas flow. The weight loss from TGA analysis was used to obtain the amount of chemical bound water (BW) as shown in Equation 3-3.

$$\text{Equation 3-3: } \text{BW} = \frac{W_{40} - W_{550}}{W_{550}}$$

Where  $W_T$  is the dry sample weight in grams at the respective temperature (°C)

A piece of sample was gently polished with a silicon carbide paper of 1200 grid to smoothen the surface. The samples were embedded in a low viscosity epoxy resin under the vacuum. The impregnated samples were hand-polished on a SiC paper of 1200 grid with isopropanol as a lubricant until the sample surface was uncovered. The sample was polished by diamond suspension of 9, 3, 1 and 1/4  $\mu\text{m}$  with 15 kN force and 150 rpm for all the polishing steps. The petroleum was used as a lubricant during the fine polishing with diamond suspension. The polishing disc was washed every hour between the steps with soap and water using a brush. The residue on the sample surface was removed with the isopropanol in an ultrasonic bath. The polished samples were stored under vacuum desiccators for at least two days to evaporate the isopropanol before coating with carbon. The SEM-EDS investigations were carried out by using a FEI Quanta 200 scanning electron microscope equipped with a Bruker ASX microanalysis XFlash 4030 silicon drift detector for the EDS point analysis and the EDS mapping (tungsten filament). The acceleration voltages were 15kV for the EDS point analysis and 12 kV for the EDS mapping with a working distance of 12.5 mm for both conditions.

The solid-state  $^{29}\text{Si}$  MAS NMR spectra were acquired on a Bruker Avance 400 NMR (9.39T) spectrometer using a 4 mm Bruker CP/MAS probe spinning speed of  $\nu_R = 10.0$  kHz, single-pulse excitation with a pulse width of 1.75  $\mu\text{s}$  for a radio-frequency (rf) field strength of  $\gamma B_1/2\pi = 40$  kHz, a relaxation delay of 30 s, and typically 2560 scans. The  $^{29}\text{Si}$  chemical shifts are referenced to neat tetramethylsilane (TMS), using a sample of  $\beta\text{-Ca}_2\text{SiO}_4$  ( $\delta(^{29}\text{Si}) = -71.33$  ppm) as a secondary reference. The simulations of the  $^{29}\text{Si}$  MAS spectra employed procedures described elsewhere for anhydrous [18,19] and hydrated Portland cements [3,20,21]. The  $^{27}\text{Al}$  MAS NMR spectra were obtained on a Varian Direct-Drive VNMR-600 spectrometer using a home-built CP/MAS probe for a 4 mm outer-diameter zirconia (PSZ) rotor, a spinning speed of  $\nu_R = 13.0$  kHz, a pulse width of 0.5  $\mu\text{s}$  for an rf field strength of  $\gamma B_1/2\pi = 60$  kHz, a relaxation delay of 2 s, and 7,000 – 16,000 scan. The excitation pulse had a pulse width well below  $\pi/6$  (for  $^{27}\text{Al}$ ,  $I = 5/2$  in a solid) which ensures quantitative reliability of the intensities for the  $^{27}\text{Al}$  central transition for sites experiencing different quadrupole couplings. A background spectrum of the probe itself with an empty spinning PSZ rotor was subtracted from the individual  $^{27}\text{Al}$  MAS spectra. The spectra and  $^{27}\text{Al}$  Chemical shifts are relative to a 1.0 M aqueous of  $\text{AlCl}_3 \cdot 6\text{H}_2\text{O}$ . The degree of reaction for alite, belite and metakaolin is calculated as  $\text{DoH}(t) = [I(t) - I(t_0)] / I(t_0)$ , from the relative intensities from the simulations of the  $^{29}\text{Si}$  MAS NMR spectra before ( $t_0$ ) and after hydration ( $t$ ). The estimated error of DoH of alite and belite for the LGC system is  $\pm 3\%$ , whereas it is higher for the blended systems. For DoH lower than 10%, the error limit is of the order of  $\pm 10\%$ .

The image analysis was carried out to confirm and identify the formation of phases of interest in the microstructure. The BSE images and EDS mapping data were linked using edxia [22]. The atomic ratio plots of the existing element in cement from the EDS map can provide the main phases and can be improvised to identify the minor elements present in the sample. Using the graphical interface of edxia, manually selected points in the ratio plots appear on the BSE image to match composition and structure.

The hydrate assemblage was calculated using GEMS-PSI software [23,24] together with the PSI-Nagra database [25] and the cement CEMDATA18 database [26] using the CSHQ model for C-S-H. The average degree of hydration (DoH) of alite and belite and the degree of reaction (DoR) of metakaolin at 90 days of hydration between Rietveld quantification and solid-state NMR were used as an input for the calculations. C-A-S-H composition was corrected for Al and sulphur uptake based on the composition found by SEM-EDS point analysis. Thaumasite is prohibited for all calculations.

### 3.3 Results and discussion

#### 3.3.1 Reaction of anhydrous phases

##### 3.3.1.1 Degree of hydration of main anhydrous phases: alite and belite

Alite and belite are the main anhydrous phases present in unreacted LGC (60.6% and 21.5%, respectively). The degree of hydration (DoH) was obtained both by XRD Rietveld refinement and from the simulations of the  $^{29}\text{Si}$ -NMR spectra. Fig. 3-1 shows a comparison of the DoH of alite and belite obtained from the two different techniques.

Alite in the LGC system has reacted by more than 90% at all temperatures. A significant difference of DoH in the LGC system between the two techniques is observed in the case of belite although similar trends are observed. The DoH of belite increases with increasing temperature, as shown in Fig. 3-1a.

In the LGCMK system, less than 10% of unreacted alite remains at all temperatures as shown in Fig. 3-1b, while the  $^{29}\text{Si}$ -NMR results indicate about 20% unreacted alite. The LGCMKLS system shows a lower DoH of alite with increasing temperature, more clearly in the  $^{29}\text{Si}$ -NMR result. In the presence of metakaolin, a significantly lower belite reaction is observed than for the LGC system by both techniques. A decreasing trend of the DoH of belite at elevated temperature is observed only in the XRD result.

The discrepancies between the DoH from the XRD Rietveld quantification and the  $^{29}\text{Si}$ -NMR results possibly come from the limitation of the techniques [19]. Overlapping peaks between alite – belite – ettringite in the XRD patterns corresponding to  $2\theta \sim 31 - 35^\circ$  cause a significant uncertainty in the refinement especially at low alite and belite content, typically below 2%. Similarly, the precision of the  $^{29}\text{Si}$ -NMR deconvolutions decreases strongly at DoH below 10% due to small changes in signal intensity, in particular for belite which only constitutes 3 – 9% of the total  $^{29}\text{Si}$  NMR intensity for the hydrated blends. To avoid over or under estimation the DoH of alite and belite, the average values as given in Fig. 3-2 are considered as an input for thermodynamic calculation.

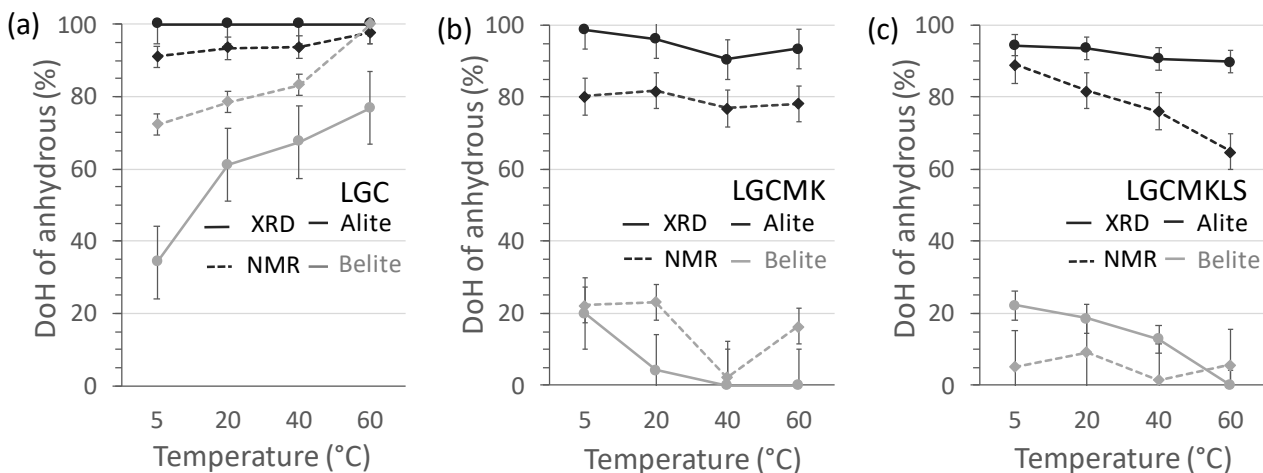


Fig. 3-1 Comparison of degree of hydration (DoH) of alite and belite calculated by XRD Rietveld quantification and  $^{29}\text{Si}$ -NMR of (a) LGC, (b) LGCMK and (c) LGCMKLS at 90 days of hydration.

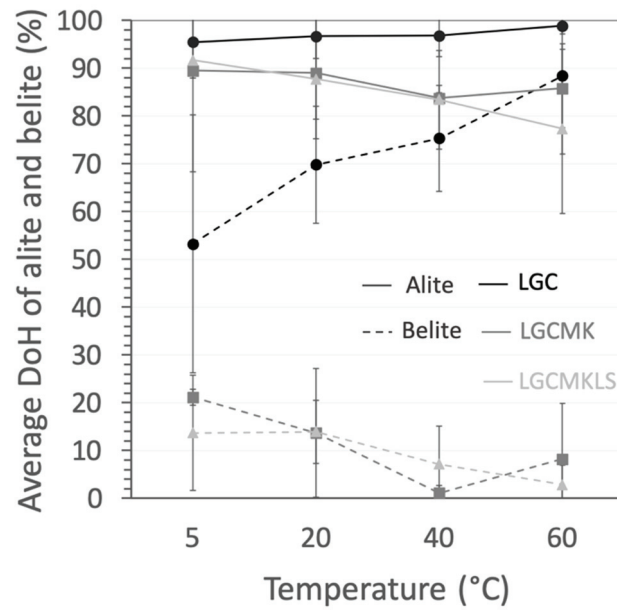


Fig. 3-2 Average degree of hydration (DoH) of alite and belite of LGC, LGCMK and LGCMKLS at 90 days of hydration at different temperatures.

### 3.3.1.2 Degree of reaction (DoR) of metakaolin

The DoR of metakaolin in the two blended systems at 90 days of hydration was obtained from the  $^{29}\text{Si}$ -NMR spectra, which give a clear reflection of the resonances from this phase as seen in earlier studies [3]. Fig. 3-3 shows an expected increasing trend of DoR for metakaolin with temperature for both systems. The DoR is 70% at 5°C and reaches about 90% in the sample cured at 60°C. The difference in DoR at different temperature leads to different amounts of Al available in the system to form the hydrates such as C-(A)-S-H and aluminates hydrates. The DoR of metakaolin in the LGCMK system is quite similar to the LGCMKLS system, indicating no significant effect of limestone on the MK reaction.

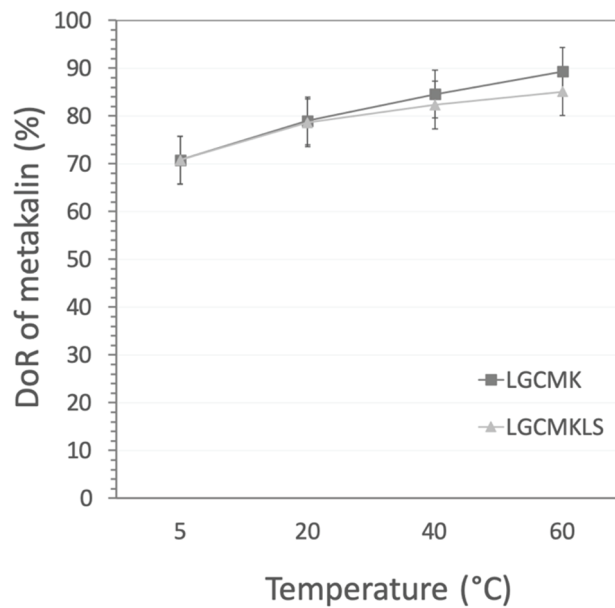


Fig. 3-3 Degree of reaction (DoR) of metakaolin calculated from  $^{29}\text{Si}$ -NMR spectra of LGCMK and LGCMKLS at 90 days of hydration at different temperatures.

### 3.3.1.3 The incorporation aluminium and sulfur in C-S-H

SEM-EDS point analyses were conducted to characterize the calcium-silicate-hydrate (C-S-H) phase, which is poorly crystalline and has a variable composition depending on the systems and temperature [27–29]. The presence of metakaolin in Portland cement blends is expected to lead more Al in C-S-H [3]. The incorporation of Al in C-S-H can reduce the available Al content in the system to form aluminates hydrates.

Fig. 3-4 shows the average composition of C-(A)-S-H of the investigated systems characterized by SEM-EDS point analysis for more than 200 points per sample. The points were manually selected in the inner C-(A)-S-H, and the C-(A)-S-H composition is determined as suggested in [30]. More scattered points were observed with the increasing temperature, thus higher error bars are given. The LGC system shows no significant change of C-S-H composition in the temperature range of 5 - 60°C which is coherent to the previous work reported in [31]. It is clearly seen that the blended systems show more incorporation of Al in C-(A)-S-H and a higher Si/Ca ratio due to metakaolin reaction. Higher Al incorporation but lower Si/Ca is detected with increasing temperature which disagrees with the recent observation in [4]. A similar temperature trend is observed for LGCMK and LGCMKLS, but slightly lower Al incorporation in C-S-H in LGCMKLS. S/Si ratio is slightly increased with increasing temperature. The average composition of C-(A)-S-H for the investigated systems at different temperatures using thermodynamic modelling is given in the atomic ratio, as shown in Table 3-4.

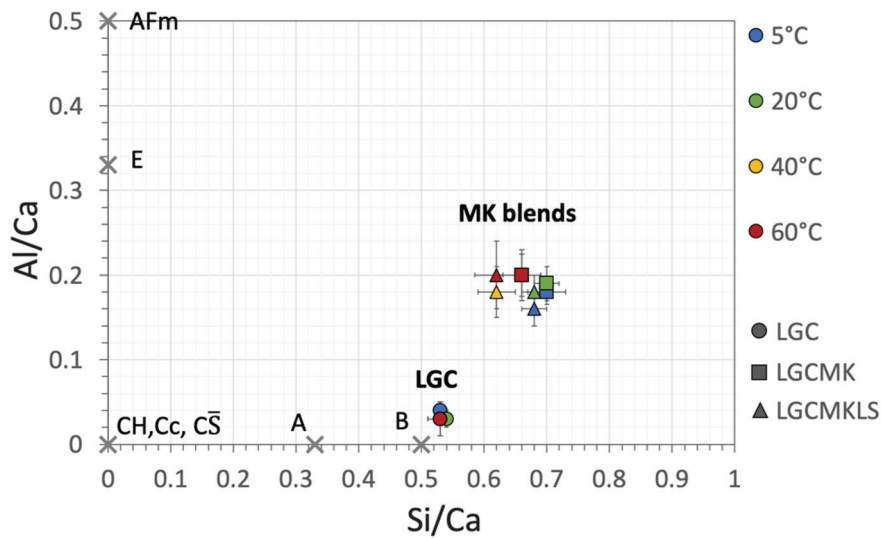


Fig. 3-4 Average C-(A)-S-H composition of the investigated systems at 5, 20, 40 and 60°C analysed by EDS point analysis: A = alite, B = belite, C-(A)-S-H = calcium aluminate silicate hydrates, CH = portlandite, Cc = calcite, E = ettringite and AFm = alumino-ferrite-mono-phase.

Table 3-4: Average C-(A)-S-H composition of the investigated systems at 5, 20, 40 and 60°C analysed by EDS point analysis.

Temperature	Atomic ratio	LGC	LGCMK	LGCMKLS
5°C	Ca/Si	1.89±0.04	1.43±0.06	1.47±0.05
	Al/Si	0.08±0.02	0.26±0.02	0.24±0.02
	S/Si	0.03±0.015	0.01±0.005	0.01±0.005
20°C	Ca/Si	1.85±0.04	1.43±0.05	1.47±0.05
	Al/Si	0.06±0.02	0.27±0.02	0.26±0.03
	S/Si	0.01±0.005	0.01±0.005	0.01±0.005
40°C	Ca/Si	1.89±0.08	1.52±0.07	1.61±0.04
	Al/Si	0.06±0.03	0.3±0.04	0.29±0.04
	S/Si	0.02±0.01	0.03±0.01	0.03±0.02
60°C	Ca/Si	1.89±0.04	1.52±0.07	1.61±0.04
	Al/Si	0.06±0.02	0.3±0.05	0.32±0.05
	S/Si	0.04±0.02	0.03±0.02	0.04±0.02

### 3.3.2 Comparison of phase assemblages based on experimental data and thermodynamic modelling

#### 3.3.2.1 Experimentally observed phase assemblages at 90 days of hydration

The effect of temperature on hydrate phase formation characterized by XRD is shown in Fig. 3-5. The hydration products can be compared based on the XRD patterns. Temperature mainly affects the kind of aluminate hydrates formed and their crystallinity. AFm has a poorly crystalline or nanocrystal size form at high temperature leading to broad and overlapping XRD peaks. This effect is more important in the blended system.

In the LGC system, hemicarbonate (Hc) is a stable form of AFm at low temperature. Two types of monosulfate (Ms) are observed:  $Ms_{12}$  ( $C_4\bar{A}\bar{S}H_{12}$ ) and  $Ms_{14}$  ( $C_2\bar{A}\bar{S}H_{14}$ ).  $Ms_{12}$  is observed only in low amounts and at temperature below 60°C. Higher temperature leads to the stabilisation of  $Ms_{14}$  ( $9.1^\circ 2\theta$ ) together with ettringite and portlandite.

The presence of metakaolin promotes the formation of AFm phases as shown in Fig. 3-5b for the blend containing metakaolin. AFm has a layered structure, which can contain different types of anions in the interlayer [32]. An AFm phase ( $AFm_{ss}$ ) containing sulfate - carbonate - hydroxide can be observed at low temperature, as has been also observed in hydrated PC blended with fly ash [11]. In addition, strätlingite, an AFm containing aluminium and silicon in the interlayer, is formed at 5 to 40°C in the presence of metakaolin: more strätlingite can be observed at low temperature and it is absent at 60°C. At 60°C,  $Ms_{14}$  becomes a main calcium aluminate hydrate phase while ettringite is absent. The portlandite content in the metakaolin blends is much lower than the LGC system, due to the pozzolanic reaction of metakaolin with portlandite. The amount of portlandite is decreased at higher temperatures and is absent at 60°C (Fig. 3-5b) due to the higher reactivity of metakaolin in agreement with the NMR results summarised in Fig. 3-3. A small broad peak of siliceous hydrogarnet structure can be identified in the LGCMK sample cured at 60°C.

When limestone is present in addition to metakaolin (LGCMKLS), hemicarbonate and monocarbonate are precipitated instead of monosulfate. High crystallinity of hemicarbonate is formed at 5 and 20°C but a poorly crystalline form, corresponding to a broader peak of hemicarbonate, is observed at 40°C. The presence of monocarbonate is found only at 5 and 20°C. The signal of strätlingite in this system is not as obvious as the LGCMK system, although some seems to be present; low intensity patterns of strätlingite can be noticed at 5 to 40°C from the XRD patterns. The presence of strätlingite was confirmed by  $^{27}Al$  NMR as discussed in detail further below.

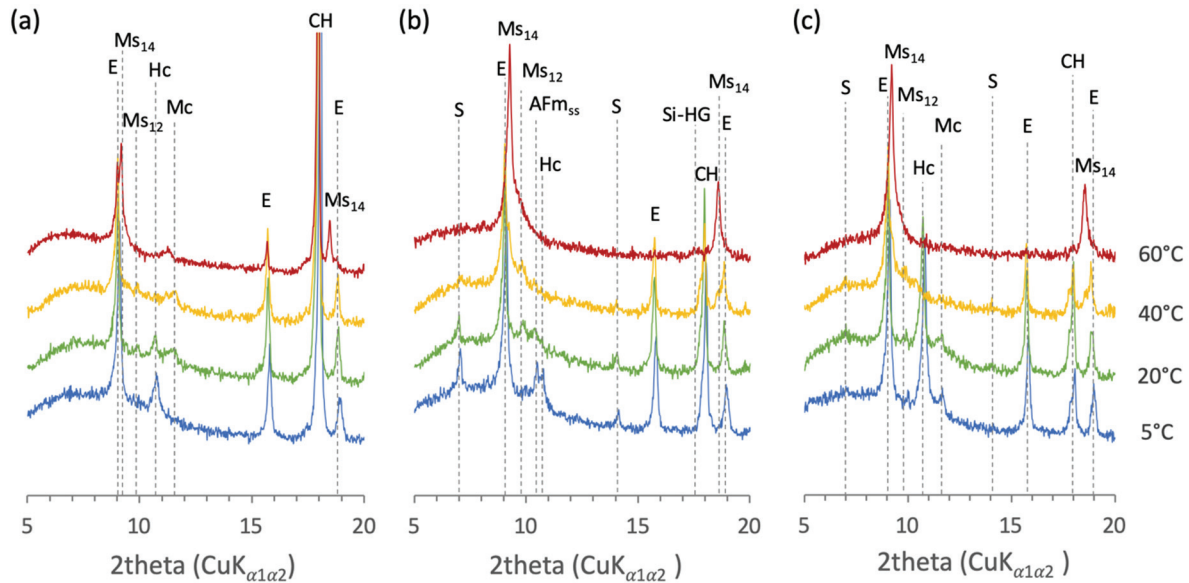


Fig. 3-5 Main hydrate phases in XRD patterns of (a) LGC, (b) LGCMK and (c) LGCMKLS cured at different temperatures at 90 days of hydration: E = ettringite, Ms = monosulfate, Hc = hemicarboxate, Mc = monocarbonate, HT = hydrotalcite and Si-HG = Siliceous hydrogarnet.

### 3.3.2.2 Phase assemblages by thermodynamic modelling

Thermodynamic modelling calculation at different temperatures was carried out to predict the phase assemblages of the investigated system at thermodynamic equilibrium at the respective DoR of anhydrous clinker and metakaolin at 90 days of hydration. The variation of the Ca/Si of C-(A)-S-H as well as the Al and S incorporation in C-S-H at different temperatures were also considered.

For LGC without metakaolin, the thermodynamic calculations predict the formation of C-S-H, portlandite, ettringite and a minor amount of siliceous hydrogarnet between 5 to 40°C. At 60°C, ettringite is calculated to partially be destabilised to monosulfate, in agreement with previous finding on Portland cement. In the presence of metakaolin, C-S-H, ettringite and more AFm (monosulfate and monocarbonate) are predicted to form, while portlandite is expected to be absent. At 40 and 60°C where a high metakaolin DoR is observed, in addition the formation of some strätlingite is calculated, and the complete destabilisation of ettringite to monosulfate. A similar behaviour is calculated in the presence of additional limestone, the calculated stabilisation of ettringite at 60°C, is related to the lower availability of CaO in this system due to the low reaction degree of alite and belite in that blend, as monosulfate is stabilised in the presence of more CaO and ettringite + strätlingite at lower CaO contents in C-S-H.

A comparison of phase assemblages between the quantification from XRD Rietveld refinement and thermodynamic modelling prediction is shown in Fig. 3-6. It should be noted that broad peaks of AFm formed in the presence of metakaolin, leads to a loss of precision in their quantification. Free water in the experimental data was calculated from the difference between mixing water and the bound water (BW) determined by TGA.

The overall results in Fig. 3-6 shows good agreement between experimental result and thermodynamic modelling, especially in the LGC system. The discrepancies are mostly found in the blended systems. The reactivity of metakaolin is an important factor for thermodynamic modelling calculation as it defines both the availability of aluminium and indirectly of calcium in the system. When limestone is present, monocarbonate is the thermodynamically stable phase at low temperatures affecting the balance between AFm and Aft phases [33]. No strätlingite is predicted in the presence of portlandite due to their thermodynamic incompatibility, while experimentally both are observed in the same



cement. High amount of strätlingite is predicted in the blended system at high temperature, while the experimental observation shows only a small amount. Moreover, some minor phases such as siliceous hydrogarnet and hydrotalcite are predicted based on the presence of the minor elements; Fe and Mg, while these phases are not quantified experimentally. The main discrepancies from the observation are listed below:

- An increasing amount of strätlingite is predicted at high temperature, while experimentally less is observed.
- Experimentally observation of the co-existence of strätlingite and portlandite
- The prediction of siliceous hydrogarnet
- The prediction of hydrotalcite
- The balance of ettringite and monosulfate content at high temperature in the presence of limestone
- The balance between monocarbonate and hemicarbonate

These points are investigated and discussed in more details in the following sections.

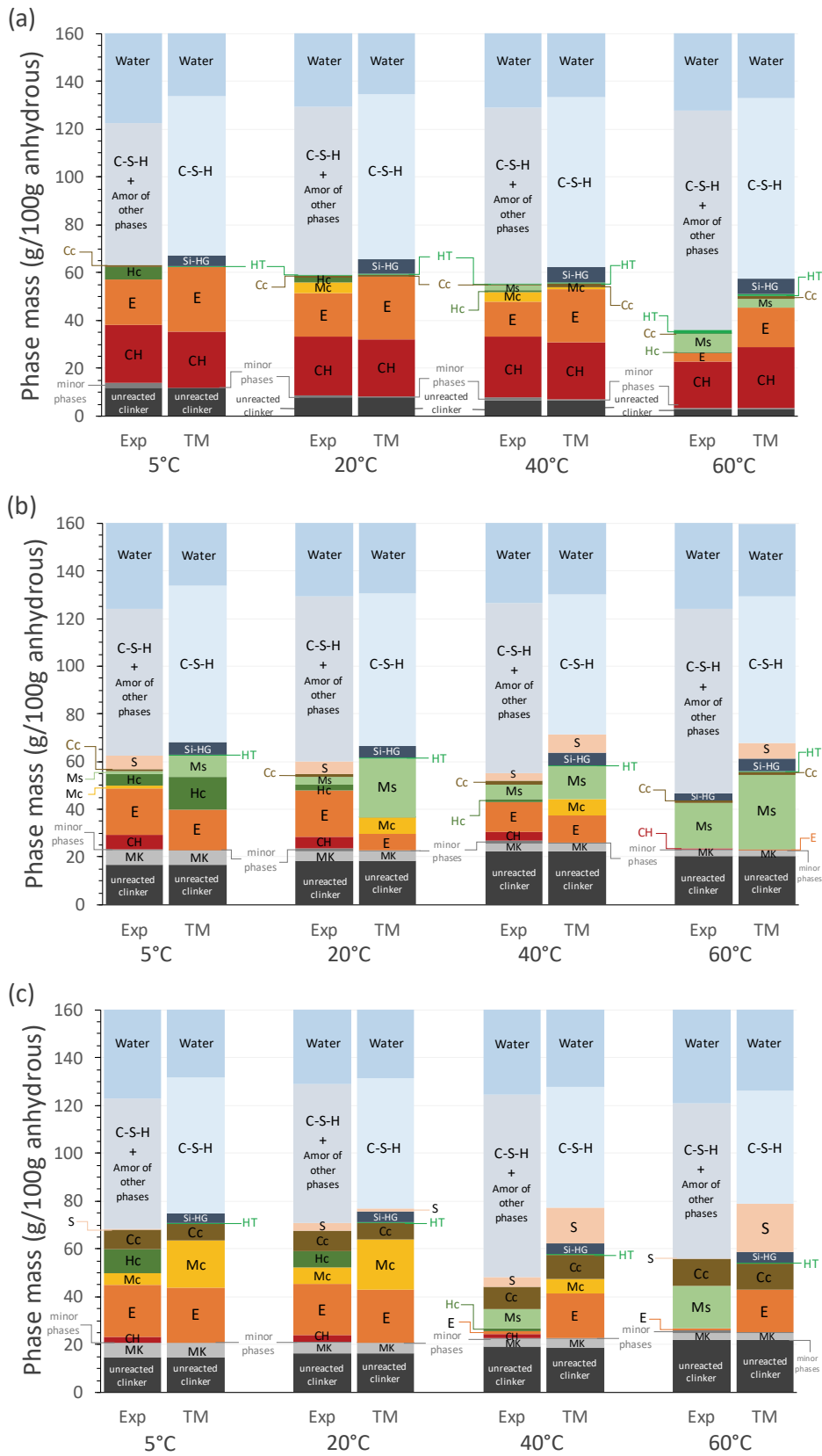


Fig. 3-6 Comparison of phase assemblages between experimental data at 90 days of hydration and thermodynamic modelling at different temperatures of (a) LGC, (b) LGCМК and (c) LGCМКLS: CH = portlandite, E = ettringite, Mc = monocarbonate, Hc = hemicarbonate, Ms = monosulfate, S = strätlingite, HT = hydrotalcite, Si-HG = siliceous hydrogarnet, MK = metakaolin, Amor = amorphous, Cc = calcite, minor phases = quartz and dolomite.

### 3.3.3 Strätlingite formation

Strätlingite,  $[\text{Ca}_4\text{Al}_2(\text{OH})_{12}]^{2+}[(\text{AlSi}(\text{OH})_8)_2 \cdot n\text{H}_2\text{O}]^{2-}$ , is an AFm phase that is stable in hydrated cement systems with high aluminosilicate and low calcium content. The two main discrepancies between experimental observation and thermodynamic modelling are the presence of strätlingite in different systems at different temperatures and the co-existence between strätlingite and portlandite in the experimental observation.

#### 3.3.3.1 Effect of temperature on strätlingite formation in the blended systems

The XRD patterns (Fig. 3-5) present a clear peak of strätlingite formation in LGCMK, at low temperatures while no reflections associated with the strätlingite are observed at 60°C at 90 days of hydration. The presence of strätlingite at low temperatures and its absence at 60°C is confirmed by the  $^{27}\text{Al}$ -NMR spectra in Fig. 3-7b, where a characteristic peak at 61 ppm is observed from the tetrahedral Al sites in strätlingite. This indicates that strätlingite favours precipitation at low temperature, even though portlandite is present. In fact, experimental investigations at very high water to solid ratios [34] found that the stability of strätlingite decreases with increasing temperature and observed its decomposition to mainly hydrogarnet above 85°C. This is coherent to the observation of siliceous hydrogarnet at 60°C from the XRD result (Fig. 3-5b).

Even though the  $\text{CaO-SiO}_2\text{-Al}_2\text{O}_3$  content in the LGCMKLS system is quite similar to the LGCMK system, the presence of limestone lowers the reaction of alite, belite and metakaolin at high temperatures and the formation of strätlingite. The amount of strätlingite from XRD and  $^{27}\text{Al}$  NMR is much lower for the LGCMKLS than for the LGCMK system. The suppression of strätlingite formation in the presence of limestone as observed by XRD has previously been reported for samples cured at 20°C in [5,35]. Also, at 5 and 60°C, no strätlingite is detected in the LGCMKLS system by XRD, probably because it is poorly crystalline or under the detection limit although  $^{27}\text{Al}$  NMR (Fig. 3-7c) indicates that a major amount of strätlingite (below 1 wt%) is present also at 5 and 60°C. At 5°C, very low intensity of the tetrahedral Al resonance from strätlingite at 61 ppm is observed, while only indications of this resonance is present for the sample cured at 60°C. Based on the NMR data in Fig. 3-7c, a higher intensity of strätlingite is observed at 40°C than 5°C for both the LGCMKLS system, quite in contrast to the LGCMK system. Presently, there is no clear explanation for the suppression of strätlingite formation at 5°C at high limestone contents.

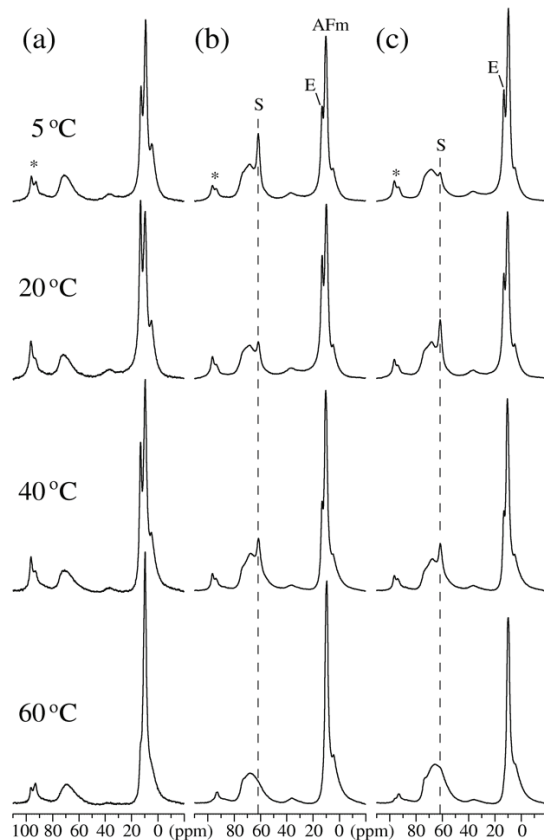


Fig. 3-7  $^{27}\text{Al}$  MAS NMR spectra (14.09 T,  $\nu_R = 13.0$  kHz) of (a) LGC, (b) LGCMK and (c) LGCMKLS at 90 days of hydration cured at 5, 20, 40 and 60°C: S = strätlingite, E = ettringite. Spinning sidebands are indicated in the first-row spectra by asterisks. The spectra in (a) for the pure LGC are vertically expanded by a factor of three compared to the LGCMK and LGCMKLS blends in (b) and (c).

The XRD and NMR observations are supplemented by BSE image analysis coupled with EDS mapping. Strätlingite in the blended cement have been observed previously based on BSE image [35], but is difficult to clearly identify as strätlingite looks similar to the other types of AFm (e.g.  $\text{SO}_3\text{-AFm}$  and  $\text{CO}_3\text{-AFm}$ ) on BSE image, but different chemical composition. Thus, EDS mapping together with image analysis [22], is used to identify strätlingite in the microstructure, as shown in Fig. 3-8- 11. Fig. 3-8 presents the ratio plots (Al/Ca vs. Si/Ca) from representative points extracted from the EDS mapping.

In LGCMK, Fig. 3-8 shows that the EDS points towards strätlingite, although its composition slightly shifted to higher Si/Ca for all temperatures, except at 60°C, where strätlingite is absent consistent to the XRD and the  $^{27}\text{Al}$  NMR results.

The region created by this point selection can be used to define an equivalent selection in the EDS mapping, creating a mask, which enables to plot the phase distribution. The strätlingite distribution is presented as a red overlay on the BSE images in Fig. 3-9. At low temperature, bigger grains of strätlingite can be identified, explaining their better visibility in XRD. Within the microstructure, it can be observed that strätlingite precipitates closely to the AFm grains and often near the calcium silicate clinker grains, which provide Ca and Si to the AFm phases. In no cases, strätlingite is observed near portlandite as discussed in more detail in the next section.

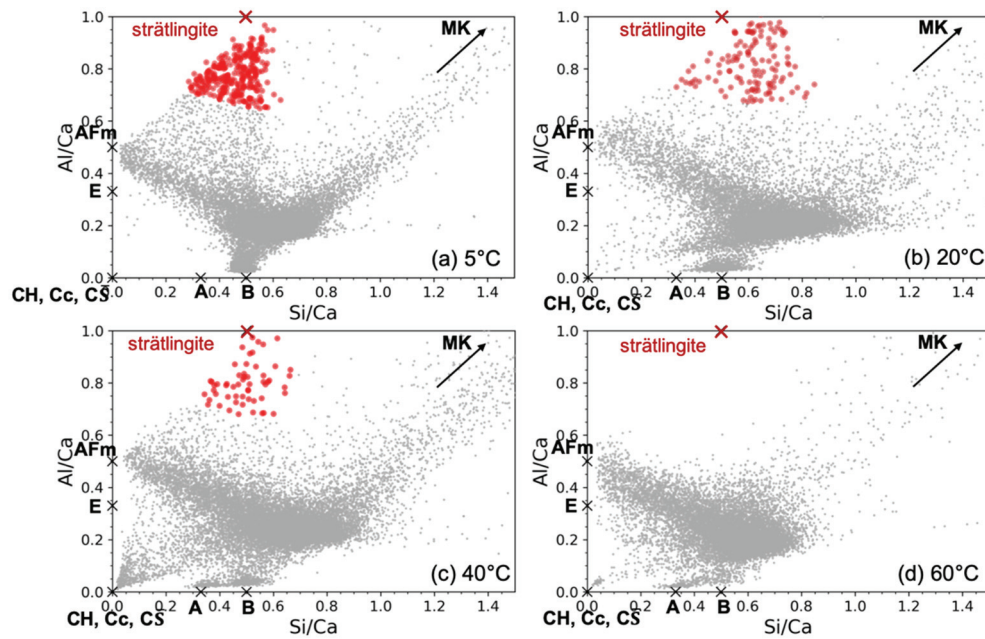


Fig. 3-8 Atomic ratio plots of Si/Ca and Al/Ca of LGCMK at 90 days of representative points obtained from EDS mapping [22] with the main composition of hydrated phases. The points around the strätlingite composition are selected in red: A = alite, B = belite, MK = metakaolin, CH = portlandite, Cc = calcite, CS = calcium sulfate, E = ettringite and AFm = alumino-ferrite-mono phase.

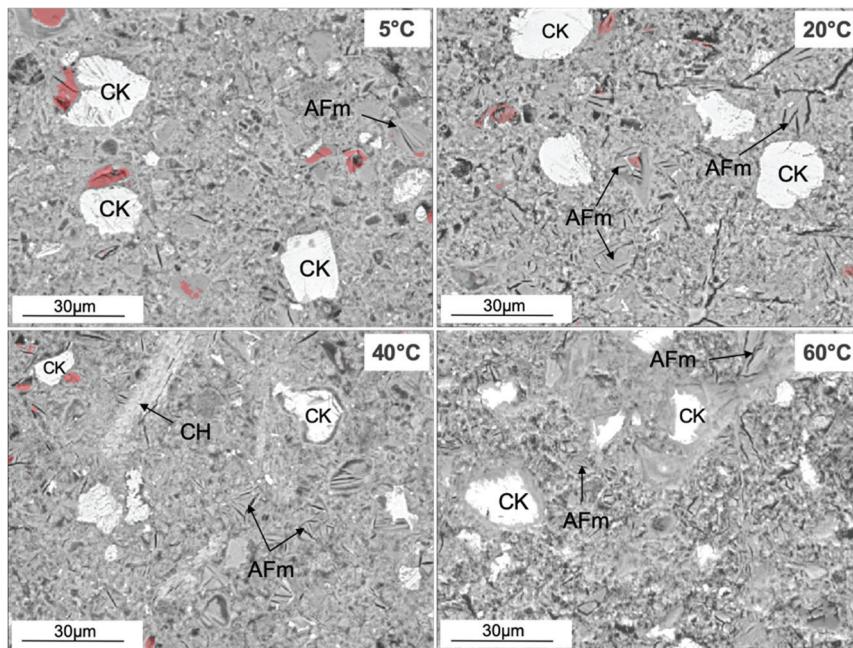


Fig. 3-9 Overlay mask of the selected points in the ratio plot identified as strätlingite (in red) on BSE images of LGCMK at 90 days cured at 5, 20, 40 and 60°C: CK = anhydrous clinker, CH = portlandite and AFm = alumino-ferrite-mono phase.



In LGCMKLS, the EDS points (Fig. 3-10) towards the strätlingite composition are less dense than the LGCMK system and contain less Al than the ideal composition as clearly observed at 20°C. Fig. 3-11 indicates that it is more difficult to observe strätlingite by XRD in LGCMKLS due to its finer distribution in the limestone containing system.

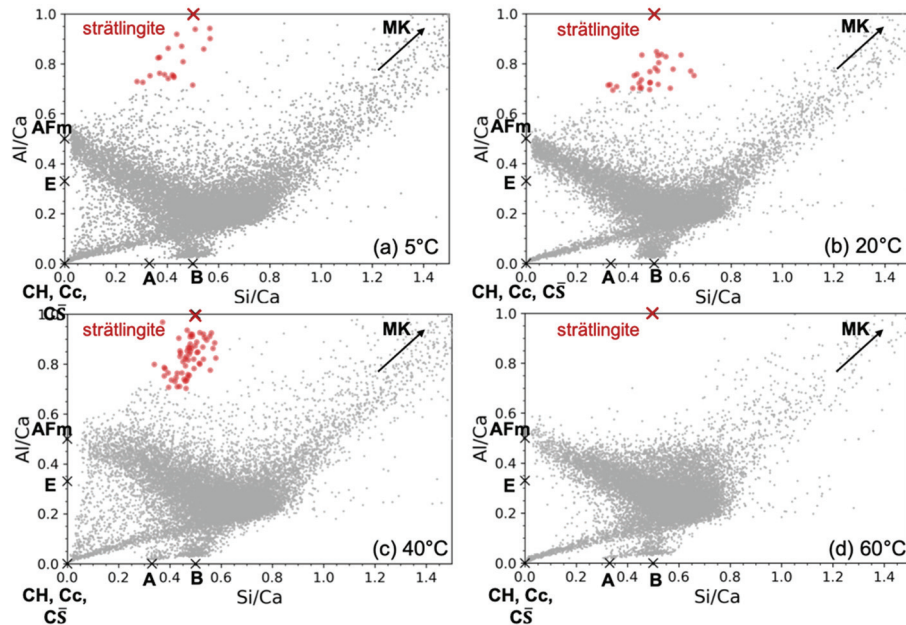


Fig. 3-10 Atomic ratio plots of Si/Ca and Al/Ca of LGCMKLS at 90 days of representative points obtained from EDS mapping [22] with the main composition of hydrated phases. The points around the strätlingite composition are selected in red: A = alite, B = belite, MK = metakaolin, CH = portlandite, Cc = calcite, C̄S = calcium sulfate, E = ettringite and AFm = aluminoferrite-mono phase.

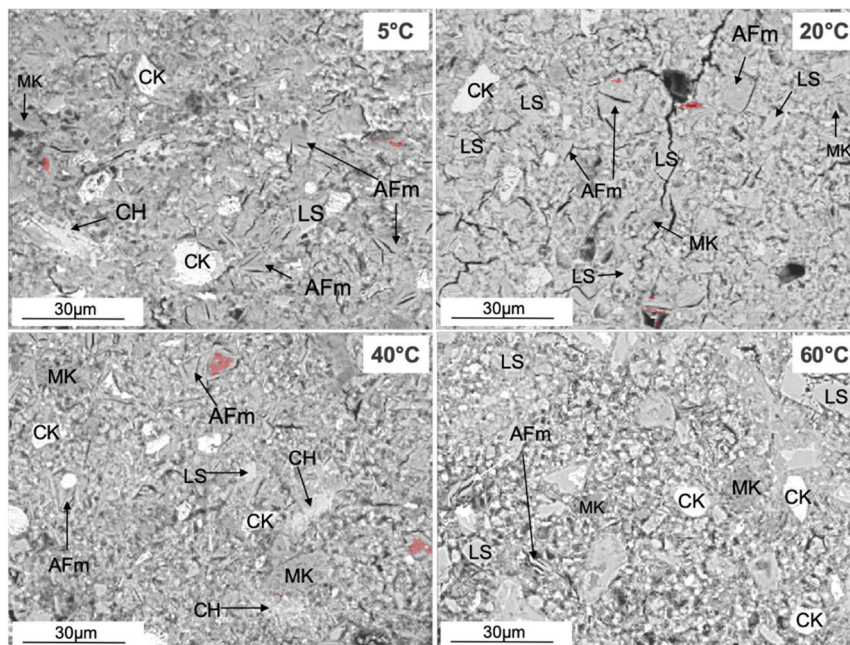


Fig. 3-11 Overlay mask of the selected points in the ratio plot identified as strätlingite (in red) on BSE images of LGCMK at 90 days cured at 5, 20, 40 and 60°C: CK = anhydrous clinker, CH = portlandite and AFm = aluminoferrite-mono phase.

### 3.3.3.2 Co-existence of strätlingite and portlandite

Strätlingite is thermodynamically incompatible with portlandite (CH), which has also been confirmed in several experimental studies in diluted systems with a high water to solid ratio [34,36]. However, many studies reported the mutual presence of portlandite and strätlingite in hydrated blended cements [5,12,35]. Both portlandite and strätlingite have also been found in this study in the blended systems in the temperature range of 5 – 40°C. Thermodynamic modelling, where a complete equilibrium is assumed, predicts only C-S-H at 5 and 20°C and C-S-H plus strätlingite at 40 and 60°C, while portlandite is expected to be absent at all temperatures due to its reaction with metakaolin.

It is interesting to note that strätlingite and portlandite occur in different places (Fig. 3-12), indicating that the thermodynamically incompatible strätlingite and portlandite can coexist at different places in the microstructure. It can be speculated that the transport between different regions of the microstructure is limited or even interrupted due to the lack of water filled pores at later hydration times as e.g. suggested by [37].

The co-existence of strätlingite and portlandite was further investigated by SEM-EDS mapping on the LGCMK samples cured at 5 and 20°C, where strätlingite is well visible, Fig. 3-12 shows the ratio plots of Si/Ca and Al/Ca from EDS mappings and BSE image with the mask of strätlingite and portlandite. Fig. 3-12b and Fig. 3-12d illustrate that monocarbonate, hemicarbonate or monosulfate can form next to portlandite, but not strätlingite. Although the formation of strätlingite is generally found closely to the AFm phase as discussed in the previous section, in no case strätlingite is precipitated next to portlandite, indicating that in a local environment the presence of portlandite excludes the presence of strätlingite and vice versa. Therefore, the co-existence of strätlingite and portlandite in bulk analysis seems to be related rather to the complexity of the microstructure and/or hindered transport, which can lead to different chemical environments with the cement. The transport of ions may be hindered by the dense microstructure of the blended cements, and the low water saturation leading to disconnected regions with the hydrated cement.

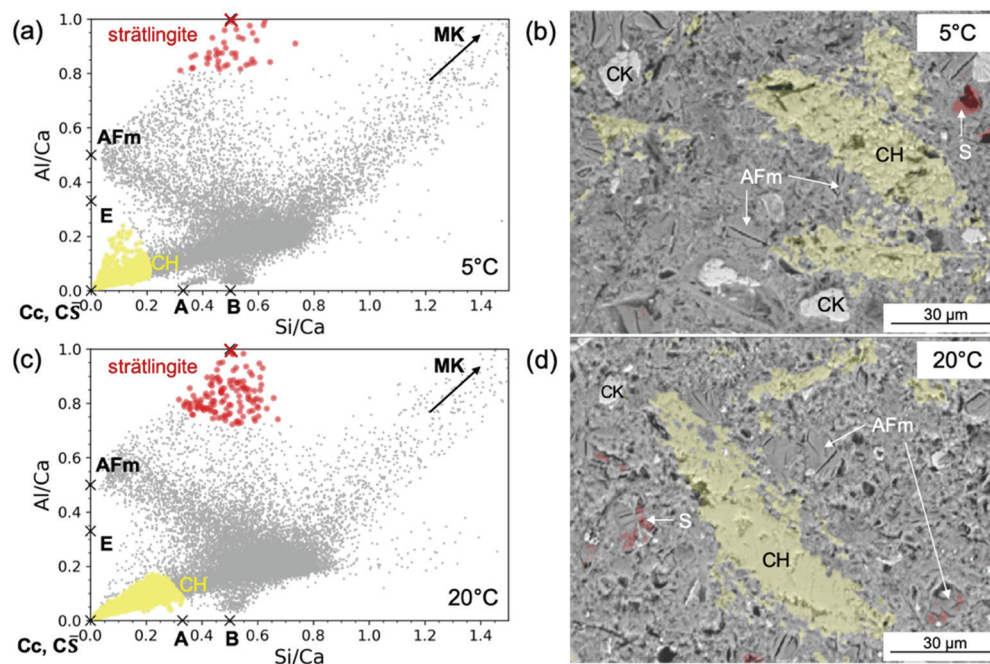


Fig. 3-12 Strätlingite (red) and portlandite (yellow) formation in the microstructure of LGCMK at 90 days of hydration cured at 5 and 20°C: CK = anhydrous clinker, CH = portlandite, S = strätlingite and AFm = alumino-ferrite-mono phase (monosulfate, monocarbonate or hemicarbonate)

### 3.3.4 Siliceous hydrogarnet

Siliceous hydrogarnet containing both Fe and Al in similar quantities has been observed as a stable Fe-containing phase in Portland cement [16]. As siliceous hydrogarnet is present in low quantities and as it is often poorly crystalline, it is challenging to be clearly detected by XRD, SEM-EDS and TGA [16]. Moreover, siliceous hydrogarnet forms easier at high temperature [8,38]. Due to the low Fe content in the investigated system ( $\text{Fe}_2\text{O}_3 < 1.2\%$ ), the possible formation of siliceous hydrogarnet was investigated by using selective dissolution and SEM-EDS mapping.

#### 3.3.4.1 Selective dissolution of the blended cement systems

The main XRD peak of siliceous hydrogarnet at  $2\theta \sim 17.5^\circ$  ( $\text{CuK}\alpha$ ) is located near the main portlandite peak and a major monosulfate peak, which makes the identification of the siliceous hydrogarnet signal challenging in hydrated Portland cements [16]. In fact, the presence of siliceous hydrogarnet cannot be clearly assessed based on XRD (Fig. 3-5), except for the LGCMK sample cured at  $60^\circ\text{C}$ , where a small peak could indicate siliceous hydrogarnet as the remaining portlandite is very low.

A selective dissolution method based on salicylic acid-methanol extraction (SAM) was applied to remove the main phases from the hydrated cement and to be able to identify the minor phases in the cement matrix [8], as shown in Fig. 3-13; the main siliceous hydrogarnet peaks are expected at  $2\theta \sim 17.5, 20.2, 26.9$  and  $28.9^\circ$ . As observed in Fig. 3-13, the presence of siliceous hydrogarnet can be identified clearly in the LGC samples at all temperatures in agreement with other observations on Portland cements [16,39], while in the blended system, siliceous hydrogarnet is observed only at  $60^\circ\text{C}$  and tentatively at  $40^\circ\text{C}$  in LGCMK, where the first peak of siliceous hydrogarnet might be present as a small broad peak interpreted as a poorly crystalline form. Although the SAM extraction is applied, there is no clear evidence of siliceous hydrogarnet formation at the temperature below  $40^\circ\text{C}$  in the blended systems from the XRD result. Whether siliceous hydrogarnet may be present as in amorphous form in the blended systems at low temperature was further investigated by SEM-BSE.

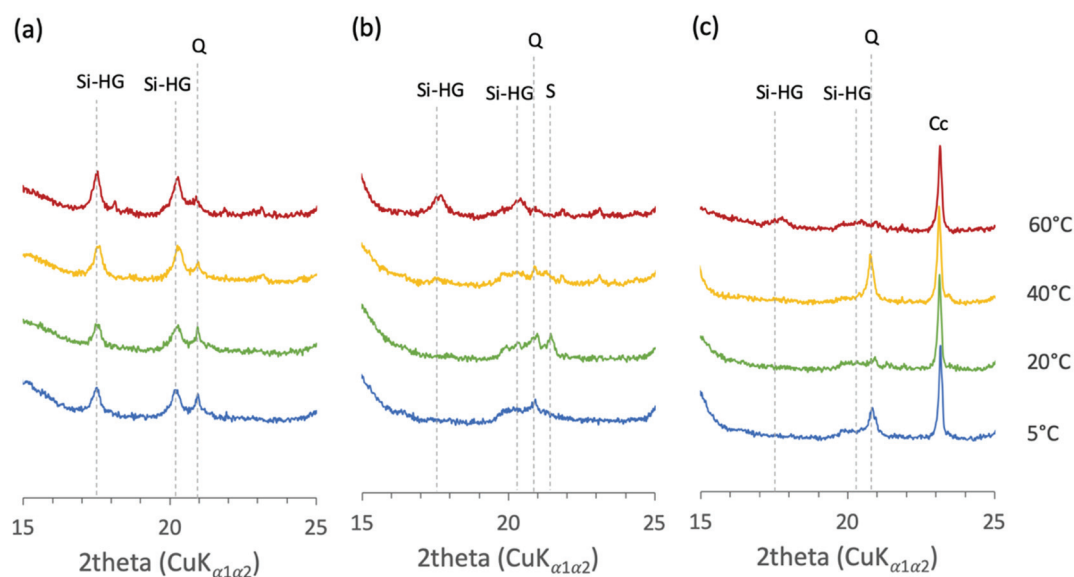


Fig. 3-13 Siliceous hydrogarnet (HG) of (a) LGC, (b) LGCMK and (c) LGCMKLS at different temperatures after selective dissolution with SAM at the zoomed section of XRD patterns between  $15 - 25^\circ$  ( $2\theta$ ): Si-HG = siliceous hydrogarnet, Q = quartz, S = strätlingite and Cc = calcite.



### 3.3.4.2 Tracking Fe-containing phase by SEM-EDS mapping

SEM-EDS mapping and image analysis were used to track high Fe phases in LGCMK and LGCMKLS at 20°C. The cluster of Fe containing phases in the LGCMK system appears in the Fe map shown in Fig. 3-14a. The EDS mapping reveals a high Fe phase as indicated on the ratio plot of Si/Ca and Fe/Ca (Fig. 3-14b) by the red cluster. The red mask from the selected cluster of points appears on the BSE image (Fig. 3-14c) and the ratio plot of Si/Ca and (Al+Fe)/Ca (Fig. 3-14d). From Fig. 3-14d, the Fe-containing phase is intermixing with C-S-H, AFm, strätlingite and siliceous hydrogarnet. The separated grain of high Fe in LGCMK can be observed which is close to siliceous hydrogarnet. Compared to the work of Dilnesa et al. [16], the high Fe-containing cluster in LGCMK contains more Si (Si/Ca~0.55) in the composition than the one formed in Portland cement given as  $C_3FS_{0.84}H_{4.32}$ .

The same approach of verification as the LGCMK system was applied to the LGCMKLS system. For the LGCMKLS sample (Fig. 3-15), Fe is more scattered compared to the LGCMK system. The high Fe points are towards siliceous hydrogarnet and strätlingite composition shown in Fig. 3-15d. Therefore, Fe is possibly in both strätlingite and siliceous hydrogarnet structure. It is not clear to confirm that the LGCMKLS sample cured at 20°C contains siliceous hydrogarnet by tracking high Fe phase in this work.

In addition, in both systems the presence of some Fe in C-S-H is observed, with a Fe/Si molar ratio of  $0.02 \pm 0.01$ . This in agreement with recent investigation on iron uptake in synthetic C-S-H, where Fe/Si of  $\approx 0.001$  to  $0.01$  were observed [40].

The result from the EDS mapping of the LGCMKLS sample cured at 20°C in Fig. 3-10b shows a cloud of points in the ratio plot of Si/Ca and Al/Ca near the strätlingite composition but with slightly too little Al. The same data set was plotted using Fe + Al, as shown in Fig. 3-15d. The cluster of points in this ratio plot (Fig. 3-15d) can reach strätlingite composition. This cloud indicates that strätlingite could contain some Fe in its structure. The synthesis of only Fe-containing strätlingite has found to be not possible [26,41], but the possibility of mixed Al-Fe containing strätlingite has never been studied and would contribute to a better understanding on Fe-containing phase in the higher alumina system.

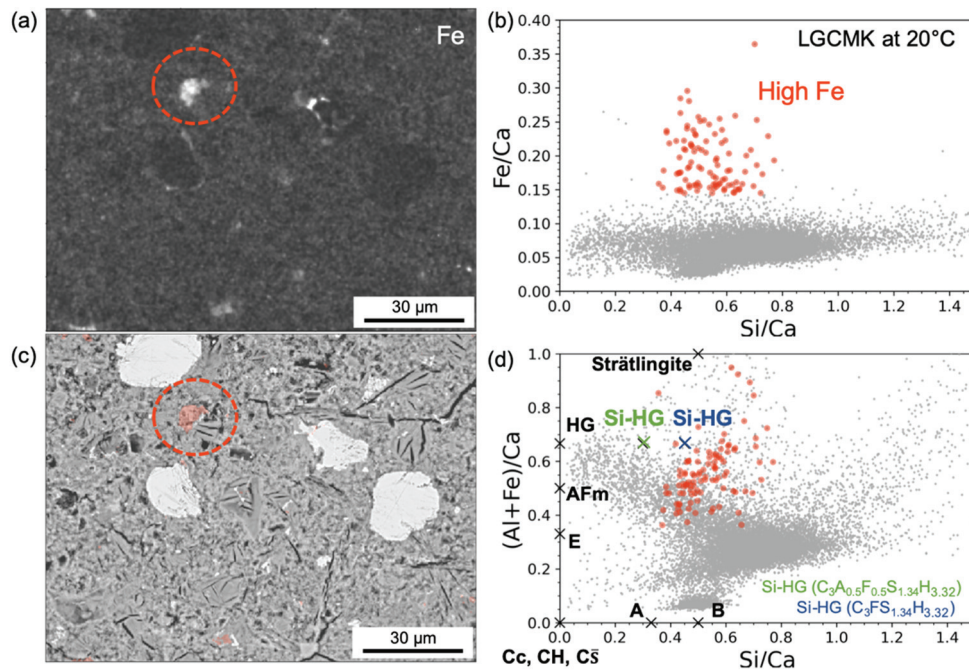


Fig. 3-14. High Fe containing hydrates (in red) in the microstructure of LGCMK at 90 days of hydration cured at 20°C (a) Fe mapping, (b) the ratio plot of Fe/Ca and Si/Ca, (c) the mask in red on BSE image and (d) the ratio plots of (Al+Fe)/Ca and SiCa. The composition is close to siliceous hydrogarnet and strätlingite.

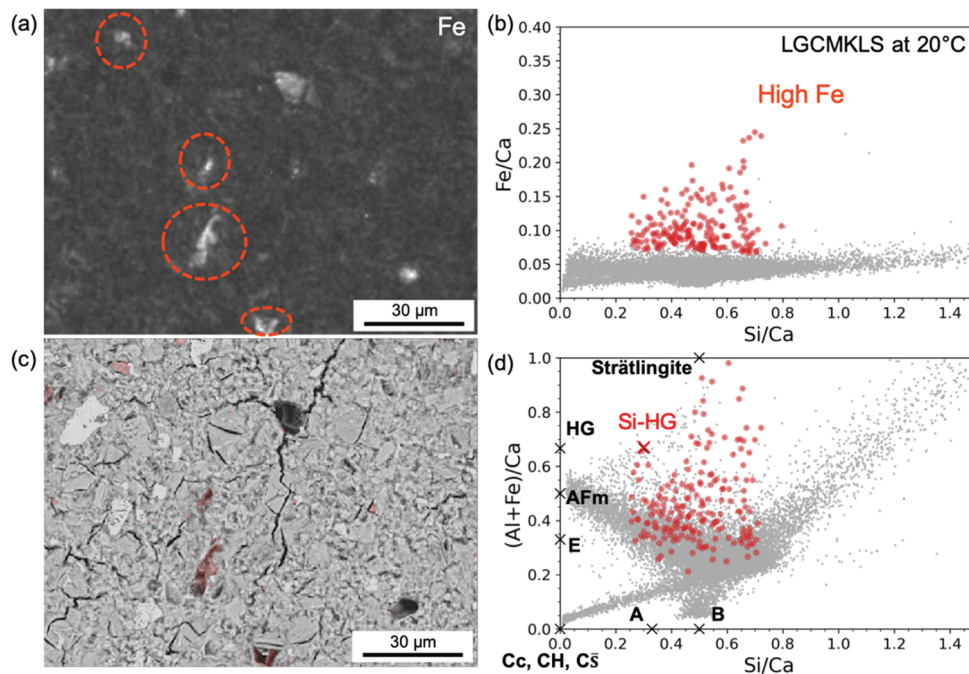


Fig. 3-15. High Fe containing hydrates (in red) in the microstructure of LGCMKLS at 90 days of hydration cured at 20°C (a) Fe mapping, (b) the ratio plot of Fe/Ca and Si/Ca, (c) the mask in red on BSE image and (d) the ratio plots of (Al+Fe)/Ca and Si/Ca.

### 3.3.5 Hydrotalcite formation

Hydrotalcite-like phases,  $(Mg_6Al_2(OH)_{18} \cdot 3(H_2O))$ , are Mg-containing hydrate phases which can have a variable Mg/Al composition and different anions in the interlayer. Since MgO is present as a minor element in LGC and limestone in very low content (less than 1%), it is difficult to detect the hydrotalcite phases by XRD or TGA. The water losses of hydrotalcite from TGA analysis are found at 270 and 400°C [13], but no clear peak is observed from Fig. 3-16. From the XRD patterns in Fig. 3-17, hydrotalcite peak ( $2\theta \sim 11.2^\circ$ ) could be present as a small broad hump in the LGC samples. Although dolomite tends to be more reactive at high temperature [42], no hydrotalcite in the blended systems is observed at 60°C in this study. This could be explained by the low initial amount of MgO in the anhydrous cement and lack of portlandite in the system at high temperature which retards the formation of hydrotalcite [42]. Thus, the TGA and XRD results cannot confirm the formation of hydrotalcite in this study, although it might be present as a minor phase.

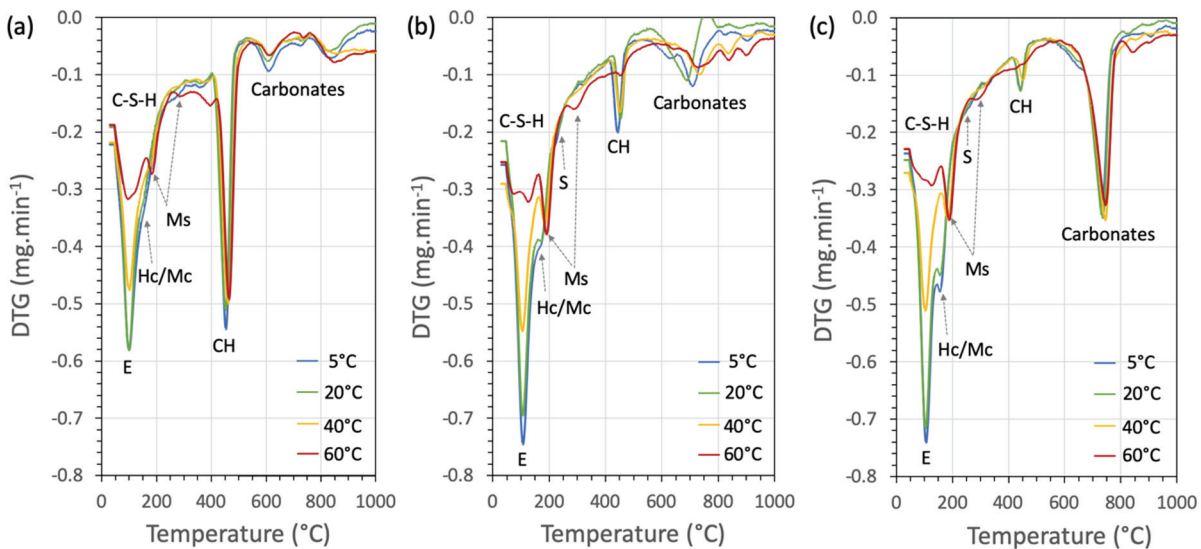


Fig. 3-16 DTG data at 90 days of hydration indicating hydrated phases of (a) LGC, (b) LGCMK and (c) LGCMKLS: E = ettringite, Hc = hemicarbonate, Mc = monocarbonate, Ms = monosulfate, S = strätlingite and CH = portlandite.

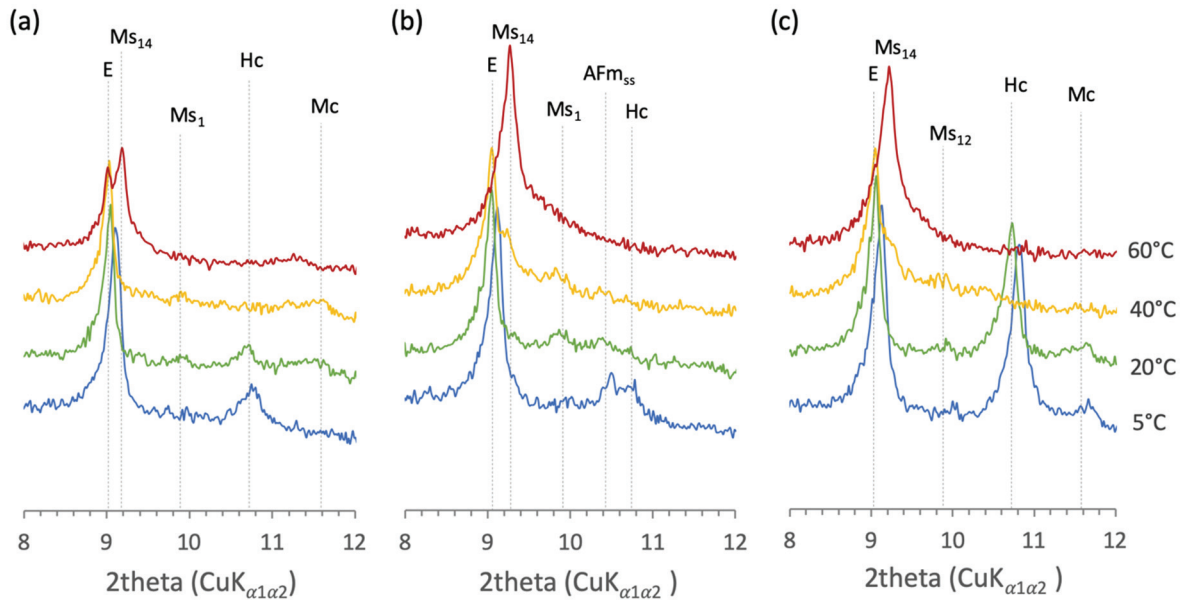


Fig. 3-17 XRD patterns at the zoomed section of between 5 - 15° (2theta) indicating hydrotalcite-like phase (HT) humps mainly in (a) LGC but not clear evidence on (b) LGCMK and (c) LGCMKLS: E = ettringite, Hc = hemicarbonate, Mc = monocarbonate, Ms = monosulfate, AFm<sub>ss</sub> = alumino-ferrite-mono phase solid solution.

### 3.3.6 The ettringite – monosulfate balance 60°C

Thermodynamic modelling at 60°C predicts high ettringite contents (Fig. 3-6a and 6c), while experimentally, rather monosulfate is observed for LGC and LGCMKLS. In the case of the LGC cement, less ettringite is observed by both XRD and <sup>27</sup>Al NMR (around 5 wt.%) than predicted by the modelling (15 wt.%), while the amount of monosulfate was comparable. This indicates the presence of another, unidentified sulfate-containing phase in the hydrates (Paul and Glasser [38] suggested the formation of a sulfate-containing hydrogarnet) or alternatively a strong underestimation of the sulfate content in C-S-H.

While experimentally monosulfate is the main sulfate bearing phase observed at 60°C (both by NMR and XRD), modelling predicts for LGCMK monosulfate (in agreement with the experiments), but rather ettringite for LGCMKLS. Sensitivity analysis of the input used in the thermodynamic modelling showed that relatively small differences in the amount of reacted alite and belite cases either the stabilization of either monosulfate (if sufficient CaO is available) or of ettringite + strätlingite (if the availability of CaO is more limited). The reaction degree of alite and belite were obtained from XRD and <sup>29</sup>Si NMR analysis, which both are associated with errors, especially in the complex case of cementitious material. The overlapping reflexion from alite and belite in the XRD patterns and the superposition of the belite on the broader resonances from alite in <sup>29</sup>Si NMR spectra reduce the precision and accuracy of these methods.

The effect of different DoH values for alite and belite (from XRD and <sup>29</sup>Si NMR) and DoR of metakaolin (from <sup>29</sup>Si NMR and GEMS) is illustrated in Fig. 3-18 and shows significant changes on phase assemblages. The DoH of alite from XRD Rietveld quantification is about 25% higher than the value obtained from <sup>29</sup>Si NMR (Fig. 3-2) and thus about 12% higher than the average value. The presence of more CaO due to the higher alite reaction using the XRD values, TM(XRD/NMR), in fact results in more monosulfate and less ettringite in the modelled results as illustrated in Fig. 3-18. Similar effect is observed when the DoR of metakaolin is decreased, TM(AVR/AVR), using the average value of metakaolin reaction obtained from <sup>29</sup>Si-NMR and the metakaolin reaction calculated from the consumption of port-

landite, underlining the central role of reliable analytics to be able to carry out meaningful thermodynamic calculations.

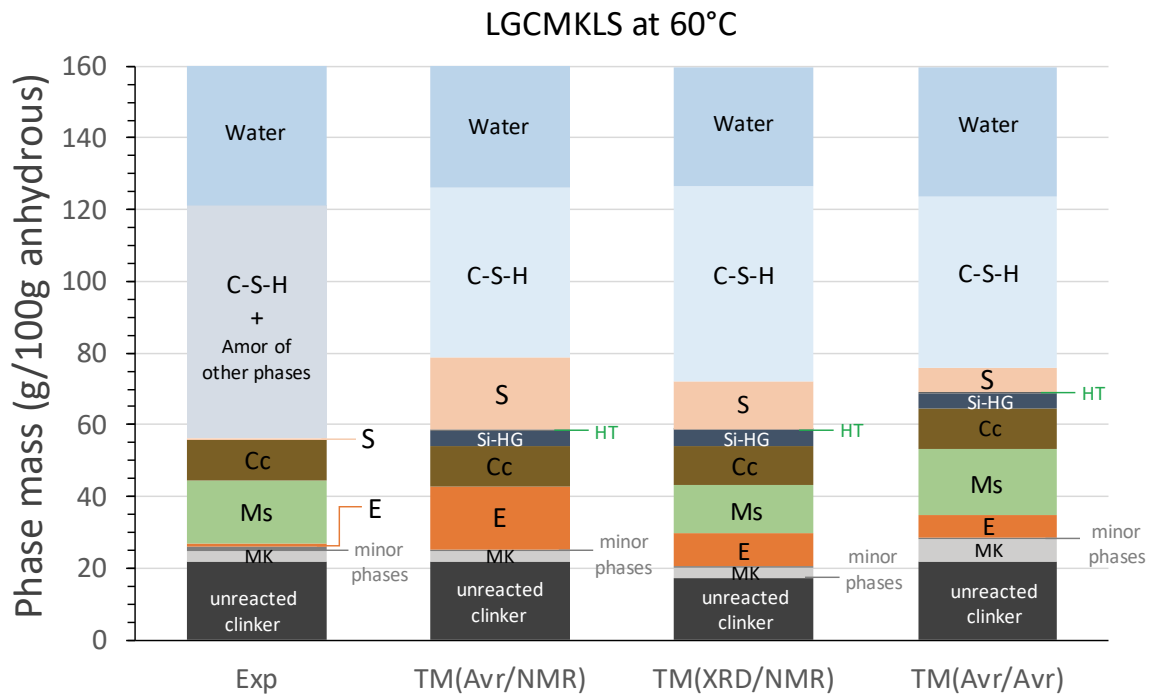


Fig. 3-18 Comparison of thermodynamic modelling based on different inputs of DoH of anhydrous clinker/DoR of metakaolin: E = ettringite, Ms = monosulfate, Cc = calcite, Si-HG = siliceous hydrogarnet, S = strätlingite, MK = metakaolin, Amor = amorphous.

### 3.3.7 Why is hemicarbonate observed ?

The presence of calcite significantly impacts the stability of ettringite and AFm phases, in particular at room temperature. It is known that calcite can stabilize monocarbonate over monosulfate and prevent the destabilization of ettringite [6,33]. However, in all samples hydrated at 5 and 20°C, the formation of hemicarbonate has been observed by XRD. Two different reasons can be envisaged that thermodynamic modelling tends to overestimate the formation of monocarbonate over hemicarbonate has been observed previously in several studies [5,43].

First, it might indicate that the system is not at equilibrium, and hemicarbonate formation is kinetically favored over monocarbonate [43]. Our experiments may not be at equilibrium after 90 days of hydration and hemicarbonate may change later to monocarbonate as e.g. observed in [8,43].

Secondly the monocarbonate in the thermodynamic database might be too stable as recently suggested [44], and/or the hemicarbonate is stabilized by the presence of foreign ions in its interlayer [45].

## 3.4 Conclusions

The presence of metakaolin in Portland cement provides more Al and Si to the system compared to the plain Portland cement and lowers the availability of CaO. As a result, portlandite is absent in such blended systems; more AFm phases (monocarbonate, monosulfate and/or strätlingite) but less ettringite is present in metakaolin blended.

The presence of metakaolin suppresses the reaction of belite at all temperatures, compared to a plain cement. Higher temperatures accelerate the initial reaction of alite, belite and metakaolin, but have less influence on the total degree of reaction after 3 months; only metakaolin reaction is with 90% DoR moderately higher at 60°C than at 5°C, with 70% DoR. Consequently, more AFm phases are present at higher temperature and more Al is incorporated in C-S-H. AFm containing sulfate-carbonate-hydroxide can be found at low temperature, while a poorly crystalline of monosulfate is precipitated at 60°C. Strätlingite is formed in the metakaolin blends and is observed at 5°C to 40°C in the blend with metakaolin, while much less strätlingite is formed in the presence of limestone in ternary blends, although the reason remains unclear. Our results seem to indicate that Fe is present in siliceous hydrogarnet and C-S-H in Portland cement, SEM-EDS points towards the possible presence of iron in strätlingite and C-S-H in the metakaolin blends. Further investigation is needed on both synthetic and real systems.

The composition predicted by thermodynamic modelling agrees generally well with the experimental data, although some discrepancies, especially for the aluminate hydrates are observed. A summary table of hydrated phase assemblage precipitation in the investigated systems at different temperatures (provided in the appendix compares the experimental observation at 90 days with thermodynamic modelling:

- 1) The simultaneous observation of portlandite and strätlingite are incompatible. The co-existence of strätlingite and portlandite in bulk analysis seems to be related to the complexity of the microstructure and/or hindered transport. The transport of ions may be hindered by the dense microstructure of the blended cements and the low water saturation leading to disconnected regions with the hydrated cement, leading to different chemical environments with the cement.
- 2) The degree of alite, belite and metakaolin reaction strongly influences the availability of CaO and influences indirectly whether monosulfate (at higher CaO availability) or ettringite and strätlingite (at low CaO availability) are calculated to form, which led in some cases to difference between modelling and experiments. Moreover, the sample at 90 days may not reach the full extent of reaction yet in the blended system because belite still remains in the system in high quantities
- 3) The detection and analysis of minor phases indicated by thermodynamic modelling is challenging. The formation of strätlingite, siliceous hydrogarnet and hydrotalcite in the blended systems as a function of temperature has to be further verified and the thermodynamic modelling database improved.

The blended systems are considered to be stable in the long term, as little changes are observed with time (see Chapter 5) and the good agreement between experimental data and thermodynamic modelling is presented in this study.

## 3.5 References

- [1] B. Lothenbach, K. Scrivener, R.D. Hooton, Supplementary cementitious materials, *Cem. Concr. Res.* 41 (2011) 1244–1256. <https://doi.org/10.1016/j.cemconres.2010.12.001>.
- [2] J. Skibsted, R. Snellings, Reactivity of supplementary cementitious materials (SCMs) in cement blends, *Cem. Concr. Res.* 124 (2019) 105799. <https://doi.org/10.1016/j.cemconres.2019.105799>.
- [3] Z. Dai, T.T. Tran, J. Skibsted, Aluminum Incorporation in the C-S-H Phase of White Portland Cement-Metakaolin Blends Studied by <sup>27</sup>Al and <sup>29</sup>Si MAS NMR Spectroscopy, *J. Am. Ceram. Soc.* 97 (2014) 2662–2671. <https://doi.org/10.1111/jace.13006>.
- [4] F. Avet, K. Scrivener, Effect of temperature on the water content of C-A-S-H in plain Portland and blended cements, *Cem. Concr. Res.* 136 (2020) 106124. <https://doi.org/10.1016/j.cemconres.2020.106124>.
- [5] W. Kunther, Z. Dai, J. Skibsted, Thermodynamic modeling of hydrated white Portland cement–metakaolin–limestone blends utilizing hydration kinetics from <sup>29</sup>Si MAS NMR spectroscopy, *Cem. Concr. Res.* 86 (2016) 29–41. <https://doi.org/10.1016/j.cemconres.2016.04.012>.
- [6] B. Lothenbach, G. Le Saout, E. Gallucci, K. Scrivener, Influence of limestone on the hydration of Portland cements, *Cem. Concr. Res.* 38 (2008) 848–860. <https://doi.org/10.1016/j.cemconres.2008.01.002>.
- [7] B. Lothenbach, F. Winnefeld, C. Alder, E. Wieland, P. Lunk, Effect of temperature on the pore solution, microstructure and hydration products of Portland cement pastes, *Cem. Concr. Res.* 37 (2007) 483–491. <https://doi.org/10.1016/j.cemconres.2006.11.016>.
- [8] B. Lothenbach, T. Matschei, G. Möschner, F.P. Glasser, Thermodynamic modelling of the effect of temperature on the hydration and porosity of Portland cement, *Cem. Concr. Res.* 38 (2008) 1–18. <https://doi.org/10.1016/j.cemconres.2007.08.017>.
- [9] T. Matschei, F.P. Glasser, Temperature dependence, 0 to 40°C, of the mineralogy of Portland cement paste in the presence of calcium carbonate, *Cem. Concr. Res.* 40 (2010) 763–777. <https://doi.org/10.1016/j.cemconres.2009.11.010>.
- [10] J.I. Escalante-García, J.H. Sharp, The microstructure and mechanical properties of blended cements hydrated at various temperatures, *Cem. Concr. Res.* 31 (2001) 695–702. [https://doi.org/10.1016/S0008-8846\(01\)00471-9](https://doi.org/10.1016/S0008-8846(01)00471-9).
- [11] F. Deschner, B. Lothenbach, F. Winnefeld, J. Neubauer, Effect of temperature on the hydration of Portland cement blended with siliceous fly ash, *Cem. Concr. Res.* 52 (2013) 169–181. <https://doi.org/10.1016/j.cemconres.2013.07.006>.
- [12] M. Antoni, J. Rossen, F. Martirena, K. Scrivener, Cement substitution by a combination of metakaolin and limestone, *Cem. Concr. Res.* 42 (2012) 1579–1589. <https://doi.org/10.1016/j.cemconres.2012.09.006>.
- [13] K. Scrivener, R. Snellings, B. Lothenbach, eds., *A practical guide to microstructural analysis of cementitious materials*, CRC Press, Boca Raton, 2016.
- [14] F. Zunino, K. Scrivener, The influence of the filler effect on the sulfate requirement of blended cements, *Cem. Concr. Res.* 126 (2019) 105918. <https://doi.org/10.1016/j.cemconres.2019.105918>.
- [15] W.A. Gutteridge, On the dissolution of the interstitial phases in Portland cement, *Cem. Concr. Res.* 9 (1979) 319–324.



- [16] B.Z. Dilnesa, E. Wieland, B. Lothenbach, R. Dähn, K.L. Scrivener, Fe-containing phases in hydrated cements, *Cem. Concr. Res.* 58 (2014) 45–55. <https://doi.org/10.1016/j.cemconres.2013.12.012>.
- [17] R. Allmann, Refinement of the hybrid layer structure  $[\text{Ca}_2\text{Al}(\text{OH})_6]^{+}[\text{1}/2\text{SO}_4\cdot 3\text{H}_2\text{O}]^{-}$ , *Neues Jahrb Miner. Monatsh.* (1977) 136–144.
- [18] J. Skibsted, H.J. Jakobsen, C. Hall, Quantification of calcium silicate phases in Portland cements by  $^{29}\text{Si}$  MAS NMR spectroscopy, *J. Chem. Soc. Faraday Trans.* 91 (1995) 4423–4430. <https://doi.org/10.1039/FT9959104423>.
- [19] S.L. Poulsen, V. Kocaba, G. Le Saoût, H.J. Jakobsen, K.L. Scrivener, J. Skibsted, Improved quantification of alite and belite in anhydrous Portland cements by  $^{29}\text{Si}$  MAS NMR: Effects of paramagnetic ions, *Solid State Nucl. Magn. Reson.* 36 (2009) 32–44. <https://doi.org/10.1016/j.ssnmr.2009.05.001>.
- [20] J. Skibsted, M.D. Andersen, The Effect of Alkali Ions on the Incorporation of Aluminum in the Calcium Silicate Hydrate (C-S-H) Phase Resulting from Portland Cement Hydration Studied by  $^{29}\text{Si}$  MAS NMR, *J. Am. Ceram. Soc.* 96 (2013) 651–656. <https://doi.org/10.1111/jace.12024>.
- [21] T.F. Sevelsted, D. Herfort, J. Skibsted,  $^{13}\text{C}$  chemical shift anisotropies for carbonate ions in cement minerals and the use of  $^{13}\text{C}$ ,  $^{27}\text{Al}$  and  $^{29}\text{Si}$  MAS NMR in studies of Portland cement including limestone additions, *Cem. Concr. Res.* 52 (2013) 100–111. <https://doi.org/10.1016/j.cemconres.2013.05.010>.
- [22] F. Georget, W. Wilson, K.L. Scrivener, edxia: Microstructure characterisation from quantified SEM-EDS hypermaps, *Cem. Concr. Res.* 141 (2021) 106327. <https://doi.org/10.1016/j.cemconres.2020.106327>.
- [23] D.A. Kulik, T. Wagner, S.V. Dmytrieva, G. Kosakowski, F.F. Hingerl, K.V. Chudnenko, U.R. Berner, GEM-Selektor geochemical modeling package: revised algorithm and GEMS3K numerical kernel for coupled simulation codes, *Comput. Geosci.* (2012). <https://doi.org/10.1007/s10596-012-9310-6>.
- [24] T. Wagner, D.A. Kulik, F.F. Hingerl, S.V. Dmytrieva, GEM-Selektor geochemical modeling package: TSolMod library and data interface for multicomponent phase models, *Can. Mineral.* 50 (2012) 1173–1195. <https://doi.org/10.3749/canmin.50.5.1173>.
- [25] W. Hummel, U. Berner, E. Curti, F.J. Pearson, T. Thoenen, Nagra/PSI Chemical Thermodynamic Data Base 01/01, *Radiochim. Acta.* 90 (2002). [https://doi.org/10.1524/ract.2002.90.9-11\\_2002.805](https://doi.org/10.1524/ract.2002.90.9-11_2002.805).
- [26] B. Lothenbach, D.A. Kulik, T. Matschei, M. Balonis, L. Baquerizo, B. Dilnesa, G.D. Miron, R.J. Myers, Cemdata18: A chemical thermodynamic database for hydrated Portland cements and alkali-activated materials, *Cem. Concr. Res.* 115 (2019) 472–506. <https://doi.org/10.1016/j.cemconres.2018.04.018>.
- [27] I.G. Richardson, G.W. Groves, The incorporation of minor and trace elements into calcium silicate hydrate (C-S-H) gel in hardened cement pastes, *Cem. Concr. Res.* 23 (1993) 131–138. [https://doi.org/10.1016/0008-8846\(93\)90143-W](https://doi.org/10.1016/0008-8846(93)90143-W).
- [28] E. L'Hôpital, B. Lothenbach, G. Le Saout, D. Kulik, K. Scrivener, Incorporation of aluminium in calcium-silicate-hydrates, *Cem. Concr. Res.* 75 (2015) 91–103. <https://doi.org/10.1016/j.cemconres.2015.04.007>.
- [29] R.J. Myers, E. L'Hôpital, J.L. Provis, B. Lothenbach, Effect of temperature and aluminium on calcium (aluminum)silicate hydrate chemistry under equilibrium conditions, *Cem. Concr. Res.* 68 (2015) 83–93. <https://doi.org/10.1016/j.cemconres.2014.10.015>.
- [30] J.E. Rossen, K.L. Scrivener, Optimization of SEM-EDS to determine the C–A–S–H composition in matured cement paste samples, *Mater. Charact.* 123 (2017) 294–306. <https://doi.org/10.1016/j.matchar.2016.11.041>.



- [31] E. Gallucci, X. Zhang, K.L. Scrivener, Effect of temperature on the microstructure of calcium silicate hydrate (C-S-H), *Cem. Concr. Res.* 53 (2013) 185–195. <https://doi.org/10.1016/j.cemconres.2013.06.008>.
- [32] H.F.W. Taylor, *Cement chemistry*, 2nd ed, T. Telford, London, 1997.
- [33] T. Matschei, B. Lothenbach, F.P. Glasser, The role of calcium carbonate in cement hydration, *Cem. Concr. Res.* 37 (2007) 551–558. <https://doi.org/10.1016/j.cemconres.2006.10.013>.
- [34] M.U. Okoronkwo, F.P. Glasser, Stability of strätlingite in the CASH system, *Mater. Struct.* 49 (2016) 4305–4318. <https://doi.org/10.1617/s11527-015-0789-x>.
- [35] M. Zajac, P. Durdzinski, C. Stabler, J. Skocek, D. Nied, M. Ben Haha, Influence of calcium and magnesium carbonates on hydration kinetics, hydrate assemblage and microstructural development of metakaolin containing composite cements, *Cem. Concr. Res.* 106 (2018) 91–102. <https://doi.org/10.1016/j.cemconres.2018.01.008>.
- [36] T. Matschei, B. Lothenbach, F.P. Glasser, The AFm phase in Portland cement, *Cem. Concr. Res.* 37 (2007) 118–130. <https://doi.org/10.1016/j.cemconres.2006.10.010>.
- [37] M. Zajac, J. Skocek, B. Lothenbach, B.H. Mohsen, Late hydration kinetics: Indications from thermodynamic analysis of pore solution data, *Cem. Concr. Res.* 129 (2020) 105975. <https://doi.org/10.1016/j.cemconres.2020.105975>.
- [38] M. Paul, F.P. Glasser, Impact of prolonged warm (85°C) moist cure on Portland cement paste, *Cem. Concr. Res.* 30 (2000) 1869–1877. [https://doi.org/10.1016/S0008-8846\(00\)00286-6](https://doi.org/10.1016/S0008-8846(00)00286-6).
- [39] M. Vespa, E. Wieland, R. Dähn, B. Lothenbach, Identification of the Thermodynamically Stable Fe-Containing Phase in Aged Cement Pastes, *J. Am. Ceram. Soc.* 98 (2015) 2286–2294. <https://doi.org/10.1111/jace.13542>.
- [40] A. Mancini, E. Wieland, G. Geng, R. Dähn, J. Skibsted, B. Wehrli, B. Lothenbach, Fe(III) uptake by calcium silicate hydrates, *Appl. Geochem.* 113 (2020) 104460. <https://doi.org/10.1016/j.apgeochem.2019.104460>.
- [41] B.Z. Dilnesa, Fe-containing hydrates and their fate during cement hydration: Thermodynamic data and experimental data, (2012).
- [42] A. Machner, M. Zajac, M. Ben Haha, K.O. Kjellsen, M.R. Geiker, K. De Weerd, Limitations of the hydrotalcite formation in Portland composite cement pastes containing dolomite and metakaolin, *Cem. Concr. Res.* 105 (2018) 1–17. <https://doi.org/10.1016/j.cemconres.2017.11.007>.
- [43] M. Zajac, A. Rossberg, G. Le Saout, B. Lothenbach, Influence of limestone and anhydrite on the hydration of Portland cements, *Cem. Concr. Compos.* 46 (2014) 99–108. <https://doi.org/10.1016/j.cemconcomp.2013.11.007>.
- [44] L. Nedyalkova, B. Lothenbach, G. Geng, U. Mäder, J. Tits, Uptake of iodide by calcium aluminate phases (AFm phases), *Appl. Geochem.* 116 (2020) 104559. <https://doi.org/10.1016/j.apgeochem.2020.104559>.
- [45] F. Georget, B. Lothenbach, W. Wilson, F. Zunino, K. Scrivener, Stability of hemicarbonates under cement paste like conditions (in preparation), (n.d.).

### 3.6 Appendix

Table 3-5 Summary hydrated phase assemblage precipitation in the investigated systems at different temperatures from the experimental observation at 90 days of hydration compared to thermodynamic modelling prediction.

Phases	LGC						LGCМК						LGCМКLS								
	5°C		20°C		40°C		5°C		20°C		40°C		5°C		20°C		40°C		60°C		
	Exp	TM	Exp	TM	Exp	TM	Exp	TM	Exp	TM	Exp	TM	Exp	TM	Exp	TM	Exp	TM	Exp	TM	
C-S-H	/	/	/	/	/	/	/	/	/	/	/	/	/	/	/	/	/	/	/	/	/
Portlandite	/	/	/	/	/	/	/	X	/	X	/	X	/	X	/	X	/	X	/	X	X
Ettringite	/	/	/	/	/	/	/	/	/	/	/	/	/	/	/	/	/	/	/	/	/
Monocarbonate	X	X	/	X	/	X	X	/	X	/	X	X	/	X	/	X	X	/	X	/	X
Hemicarbonate	/	X	/	X	/	X	/	/	/	X	/	X	X	/	X	/	X	/	X	/	X
Monosulfate	X	X	X	X	/	/	/	/	/	/	/	/	/	X	X	X	X	/	X	/	X
Calcite	/	X	/	/	/	/	/	X	/	X	/	X	/	/	/	/	/	/	/	/	/
Hydroxalcite	?	/	?	/	?	/	?	/	?	/	?	/	?	/	?	/	?	/	?	/	/
Si-hydrogarnet	/	/	/	/	/	/	/	/	/	/	/	/	/	?	/	?	/	?	/	?	/
Strätlingite	X	X	X	X	X	X	X	/	X	/	X	/	X	/	X	/	X	/	X	/	/

Note: / = yes, X = no, ? = not confirmed



# Chapter 4 Phase assemblages of the CSA system

**Note:** This chapter is based on an article in preparation for submission to a peer reviewed journal.

Contribution of the doctoral candidate: Writing of the first manuscript draft, experimental design, conduction of the experiment and thermodynamic modelling.

## Abstract

This study investigates the effects of temperature on phase assemblages of belite-ye'elimite cement. A comparison is made between thermodynamic modelling and the experimental data after 90 days of hydration at 5, 20, 40 and 60°C. An overall good agreement is found, with some discrepancies which are discussed in this paper. The degree of reaction of belite was observed to be a non-monotonous function of the temperature, leading to important changes of phase assemblages at different temperatures. In particular, C-S-H was predicted and observed at 5 and 60°C where the belite reaction is high. Siliceous hydrogarnet was only observed experimentally at 60°C, where its amount needs to be restricted in thermodynamic modelling. Finally, strätlingite was observed to be finely intermixed with the AFm phase from EDS mapping.

**Keywords:** Belite-ye'elimite cement, Hydration, Phase assemblages, Thermodynamic modelling, Temperature.

---

**CONTENTS**

---

<b>Chapter 4</b>	<b>Phase assemblages of the CSA system.....</b>	<b>73</b>
4.1	Introduction .....	75
4.2	Materials and methods .....	76
4.2.1	Raw materials and mixture design.....	76
4.2.2	Raw materials characterization .....	76
4.2.3	Preparation of cement pastes.....	77
4.2.4	Methods.....	77
4.3	Results and discussion.....	79
4.3.1	Reaction of belite and ye'elimite in BY cement paste .....	79
4.3.2	Comparison of phase assemblages between experimental data at 90d and thermodynamic modelling .....	80
4.3.3	Identification of C-S-H formation.....	81
4.3.4	Formation of siliceous hydrogarnet at 60°C .....	85
4.3.5	Quantification and validation of AFm formation in BY cement.....	86
4.4	Conclusions .....	89
4.5	References.....	90
4.6	Appendix .....	93

---

## 4.1 Introduction

Calcium sulfoaluminate cement (CSA) is used as an alternative binder generating lower CO<sub>2</sub> emission than Portland cement (PC) [1], due to its lower sintering temperature and its lower decarbonation of limestone, its production is more environmentally friendly [2]. CSA is a general term for binders containing ye'elimite (C<sub>4</sub>A<sub>3</sub>S̄, Ca<sub>4</sub>(AlO<sub>2</sub>)<sub>6</sub>SO<sub>3</sub>). CSA cements contain more alumina than PC and can be classified into two main groups: (i) high ye'elimite CSA and (ii) low ye'elimite CSA commonly called BYF (Belite-Ye'elimite-Ferrite). The different clinker composition changes the hydrated phase assemblages, leading to different properties of the concrete made from these binders [3–5]. High ye'elimite CSA cements are generally used for niche applications such as rapid hardening, shrinkage compensation and fast setting, while BYF cements are used as a PC replacement with a lower carbon footprint [2,6,7].

The reactivity of BYF cements depends on many factors such as the amount of calcium sulfate [8,9], mixing water [10], and the presence and amount of minor phases, in particular mayenite [11]. BYF is also very sensitive to temperature which affects not only the hydration kinetics, but also the types of hydrates formed [12–14]. Ettringite can be destabilized in favour of the monosulfate due to the increase of ettringite solubility at high temperature, while the stability of monosulfate varies little with temperature [15,16]. Ettringite can present in the ye'elimite-rich cements up to 90°C [13]. The kind and solubility of aluminium hydroxide (AH<sub>3</sub>) formed depends also on temperature. Well soluble amorphous or microcrystalline AH<sub>3</sub> is formed at ambient temperatures and below. The ordering and thus crystallinity increase with temperature. Gibbsite seems to form above 60°C [16]. Even though the hydration of BYF cements has been widely studied, most studies have been carried out at room temperature.

In a BYF system, the reaction of ye'elimite and calcium sulfate with water occurs fast resulting in the formation of ettringite and aluminium hydroxide (AH<sub>3</sub>) gel during the first hours. After sulfate depletion monosulfate [Ca<sub>4</sub>Al<sub>2</sub>(OH)<sub>12</sub>]<sup>2+</sup>[SO<sub>4</sub>·nH<sub>2</sub>O]<sup>2-</sup>, an AFm-type phase and AH<sub>3</sub> form. Ettringite and AFm are crystalline structures, while AH<sub>3</sub> is generally present as an amorphous or microcrystalline phase in this type of cement [17–19]. Belite reacts at later age, forming calcium silicate hydrates (C-S-H) and strätlingite (C<sub>2</sub>ASH<sub>8</sub>, [Ca<sub>4</sub>Al<sub>2</sub>(OH)<sub>12</sub>]<sup>2+</sup>[(AlSi(OH)<sub>8</sub>)<sub>2</sub>·nH<sub>2</sub>O]<sup>2-</sup>), another AFm-type phase [8,10,18]. In addition, sometimes, siliceous-hydrogarnet can be observed at late ages due to the reaction of ferrite [10,20].

Thermodynamic modelling can be used as a tool to predict the composition of the phase assemblages in long term or at equilibrium state [17,18,21–23], or the changes occurring during hydration, if the reaction of the clinkers is well characterized. Thermodynamic modelling can also be used to predict the stability of these binders under a wide range of conditions (temperature, pressure, interaction with the environment, etc.) [13,23]. However, the validity of these models needs to be verified experimentally.

Different phases are formed during hydration, which might destabilise again with time such as e.g. Al(OH)<sub>3</sub>, which forms, once belite reacts, strätlingite and or C-S-H [10]. These changes during hydration and their effect on the microstructure is poorly understood as particularly C-S-H and strätlingite are difficult to observe and quantify in low quantities due to their poor crystallinity. In particular, the identification of C-S-H in the microstructure next to the X-ray amorphous Al(OH)<sub>3</sub> is challenging [22]

This work aims to compare long-term phase assemblages in CSA-belite cements at different temperatures based on the experimental data, including in-depth analysis of phase assemblages and microstructure observed by various techniques, and thermodynamic modelling. A simplified system based on belite, ye'elimite and calcium sulfate, a belite-ye'elimite (BY) cement, is used. The hydration of this BY cement is investigated from 5 to 60°C at 90 days of hydration. The water to binder ratio was fixed at 0.6 and ye'elimite to calcium sulfate molar ratio at 1:1. The hydrated cements were characterized in detail by XRD, TGA, SEM-EDS mapping and image analysis.

## 4.2 Materials and methods

### 4.2.1 Raw materials and mixture design

A laboratory prepared belite-ye'elinite clinker, mayenite clinker and a natural anhydrite source were used in this study. The belite-ye'elinite clinker was prepared using an adaptation of the cylinder method presented by X. Li et al. [24]. Chemical reagents (calcium carbonate, nano silica, calcium sulfate dihydrate and aluminium oxide) were ground for 24 hours with water. Then, the mix was poured in cylinders and dried at least 48 hours at 105°C. The cylinders were inserted in a static furnace, burned at 1300°C for 1 hour with a heating rate of 7°C/min, and quenched at room temperature. Mayenite ( $C_{12}A_7$ ) was synthesized following the steps in [11]. The laboratory prepared BY clinker was blended with anhydrite, ground from a natural source. Anhydrite was added to obtain a calcium sulfate to ye'elinite molar ratio of 1:1. A small amount of mayenite was added to accelerate the ye'elinite reaction [11]. The investigated system (BY) composed of 89.3% of BY clinker, 10.6% of micro-anhydrite and 0.25% of mayenite i.e. a total content of  $C_2S$  is 52.3% and ye'elinite is 36.9%. The relative amount of Al, Ca and Si oxides corresponds approximately to a PC system blended with 20% of metakaolin.

### 4.2.2 Raw materials characterization

The chemical composition, mineralogy and particle size distribution value of the raw materials in this study were characterized by X-ray fluorescence (XRF), quantitative powder X-ray diffraction (XRD) and laser diffraction (Malvern MasterSizer S), as shown in Table 4-1.

Table 4-1: Chemical composition, mineralogy and distribution value of the raw materials

PSD [ $\mu\text{m}$ ]	BY clinker	Mayenite	Anhydrite	XRD (wt.%)	BY clinker	Mayenite	Anhydrite
$D_{v,10}$	0.54	2.77	0.25	$C_2S$	60.3	-	-
$D_{v,50}$	4.34	8.49	8.97	$C_3A$	-	1.9	-
$D_{v,90}$	15.88	30.14	31.75	$C_4A_3\bar{S}$	39.4	-	-
XRF (wt.%)				CA	-	0.6	-
$SiO_2$	18.9	0.1	2.5	$C_{12}A_7$	-	97.5	-
$Al_2O_3$	20.9	50.1	0.6	Dolomite	-	-	6.9
$Fe_2O_3$	0.0	0.1	0.3	Portlandite	-	-	0.1
CaO	53.2	47.6	38.7	Gypsum	-	-	2.5
MgO	0.1	-	1.9	Lime	0.3	-	-
$SO_3$	6.3	0.1	52.2	Anhydrite	-	-	77.7
$K_2O$	-	-	0.2	Quartz	-	-	2.3
$Na_2O$	0.1	0.1	0.1	Rutile	-	-	1.2
Others	0.0	0.0	0.2	Muscovite	-	-	8.5
LOI*	0.6	1.2	3.4	Cristobalite	-	-	0.7
SUM	100.1	99.4	100.2	SUM	100.0	100.0	99.9

\*LOI = Loss of ignition

The BY clinker was ground for 60 seconds in a concentric disc mill in batches of 100 g with 7-10 drops of isopropanol added as a grinding aid. The mineralogy of raw materials was determined by Rietveld XRD. Back-loading method was applied to reduce the effects of preferred orientation. The samples were characterized in Bragg-Brentano mode by a X'Pert PANalytical diffractometer with a  $\text{CuK}\alpha_{1\alpha 2}$  source with 45 kV and 40 mA. Continuous rotation was applied during the acquisition. Samples were scanned from 2 theta between 5 and 70 degrees for a total duration of 30 minutes.

Particle size distributions were measured by laser diffraction using MalvernSizer S. The powder approximately 0.1 g was mixed in the isopropanol. The suspension was stirred and placed in an ultrasonic probe for 15 minutes. Then, the suspension was transferred to the measuring unit filled with isopropanol until the proper level of obscuration was reached. The refractive index:imaginary index of clinker, mayenite and anhydrite are 1.66:0.001, 1.62:0.001 and 1.53:0.001, respectively.

### 4.2.3 Preparation of cement pastes

The binders and deionized water were equilibrated overnight at the intended curing temperature before mixing. The dry powders were blended with a lab mixer for 1 minute. Cement pastes were prepared with water to binder ratio (w/b) of 0.6 at 1600 rpm for 2 minutes. The samples were cast in a 50 ml polypropylene container under sealed condition with a few drops of distilled water on top of the paste to keep saturated curing. The samples were stored up to 90 days of hydration at 5, 20, 40 and 60°C with a variation less than  $\pm 1^\circ\text{C}$ . The samples were analysed by X-ray diffraction (XRD), thermogravimetric analysis (TGA), scanning electron microscopy and energy dispersive X-ray spectroscopy (SEM-EDX).

### 4.2.4 Methods

The cement pastes were cut by a circular saw with water-cooling. The fresh slices of 2-3 mm thickness were analysed with a PANalytical X'Pert Pro diffractometer using  $\text{CuK}\alpha_{1\alpha 2}$  source. The X-ray tube worked at 45 kV and 40 mA and the Bragg-Brentano configuration included a fixed diverge slit of  $1/2^\circ$ , a Soller slit of 0.04 rad and mask of 15 mm. The patterns were recorded between 5 and  $70^\circ$  (2 theta) using a step size of  $0.017^\circ$  for a total duration of 14 min. Rutile was used as an external standard to quantify the amorphous content in the cement paste. The quantitative phase assemblage was carried out by using Rietveld refinement method using the High Score Plus software. The degree of hydration (DoH) of anhydrous phases at time t was calculated from the mass fraction of reacted to initial amount. The formula for the calculation is shown in Equation 4-1. The experimental errors of XRD were estimated on belite and ye'elimite on 28 days samples analysed with two replicates. The error limits of the XRD Rietveld quantification is around 2% mass.

Equation 4-1:

$$\text{DoH } (\%)_t = \left( \frac{W_0 - W_t}{W_0} \right) \times 100$$

Where  $W_0$  is initial amount,  $W_t$  is the amount at time t.

Full scaled XRD patterns are presented in the appendix.



The hydration of the cement pastes was stopped by solvent exchange using isopropanol [25]. The sample slices were immersed in the isopropanol for one week. The isopropanol was changed at 1, 3 and 7 days. The samples were dried in a desiccator under light vacuum at least 7 days before the analysis. A small piece of the sample was polished on every sides of the surface to remove the carbonated area before being gently grinded in a ceramic mortar. 50 mg of sample powder was placed in a 150  $\mu$ L alumina crucible with a lid, then was analysed by TGA (Mettler Toledo TGA/SDTA 851 instrument) from 30°C to 1000°C with the rate of 10°C/min and under 30 ml/min N<sub>2</sub> gas flow. The weight loss from TGA analysis was used to obtain the amount of chemical bound water (BW) as shown in Equation 4-2.

Equation 4-2:

$$BW = \frac{W_{40} - W_{550}}{W_{550}}$$

where  $W_t$  is the dry sample weight in grams at the respective temperature (°C).

The same method of stopping hydration for TGA analysis was applied to the SEM-EDX analysis. A piece of sample was gently polish with a silicon carbide paper of 1200 grid to smooth the surface. The samples were embedded in a low viscosity epoxy resin under the vacuum. The impregnated samples were hand-polished on a SiC paper of 1200 grid with isopropanol as a lubricant until the sample surface was uncovered. The sample was polished by diamond suspension of 9, 3, 1 and 1/4  $\mu$ m. The force of 15 kN with 150 rpm was applied for all the polishing steps and the petroleum was used as a lubricant during the fine polishing. After each hour of polishing, the polishing disc was washed between the steps with soap and water using a brush. The samples were washed with the isopropanol in an ultrasonic bath to remove the residue from the surface. The polished samples were stored in a vacuum desiccator for at least two days to evaporate the isopropanol before coating with carbon. Full detail and justification of the method is given in [25]. A polished section was analysed by using a GeminiSEM 300 under high vacuum mode for the high-resolution BSE image (field emission) and using a FEI Quanta 200 scanning electron microscope equipped with a Bruker ASX microanalysis XFlash 4030 silicon drift detector for the EDS mapping (tungsten filament). The acceleration voltage was 12 kV in both instruments, with a working distance of 8.5 mm for BSE image acquisition, and 12.5 mm for EDS mapping.

The image analysis was carried out to identify the formation of interesting phases in the microstructure. The BSE images and EDS mapping data were linked using edxia [26]. The ratio plots of Si/Ca – Al/Ca and Al/Ca – S/Ca from EDS maps provide the composition of the main phases present in the sample. Using the graphical interface of edxia, manually selected points in the ratio plots appear on the BSE image to match composition and structure.

Thermodynamic modelling was carried out using GEMS-PSI software [27,28] with the PSI-Nagra database [29] and the cement CEMDATA18 database [16]. The degrees of hydration from Rietveld quantification of the main clinker phases at 90 days of hydration were used as an input for the calculations. Some minor phases in the natural anhydrite (quartz, muscovite, cristobalite and rutile) were considered as inert phases and thus excluded from the calculations. The Al-incorporation in C-S-H is not included in this model as it cannot be measured accurately. The formation of microcrystalline Al(OH)<sub>3</sub> only was allowed at 5, 20 and 40°C, while gibbsite formation was allowed at 60°C [16].

## 4.3 Results and discussion

### 4.3.1 Reaction of belite and ye'elimite in BY cement paste

The unreacted amount of belite and ye'elimite in the BY cement paste from 1 up to 90 days of hydration is shown in Fig. 4-1. Ye'elimite reacts very quickly and nearly fully (>90%) during the first day of hydration; changes are negligible between 1 and 90 days. The consumption of ye'elimite at 5°C is slightly higher than at the other curing temperatures. For belite, a slow reaction is observed with no significant difference between the different curing temperatures during the first 28 days. However, after 90 days more belite is consumed at 60°C in higher amounts compared to the other temperatures, followed by 5°C, while little reaction of belite at 20 and 40°C was observed. Presently, there is no clear explanation why belite is more reactive at 5°C than at 20 and 40°C.

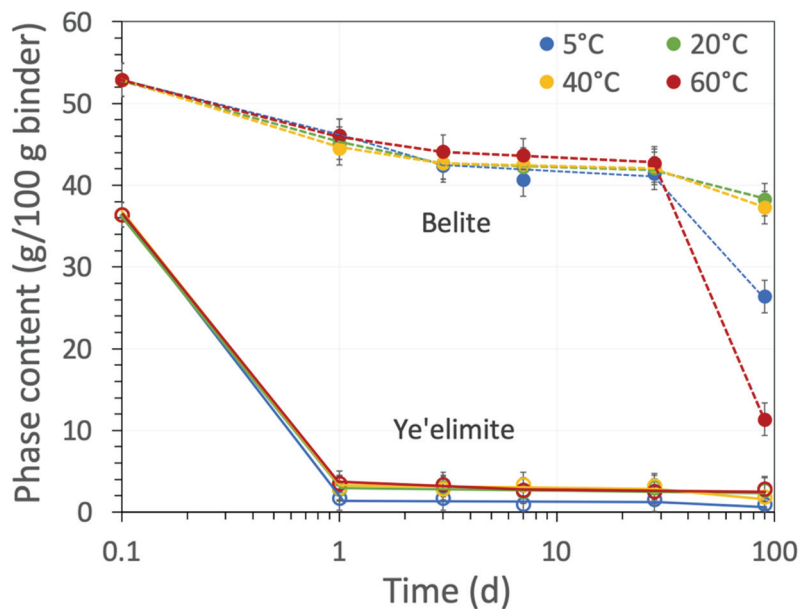


Fig. 4-1. Phase content of anhydrous phases in BY cement paste up to 90 days of hydration obtained by XRD with Rietveld refinement.

The DoH all of the anhydrous phases after 90 days of hydration are shown in Fig. 4-2. The DoH of ye'elimite is higher than 90% for all temperatures, although it is slightly lower at higher temperatures. Also, anhydrite has a high DoH of more than 80% at low temperature and is almost fully reacted at 40°C and above. As shown in Fig. 4-1, more belite has reacted at 5 and 60°C than at 20 and 40°C.

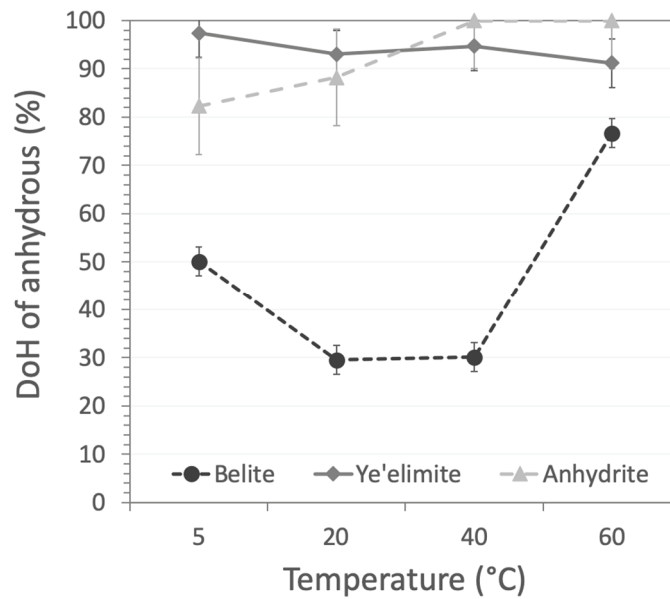


Fig. 4-2. Degree of hydration (DoH) of belite, ye'elimite and anhydrite at 90 days of hydration obtained by XRD with Rietveld refinement.

#### 4.3.2 Comparison of phase assemblages between experimental data at 90d and thermodynamic modelling

The measured reaction degrees of ye'elimite, anhydrite and belite were used to predict with the help of thermodynamic modelling, the phases and their quantities, which are expected to form after 90 days as summarized in Fig. 4-3. The modelling results are compared to the hydrates formed after 90 days of hydration analysed by XRD-Rietveld and TGA.

The main hydrates observed experimentally include ettringite, monosulfate,  $\text{Al}(\text{OH})_3$ , strätlingite and some additional amorphous phase at 20°C and at 40°C. At 5 and 60°C, where more belite had reacted, C-S-H and siliceous hydrogarnet are observed, while  $\text{Al}(\text{OH})_3$  is absent. The amount of free water was calculated from the difference between mixing water and the bound water (BW) determined by TGA.

In general, thermodynamic modelling matches well with the experimental data. The amount of ettringite, Ms and  $\text{Al}(\text{OH})_3$  predicted by thermodynamic modelling at 20 and 40°C is comparable to the experimental results. More strätlingite is predicted than experimentally observed by XRD, indicating that a part of the strätlingite is rather amorphous. The amount of ettringite detected by XRD-Rietveld is the lowest at 60°C which is consistent with the thermodynamic modelling prediction, although the predicted value is even lower. Instead of ettringite, a higher amount of Ms is predicted by thermodynamic modelling at 60°C, which could be related to the presence of X-ray amorphous monosulfate or due to the formation of siliceous hydrogarnet. At 5°C, where more belite has reacted, the formation of C-S-H and the absence of  $\text{Al}(\text{OH})_3$  are predicted. Somewhat more strätlingite is predicted than experimentally observed. Both experimental data and thermodynamic modelling present a similar trend of decreasing strätlingite at elevated temperature but the amounts are significantly different. If Si is not present in strätlingite, it should be present in another silicate phase such as C-S-H. This needs to be verified. As a summary, the experimental data and thermodynamic modelling show overall good agreement in qualitative analysis but still present some discrepancies as listed below;

- (i) The formation of C-S-H at 5 and 60°C by thermodynamic modelling need to be verified experimentally
- (ii) The absence of siliceous hydrogarnet at 60°C is predicted by thermodynamic modelling
- (iii) A higher amount of AFm type phases (Ms and strätlingite) is predicted by thermodynamic modelling

In the remaining of this paper, the discrepancies between experimental data and thermodynamic modelling are investigated in more detail.

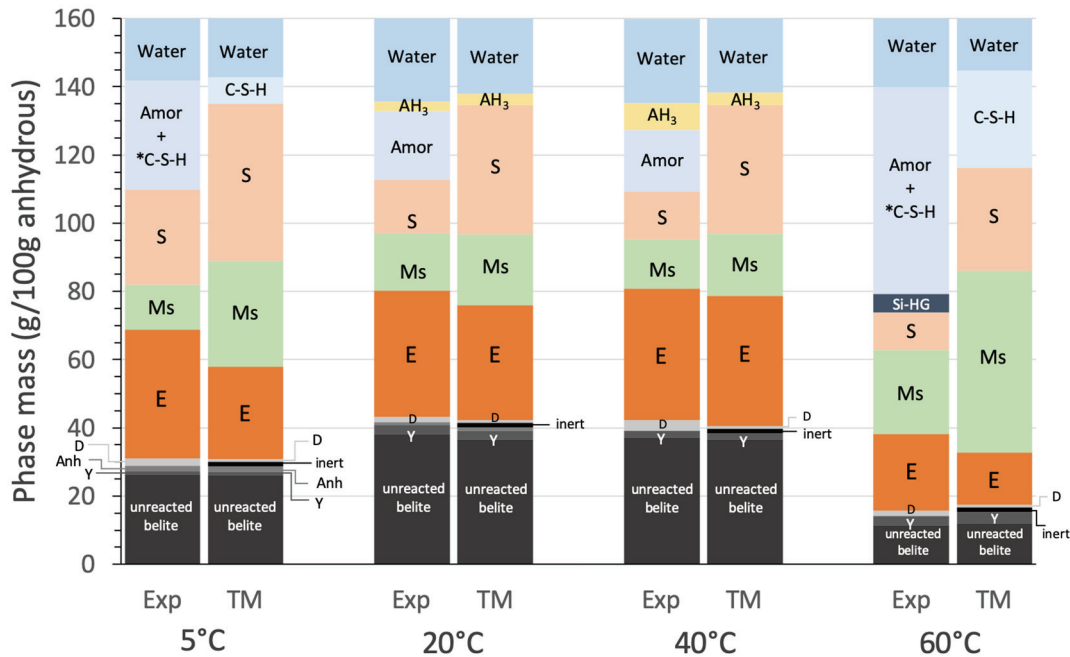


Fig. 4-3. Comparison of phase assemblages at different temperatures between thermodynamic modelling and the experimental data at 90 days: Y = ye'elimite, Anh = anhydrite, D = dolomite, E = ettringite, Ms = total monosulfate, S = strätlingite, AH<sub>3</sub> = aluminium hydroxide, Amor = amorphous and C-S-H = calcium silicate hydrates.

#### 4.3.3 Identification of C-S-H formation

The formation of C-S-H is predicted in thermodynamic modelling at 5 and 60°C, i.e. in those systems where a higher reaction of belite has been observed. The presence of C-S-H can potentially be verified qualitatively by XRD pattern and SEM-EDS. Fig. 4-4 shows the XRD patterns after 90 days of hydration at different temperatures focusing on the patterns between 28 - 34° (2theta), where the broad peak typical for C-S-H should be present [30]. In fact, a clear hump at around 29 – 30° typical for C-S-H is observed at 5 and 60 °C, indicating the presence of C-S-H in those two samples.

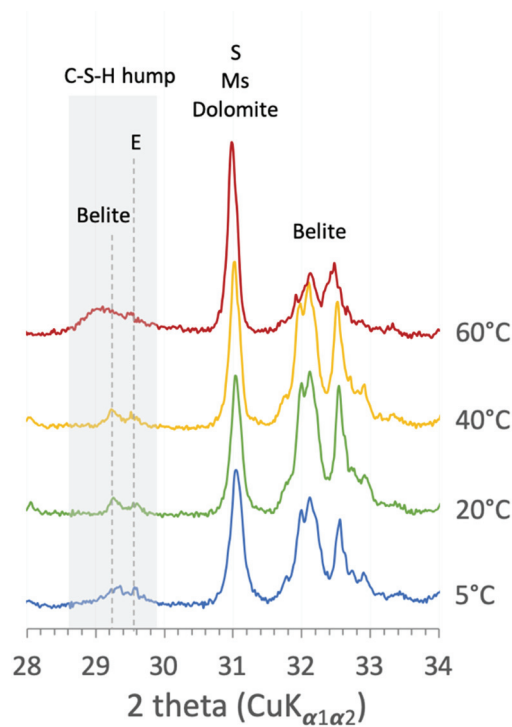


Fig. 4-4. C-S-H humps at different temperatures at the zoomed section of XRD patterns between  $2\theta$  28 - 34°: C-S-H = calcium silicate hydrates, E = ettringite, S = strätlingite, Ms = monosulfate.

The formation of C-S-H in the microstructure cured at 5 and 60°C was also observed by SEM. In contrast to Portland cement system, where C-S-H generally grows from the surface of cement clinkers [31], no rim of inner C-S-H around belite grains was observed at 90 days (Fig. 4-5). At low magnification of the BSE image, C-S-H is difficult to detect due to its small size and as it is finely distributed between ettringite and Ms (present as platelets), as shown in Fig 6a and 6b. C-S-H is generally distributed in the available space rather than next to the belite grains. At high magnification, as shown Fig. 4-6C and 6d, C-S-H is well visible; EDS mapping together with image analysis were used to identify C-S-H and obtain its composition.

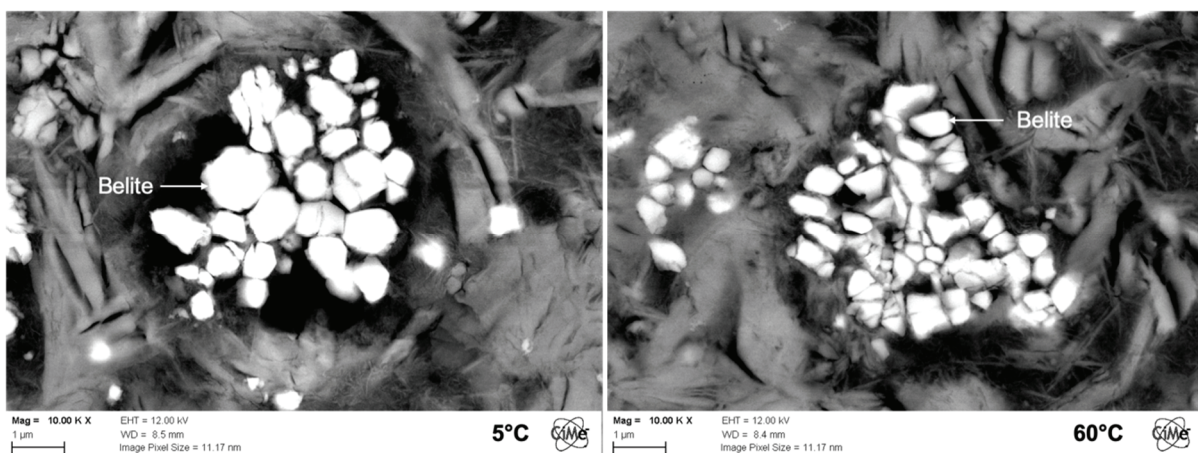


Fig. 4-5 Microstructure around belite grains at 5 and 60°C with high resolution SEM



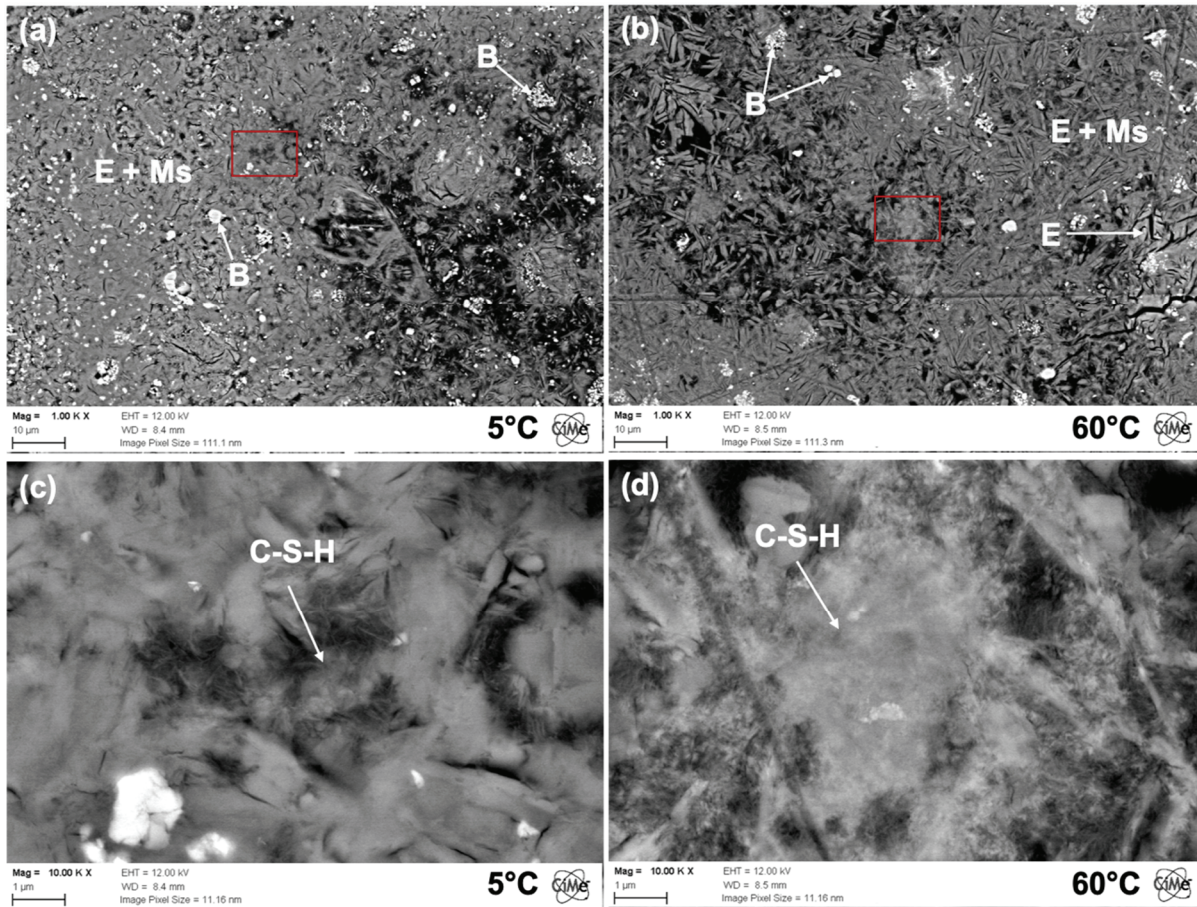


Fig. 4-6. Microstructure of C-S-H at 5 and 60°C with magnification (a, b) 1,000x and (c, d) 10,000x.

EDS mapping together with image analysis were used to verify C-S-H. Fig. 4-7 and Fig. 4-8 shows the BSE images of the region of interest, and the atomic ratio plots of Si/Ca-Al/Ca and Al/Ca-S/Ca from EDS mapping of BY cement cured at 5 and 60°C, respectively. The ratio plots of Si/Ca-Al/Ca in both samples (Fig. 4-7c and Fig. 4-8c) present a cloud of points towards to high Si. The points with high Si content in the ratio plot was selected to identify the location of C-S-H, and displayed on the BSE image (using the edxia framework [26]). By comparison with Fig. 4-7b and Fig. 4-8b, it can be confirmed that the “fluffy” phase identified in Fig. 4-6 is indeed C-S-H. The C-S-H at 60°C appears at higher Al content in the ratio plots compared to the sample cured at 5°C, consistent with the higher Al-concentrations observed at 60°C in the pore solution. Even though the EDS mapping is often used to characterise the chemical composition of C-S-H, it is difficult to analyse its composition in the BY cement due to its sparsity in the microstructure, and its fine intermixing with aluminate hydrates. The same plots for the 20 and 40°C sample indicated no C-S-H.

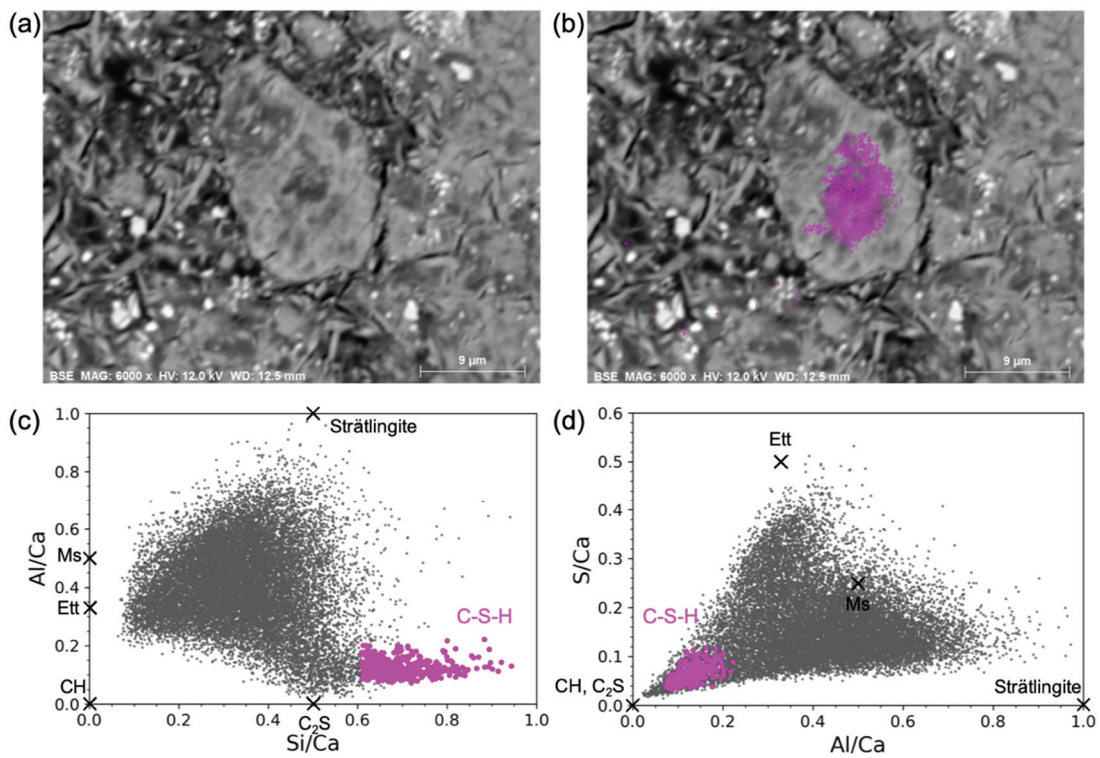


Fig. 4-7. Identification of C-S-H formation in BY cement at 5°C (a) BSE image (b) BSE image with C-S-H overlay as detected in (c) Si/Ca – Al/Ca ratio plot and (d) Al/Ca – S/Ca ratio plot. Ideal compositions of relevant phases are added to the ratio plots as guidelines.

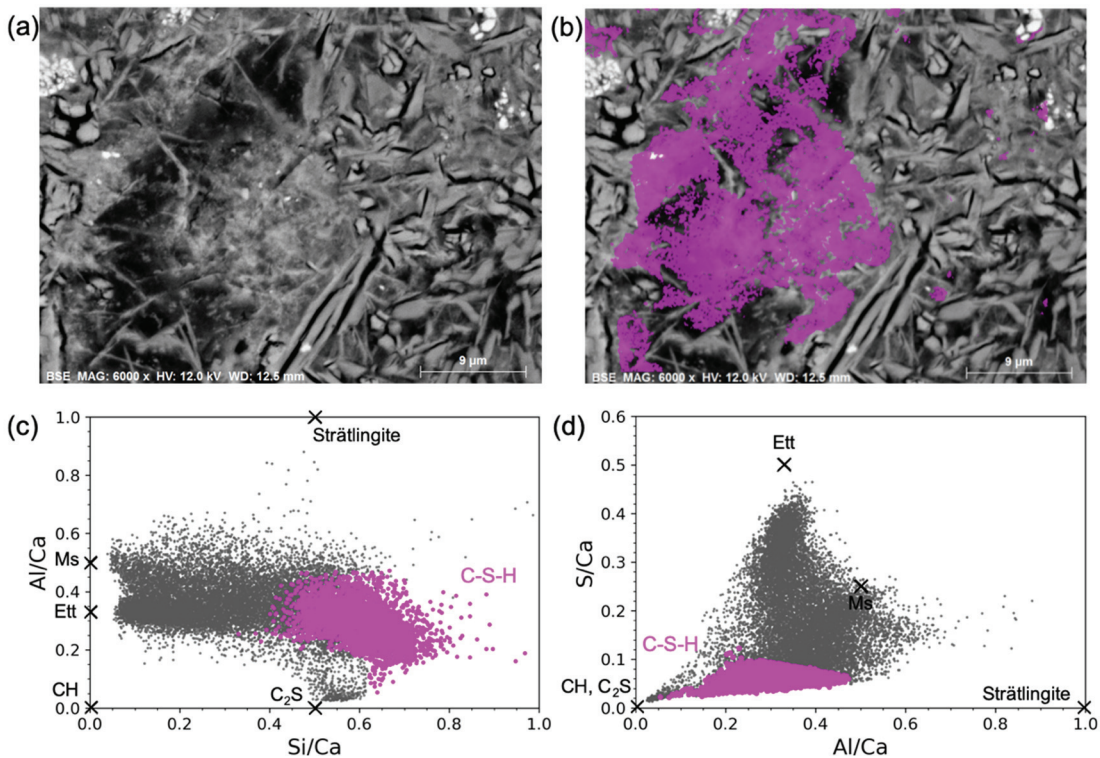


Fig. 4-8. Identification of C-S-H formation in BY cement at 60°C (a) BSE image (b) BSE image with C-S-H overlay as detected in (c) Si/Ca – Al/Ca ratio plot and (d) Al/Ca – S/Ca ratio plot.



#### 4.3.4 Formation of siliceous hydrogarnet at 60°C

Siliceous hydrogarnet is observed at 60°C in the experimental data. In the modelling, generally only the formation of mixed Al-Fe containing hydrogarnets is allowed as such Al-Fe-containing siliceous hydrogarnet ( $C_3(AF)S_{0.84}H$ ) form readily also at ambient temperature [32]. As no significant amount of iron is present in the BY clinker studied, also no siliceous hydrogarnet has been predicted.

Aluminium containing siliceous hydrogarnet are usually observed at high temperatures only [12,13,33], as a solid solution between katoite ( $C_3AH_6$ ,  $Ca_3Al_2(OH)_{12}$ ) and grossularite ( $C_3AS_3$ ,  $C_3Al_2Si_3O_{12}$ ). Their formation is generally prevented at ambient temperature in thermodynamic modelling based on the Cemdata18 database, due to their slow formation kinetics [34,35], although aluminium containing siliceous hydrogarnet would be thermodynamically more stable than AFm phases. As the formation of siliceous hydrogarnet is faster at high temperature, the formation of aluminium-based siliceous hydrogarnet was allowed in the thermodynamic modelling calculation at 60°C.

Fig. 4-9 shows a comparison between the experimental data at 60°C and thermodynamic modelling thermodynamic modelling based on three different assumptions: i) without, ii) with a restricted amount and iii) with free formation of aluminium based-siliceous hydrogarnet. If the formation of siliceous hydrogarnet is not constrained, a large amount of aluminium-based siliceous hydrogarnet forms as a stable phase while monosulfate and strätlingite are destabilised, and ettringite content is significantly increased. The comparison of the experimental data with the different modelling results indicates that the phase assemblages at 90 day at 60°C is not yet at equilibrium; the observed phase assemblage corresponds best to the intermediate case where only a limited amount of aluminium-based siliceous hydrogarnet is considered. Even under these conditions, the amount of monosulfate and strätlingite is higher than the experimental observation.

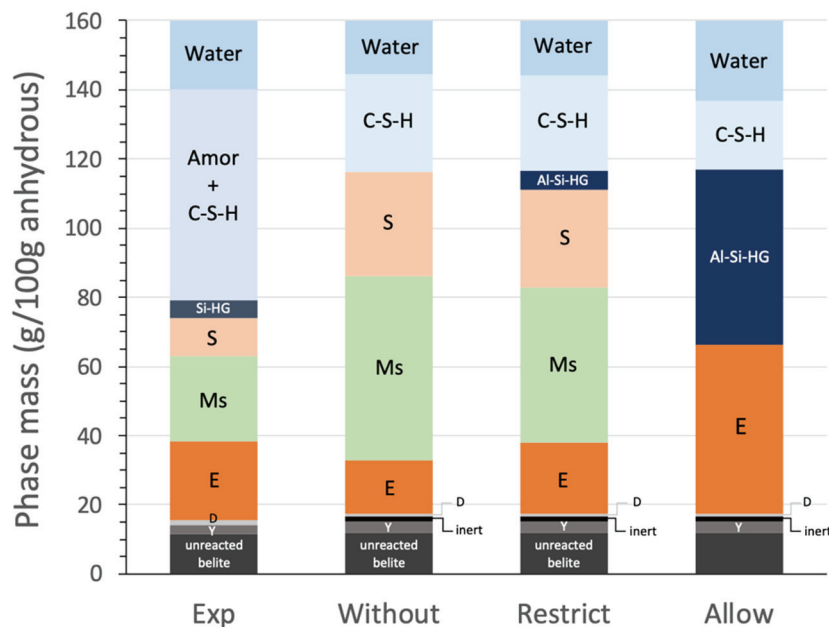


Fig. 4-9 Thermodynamic modelling calculations: without Al-containing siliceous hydrogarnet (Al-Si-HG), a restricted amount of Al-Si-HG and freely allowed Al-Si-HG at 60°C compared to experimental data.



### 4.3.5 Quantification and validation of AFm formation in BY cement

Fig. 4-10 illustrates the main peaks of hydrated BY cement between  $\sim 5^\circ$  to  $15^\circ$  ( $2\theta$ ). From the XRD pattern, two forms of Ms can be observed:  $Ms_{12}$  ( $C_4\bar{A}\bar{S}H_{12}$ ) and  $Ms_{14}$  ( $C_2\bar{A}\bar{S}H_{14}$ ) [36]. The peak position of  $Ms_{14}$  ( $2\theta \sim 9.2^\circ$ ) is close to the main peak of ettringite ( $2\theta \sim 9.0^\circ$ ), but clearly distinguishable in particular at  $60^\circ\text{C}$ . The  $Ms_{14}$  peak is broader at lower temperature leading to more overlapping with the ettringite peaks. The amount of  $Ms_{14}$  was quantified by using the kuzelite crystal structure (ICSD-100138) [37] with refined lattice parameters of  $a \sim 5.75 \pm 0.01 \text{ \AA}$  and  $c \sim 28.63 \pm 0.01 \text{ \AA}$  for all temperature except at  $60^\circ\text{C}$  ( $c \sim 28.53 \text{ \AA}$ ). The overlapping peaks and the modified crystal structure lead to a higher error of the quantification.

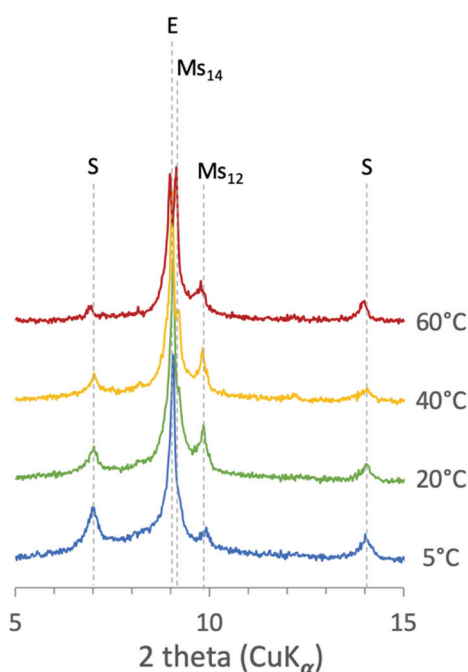


Fig. 4-10 Main hydration products at all curing temperatures at the zoomed section of XRD patterns between  $2\theta$  5 -  $15^\circ$ : E = Ettringite, Ms = monosulfate and S = strätlingite.

Thermodynamic modelling predicted in particular at  $60^\circ\text{C}$  more monosulfate and strätlingite than experimentally observed by XRD. Similar observation on too high amounts of  $\text{SO}_4$ -AFm predicted by the modelling has been reported previously for BYF cement [10]. The two main AFm phases forming in hydrated BY cement are monosulfate (Ms) and strätlingite (S). The AFm-type phase has a layer structure with the general formula  $[\text{Ca}_2\text{Al}(\text{OH})_6]\text{X}\cdot\text{yH}_2\text{O}$ , where X is the interlayer ions. AFm are often difficult to analyse quantitatively by XRD since interlayer content can vary due to solid solution formation, which can result in broad XRD signals and an underestimation of the amount of AFm phases by XRD. Alternatively, AFm can be quantified by TGA. The weight loss around  $200^\circ\text{C}$  in Fig. 4-11 is attributed to the dehydration of AFm phases, thus to monosulfate and strätlingite. The sample cured at  $60^\circ\text{C}$  (and to some extents also those at  $5^\circ\text{C}$ ) shows bigger water losses peaks compared to the samples cured at 20 and  $40^\circ\text{C}$ , indicating the presence of more AFm phases at  $60^\circ\text{C}$  than quantified by XRD. The TGA data confirms that a significant amount of AFm phase are formed also at 5 and  $60^\circ\text{C}$ , but it is present in rather as amorphous and/or microcrystalline phase at 5 and  $60^\circ\text{C}$ . The poor crystallinity might be related to higher disorder generated by a more pronounced solid solution formation or due to a formation of very small AFm phases.

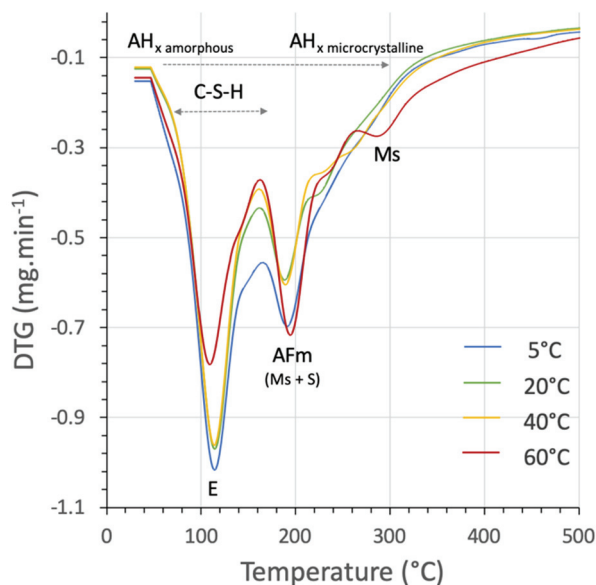


Fig. 4-11 Main hydration products after 90 days of hydration at all curing temperature analysed by TGA curve.

The XRD patterns in (Fig. 4-10) confirm the precipitation of strätlingite at all temperatures. The formation of strätlingite at 60°C has been reported in [38]. The intensity of the characteristic peak of strätlingite around  $7^{\circ}$  2theta is increased at lower temperature. The peaks of strätlingite at 5°C are quite broad, indicating a poorly crystalline form compared to the crystal structure used for quantification (ICSD 69413). At 60°C, the basal peak at  $7^{\circ}$  2theta of strätlingite is slightly shifted to a lower angle, indicating an increase of basal spacing. I. Santacruz, et al [39] reported a shift of the basal strätlingite peak to higher diffraction angles after stopping hydration, which is related to dehydration during drying. The increase of the basal spacing observed here at 60°C cannot be related to drying but could indicate change of the Al and Si contents in the interlayer. The chemical composition of strätlingite in hydrated cements cannot be easily analysed by manual EDS point analysis as it is difficult to distinguish the strätlingite microstructure on a BSE image and as Si, Ca and Al are the main elements in most hydrates. Therefore, EDS mapping was carried out to identify strätlingite in the microstructure and estimate its composition. The ratio plots of Si/Ca and Al/Ca of the mappings at different temperatures are shown in Fig. 4-12.

The chemical composition of pure strätlingite is  $\text{C}_2\text{ASH}_8$  corresponding to  $\text{Si}/\text{Ca} = 0.5$  and  $\text{Al}/\text{Ca} = 1$ . The cloud of points at 20°C in Fig. 4-12 is aligned between the composition of strätlingite and other AFm phases and ettringite, indicating intermixing. Fig. 4-13 shows the identification of strätlingite formation in the microstructure of BY at 20°C analysed by image analysis. The EDS points to the composition of strätlingite were indicated in red; strätlingite in the hydrated BY cement is present as elongated grains, as shown in Fig. 4-13b.

The EDS mapping at 5°C shows that the points go towards the composition of strätlingite but contain less Al than expected. At 40°C, the points are quite scattered towards the high Al content. At 60°C, EDS points cannot clearly indicate the presence of strätlingite in the ratio plot at the magnification of 2000x, indicating either the presence of little strätlingite or an intimate intermixing of fine strätlingite in C-S-H. No separate grains of strätlingite precipitation in the microstructure were observed from EDS mapping at 5, 40 or 60°C.

The comparison of the chemical data with the EDS map indicates tentatively a fine distribution of strätlingite in microstructure; the grains of strätlingite seem to be smaller than the interaction volume of the beam, therefore it is not detected as a separate phase.

However, the result from this study is not sufficient to show where strätlingite forms, e.g. in the area where  $AH_3$  might have formed initially or close to reacted belite, as expected from Equation 4-3. The higher AFm content predicted by thermodynamic modelling than observed experimentally seems to be related to their microcrystalline size, close intermixing with other phases and possibly variable interlayer composition. This limits the accuracy of XRD quantification. Similar limitations are also discussed in previous study [8].

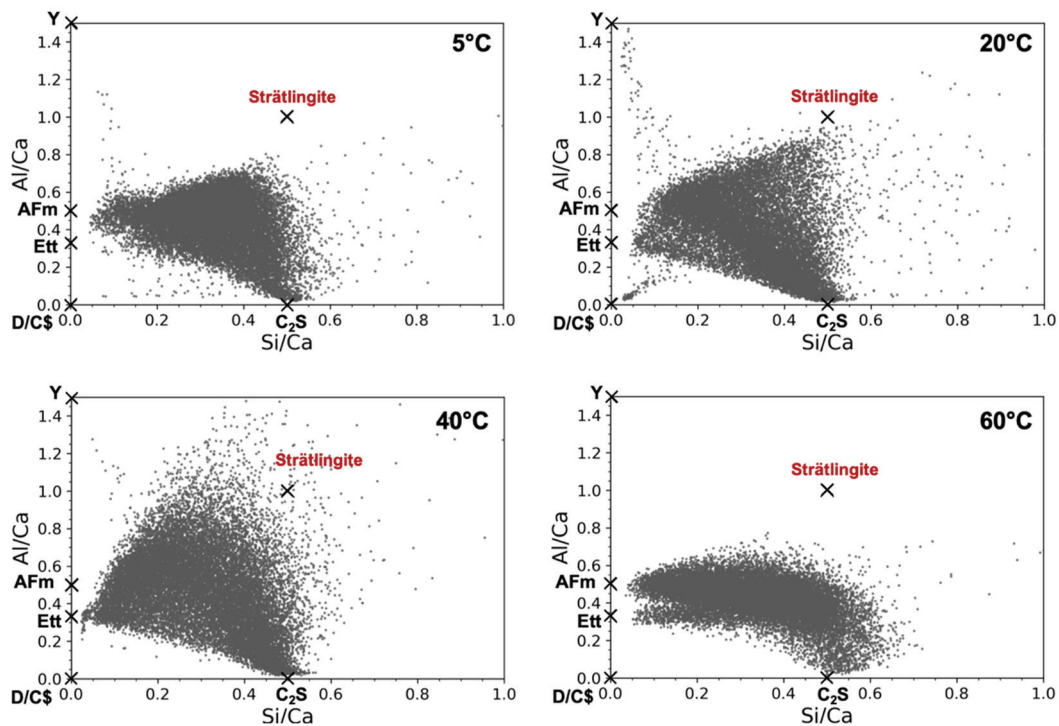


Fig. 4-12 Strätlingite intermixed with AFm at different temperatures after 90 days obtained by SEM-EDS mapping at magnification of 2000x. The cross indicates the pure composition of each phase.

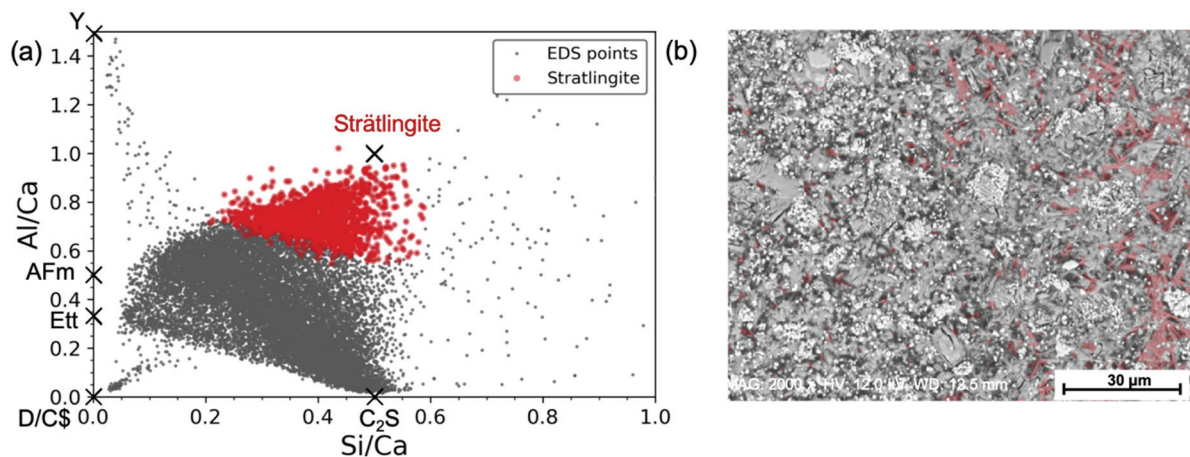


Fig. 4-13 . Strätlingite formation (red) in the microstructure at 20°C (a) Si/Ca – Al/Ca ratio plot and (b) BSE image.

## 4.4 Conclusions

This study aims to investigate the effect of temperature on phase assemblages at late age of hydration. The comparison of the experimental data to at 90 days of hydration with thermodynamic modelling show an overall good agreement. Some discrepancies were observed in the quantities of AFm phases, which is discussed and investigated in more detail.

The ye'elimite reacted almost completely in one day at all temperatures. Since the reaction of ye'elimite is so fast, temperature does not show significant effect on ye'elimite reactivity beyond 1 day. Belite reacts on slightly during the first day and continues to slow up to 28 days of hydration. The reactivity of belite becomes more important again after 28 days and significant belite reaction is observed at 5 and 60°C at 90 days of hydration, but not at 20 and 40°C, leading to important differences in the phase assemblages at different temperatures.

C-S-H is predicted to form at 5 and 60°C, where the reactivity of belite is high. Although XRD Rietveld cannot quantify the amount of C-S-H due to its amorphous form, the formation of C-S-H in the sample cured at 5 and 60°C was confirmed by XRD pattern, high resolution SEM and EDS mapping results. C-S-H is formed with a fine intermixed microstructure, so it is difficult to observe with low magnification. Inner C-S-H cannot be observed around belite grains at 90 days of hydration. C-S-H forming at 60°C shows highly intermixing with aluminates hydrates; ettringite and monosulfate. Therefore, the composition of C-S-H cannot be estimated accurately.

Siliceous hydrogarnet in this study is formed at 60°C as the Al-containing hydrogrossular due to low amount of Fe in the system. The thermodynamic modelling prediction of aluminium siliceous hydrogarnet needs to be activated only at 60°C but with a restricted amount in order to compare with the non-equilibrium state of experimental observation at 90 days.

The difference on the quantification of AFm phases between thermodynamic modelling and the experimental data can be explained by the formation of poorly or microcrystalline of AFm.  $MS_{14}$  becomes more stable form when temperature increases, while strätlingite is less stable at high temperature. Strätlingite forms highly fine intermixing with AFm. Lower Al content in strätlingite structure was observed in the real system at 5°C. The calcium-aluminate-silicate phase observed at 60°C is not yet confirmed that it could be strätlingite. In this BY system, strätlingite presents as an elongated microstructure at 20°C. One aspect that has not been fully investigated is the nature of strätlingite formation whether it forms a true solid-solution or the fine intermix of separated grains in the real BY cement as a function of temperature.

## 4.5 References

- [1] E. Gartner, Industrially interesting approaches to “low-CO<sub>2</sub>” cements, *Cem. Concr. Res.* 34 (2004) 1489–1498. <https://doi.org/10.1016/j.cemconres.2004.01.021>.
- [2] E. Gartner, H. Hirao, A review of alternative approaches to the reduction of CO<sub>2</sub> emissions associated with the manufacture of the binder phase in concrete, *Cem. Concr. Res.* 78 (2015) 126–142. <https://doi.org/10.1016/j.cemconres.2015.04.012>.
- [3] F. Winnefeld, B. Lothenbach, Hydration of calcium sulfoaluminate cements — Experimental findings and thermodynamic modelling, *Cem. Concr. Res.* 40 (2010) 1239–1247. <https://doi.org/10.1016/j.cemconres.2009.08.014>.
- [4] D. Londono-Zuluaga, J.I. Tobón, M.A.G. Aranda, I. Santacruz, A.G. De la Torre, Clinkering and hydration of belite-alite-ye’elinite cement, *Cem. Concr. Compos.* 80 (2017) 333–341. <https://doi.org/10.1016/j.cemconcomp.2017.04.002>.
- [5] K. Quillin, Performance of belite–sulfoaluminate cements, *Cem. Concr. Res.* 31 (2001) 1341–1349. [https://doi.org/10.1016/S0008-8846\(01\)00543-9](https://doi.org/10.1016/S0008-8846(01)00543-9).
- [6] E. Gartner, G. Li, High belite-containing sulfoaluminous clinker, method for the production and the use thereof for preparing hydraulic binders, US7850776B2, 2010. <https://patents.google.com/patent/US7850776B2/en> (accessed November 24, 2020).
- [7] M. Ben Haha, F. Winnefeld, A. Pisch, Advances in understanding ye’elinite-rich cements, *Cem. Concr. Res.* 123 (2019) 105778. <https://doi.org/10.1016/j.cemconres.2019.105778>.
- [8] M. Zajac, J. Skocek, C. Stabler, F. Bullerjahn, M. Ben Haha, Hydration and performance evolution of belite–ye’elinite–ferrite cement, *Adv. Cem. Res.* 31 (2019) 124–137. <https://doi.org/10.1680/jadcr.18.00110>.
- [9] G. Álvarez-Pinazo, I. Santacruz, M.A.G. Aranda, Hydration of belite–ye’elinite–ferrite cements with different calcium sulfate sources, *Adv. Cem. Res.* 28 (2016) 529–543. <https://doi.org/10.1680/jadcr.16.00030>.
- [10] V. Morin, P. Termkhajornkit, B. Huet, G. Pham, Impact of quantity of anhydrite, water to binder ratio, fineness on kinetics and phase assemblage of belite-ye’elinite-ferrite cement, *Cem. Concr. Res.* 99 (2017) 8–17. <https://doi.org/10.1016/j.cemconres.2017.04.014>.
- [11] F. Bullerjahn, M. Zajac, M. Ben Haha, K.L. Scrivener, Factors influencing the hydration kinetics of ye’elinite; effect of mayenite, *Cem. Concr. Res.* 116 (2019) 113–119. <https://doi.org/10.1016/j.cemconres.2018.10.026>.
- [12] P. Wang, N. Li, L. Xu, Hydration evolution and compressive strength of calcium sulphoaluminate cement constantly cured over the temperature range of 0 to 80 °C, *Cem. Concr. Res.* 100 (2017) 203–213. <https://doi.org/10.1016/j.cemconres.2017.05.025>.
- [13] J. Kaufmann, F. Winnefeld, B. Lothenbach, Stability of ettringite in CSA cement at elevated temperatures, *Adv. Cem. Res.* 28 (2016) 251–261. <https://doi.org/10.1680/jadcr.15.00029>.
- [14] E. Gartner, T. Sui, Alternative cement clinkers, *Cem. Concr. Res.* 114 (2018) 27–39. <https://doi.org/10.1016/j.cemconres.2017.02.002>.
- [15] R.B. Perkins, C.D. Palmer, Solubility of ettringite (Ca<sub>6</sub>[Al(OH)<sub>6</sub>]<sub>2</sub>(SO<sub>4</sub>)<sub>3</sub> · 26H<sub>2</sub>O) at 5–75°C, *Geochim. Cosmochim. Acta.* 63 (1999) 1969–1980. [https://doi.org/10.1016/S0016-7037\(99\)00078-2](https://doi.org/10.1016/S0016-7037(99)00078-2).

- [16] B. Lothenbach, D.A. Kulik, T. Matschei, M. Balonis, L. Baquerizo, B. Dilnesa, G.D. Miron, R.J. Myers, Cemdata18: A chemical thermodynamic database for hydrated Portland cements and alkali-activated materials, *Cem. Concr. Res.* 115 (2019) 472–506. <https://doi.org/10.1016/j.cemconres.2018.04.018>.
- [17] J.J. Wolf, D. Jansen, F. Goetz-Neunhoeffler, J. Neubauer, Application of thermodynamic modeling to predict the stable hydrate phase assemblages in ternary CSA-OPC-anhydrite systems and quantitative verification by QXRD, *Cem. Concr. Res.* 128 (2020) 105956. <https://doi.org/10.1016/j.cemconres.2019.105956>.
- [18] F. Winnefeld, B. Lothenbach, Phase equilibria in the system  $\text{Ca}_4\text{Al}_6\text{O}_{12}\text{SO}_4 - \text{Ca}_2\text{SiO}_4 - \text{CaSO}_4 - \text{H}_2\text{O}$  referring to the hydration of calcium sulfoaluminate cements, *RILEM Tech. Lett.* (2016) 7.
- [19] F. Song, Z. Yu, F. Yang, Y. Lu, Y. Liu, Microstructure of amorphous aluminum hydroxide in belite-calcium sulfoaluminate cement, *Cem. Concr. Res.* 71 (2015) 1–6. <https://doi.org/10.1016/j.cemconres.2015.01.013>.
- [20] J. Wang, I. Baco, V. Morin, G. Walenta, D. Damidot, E. Gartner, Hydration mechanism of cements based on low-CO<sub>2</sub> clinkers containing belite, ye’elimite and calcium alumino-ferrite, in: 2010.
- [21] D. Jansen, J.J. Wolf, N. Fobbe, The hydration of nearly pure ye’elimite with a sulfate carrier in a stoichiometric ettringite binder system. Implications for the hydration process based on in-situ XRD, <sup>1</sup>H-TD-NMR, pore solution analysis, and thermodynamic modeling, *Cem. Concr. Res.* 127 (2020) 105923. <https://doi.org/10.1016/j.cemconres.2019.105923>.
- [22] L.H.J. Martin, F. Winnefeld, E. Tschopp, C.J. Müller, B. Lothenbach, Influence of fly ash on the hydration of calcium sulfoaluminate cement, *Cem. Concr. Res.* 95 (2017) 152–163. <https://doi.org/10.1016/j.cemconres.2017.02.030>.
- [23] C.W. Hargis, B. Lothenbach, C.J. Müller, F. Winnefeld, Carbonation of calcium sulfoaluminate mortars, *Cem. Concr. Compos.* 80 (2017) 123–134. <https://doi.org/10.1016/j.cemconcomp.2017.03.003>.
- [24] X. Li, A. Ouzia, K. Scrivener, Laboratory synthesis of C<sub>3</sub>S on the kilogram scale, *Cem. Concr. Res.* 108 (2018) 201–207. <https://doi.org/10.1016/j.cemconres.2018.03.019>.
- [25] K. Scrivener, R. Snellings, B. Lothenbach, eds., *A practical guide to microstructural analysis of cementitious materials*, CRC Press, Boca Raton, 2016.
- [26] F. Georget, W. Wilson, K.L. Scrivener, edxia: Microstructure characterisation from quantified SEM-EDS hypermaps, *Cem. Concr. Res.* 141 (2021) 106327. <https://doi.org/10.1016/j.cemconres.2020.106327>.
- [27] D.A. Kulik, T. Wagner, S.V. Dmytrieva, G. Kosakowski, F.F. Hingerl, K.V. Chudnenko, U.R. Berner, GEM-Selektor geochemical modeling package: revised algorithm and GEMS3K numerical kernel for coupled simulation codes, *Comput. Geosci.* (2012). <https://doi.org/10.1007/s10596-012-9310-6>.
- [28] T. Wagner, D.A. Kulik, F.F. Hingerl, S.V. Dmytrieva, GEM-Selektor geochemical modeling package: TSoMod library and data interface for multicomponent phase models, *Can. Mineral.* 50 (2012) 1173–1195. <https://doi.org/10.3749/canmin.50.5.1173>.
- [29] W. Hummel, U. Berner, E. Curti, F.J. Pearson, T. Thoenen, Nagra/PSI Chemical Thermodynamic Data Base 01/01, *Radiochim. Acta.* 90 (2002). [https://doi.org/10.1524/ract.2002.90.9-11\\_2002.805](https://doi.org/10.1524/ract.2002.90.9-11_2002.805).
- [30] E. L’Hôpital, B. Lothenbach, D.A. Kulik, K. Scrivener, Influence of calcium to silica ratio on aluminium uptake in calcium silicate hydrate, *Cem. Concr. Res.* 85 (2016) 111–121. <https://doi.org/10.1016/j.cemconres.2016.01.014>.

- [31] J.E. Rossen, K.L. Scrivener, Optimization of SEM-EDS to determine the C–A–S–H composition in matured cement paste samples, *Mater. Charact.* 123 (2017) 294–306. <https://doi.org/10.1016/j.matchar.2016.11.041>.
- [32] B.Z. Dilnesa, E. Wieland, B. Lothenbach, R. Dähn, K.L. Scrivener, Fe-containing phases in hydrated cements, *Cem. Concr. Res.* 58 (2014) 45–55. <https://doi.org/10.1016/j.cemconres.2013.12.012>.
- [33] M. Paul, F.P. Glasser, Impact of prolonged warm (85°C) moist cure on Portland cement paste, *Cem. Concr. Res.* 30 (2000) 1869–1877. [https://doi.org/10.1016/S0008-8846\(00\)00286-6](https://doi.org/10.1016/S0008-8846(00)00286-6).
- [34] B. Lothenbach, T. Matschei, G. Möschner, F.P. Glasser, Thermodynamic modelling of the effect of temperature on the hydration and porosity of Portland cement, *Cem. Concr. Res.* 38 (2008) 1–18. <https://doi.org/10.1016/j.cemconres.2007.08.017>.
- [35] B.Z. Dilnesa, B. Lothenbach, G. Renaudin, A. Wichser, D. Kulik, Synthesis and characterization of hydrogarnet  $\text{Ca}_3(\text{Al}_x\text{Fe}_{1-x})_2(\text{SiO}_4)_y(\text{OH})_{4(3-y)}$ , *Cem. Concr. Res.* 59 (2014) 96–111. <https://doi.org/10.1016/j.cemconres.2014.02.001>.
- [36] L.G. Baquerizo, T. Matschei, K.L. Scrivener, M. Saeidpour, A. Thorell, L. Wadsö, Methods to determine hydration states of minerals and cement hydrates, *Cem. Concr. Res.* 65 (2014) 85–95. <https://doi.org/10.1016/j.cemconres.2014.07.009>.
- [37] R. Allmann, Refinement of the hybrid layer structure  $[\text{Ca}_2\text{Al}(\text{OH})_6]^+ \cdot [1/2\text{SO}_4 \cdot 3\text{H}_2\text{O}]^-$ , *Neues Jahrb Miner. Monatsh.* (1977) 136–144.
- [38] H. Nguyen, V. Carvelli, W. Kunther, M. Illikainen, P. Kinnunen, Phase evolution and mechanical performance of an ettringite-based binder during hydrothermal aging, *Cem. Concr. Res.* 143 (2021) 106403. <https://doi.org/10.1016/j.cemconres.2021.106403>.
- [39] I. Santacruz, Á.G.D. la Torre, G. Álvarez-Pinazo, A. Cabeza, A. Cuesta, J. Sanz, M.A.G. Aranda, Structure of stratlingite and effect of hydration methodology on microstructure, *Adv. Cem. Res.* 28 (2016) 13–22. <https://doi.org/10.1680/adcr.14.00104>.

## 4.6 Appendix

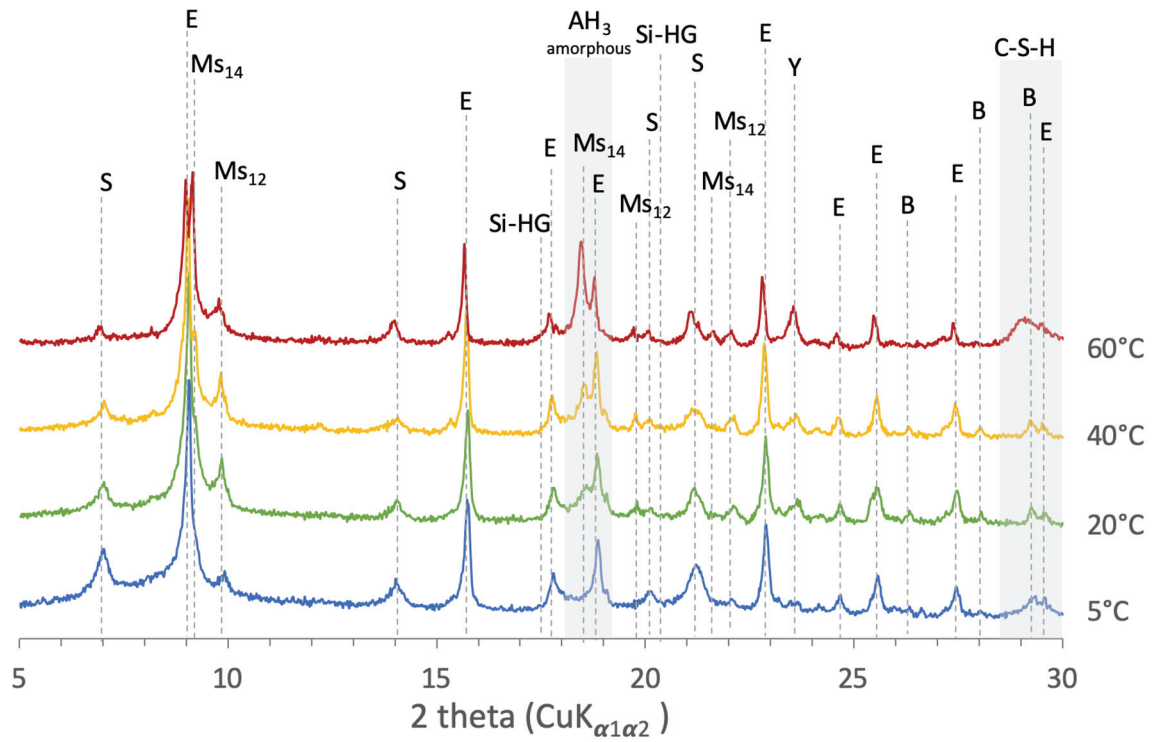


Fig. 4-14 Full scaled XRD patterns of BY cement after 90 days of hydration cured at 5, 20, 40 and 60°C.





# Chapter 5 Hydration, microstructure and compressive strength

**Note:** This chapter is based on an article in preparation for submission to a peer reviewed journal.

Contribution of the doctoral candidate: Writing of the first manuscript draft, experimental design, conduction of the experiment.

## Abstract

The effect of temperature on phase assemblage, microstructure, porosity and mechanical property of higher alumina systems with similar chemical composition but different clinker phases are investigated from 5 to 60°C. An OPC blended with metakaolin, and calcium sulfoaluminate (CSA) clinkers are studied. Temperature accelerates the hydration kinetics, and this effect is more marked in the CSA system. Both higher alumina systems show low belite reaction at all temperatures. The reaction of belite in CSA starts to progress when the formation of aluminate hydrates ( $AH_3$  and/or  $CAH_{10}$ ) has finished. Temperature affects the phase assemblage mainly in terms of the aluminate hydrates formed. The change of phase assemblages between two types of cement, C-S-H dominated (OPC/MK) and ettringite dominated (CSA), and how the hydrates are formed are also impacts on the microstructure and porosity refinement. The impact of microstructure of strength is examined through the metric of the combined water fraction (CWF), which can be simply calculated from bound water content, and porosity measured by MIP. Although there are clear trends of increasing strength with increasing CWF and decreasing porosity, these cannot be generalised across the different temperatures and systems.

**Keywords:** Temperature, Hydration kinetics, Phase assemblage, Microstructure, Compressive strength, Metakaolin, Blended cement, Calcium sulfoaluminate cement.

---

**CONTENTS**

---

<b>Chapter 5</b>	<b>Hydration, microstructure and compressive strength</b>	<b>95</b>
5.1	Introduction	97
5.2	Materials and methods	98
5.2.1	Raw materials	98
5.2.2	Mix design and hydration stoppage	99
5.2.3	Methods of analysis	100
5.3	Results	102
5.3.1	Hydration kinetics	102
5.3.2	Hydration	105
5.3.3	Microstructure and porosity at 90d	110
5.3.4	Compressive strength	115
5.4	Discussion	117
5.4.1	Degree of hydration of belite in CSA	117
5.4.2	Correlation between degree of hydration and compressive strength	117
5.4.3	Correlation between porosity VS compressive strength	119
5.4.4	Correlation between combined water fraction (CWF) and compressive strength	120
5.4.5	The contribution of C-S-H to compressive strength in CSA	121
5.4.6	Effect of microstructure	121
5.5	Conclusions	122
5.6	References	123
5.7	Appendix	126

---

## 5.1 Introduction

The cement production is responsible for 5-7% of anthropogenic CO<sub>2</sub> emissions [1]. The CO<sub>2</sub> emissions come from the decarbonation of limestone, the use of fuel and electricity production [1]. Sustainability in the cement industry is becoming an important concern. There are two main approaches to lower the CO<sub>2</sub> emission. The first approach is the use of supplementary cementitious materials (SCMs) blended with Portland cement. This approach reduces the clinker factor in cements. The SCMs most commonly used are fine limestone, coal combustion fly ashes, granulated blast furnace slag [2]. However, the availability of fly ash and slag are relatively low compared to the global demand for cement. For this reason, calcined clay containing metakaolin (MK) is one of the promising SCMs for sustainable cement [3]. The other approach is the use of alternative binders such as calcium sulfoaluminate cement (CSA) [4,5]. CSA is composed mainly of ye'elimite, belite and calcium ferrite phases. The clinker can be produced at lower temperatures than Portland cement clinker and there is less limestone in the raw meal [6]. For these reasons CSA clinkers may have lower CO<sub>2</sub> emissions than OPC.

A common aspect of these two new binder systems is that they contain higher levels of aluminium oxide compared to the conventional Portland cement composition. The main hydration reactions are quite different between these two higher alumina systems. In the blended cement of PC + MK, the early reaction is dominated by alite hydration to form calcium aluminate silicate hydrates C-S-H and portlandite as initial hydration products. Alumino-ferrite-mono phase (AFm) and C-(A)-S-H occur later due to the pozzolanic reaction of metakaolin [2]. Moreover, strätlingite can form when the metakaolin content is high [7,8]. On the other hand, the early reaction of CSA is dominated by the reaction of ye'elimite with calcium sulfate to forms ettringite, AFm and aluminium hydroxide (AH<sub>3</sub>), then later C-(A)-S-H and strätlingite form attributed to belite reaction [9]. These higher alumina systems have been mainly studied at room temperature [7–11]. Zajac et al. made a preliminary comparison of the hydration kinetics and microstructure of these two systems at 20°C [12].

Cementitious materials are widely used under different climate conditions and hydration is sensitive to temperature. The influence of temperature on the hydration of Portland cement [13–16] and some blended cements have been studied [17–21]. At low temperatures, the hydration rate is reduced [22]. The hydration kinetics is enhanced with the increasing temperature, leading to the change of phase assemblages and pore solution [14]. At higher temperatures the solubility of ettringite is increase leading to the formation of more monosulfate and higher sulfate concentration in pore solution [14]. Temperature also affects the C-S-H which has less gel porosity and is more dense at higher temperatures [23–25]. These changes in phase assemblage mean that although the increases rate of hydration may lead to higher early strengths, late age strengths are slightly lower [19,26,27]. The relationship between microstructure and compressive strength have been investigated using the porosity, pore network structure (e.g. pore entry size), or the hydrates phase formation in the microstructure [19,28–30]. It has been reported that the pore entry size is reduced in the metakaolin blended cement observed at 20°C [10,31].

Few studies have been made of the effect of temperature on metakaolin blends and CSA cement [25,32] The objective of this paper is to study the effect of temperature between 5 to 60°C on the change of the higher alumina systems with similar chemical composition; Portland cement blended with metakaolin and CSA. The hydration kinetics, phase assemblages, microstructure and compressive strength between 1 to 365 days of hydration were investigated with various techniques. The results of higher alumina systems were compared between the PC base and the CSA base.

## 5.2 Materials and methods

### 5.2.1 Raw materials

The raw materials used in the PC system are light grey cement (LGC), metakaolin (MK), limestone (LS) and a chemical grade gypsum. In the CSA system, a laboratory prepared belite-ye'elinite clinker, anhydrite and a laboratory prepared mayenite were used as raw materials. The chemical composition and particle size value of these materials determined by X-Ray fluorescence (XRF) and laser diffraction (Malvern MasterSizer S) are given in Table 5-1. The phase composition quantified by XRD is shown in Table 5-2.

Table 5-1: Chemical composition and particle size value of the raw materials

PSD	LGC	MK	LS	BY clinker	Anhydrite	MY
Dv,10	1.26	0.54	2.27	0.54	2.7	0.25
Dv,50	8.44	5.13	7.71	4.34	8.41	8.97
Dv,90	24.37	20.17	19.3	15.88	29.88	31.75
XRF (wt.%)						
SiO <sub>2</sub>	22.4	52.0	0.11	18.9	2.5	0.1
Al <sub>2</sub> O <sub>3</sub>	3.8	43.8	0.00	20.9	0.6	50.1
Fe <sub>2</sub> O <sub>3</sub>	1.2	0.3	0.04	0.0	0.3	0.1
CaO	65.6	0.0	56.2	53.1	38.7	47.6
MgO	0.8	0.0	0.15	0.1	1.9	-
SO <sub>3</sub>	3.3	0.1	0.03	6.4	52.2	0.1
K <sub>2</sub> O	0.7	0.1	0.01	-	0.2	-
Na <sub>2</sub> O	0.2	0.3	0.06	0.1	0.1	0.1
TiO <sub>2</sub>	0.2	1.5	0.01			
P <sub>2</sub> O <sub>5</sub>	0.1	0.2	0.00	0.0	0.0	0.0
Others	0.0	0.1	0.00	0.0	0.2	0.0
*LOI	1.1	1.5	43.4	0.6	3.4	1.2
Sum	99.6	100.0	100.0	100.0	100.2	99.4

\*LOI = Loss of ignition

Table 5-2: Phase composition of the raw materials

XRD (wt.%)	LGC	MK	LS	BY clinker	Anhydrite	MY
C <sub>3</sub> S	60.6	-	-	-	-	-
C <sub>2</sub> S	21.5	-	-	60.3	-	-
C <sub>3</sub> A	9.1	-	-	-	-	1.9
C <sub>4</sub> AF	1.4	-	-	-	-	-
C <sub>4</sub> A <sub>3</sub> \$	-	-	-	39.4	-	-
C <sub>12</sub> A <sub>7</sub>	-	-	-	-	-	97.5
CA	-	-	-	-	-	0.6
Dolomite	-	-	-	-	6.9	-
Free lime	-	-	-	0.3	-	-
Portlandite	-	-	-	-	0.1	-
Calcite	1.5	-	99	-	-	-
Dolomite	0.7	-	0.7	-	-	-
Gypsum	0.2	-	-	-	2.5	-
Anhydrite	4.7	-	-	-	77.7	-
Quartz	0.3	-	0.3	-	2.3	-
Metakaolin	-	94.2	-	-	1.2	-
Rutile	-	-	-	-	8.5	-
Anatase	-	1.2	-	-	0.7	-
Mullite	-	4.6	-	-	-	-
Muscovite	-	-	-	-	-	-
Cristobalite	-	-	-	-	-	-
Sum	100.0	100.0	100.0	100.0	99.9	100.0

### 5.2.2 Mix design and hydration stoppage

The systems investigated in this study are divided into two main groups; the PC systems and the CSA systems. In the PC system, there are three subsystems; LGC, LGCMK and LGCMKL. The LGC is used as a reference. The system containing metakaolin is a higher alumina system based on PC similar in overall chemistry to the CSA system. The CSA system is composed of BY clinker blended with anhydrite at an anhydrite to ye'elimite molar ratio of 1:1. The BY clinker prepared in the laboratory showed a very long induction time, due to the absence of mayenite, usually present in very small amounts in commercial CSA clinkers. To obtain a reaction rate similar to commercial cement, small amount of mayenite was added to accelerate the ye'elimite reaction [33] to be able to react during 6 – 12 hours at 20°C (see Chapter 2). The mix proportion and the molar ratio of the main elements are given in Table 5-3 and Table 5-4, respectively.

Table 5-3: Composition of the investigated systems (mass %).

Materials	LGC	LGCMK	LGCMKLS	CSA
LGC	97	76	66	0
MK	0	20	20	0
LS	0	0	10	0
GS	3	4	4	0
BY	0	0	0	89
Anhydrite	0	0	0	10.5
MY	0	0	0	0.25-0.5*

\*the amount of mayenite depends on the reactivity of the batch

Table 5-4: Molar ratio of the main elements in the investigated system

Materials	LGC	LGCMK	LGCMKLS	CSA
SO <sub>3</sub> /Al <sub>2</sub> O <sub>3</sub>	1.59	0.48	0.46	0.73
Al <sub>2</sub> O <sub>3</sub> /CaO	0.03	0.13	0.12	0.20
SiO <sub>2</sub> /CaO	0.31	0.50	0.47	0.31
(Al <sub>2</sub> O <sub>3</sub> +SiO <sub>2</sub> )/CaO	0.14	0.27	0.25	0.24

The binders and deionized water were equilibrated overnight at the intended curing temperature before mixing. The dry powders were blended with a lab mixer for 1 minute. Cement pastes were prepared with water to binder ratio (w/b) of 0.6 at 1600 rpm for two minutes. The samples were cast into 50 ml polypropylene containers under sealed condition with a few drops of distilled water on top of the paste to keep saturated curing. The samples were stored until testing at 5, 20, 40 and 60°C.

Hydration was stopped by the solvent exchange method as prescribed in [34] The cement pastes were cut on a bench-top by a circular saw with water-cooling. The fresh slices of 2-3 mm thickness were immersed in the isopropanol for one week. The isopropanol was changed at 1, 3 and 7 days. The samples were dried in a desiccator under light vacuum at least 7 days before the analysis.

### 5.2.3 Methods of analysis

The heat evolution was measured in an isothermal calorimetry (TAM Air, TA instrument). Dry binders, deionized water, glass ampules and caps were equilibrated overnight at 5, 20, 40 and 60°C before mixing. Cement pastes were prepared as mentioned in the previous section. 10 g of paste were put into a glass ampoule, sealed and placed in the calorimeter directly after mixing. Water was used as a reference sample with the same specific heat as the paste.

X-ray diffraction was conducted on fresh discs before solvent exchange with a PANalytical X'per Pro diffractometer using  $\text{CuK}\alpha_{1\alpha 2}$  source. The x-ray tube worked at 45 kV and 40 mA and the Bragg-Brentano configuration included a fixed diverge slit of  $1/2^\circ$ , a soller slit of 0.04 rad and mask of 15 mm. The patterns were recorded between 5 and  $70^\circ$  (2 theta) using a step size of  $0.017^\circ$  for a total duration of 14 min. Rutile was used as an external standard to quantify the amorphous content in the cement paste. The quantitative phase assemblage was carried out by using Rietveld refinement method using the High Score Plus software. The experimental errors of XRD were estimated on alite - belite on 90 days samples for PC systems and on belite - ye'elite on 28 days samples analysed with two replicates. The error limits of the XRD Rietveld quantification is around 2% mass. The experimental error of the hydrates is not estimated here.

The quantification of is normalized per 100g of anhydrous using the water to binder ratio (w/b) by Equation 5-1 [34].

Equation 5-1: 
$$W_{i,\text{rescaled}} = W_{i,\text{Rietveld}} \times \left(1 + \frac{w}{b}\right)$$

where  $W_i$  is weight percent.

The degree of hydration (DoH) of anhydrous phases at time t was calculated from the mass fraction of reacted phases relative to the initial amount. The formula for the calculation is shown in Equation 5-2.

Equation 5-2: 
$$\text{DoH } (\%)_t = \left(\frac{W_0 - W_t}{W_0}\right) \times 100$$

where  $W_0$  is initial amount,  $W_t$  is the amount at time t.

A small piece of the dried sample was polished on every side of the surface to remove the carbonated area before being gently ground in a ceramic mortar. About 50 mg of powder was placed in a 150  $\mu\text{L}$  alumina crucible with a lid, then was analysed by TGA (Mettler Toledo TGA/SDTA 851 instrument) from  $30^\circ\text{C}$  to  $1000^\circ\text{C}$  with the rate of  $10^\circ\text{C}/\text{min}$  and under 30 ml/min  $\text{N}_2$  gas flow. The weight loss from TGA analysis was used to obtain the amount of chemical bound water (BW) as shown in Equation 5-3.

Equation 5-3: 
$$\text{BW} = \frac{W_{40} - W_{550}}{W_{550}}$$

where  $W_i$  is the dry sample weight in grams at the respective temperature ( $^\circ\text{C}$ )

The solid-state  $^{29}\text{Si}$  MAS NMR spectra were acquired on a Bruker Avance 400 NMR (9.39T) spectrometer using a 4 mm Bruker CP/MAS probe spinning speed of  $\nu_R = 10.0$  kHz, single-pulse excitation with a pulse width of 1.75  $\mu\text{s}$  for a radio-frequency (rf) field strength of  $\gamma B_1/2\pi = 40$  kHz, a relaxation delay of 30 s, and typically 2560 scans. The  $^{29}\text{Si}$  chemical shifts are referenced to neat tetramethylsilane (TMS), using a sample of  $\beta\text{-Ca}_2\text{SiO}_4$  ( $\delta(^{29}\text{Si}) = -71.33$  ppm) as a secondary reference. The simulations of the  $^{29}\text{Si}$  MAS spectra employed procedures described elsewhere for anhydrous [7,8].



The degree of reaction for alite, belite and metakaolin is calculated as  $DoH(t) = [I(t_0) - I(t)] / I(t_0)$ , from the relative intensities from the simulations of the  $^{29}Si$  MAS NMR spectra before ( $t_0$ ) and after hydration ( $t$ ).

A piece of sample was gently polished with a silicon carbide paper of 1200 grid to smooth the surface. The samples were embedded in a low viscosity epoxy resin under the vacuum. The impregnated samples were hand-polished on a silicon carbide paper of 1200 grid with isopropanol as a lubricant until the sample surface was uncovered. The sample was polished by diamond suspensions of 9, 3, 1 and 1/4  $\mu m$  with 15 kN force and 150 rpm for all the polishing steps. The polished samples were stored in a vacuum desiccator for at least two days to evaporate the isopropanol before coating with carbon. The SEM-EDS investigations were carried out by using a FEI Quanta 200 scanning electron microscope equipped with a Bruker ASX microanalysis XFlash 4030 silicon drift detector for the EDS point analysis and the EDS mapping (tungsten filament). The acceleration voltages were 15kV for the EDS point analysis and 12 kV for the EDS mapping with a working distance of 12.5 mm for both conditions.

Image analysis was carried out to confirm and identify the formation of phases of interest in the microstructure. The BSE images and EDS mapping data were linked using edxia [35]. The atomic ratio plots of the element in the EDS map can identify the main phases in the sample. Using the graphical interface of edxia, manually selected points in the ratio plots appear on the BSE image.

The pore solutions of the hardened samples were extracted by the steel die method [36] using pressures up to 250 N/mm<sup>2</sup>. The solutions were filtered immediately with nylon filters (0.45 $\mu m$ ). The hydroxide concentrations of the pore solutions were calculated from pH measurements with a pH electrode, calibrated against KOH solutions with known concentrations. The concentrations of Na, K, Ca, Si, S, Al and Cl were determined with a Dionex DP ICS-3000 ion chromatography. Each sample was diluted by a factor 10, 100 and 1000 depending on the ion concentration. Standards from 0.1 – 50 mg/L were used. The relative error of the measurements was about 10%.

Micromeritics AutoPore IV 9500 porosimeter was used for measuring porosity in the range from 1 mm down to 2 nm. A slice about 1 g of hardened paste samples at 90 days was polished on every side of the surface to remove the carbonated area and broken into 4 to 5 pieces. Then, the small pieces of sample were placed in a glass dilatometer. A pressure for the intrusion was applied up to 440 MPa. A contact angle of 140° was assumed between mercury and the cement paste.

Mortar samples were prepared following the EN196-1 standard except the water to binder ratio (w/b) was set to 0.6, similar to the cement paste samples. The homogenized dry binders and the deionized water were equilibrated overnight at the intended curing temperature before mixing. The mixing was carried out at room temperature. The standardized sand was used in a sand to binder ratio (S/B) of 3 by mass. The mortar samples were placed in the boxes and cured at 5, 20, 40 and 60 °C until the time of testing from 1 up to 365 days.

## 5.3 Results

### 5.3.1 Hydration kinetics

#### 5.3.1.1 Heat of hydration

Fig. 5-1 shows the heat of hydration of the PC and CSA systems normalized per gram of clinker at different temperatures. For the different temperatures, the scales of intensity and time are different in order to have the PC curve roughly at the same position to be able to compare the CSA curves relative to the PC system. Increasing temperature accelerates the hydration kinetics, more strongly for the CSA system.

Considering the alite peak in the PC system, the alite reaction is enhanced for the blended systems due to the filler effect of metakaolin and limestone, as shown by the higher intensity of the silicate peak. The enhancement of the aluminate reaction can be observed at 40 and 60°C because of high adsorption of sulfate in C-(A)-S-H [37]. As temperature is increasing, the reaction rate of silicate clinker phases is increased. More C-S-H precipitates in the system leading to more sulfate adsorption in the C-(A)-S-H. As a result, gypsum is depleted earlier and triggers the C<sub>3</sub>A reaction. The reaction of CSA is very fast at high temperature. It combines all the small peaks, present at lower temperature, into one peak. In fact, the addition mayenite is not required at the high temperature.

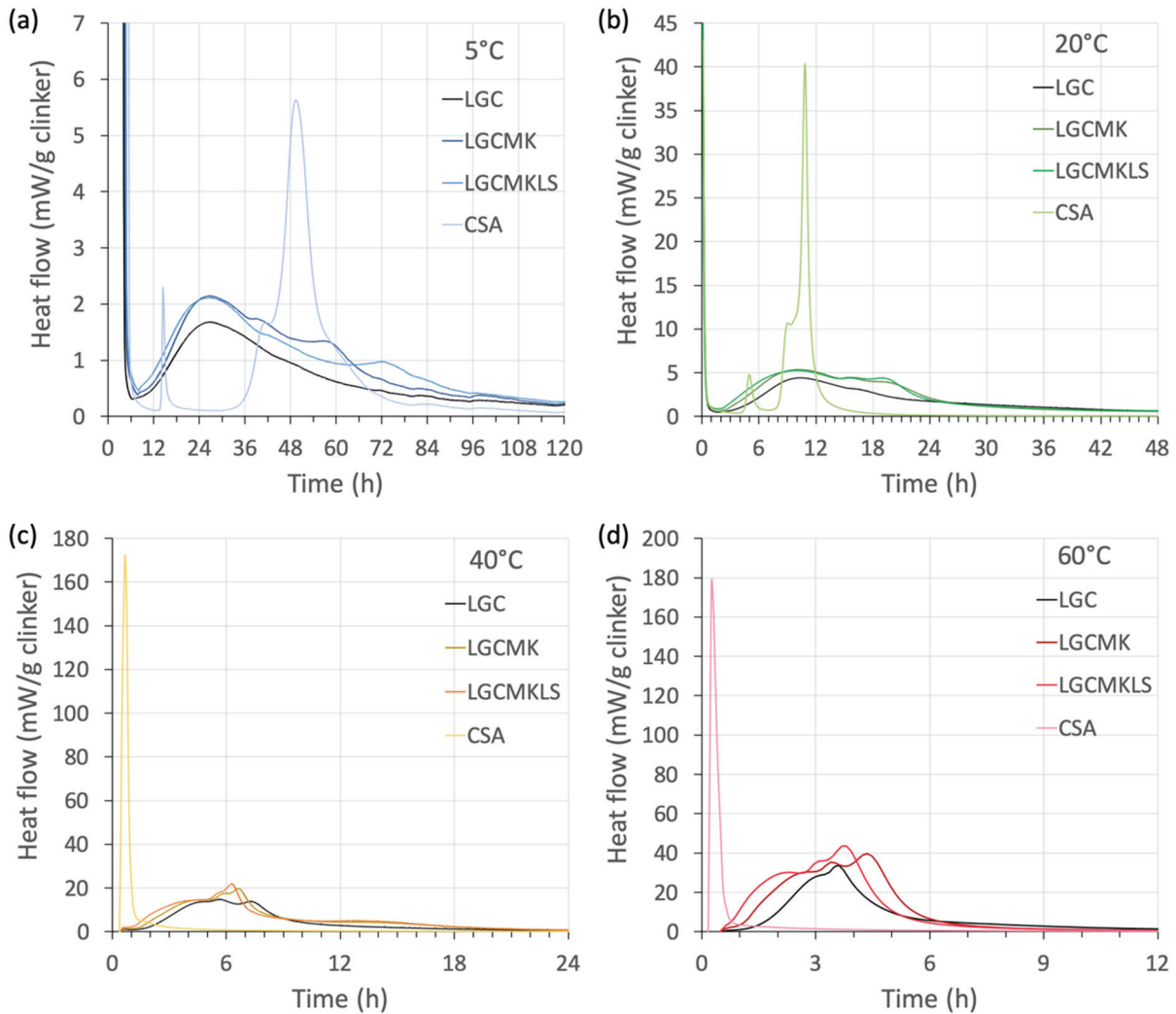


Fig. 5-1 Heat flow curves of the investigated system measured at (a) 5, (b) 20, (c) 40 and (d) 60°C.

The cumulative heat release in Fig. 5-2 shows a gradual acceleration of the reaction with the temperature in the PC system. The cumulative heat at different temperatures reaches a similar value at 28 days. At 5°C, the cumulative heat of the PC systems still continues after 28 days of hydration. The reaction slows down earlier when the temperature is increased. With the presence of metakaolin, three stages of reaction rate can be observed at 5 - 40°C. The second stage could indicate the metakaolin reaction. For the CSA system, the total heat is much lower than the PC system. A big gap difference in the reaction time is observed between 20 and 40°C.

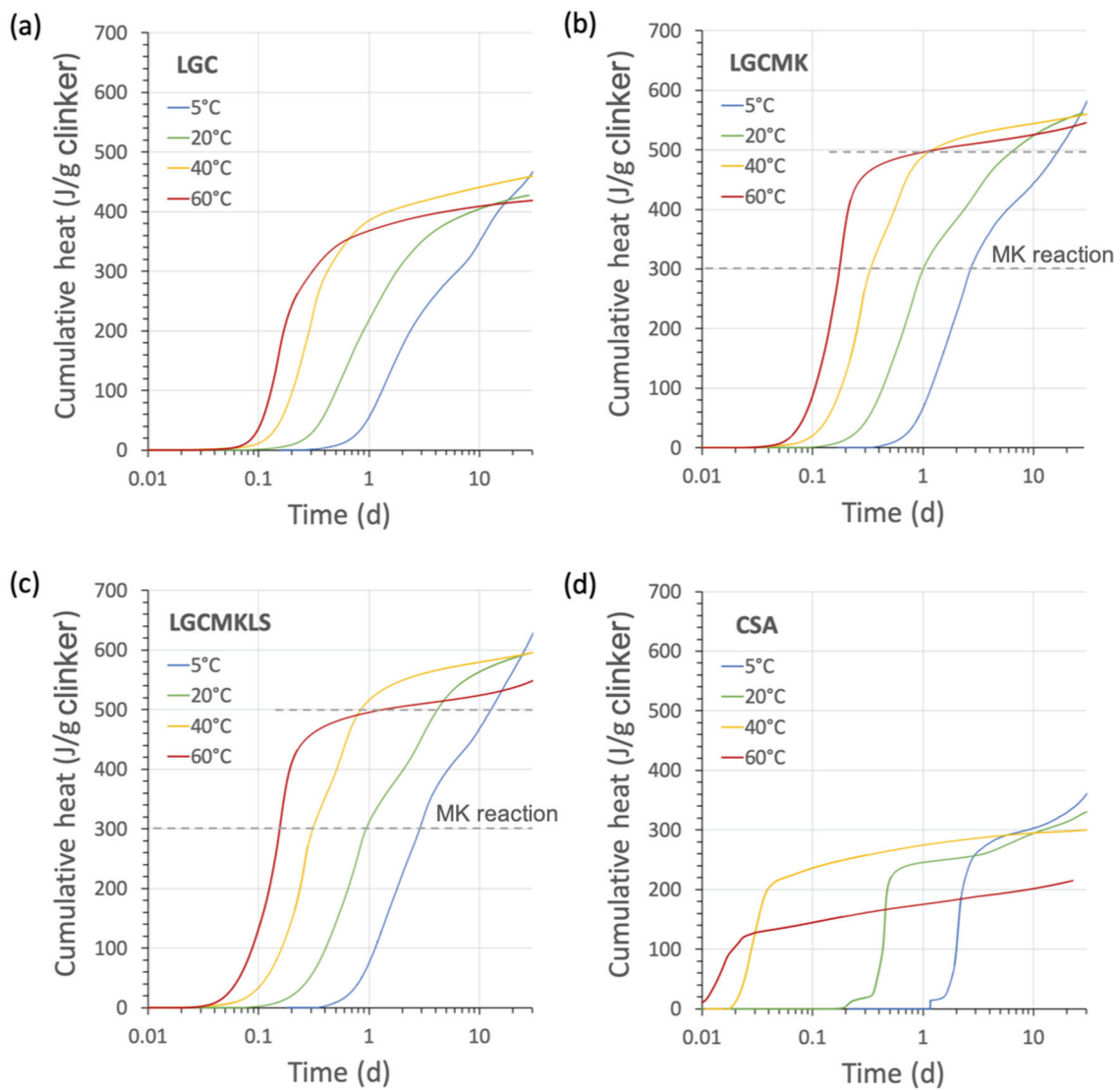


Fig. 5-2 Cumulative heat release of the investigated systems at different temperatures up to 28 days of hydration; (a) LGC, (b) LGCMK, (c) LGCMKLS and (d) CSA.

### 5.3.1.2 Degree of hydration (DoH) of anhydrous

The effect of temperature on the degree of hydration of the main clinker phase, determined by XRD Rietveld, are shown in Fig. 5-3. Alite and belite are the main clinker phases for the PC system, while belite and ye'elinite are the main clinker phases for the CSA system. Both alite and belite reactions in the LGC system are increased as a function of temperature. The extent of this reaction is slightly lower at high temperature compared to the LGC system. The reaction of belite in the blended systems is much lower than the LGC system. For the CSA system, the reaction of ye'elinite reaches 90% of DoH in 1 day at all temperatures. Belite reaction slightly reacts at early age and slows down. After 28 days, the reaction of belite is significantly increased.

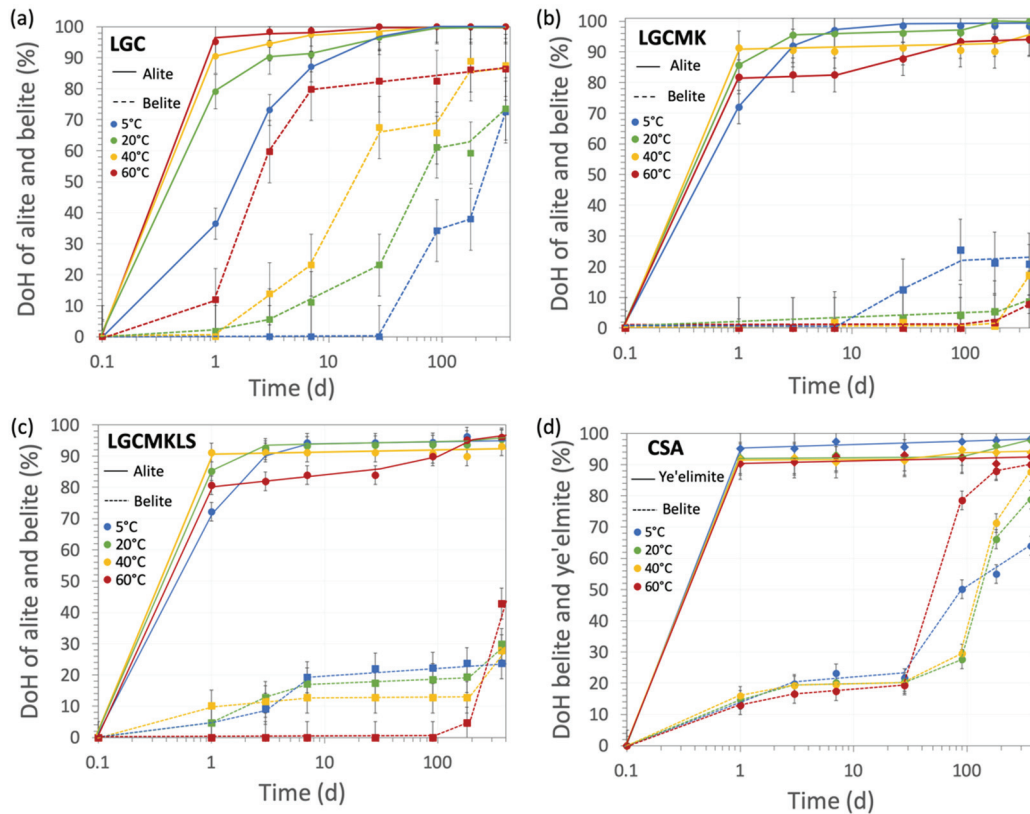


Fig. 5-3 Comparison of the DoH of the main clinker phase calculated from XRD Rietveld refinement of (a) LGC, (b) LGCMK, (c) LGCMKLS and (d) CSA at different temperatures. The main clinker phases of the PC systems are alite and belite. The main clinker phases of CSA are belite and ye'elimite.

## 5.3.2 Hydration

### 5.3.2.1 Hydration development

Fig. 5-4 and Fig. 5-5 illustrate the XRD patterns up to  $30^\circ 2\theta$  at 1 and 90 days of hydration. LGC forms C-S-H, portlandite (CH), ettringite as the main hydrates with a small amount of AFm. In the higher alumina systems, the higher  $Al_2O_3/SO_3$  ratio in the system promotes the AFm formation. Generally, the two AFm phases that form in presence of metakaolin are monosulfate (Ms) and strätlingite (S).  $CO_3$ -AFm (hemi or monocarboaluminate) can be formed as the main AFm phase when limestone is present in the system.

At 1 day of hydration, the main hydrates in the LGC system are C-S-H, portlandite and ettringite at all temperatures. Monosulfate and hemicarboaluminate are formed in small quantity between 20 - 40°C. Monosulfate-14 [38] is formed as a main phase instead of ettringite at 60°C. The hydration products in the LGCMK system are quite similar to the LGC system, except at 60°C. Only a smaller portlandite content and a higher monosulfate-14 content are observed at 60°C compared to the LGC system. A broad peak of AFm at 40°C indicates a poorly crystalline structure of AFm phases compared to lower temperatures. Hemicarboaluminate peak is present at 40°C, its presence is due to the calcite present in the LGC (see Table 5-1). In the LGCMKLS system, a similar trend of hydrate formation as the LGCMK system can be observed. Additional broad peak of monocarboaluminate can be observed at 40°C. For the CSA system, the main hydrates are different from the LGCMK system, especially at 5°C. When comparing at different curing temperature, similar phase assemblages are observed between 20 - 60°C. Ettringite, monosulfate-14 and aluminium hydroxide ( $AH_3$ ) are the main hydrated phases of the CSA system at this age.  $CAH_{10}$ , which is a metastable phase forming at an early age, can be observed only at 5°C [39]. Belite, ye'elimite and anhydrite are still present at all temperatures.

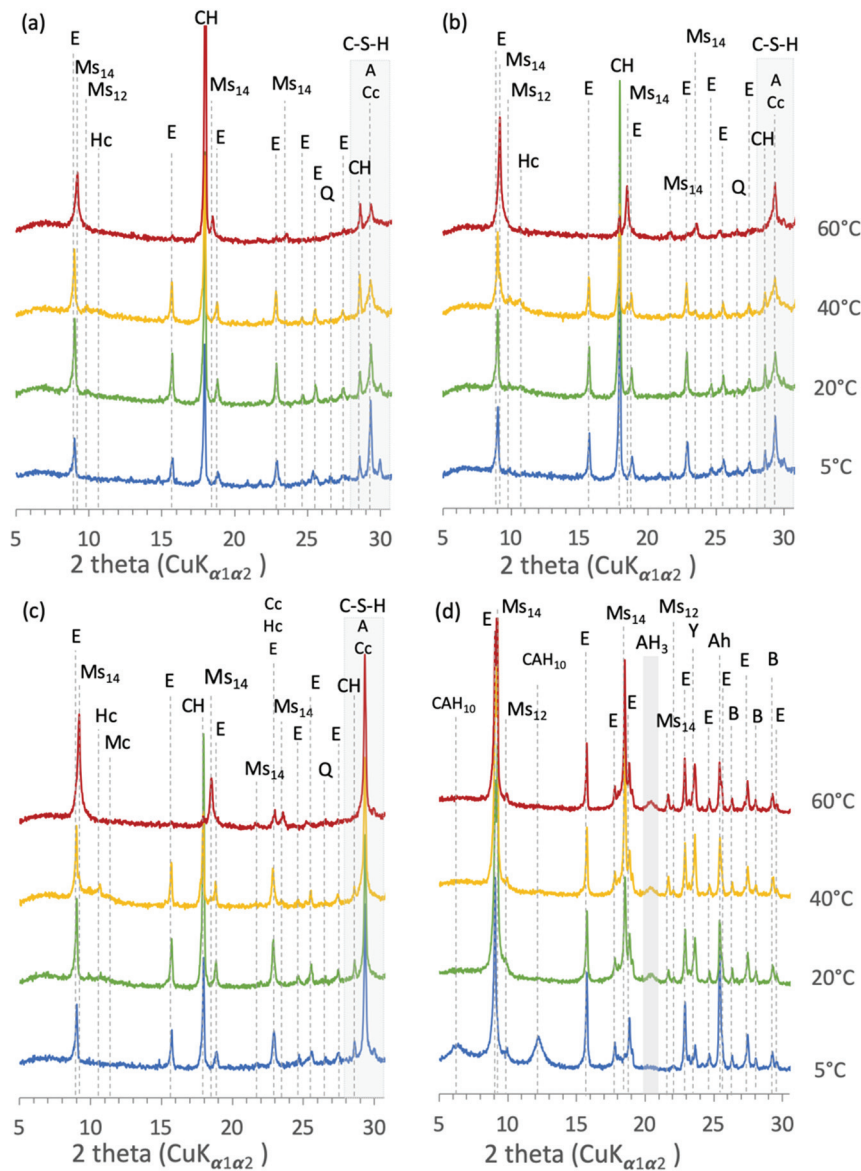


Fig. 5-4 Comparison of XRD patterns of (a) LGC, (b) LGCMK, (c) LGCMKLS and (d) CSA after 1 day of hydration at 5, 20, 40 and 60°C: E = ettringite, CH = Portlandite, Ms = monosulfate, Hc = hemihydrate, Mc = monocarbonate, Q = Quartz, Cc = calcite, A = alite, B = belite, Y = ye'elimite, Ah = anhydrite, CAH<sub>10</sub> = calcium aluminate hydrates, AH<sub>3</sub> = aluminium hydroxide.

At 90 days of hydration (Fig. 5-5), C-S-H, portlandite and ettringite are present in the LGC system at all temperatures. Hemihydrate and monocarbonate can be observed at the temperature below 60°C. More ettringite is precipitated with monosulfate-14 at 60°C at this age. The LGCMK system shows a change of phase assemblage with temperatures, especially for the aluminate hydrates, particularly the types of AFm phases. At 5 and 20°C, the main hydrates are quite similar but an undefined AFm solid solution hereafter called AFm<sub>ss</sub> is found at 5°C. It is most likely a solid solution of the AFm phase containing sulfate, hydroxide and carbonate [40]. Monosulfate-14 starts to form at 40°C with ettringite and it becomes more stable at 60°C without ettringite precipitation. A small broad peak of siliceous hydrogarnet can be observed only at 60°C. The co-existence of strätlingite and portlandite can be observed in the LGCMK system be-



tween 5 and 40°C. The intensity of portlandite is significantly lower when compared to the LGC system due to the pozzolanic reaction. In LGCMKLS, hemicarbonate and monocarbonate are precipitated instead of monosulfate due to the presence of limestone. Hemicarbonate is observed at 5 and 20°C as a main AFm phase, while monosulfate-14 is observed instead of hemicarbonate and monocarbonate at higher temperatures. Similar to the LGCMK system, monosulfate-14 is formed instead of ettringite at 60°C. Moreover, portlandite cannot be observed at 60°C. The phase assemblage in the CSA system changed compared to 1 day of hydration.  $CAH_{10}$  at 5°C and  $AH_3$  at 60°C have disappeared at a late age. Only a very small hump of  $AH_3$  is still present at 20 and 40°C. Strätlingite is formed as a main hydrate phase at all temperatures. Moreover, a typical C-S-H hump can be found at 5 and 60°C due to the high belite reaction (see Fig. 5-3). Similar to the PC system, more monosulfate-14 is formed at elevated temperature.

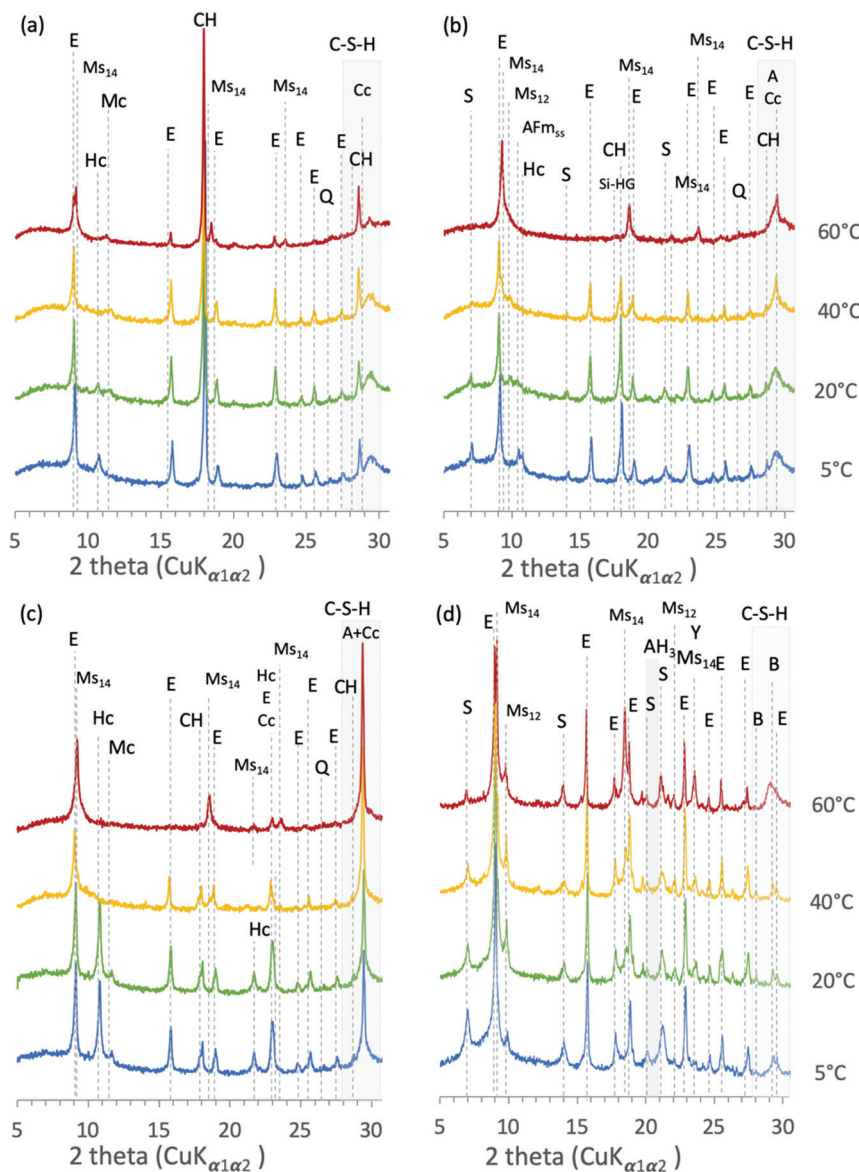


Fig. 5-5 Comparison of XRD patterns of (a) LGC, (b) LGCMK, (c) LGCMKLS and (d) CSA at 90 days of hydration at 5, 20, 40 and 60°C: E = ettringite, CH = Portlandite, Ms = monosulfate, Hc = hemicarbonate, Mc = monocarbonate,  $AFm_{55}$  = solid solution of AFm ( $SO_3$ -OH- $CO_3$ ), S = strätlingite, Si-HG = siliceous hydrogarnet, Q = Quartz, Cc = calcite, B = belite, Y = ye'elimite,  $AH_3$  = aluminium hydroxide.

Fig. 5-6 shows the quantitative analysis of phase assemblages at 90 days of hydration of the investigated systems at different temperatures obtained by XRD Rietveld quantification, and TGA (bound water). Temperature affects mainly the aluminates hydrates. The ettringite content is decreased with increasing temperature in all systems. The content of monosulfate is significantly higher at 60°C. C-S-H is included in the amorphous part because it cannot be quantified by this technique.

Considering LGCMK and CSA in Fig. 5-6b and Fig. 5-6d, the hydrate phase assemblage is quite similar but the amount of aluminate phases is different. The total content of aluminate hydrates (ettringite, monosulfate and strätlingite) in the CSA system is significantly higher than the LGCMK system, due to the low reaction of belite, reducing the Si available (see Fig. 5-3).

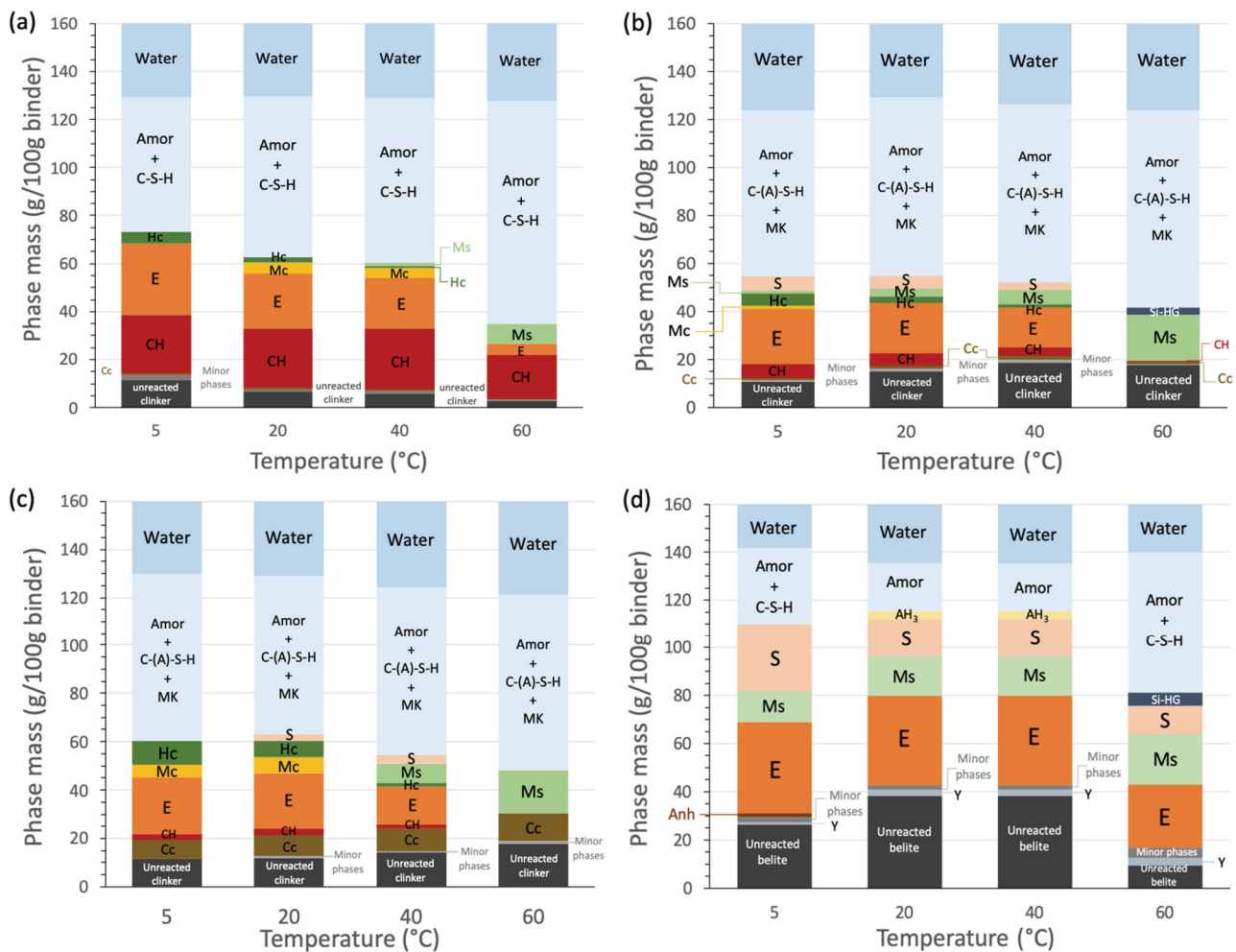


Fig. 5-6 Comparison of the phase assemblages in (a) LGC, (b) LGCMK, (c) LGCMKLS and (d) CSA after 90 days of hydration at different temperatures determined by XRD Rietveld analysis.

### 5.3.2.2 Bound water content

The bound water content was measured by TGA. The results are shown in Fig. 5-7. In the PC system, bound water in the sample cured at high temperature after 1 day of hydration is higher than the sample cured at low temperature and it is slightly increased with time, in agreement with the evolution of the DoH (see Fig. 5-3). The development of

bound water in the sample cured at low temperature is higher than the sample cured at high temperature, leading to high content of bound water at late age. The amount of bound water in the CSA system is higher than the PC system but quite similar across the temperature. After 28 days, bound water is significantly increased because belite continues to react. Similar to the blended systems, bound water content is increased when the temperature is decreased.

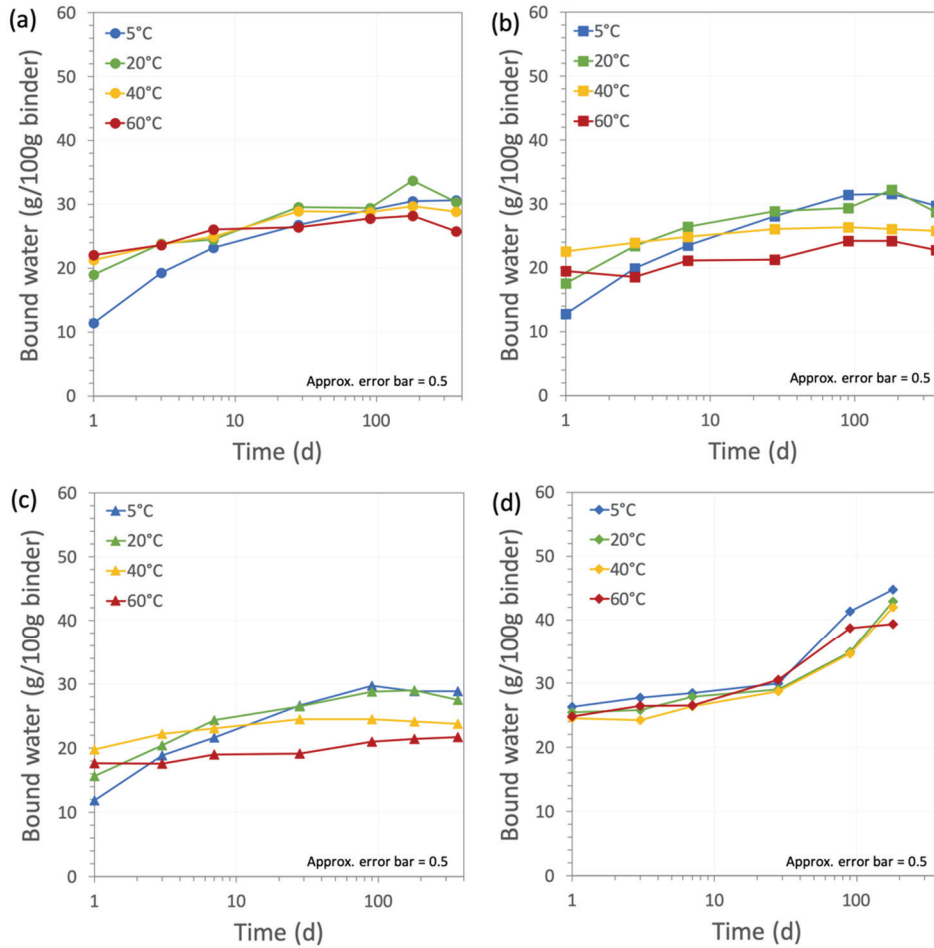


Fig. 5-7 Comparison of bound water content at different temperatures in (a) LGC, (b) LGCMK, (c) LGCMKLS and (d) CSA.



### 5.3.3 Microstructure and porosity at 90d

#### 5.3.3.1 Microstructure by SEM

The effect of temperature on the microstructure of the investigated systems at 90 days of hydration is shown in Fig. 5-8 - Fig. 5-11. The BSE images of the LGC microstructures (in Fig. 5-8) are similar at temperatures between 5 to 40°C. The microstructure at 60°C is significantly different. More large pores and fully hydrated grains replaced by the formation of C-S-H can be observed at high temperature.

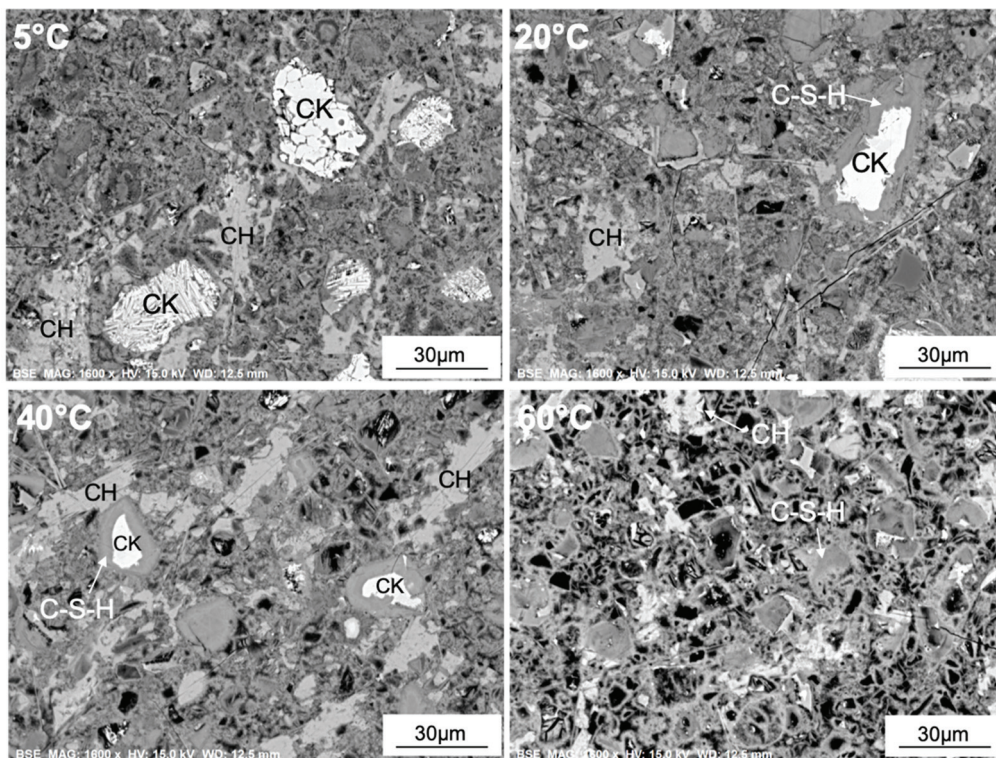


Fig. 5-8 Comparison of the microstructures of LGC at 90 days cured at 5, 20, 40 and 60°C.

Fig. 5-9 shows the effect of temperature on the microstructure of the LGCMK system. There are more clinker grains remaining in the microstructure compared to the LGC system. The microstructure of the LGCMK system is quite dense and homogenous across the temperatures. It does not show a significant change when the temperature is increased. At 60°C, there are far fewer large pores in the BSE image compared to the LGC system. The presence of portlandite in the microstructure of the LGCMK system is also less than the LGC system. Portlandite is rarely found in the microstructure at 60°C which corresponds to the XRD results. Many regions of AFm can be found in the microstructure of the LGCMK system. It is formed in the pores left by the dissolution of clinker grains.



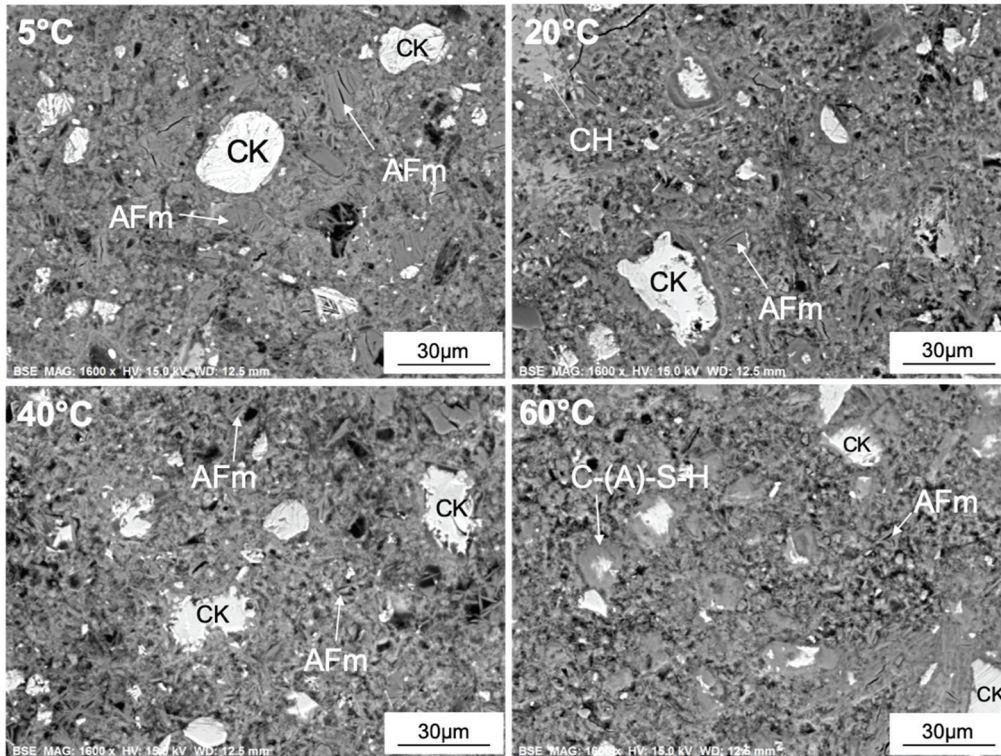


Fig. 5-9 Comparison of the microstructures of LGCMK at 90 days cured at 5, 20, 40 and 60°C.

The microstructure of LGCMKLS (Fig. 5-10) is quite similar to LGCMK. Some large limestone grains can be seen.

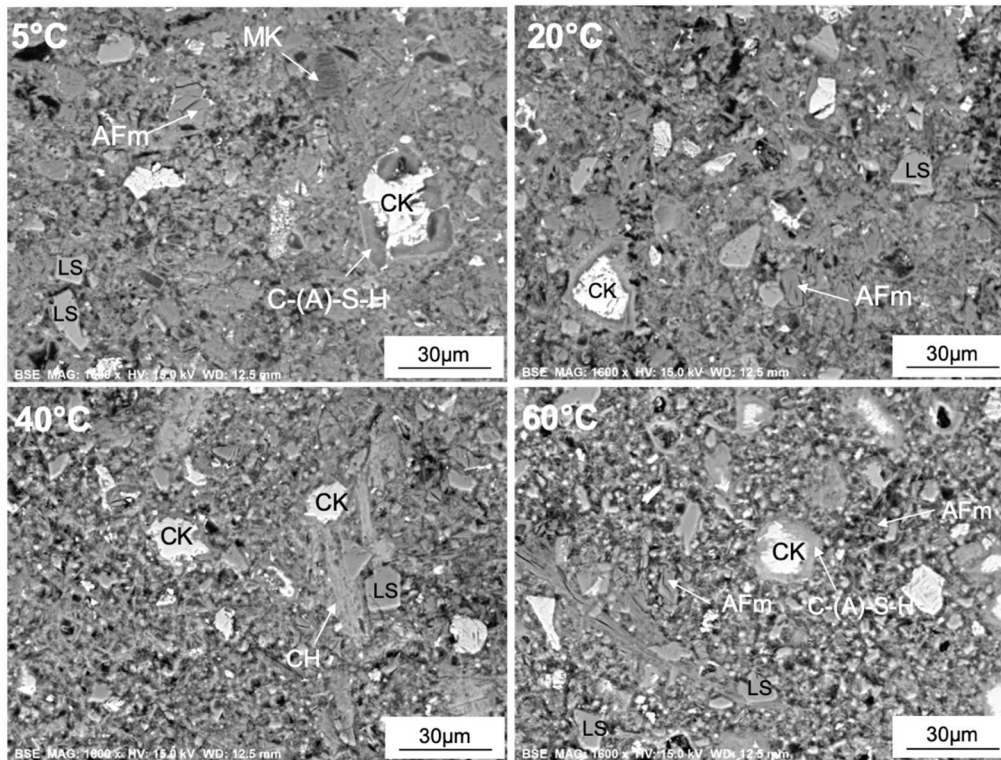


Fig. 5-10 Comparison of the microstructures of LGCMKLS at 90 days cured at 5, 20, 40 and 60°C.



BSE images in Fig. 5-11 show the microstructures of the CSA system at different temperatures. Belite grains are much smaller than the PC system. Some dense areas corresponding to ettringite and monosulfate formation can be observed at 5 and 60°C. However, the microstructure at these two temperatures is not homogenous, particularly at 60°C. The microstructure at 20 and 40°C looks similar and more homogenous. As a result, it is more difficult to find the C-S-H on the BSE.

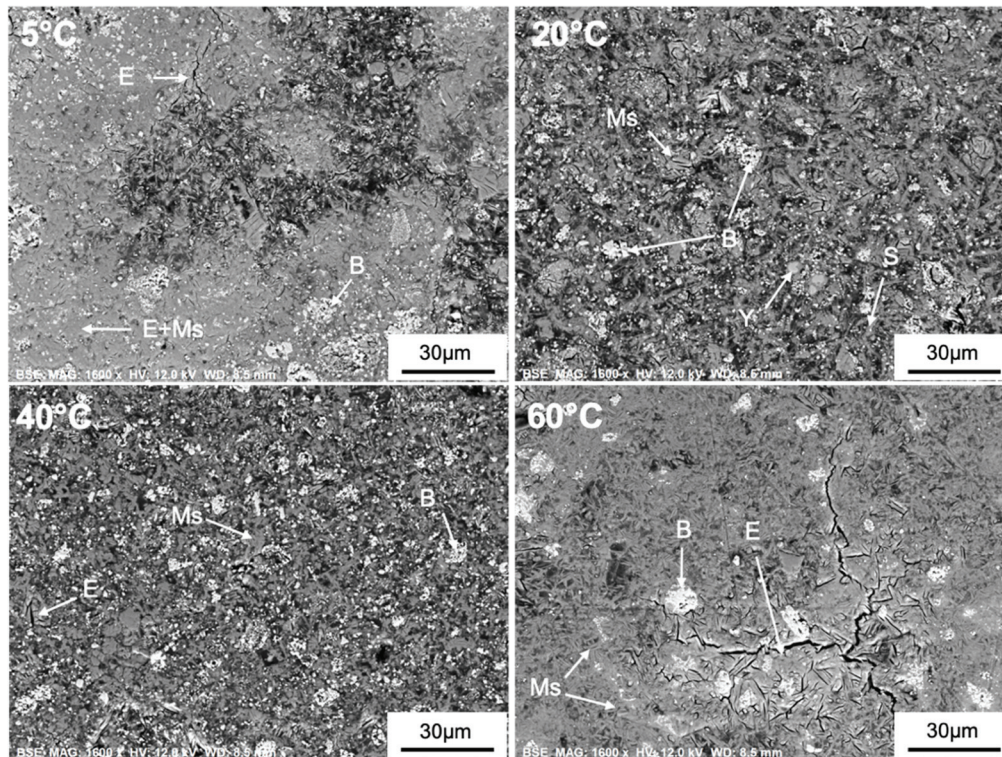


Fig. 5-11 Comparison of the microstructures of CSA at 90 days cured at 5, 20, 40 and 60°C.

### 5.3.3.2 C-(A)-S-H formation in the microstructure of higher alumina systems

Generally, the C-(A)-S-H in the PC based system is found as an inner product and an outer product. Inner C-S-H is formed next to the clinker grains while outer C-S-H forms in the available space, as shown in Fig. 5-12a.

According to the XRD result in Fig. 5-5d, a typical hump of C-S-H formed in the CSA system can be observed at 5 and 60°C due to high belite reaction. The comparison between the LGCMK system and the CSA system is made only at 60°C to provide a general idea. More details were discussed in the previous chapter. Inner C-S-H is not seen around belite grains for the CSA system, unlike the PC system.

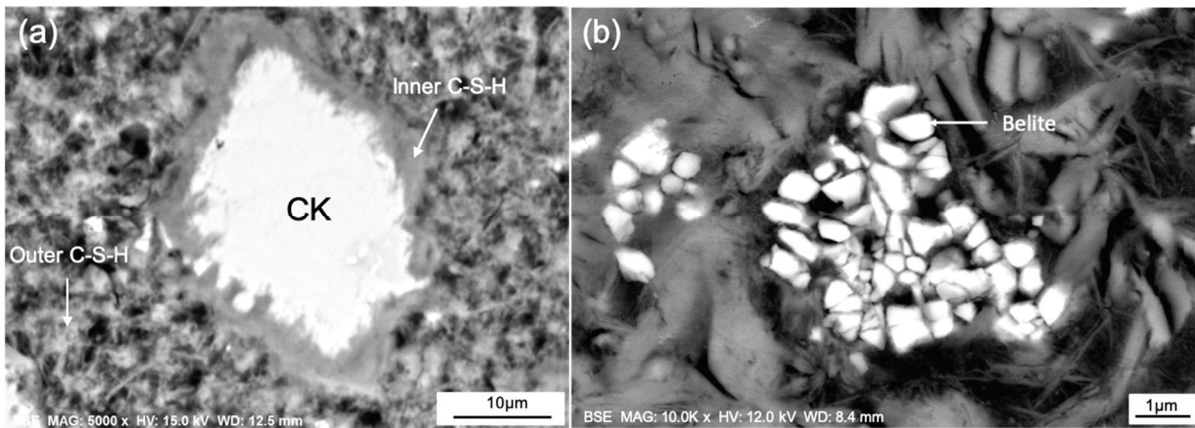


Fig. 5-12 Comparison of the C-S-H formation around the clinker grains of (a) LGCMK and (b) CSA at 90 days of hydration cured at 60°C.

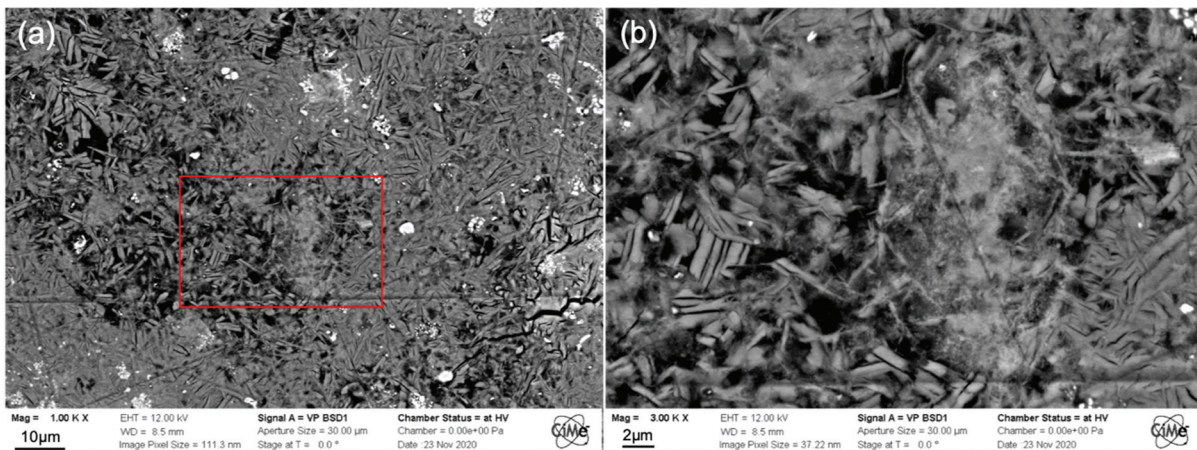


Fig. 5-13 The BSE image of the microstructure of C-S-H formed in the CSA system at 90 days of hydration cured at 60°C with magnification of (a) 1000x and (b) 3000.

### 5.3.3.3 Strätlingite formation in the microstructure of higher alumina systems

Strätlingite is another important phase forming in the higher Al systems. It is difficult to identify this phase in BSE images. Therefore, *edxia* is used to indicate the location of strätlingite in the microstructure from the quantified EDS mapping [35]. In this part the formation of strätlingite is compared in the LGCMK system and CSA at 20°C because the cluster of points around the composition of strätlingite in the CSA system can be observed only at 20°C. The atomic ratio plot of Si/Ca and Al/Ca of both systems at 20°C are shown in Fig. 5-14. The cluster of points around the strätlingite composition was selected in red.



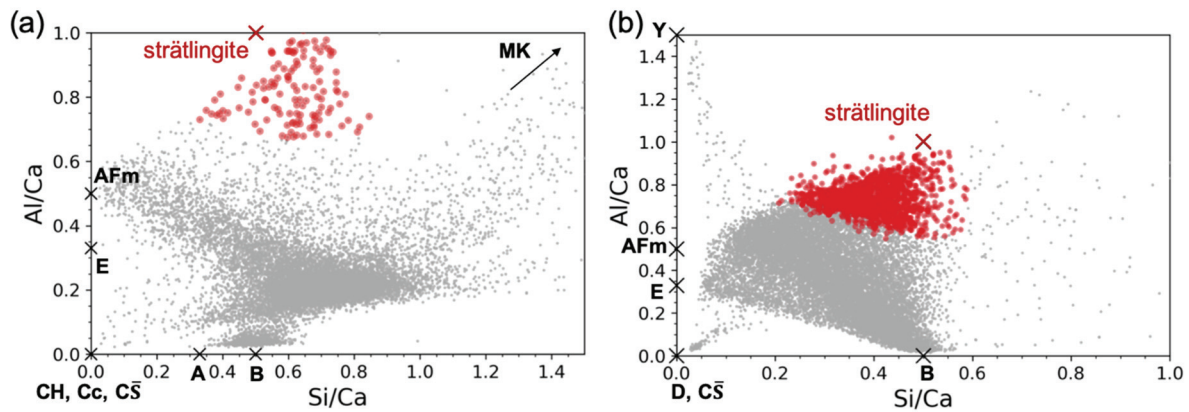


Fig. 5-14 EDS ratio plot of Si/Ca and Al/Ca from the mapping data of (a) LGCMK and (b) CSA at 20°C. Strätlingite was selected as red with the edixa interface [35].

From Fig. 5-15, Strätlingite in the LGCMK system forms next to the AFm grains, whereas strätlingite in the CSA system forms more in the available space. In LGCMK, it is very difficult to distinguish the morphology in the polished section due partly to the similarity in grey level between AFm and strätlingite. It forms as masses similar to AFm phase but edixa reveals the different chemical composition. Strätlingite in the CSA systems forms elongated shapes, but It is also difficult to differentiate without applying the image analysis methodology.

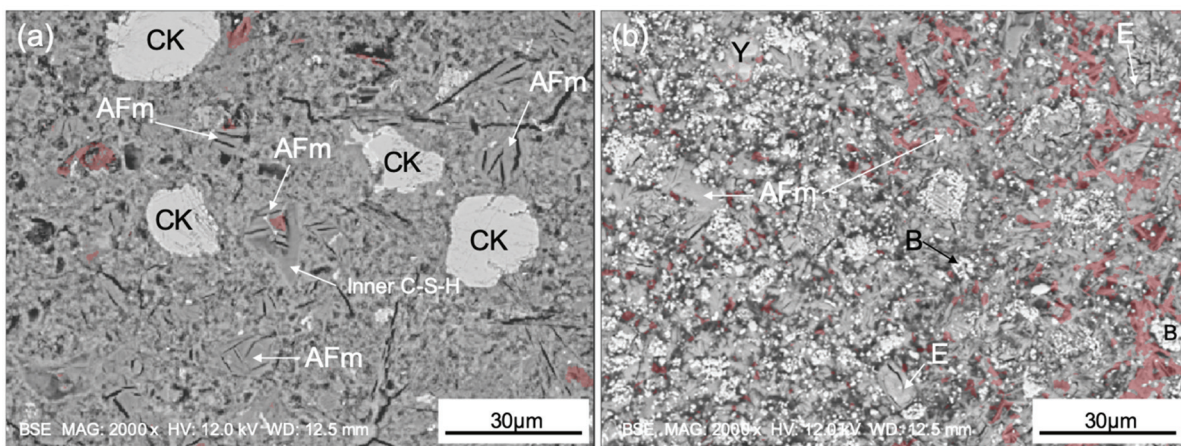


Fig. 5-15 Comparison of strätlingite formation in the microstructure of (a) LGCMK and (b) CSA cured at 20°C.

#### 5.3.3.4 Porosity at 90 days of hydration

The influence of temperature on porosity of the systems at 90 days measured by MIP is shown in Fig. 5-16. The PC system shows an increase of total porosity as a function of temperature. The critical pore entry diameters in LGC are much lower at 5 - 20°C than 40 - 60°C. The blended systems have higher total porosity than the LGC system. The critical pore entry for the system blended with metakaolin is reduced compared with the plain system at all temperatures. LGCMK has similar critical pore entry diameters over the range of temperatures, while the critical pore entry diameter in LGCMKLS at 5-20°C is slightly smaller than at 40-60°C. For the CSA system, the relation between the total porosity and temperature is non-monotonous: the samples cured at 5 and 60°C show a lower total porosity than 20 and 40°C. The CSA sample cured at 5°C has the lowest total porosity as the total hydrate formation is higher (higher

bound water content with C-S-H and strätlingite present). The CSA system shows a small critical pore entry at 5 and 60°C compared to the other two temperatures.

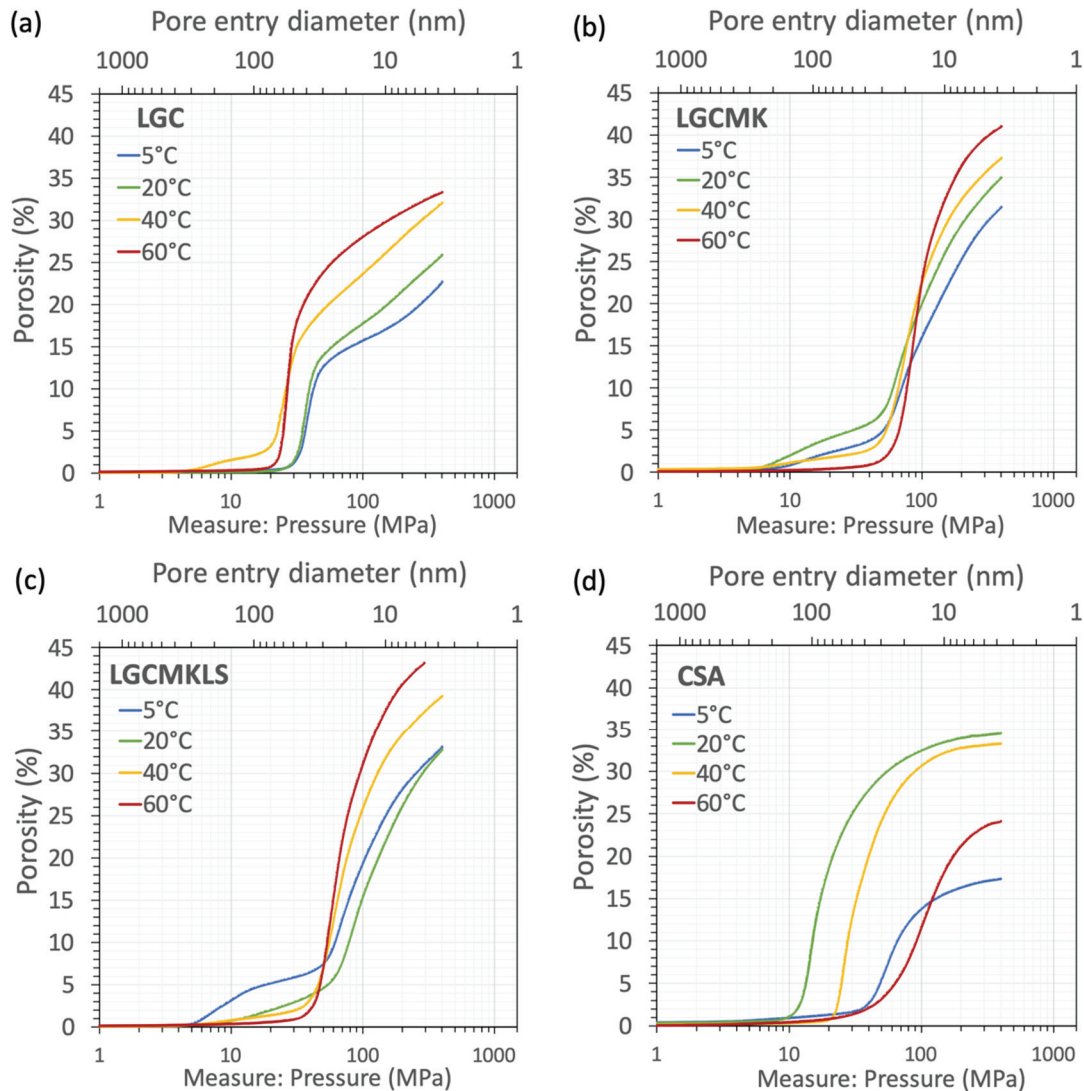


Fig. 5-16 MIP porosity of the investigated systems (a) LGC, (b) LGCMK, (c) LGCMKLS and (d) CSA at different curing temperatures at 90 days of hydration.

### 5.3.4 Compressive strength

Fig. 5-17 shows the effect of temperature on the mortar compressive strengths. Temperature accelerates the development of compressive strength at early age, then slow development is observed leading to a lower compressive strength at late age. At 5°C, LGC shows a very low compressive strength at 1 day but it reaches a similar range of the compressive strength as the other temperature after 7 days. In the blended systems, the comparable strengths are observed after 28 days.

The strength of CSA is lower than the LGCMK system. Fig. 5-17 shows no clear trend of compressive strength development as a function of temperature. However, there are two groups showing similar compressive strength. The compressive strength at 5°C is higher at early ages than the sample at 20°C. After 28 days, the compressive strength is increased significantly at 5 - 40°C, while it remains the same at 60°C.

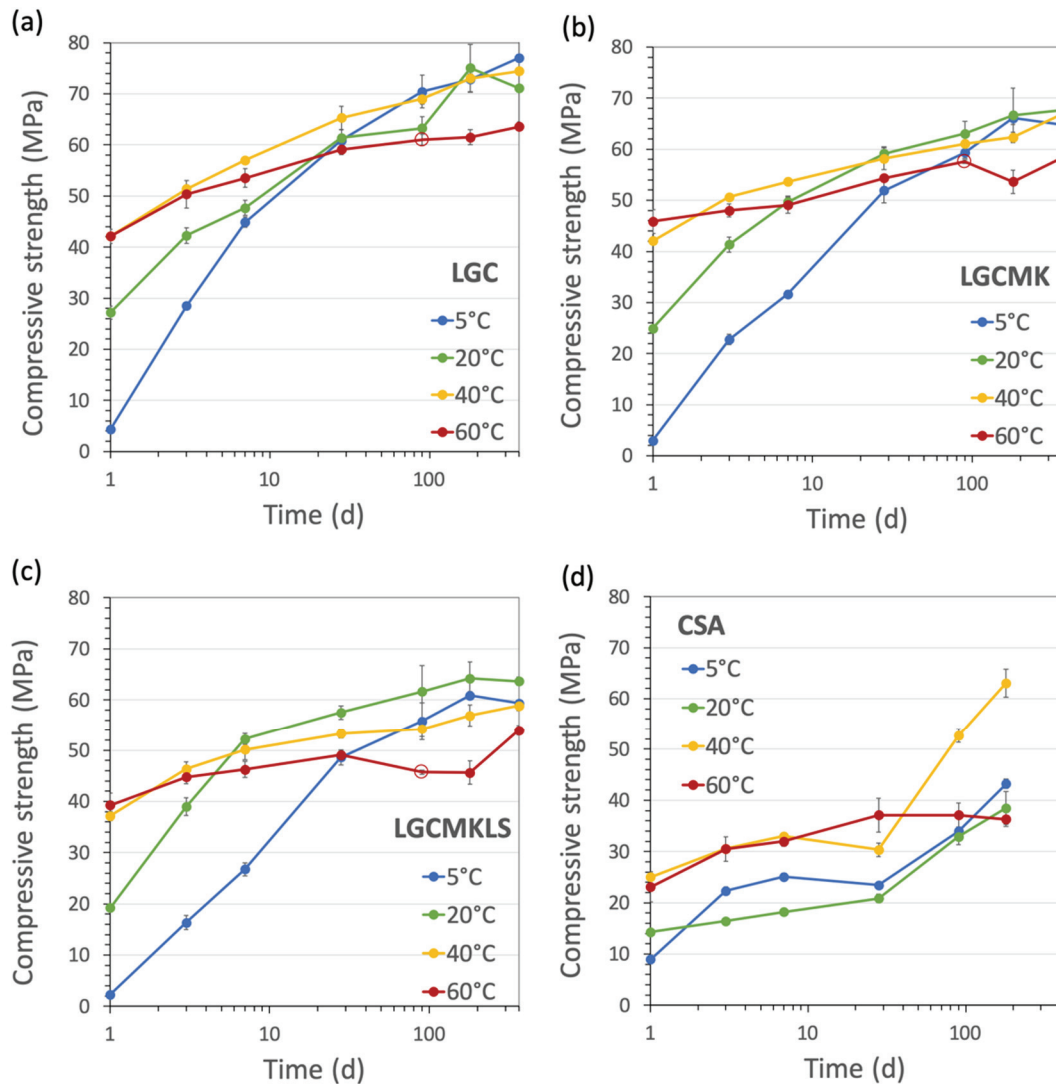


Fig. 5-17 The effect of temperature on the compressive strength development of (a) LGC, (b) LGCMK, (c) LGCMKLS and (d) CSA.

## 5.4 Discussion

### 5.4.1 Degree of hydration of belite in CSA

The DoH of belite in CSA is low before 28 days of hydration, then it extensively reacts at 5 and 60°C after 28 days. At 180 days of hydration, the DoH of belite at 20 and 40°C is significantly increased. The low belite reactivity could be related to the aluminate hydrates,  $AH_3$  and/or  $CAH_{10}$ , formation as shown in Fig. 5-18. The result shows that the reaction of belite is low when  $AH_3$  and/or  $CAH_{10}$  are present in the system. After the depletion of  $AH_3$  and  $CAH_{10}$ , belite starts to react. The presence of aluminium in the pore solution could be slowing down the dissolution of silicate phase [41]. However, the Al concentration in the pore solution at 90 days shown in Fig. 5-27b of CSA at 60°C is high, while the Al concentration at 5°C is nearly zero. Therefore, the real mechanism that governs the reaction of belite in the CSA system is not clear. For further studies, the pore solution at all ages should be obtained. Similar low reactivity of belite with metakaolin blends which is the PC based higher aluminium system is also observed.

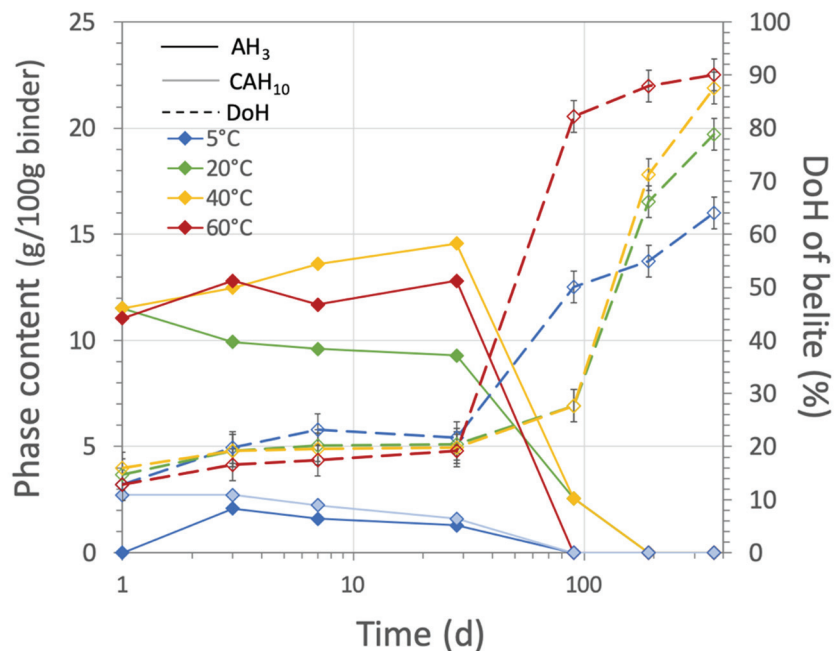


Fig. 5-18 Relation between the formation of  $CAH_{10}$  at 5°C and/or  $AH_3$  at 20 - 60°C and belite reaction in the CSA system.

### 5.4.2 Correlation between degree of hydration and compressive strength

The clinker in the LGC system is almost fully reacted, while the DoH of clinker in the blended system is limited to around 80% after 1 year of hydration, as shown in Fig. 5-19a - Fig. 5-19c. The reaction of the clinker in the CSA system (Fig. 5-19d) is increased at elevated temperature. At 180 days of hydration, the reaction is in between 70 - 90% DoH.

Fig. 5-20 shows a comparison of compressive strength as a function of DoH of clinker. LGC shows a good correlation between compressive strength and DoH of clinker across the temperature. However, a change of slope at 60°C can be observed at a later age. It shows that the DoH does not increase while the compressive strength development continues at late age. Dissolution of hydrates/metastable phases, and reprecipitation in a different configuration might be



an explanation. Higher alumina systems (Fig. 5-20b - Fig. 5-20d) reveal quite similar characteristics. Although the compressive strength is increased, the DoH remains similar. Only the initial stage of hydration that the development of compressive strength follows the DoH of clinker. These trends are related to the metakaolin. The CSA system has two points which are out of the trend at 5 and 60°C. The compressive strength remains the same where the DoH is significantly developed, especially at late age. Therefore, DoH of clinker is not the only factor that can relate the compressive strength result in higher alumina systems. In the blended system, the reaction of metakaolin is contributed to the compressive strength and it should be considered.

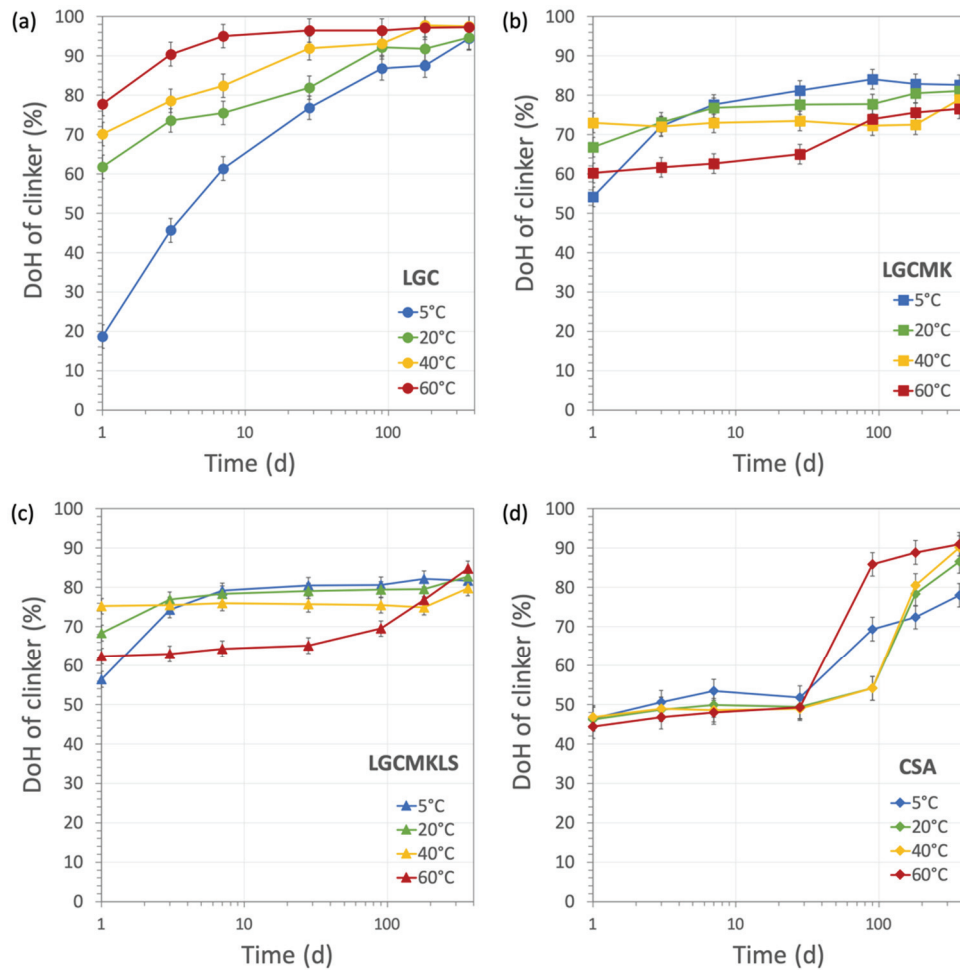


Fig. 5-19 The DoH of clinker of (a) LGC, (b) LGCMK, (c) LGCMKLS and (d) CSA at different curing temperatures.

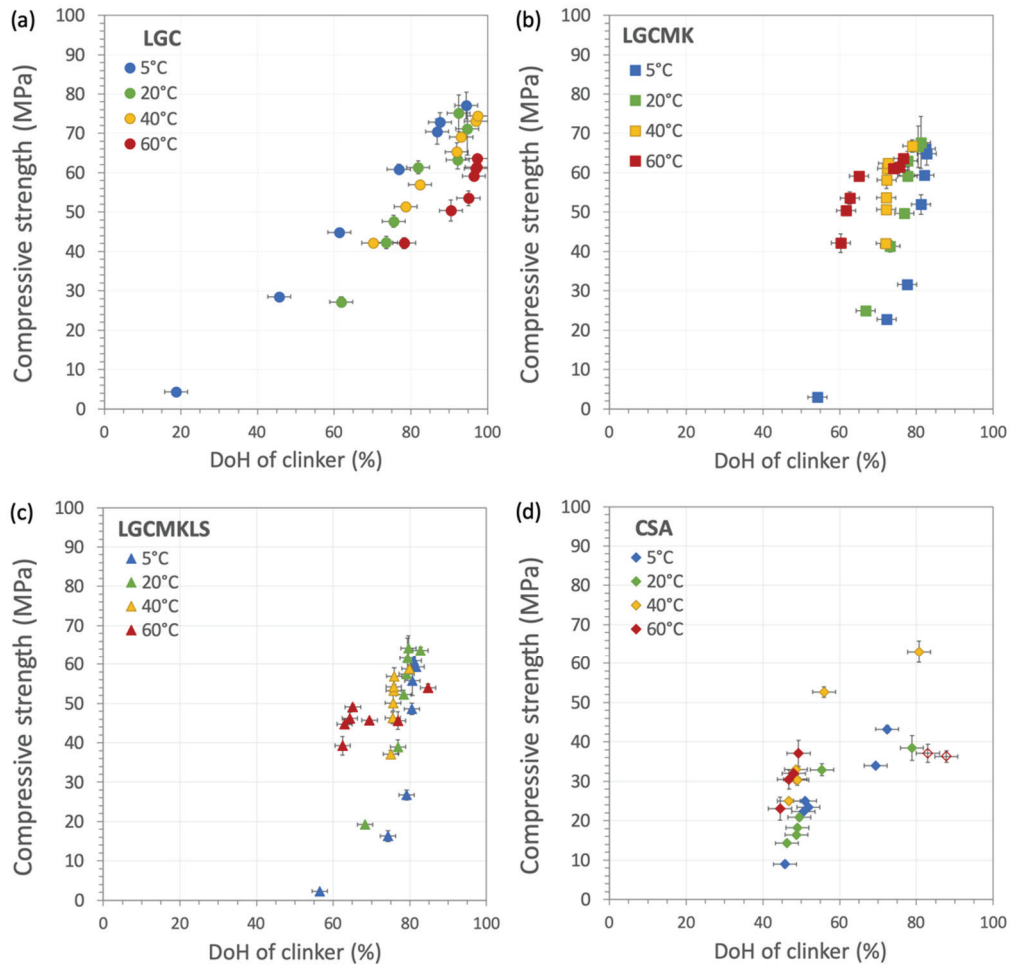


Fig. 5-20 Comparison of compressive strength and degree of hydration (DoH) of clinker calculated by XRD Rietveld quantification: (a) LGC, (b) LGCMK, (c) LGCMKLS and (d) CSA.

### 5.4.3 Correlation between porosity VS compressive strength

Generally, the mechanical property of cement is related to the pore volume and the pore distribution in cement [42]. In this study, the total porosity of different systems cured at different temperatures was measured by MIP. Fig. 5-21 shows the relationship between the total porosity and compressive strength at 90 days of hydration. Globally, the PC systems show some relationship between these two parameters, but with a large scatter. However, the CSA system does not really show any correlation. Thus, the total porosity cannot explain the compressive strength across the systems at different temperatures. Similar results have been reported in previous studies [13,30].

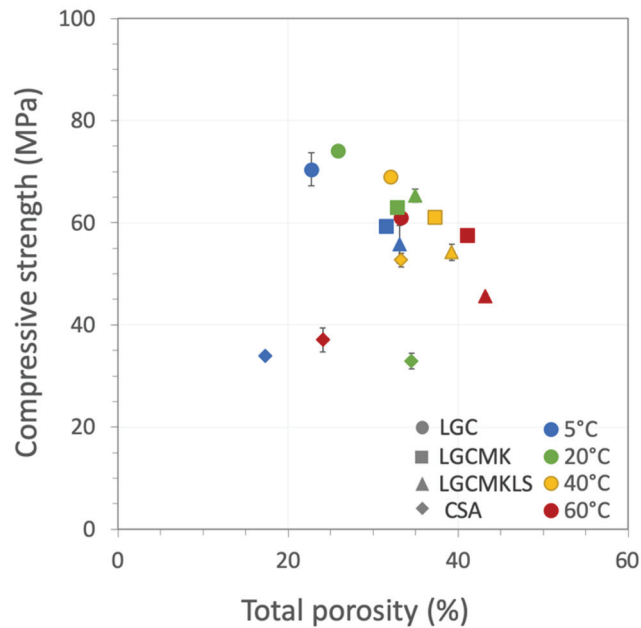


Fig. 5-21 Comparison of compressive strength and total porosity measured by MIP at 90 days.

#### 5.4.4 Correlation between combined water fraction (CWF) and compressive strength

To relate the hydrate formation to the compressive strength, the concept of combined water fraction (CWF) was investigated [43]. This method is easier to calculate than the gel space ratio (GSR)[29,44] because it only needs bound water obtained by TGA result. The difficulty of quantifying the amounts of many individual phases (particularly those which are amorphous or poorly crystalline) means that large errors accumulate in the GSR calculation.

The plot of compressive strength as a function of CWF is shown in Fig. 5-22. The PC systems are C-S-H dominated system, while the CSA system is ettringite dominated. The LGC system has good correlation between compressive strength at CWF. The blended systems present overall good correlation but more scattered points than the LGC system. A significant change of phase assemblages occurs at 60°C, it could affect bound water content in the total hydrates. For the CSA system, the CWF is not related well to the strength.

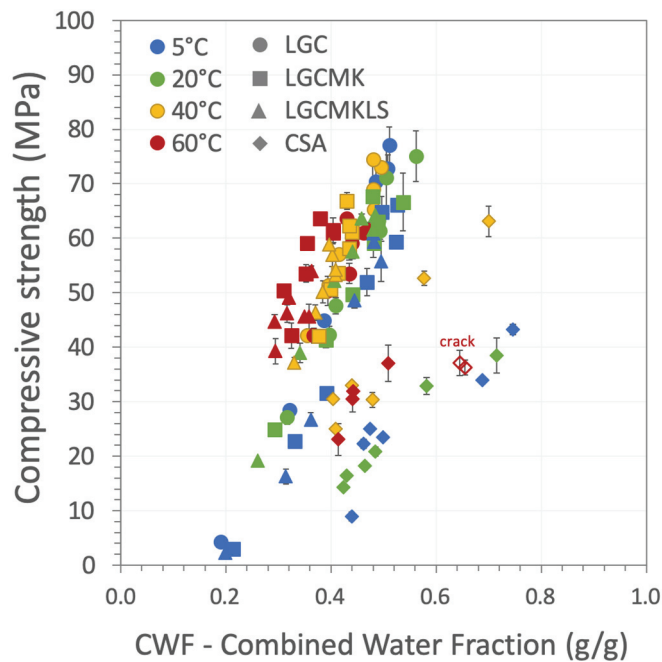


Fig. 5-22 Comparison of compressive strength and CWF of the investigated systems at different temperatures.

#### 5.4.5 The contribution of C-S-H to compressive strength in CSA

In the PC system, C-S-H is considered as a main hydration product initially formed in the cement matrix. It is linked to the macroscopic property of cement. Even though phase assemblage is slightly transformed in the blended system, C-(A)-S-H is still formed as a dominant phase due to the pozzolanic reaction. Therefore, C-(A)-S-H forming in the PC based system contributes to compressive strength.

In the case of the CSA system, the hydrated phase assemblages at early age and late age are different. Due to the slow reaction of belite, C-S-H is formed at a late age when the microstructure is full of ettringite and monosulfate. The C-S-H in the CSA system is formed in the samples cured at 5 and 60°C (see Fig. 5-5). It decreased the pore entry diameter to a similar range as the LGCMK system and reduced the total porosity at 90 days measured by MIP (see Fig. 5-16). However, the compressive strength of these two samples is not significantly increased (see Fig. 5-17). The compressive strength between 5 - 20°C is quite similar after 28 days, while the compressive strength at 60°C remains the same. The explanation for the constant compressive strength of the sample cured at 60°C is probably due to the heterogeneous microstructure and the internal micro cracks observed at late age. Therefore, it seems that the contribution of C-S-H formation in the CSA system is less than expected. This is probably due to low content and poor distribution.

#### 5.4.6 Effect of microstructure

Neither phase assemblage or porosity can directly explain the development of compressive strength. The MIP result shows that C-S-H formation can refine the porosity of cement. However, the pore entry radius of the LGC system is larger than the higher alumina systems, even though it forms C-S-H. Therefore, how and which C-(A)-S-H forms in the microstructure is also important.

Moreover, the difference of microstructure between the PC system and the CSA system could be a major effect on the compressive strength. In general, the PC system shows a good distribution of hydrates in the matrix, resulting in a homogenous microstructure. The CSA system with ettringite and AFm as main phases has a much more heterogeneous microstructure. These differences could explain the lack of a clear relation between porosity of hydrates and strength.

The non-uniform microstructure might be due to the lab produced clinker. A commercial cement could have a better optimized particle size distribution and reactivity. It might improve microstructure and strength. However, a synthetic clinker has a relevant chemical composition and phase assemblages.

## 5.5 Conclusions

This study looked at the effect of temperature on the hydration kinetics, phase assemblages, microstructure and porosity, and linked these to the compressive strength of the higher Aluminium systems.

Temperature accelerates the hydration kinetics. This effect is more pronounced in the CSA system. Temperature generally enhances the reaction of alite and belite. However, the higher Aluminium systems, both LGCMK and CSA, had low belite reaction even at high temperatures. The role of belite reaction is important because it controls the final phase assemblage. In metakaolin blends, the competition between clinker and metakaolin reaction depending on the temperature leads to the difference of silicate phase dissolution. In the case of CSA, the increase of reactivity of belite with temperature cannot compensate for the presence of aluminium hydrates ( $AH_3$  or  $CAH_{10}$ ). However, the mechanism that governs belite reaction in higher Aluminium systems is still not clear.

Although the initial chemical composition of the higher aluminium systems is close, the differences between PC which is alite dominated and CSA which is dominated by the reactivity of ye'elinite can be observed. Ettringite and AFm form as the initial products in CSA, while LGCMK forms C-S-H first. Consequently, the bound water of CSA, associated with the water content in ettringite and AFm, is generally higher than the PC system. The influence of temperature is mainly on the aluminate hydrates. More monosulfate is increased instead of ettringite and more strätlingite formation is decreased at elevated temperature.

The temperature affects not only the phase assemblage, but also the microstructure. As the temperature is increased, the microstructure of the LGC system becomes significantly more porous at 60°C. In the presence of metakaolin there are much less obvious changes of microstructure with increasing temperature. The microstructure of the CSA system is more heterogeneous than the LGCMK system. The precipitation of C-S-H and strätlingite is different between the two types of cement. C-S-H precipitates as inner and outer product in the PC systems, while it is formed mainly in the available space finely intermixed with AFm and ettringite in the CSA system and not dense structure. Moreover, strätlingite in the LGCMK system is formed closely to monosulfate grains. The formation of strätlingite in the CSA system is finely intermixing in the matrix which cannot be observed at low magnification, except at 20°C.

The degree of hydration of clinker correlates well with the compressive strength in the plain LGC system. In the blended systems, the degree of reaction of metakaolin is also contributed to compressive strength, thus it should be considered. A general relation between the MIP porosity and the compressive strength can be observed but it is quite scattered. The combined water fraction (CWF) concept shows globally good correlation with the compressive strength in the PC systems, but less good at high temperature. In the CSA system, there is no clear explanation on the compressive strength.

## 5.6 References

- [1] L. Barcelo, J. Kline, G. Walenta, E. Gartner, Cement and carbon emissions, *Mater. Struct.* 47 (2014) 1055–1065. <https://doi.org/10.1617/s11527-013-0114-5>.
- [2] B. Lothenbach, K. Scrivener, R.D. Hooton, Supplementary cementitious materials, *Cem. Concr. Res.* 41 (2011) 1244–1256. <https://doi.org/10.1016/j.cemconres.2010.12.001>.
- [3] K. Scrivener, F. Martirena, S. Bishnoi, S. Maity, Calcined clay limestone cements (LC<sup>3</sup>), *Cem. Concr. Res.* 114 (2018) 49–56. <https://doi.org/10.1016/j.cemconres.2017.08.017>.
- [4] E. Gartner, H. Hiraio, A review of alternative approaches to the reduction of CO<sub>2</sub> emissions associated with the manufacture of the binder phase in concrete, *Cem. Concr. Res.* 78 (2015) 126–142. <https://doi.org/10.1016/j.cemconres.2015.04.012>.
- [5] K.L. Scrivener, V.M. John, E.M. Gartner, Eco-efficient cements: Potential economically viable solutions for a low-CO<sub>2</sub> cement-based materials industry, *Cem. Concr. Res.* 114 (2018) 2–26. <https://doi.org/10.1016/j.cemconres.2018.03.015>.
- [6] M.C.G. Juenger, F. Winnefeld, J.L. Provis, J.H. Ideker, Advances in alternative cementitious binders, *Cem. Concr. Res.* 41 (2011) 1232–1243. <https://doi.org/10.1016/j.cemconres.2010.11.012>.
- [7] Z. Dai, T.T. Tran, J. Skibsted, Aluminum Incorporation in the C-S-H Phase of White Portland Cement-Metakaolin Blends Studied by <sup>27</sup>Al and <sup>29</sup>Si MAS NMR Spectroscopy, *J. Am. Ceram. Soc.* 97 (2014) 2662–2671. <https://doi.org/10.1111/jace.13006>.
- [8] W. Kunther, Z. Dai, J. Skibsted, Thermodynamic modeling of hydrated white Portland cement–metakaolin–limestone blends utilizing hydration kinetics from <sup>29</sup>Si MAS NMR spectroscopy, *Cem. Concr. Res.* 86 (2016) 29–41. <https://doi.org/10.1016/j.cemconres.2016.04.012>.
- [9] F. Winnefeld, B. Lothenbach, Hydration of calcium sulfoaluminate cements — Experimental findings and thermodynamic modelling, *Cem. Concr. Res.* 40 (2010) 1239–1247. <https://doi.org/10.1016/j.cemconres.2009.08.014>.
- [10] M. Antoni, J. Rossen, F. Martirena, K. Scrivener, Cement substitution by a combination of metakaolin and limestone, *Cem. Concr. Res.* 42 (2012) 1579–1589. <https://doi.org/10.1016/j.cemconres.2012.09.006>.
- [11] M. Zajac, J. Skocek, C. Stabler, F. Bullerjahn, M. Ben Haha, Hydration and performance evolution of belite–ye’elinite–ferrite cement, *Adv. Cem. Res.* 31 (2019) 124–137. <https://doi.org/10.1680/jadcr.18.00110>.
- [12] M. Zajac, S. Hoock, C. Stabler, M. Ben Haha, Effect of hydration kinetics on properties of compositionally similar binders, *Cem. Concr. Res.* 101 (2017) 13–24. <https://doi.org/10.1016/j.cemconres.2017.08.005>.
- [13] Thesis TH3725 Xinyu Zhang - Quantitative microstructural characterisation of concrete cured under realistic temperature conditions\_EPFL.pdf, (n.d.).
- [14] B. Lothenbach, F. Winnefeld, C. Alder, E. Wieland, P. Lunk, Effect of temperature on the pore solution, microstructure and hydration products of Portland cement pastes, *Cem. Concr. Res.* 37 (2007) 483–491. <https://doi.org/10.1016/j.cemconres.2006.11.016>.
- [15] B. Lothenbach, T. Matschei, G. Möschner, F.P. Glasser, Thermodynamic modelling of the effect of temperature on the hydration and porosity of Portland cement, *Cem. Concr. Res.* 38 (2008) 1–18. <https://doi.org/10.1016/j.cemconres.2007.08.017>.

- [16] J.I. Escalante-García, J.H. Sharp, Effect of temperature on the hydration of the main clinker phases in portland cements: part i, neat cements, *Cem. Concr. Res.* 28 (1998) 1245–1257. [https://doi.org/10.1016/S0008-8846\(98\)00115-X](https://doi.org/10.1016/S0008-8846(98)00115-X).
- [17] J.I. Escalante-García, J.H. Sharp, Effect of temperature on the hydration of the main clinker phases in portland cements: part ii, blended cements, *Cem. Concr. Res.* 28 (1998) 1259–1274. [https://doi.org/10.1016/S0008-8846\(98\)00107-0](https://doi.org/10.1016/S0008-8846(98)00107-0).
- [18] T. Matschei, F.P. Glasser, Temperature dependence, 0 to 40°C, of the mineralogy of Portland cement paste in the presence of calcium carbonate, *Cem. Concr. Res.* 40 (2010) 763–777. <https://doi.org/10.1016/j.cemconres.2009.11.010>.
- [19] F. Deschner, B. Lothenbach, F. Winnefeld, J. Neubauer, Effect of temperature on the hydration of Portland cement blended with siliceous fly ash, *Cem. Concr. Res.* 52 (2013) 169–181. <https://doi.org/10.1016/j.cemconres.2013.07.006>.
- [20] T.T.H. Bach, C.C.D. Coumes, I. Pochard, C. Mercier, B. Revel, A. Nonat, Influence of temperature on the hydration products of low pH cements, *Cem. Concr. Res.* 42 (2012) 805–817. <https://doi.org/10.1016/j.cemconres.2012.03.009>.
- [21] M. Zajac, S.K. Bremseth, M. Whitehead, M. Ben Haha, Effect of  $\text{CaMg}(\text{CO}_3)_2$  on hydrate assemblages and mechanical properties of hydrated cement pastes at 40°C and 60°C, *Cem. Concr. Res.* 65 (2014) 21–29. <https://doi.org/10.1016/j.cemconres.2014.07.002>.
- [22] K.O. Kjellsen, R.J. Detwiler, O.E. GjØrv, Development of microstructures in plain cement pastes hydrated at different temperatures, *Cem. Concr. Res.* 21 (1991) 179–189. [https://doi.org/10.1016/0008-8846\(91\)90044-I](https://doi.org/10.1016/0008-8846(91)90044-I).
- [23] E. Gallucci, X. Zhang, K.L. Scrivener, Effect of temperature on the microstructure of calcium silicate hydrate (C-S-H), *Cem. Concr. Res.* 53 (2013) 185–195. <https://doi.org/10.1016/j.cemconres.2013.06.008>.
- [24] A.M. Gajewicz-Jaromin, P.J. McDonald, A.C.A. Muller, K.L. Scrivener, Influence of curing temperature on cement paste microstructure measured by  $^1\text{H}$  NMR relaxometry, *Cem. Concr. Res.* 122 (2019) 147–156. <https://doi.org/10.1016/j.cemconres.2019.05.002>.
- [25] F. Avet, K. Scrivener, Effect of temperature on the water content of C-A-S-H in plain Portland and blended cements, *Cem. Concr. Res.* 136 (2020) 106124. <https://doi.org/10.1016/j.cemconres.2020.106124>.
- [26] J.I. Escalante-García, J.H. Sharp, The microstructure and mechanical properties of blended cements hydrated at various temperatures, *Cem. Concr. Res.* 31 (2001) 695–702. [https://doi.org/10.1016/S0008-8846\(01\)00471-9](https://doi.org/10.1016/S0008-8846(01)00471-9).
- [27] K. De Weerd, M. Ben Haha, G. Le Saout, K.O. Kjellsen, H. Justnes, B. Lothenbach, The effect of temperature on the hydration of composite cements containing limestone powder and fly ash, *Mater. Struct.* 45 (2012) 1101–1114. <https://doi.org/10.1617/s11527-011-9819-5>.
- [28] B. Pichler, C. Hellmich, J. Eberhardsteiner, J. Wasserbauer, P. Termkhajornkit, R. Barbarulo, G. Chanvillard, Effect of gel–space ratio and microstructure on strength of hydrating cementitious materials: An engineering micro-mechanics approach, *Cem. Concr. Res.* 45 (2013) 55–68. <https://doi.org/10.1016/j.cemconres.2012.10.019>.
- [29] P. Termkhajornkit, Q.H. Vu, R. Barbarulo, S. Daronnat, G. Chanvillard, Dependence of compressive strength on phase assemblage in cement pastes: Beyond gel–space ratio — Experimental evidence and micromechanical modeling, *Cem. Concr. Res.* 56 (2014) 1–11. <https://doi.org/10.1016/j.cemconres.2013.10.007>.

- [30] M. Zajac, J. Skocek, S. Adu-Amankwah, L. Black, M. Ben Haha, Impact of microstructure on the performance of composite cements: Why higher total porosity can result in higher strength, *Cem. Concr. Compos.* 90 (2018) 178–192. <https://doi.org/10.1016/j.cemconcomp.2018.03.023>.
- [31] F. Avet, K. Scrivener, Investigation of the calcined kaolinite content on the hydration of Limestone Calcined Clay Cement (LC3), *Cem. Concr. Res.* 107 (2018) 124–135. <https://doi.org/10.1016/j.cemconres.2018.02.016>.
- [32] P. Wang, N. Li, L. Xu, Hydration evolution and compressive strength of calcium sulphoaluminate cement constantly cured over the temperature range of 0 to 80 °C, *Cem. Concr. Res.* 100 (2017) 203–213. <https://doi.org/10.1016/j.cemconres.2017.05.025>.
- [33] F. Bullerjahn, M. Zajac, M. Ben Haha, K.L. Scrivener, Factors influencing the hydration kinetics of ye'elimite; effect of mayenite, *Cem. Concr. Res.* 116 (2019) 113–119. <https://doi.org/10.1016/j.cemconres.2018.10.026>.
- [34] K. Scrivener, R. Snellings, B. Lothenbach, eds., *A practical guide to microstructural analysis of cementitious materials*, CRC Press, Boca Raton, 2016.
- [35] F. Georget, W. Wilson, K.L. Scrivener, edxia: Microstructure characterisation from quantified SEM-EDS hypermaps, *Cem. Concr. Res.* 141 (2021) 106327. <https://doi.org/10.1016/j.cemconres.2020.106327>.
- [36] R.S. Barneyback, S. Diamond, Expression and analysis of pore fluids from hardened cement pastes and mortars, *Cem. Concr. Res.* 11 (1981) 279–285. [https://doi.org/10.1016/0008-8846\(81\)90069-7](https://doi.org/10.1016/0008-8846(81)90069-7).
- [37] F. Zunino, K. Scrivener, The influence of the filler effect on the sulfate requirement of blended cements, *Cem. Concr. Res.* 126 (2019) 105918. <https://doi.org/10.1016/j.cemconres.2019.105918>.
- [38] L.G. Baquerizo, T. Matschei, K.L. Scrivener, M. Saeidpour, L. Wadsö, Hydration states of AFm cement phases, *Cem. Concr. Res.* 73 (2015) 143–157. <https://doi.org/10.1016/j.cemconres.2015.02.011>.
- [39] B. Lothenbach, L. Pelletier-Chaignat, F. Winnefeld, Stability in the system CaO–Al<sub>2</sub>O<sub>3</sub>–H<sub>2</sub>O, *Cem. Concr. Res.* 42 (2012) 1621–1634. <https://doi.org/10.1016/j.cemconres.2012.09.002>.
- [40] T. Matschei, B. Lothenbach, F.P. Glasser, The AFm phase in Portland cement, *Cem. Concr. Res.* 37 (2007) 118–130. <https://doi.org/10.1016/j.cemconres.2006.10.010>.
- [41] L. Nicoleau, E. Schreiner, A. Nonat, Ion-specific effects influencing the dissolution of tricalcium silicate, *Cem. Concr. Res.* 59 (2014) 118–138. <https://doi.org/10.1016/j.cemconres.2014.02.006>.
- [42] H.F.W. Taylor, *Cement chemistry*, 2nd ed, T. Telford, London, 1997.
- [43] V.M. John, M. Quattrone, P.C.R.A. Abrão, F.A. Cardoso, Rethinking cement standards: Opportunities for a better future, *Cem. Concr. Res.* 124 (2019) 105832. <https://doi.org/10.1016/j.cemconres.2019.105832>.
- [44] T.C. Powers, Structure and Physical Properties of Hardened Portland Cement Paste, *J. Am. Ceram. Soc.* 41 (1958) 1–6. <https://doi.org/10.1111/j.1151-2916.1958.tb13494.x>.
- [45] R.B. Perkins, C.D. Palmer, Solubility of ettringite (Ca<sub>6</sub>[Al(OH)<sub>6</sub>]<sub>2</sub>(SO<sub>4</sub>)<sub>3</sub> · 26H<sub>2</sub>O) at 5–75°C, *Geochim. Cosmochim. Acta.* 63 (1999) 1969–1980. [https://doi.org/10.1016/S0016-7037\(99\)00078-2](https://doi.org/10.1016/S0016-7037(99)00078-2).



## 5.7 Appendix

### Appendix 5-A: The formation of hydrates

The ettringite content of the investigated systems at different temperatures quantified by Rietveld analysis are shown in Fig. 5-23. Ettringite is slightly decreased at late age in the blended systems. At 60°C, a small amount of ettringite is formed in the LGC system, while it cannot be observed in the blended system. For the CSA system, the change of ettringite with time can be observed. Ettringite is increased as the hydration develops at 5 and 20°C. However, a significant decrease of ettringite is observed at 40 and 60°C after 28 days and 90 days of hydration, respectively.

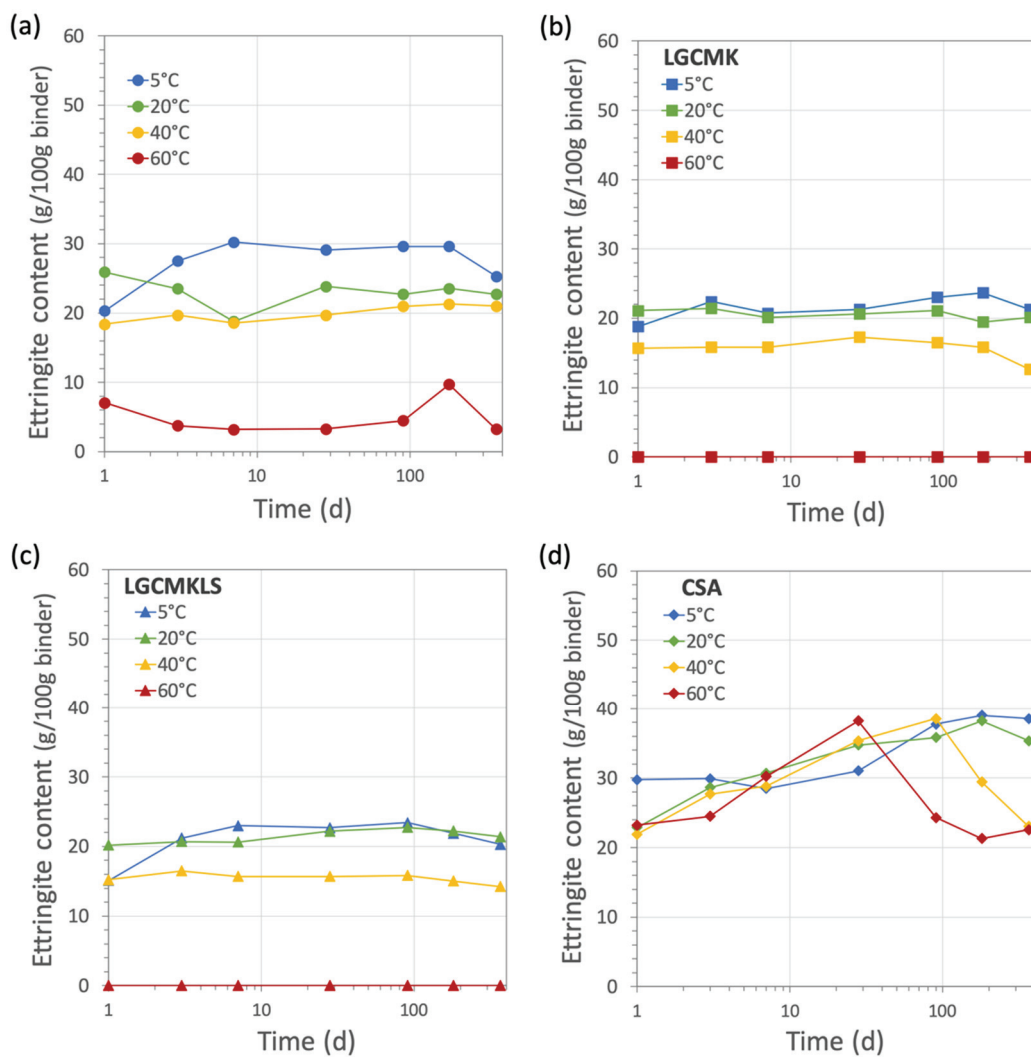


Fig. 5-23 Comparison of ettringite content at different temperatures of (a) LGC, (b) LGCMK, (c) LGCMKLS and (d) CSA.

The quantitative analysis of monosulfate at different temperatures are shown in Fig. 5-24. The amount of monosulfate in the PC system is related to the formation of ettringite. The content of monosulfate is relatively high when the ettringite content is low. The formation of monosulfate in the CSA system is shown in Fig. 5-24d. High content of monosulfate is formed after 1 day of hydration at the temperature above 5°C. It is quite constant after 90 days at 20

and 40°C. At 60°C, the content of monosulfate does not vary before 28 days and lower than 20 and 40°C. After 28 days of hydration, a significant increase of monosulfate formation is observed. Monosulfate forming at 5°C is increased with time.

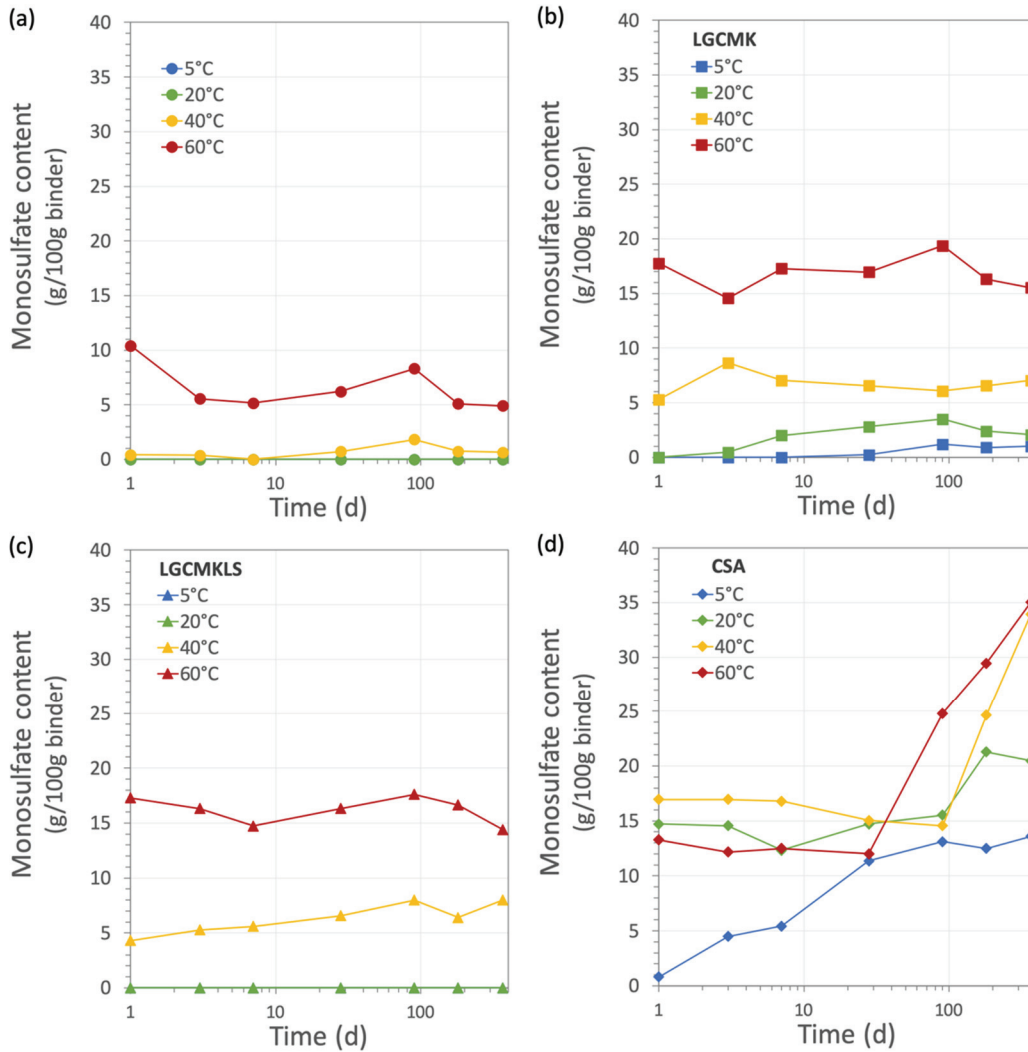


Fig. 5-24 Comparison of monosulfate content at different temperatures of (a) LGC, (b) LGCMK, (c) LGCMKLS and (d) CSA.

Fig. 5-25 shows the content of strätlingite formation of the higher alumina systems at different temperatures. Strätlingite in the PC system starts to form earlier than the CSA system. However, the amount of strätlingite at late age in the CSA system is significantly higher than the PC system after 28 days of hydration corresponding to high belite reaction.

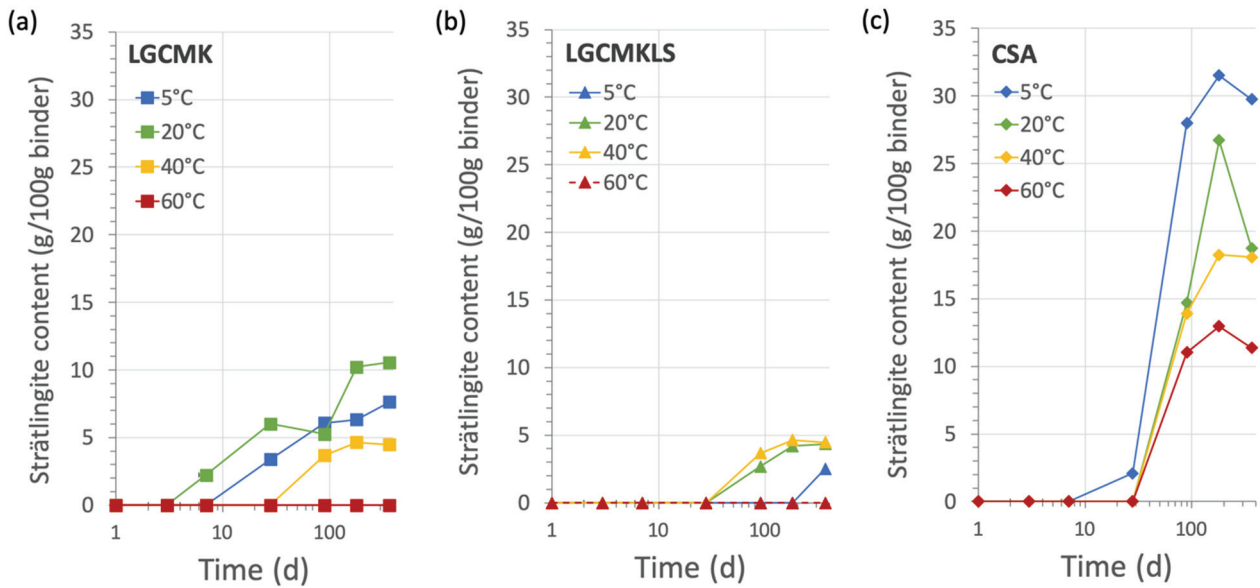


Fig. 5-25 Comparison of strätlingite content at different temperatures of (a) LGCMK, (b) LGCMKLS, and (c) CSA.

Portlandite is the main hydration product of calcium silicate phase. Portlandite content in the blended system is reduced due to the pozzolanic reaction from metakaolin. The amount of portlandite is low with increasing temperature because of higher DoR of metakaolin at high temperature, as shown in Fig. 5-26. At 5°C, portlandite content is initially increased, then dramatically dropped after 7 days of hydration. Similar trend between LGCMK and LGCMKLS is observed. The change of portlandite content comes from the competition between alite and metakaolin. After alite reaches 90% of DoH, faster portlandite consumption from metakaolin is observed, showing a drastic drop of portlandite content after 7 days of hydration.

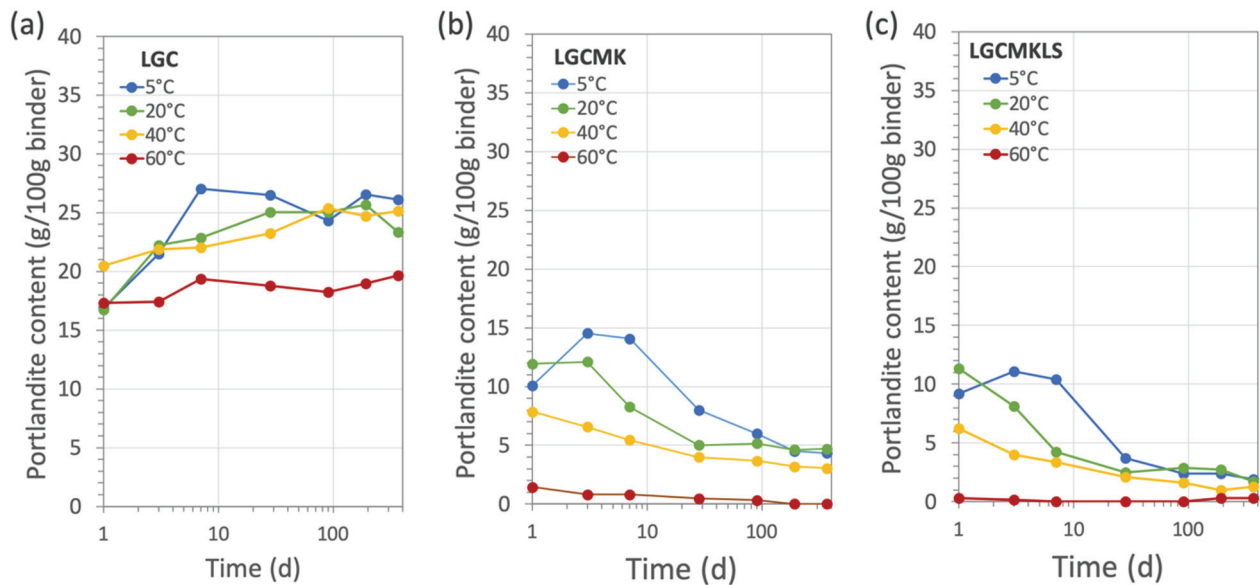


Fig. 5-26 Comparison of portlandite content at different temperatures of (a) LGC, (b) LGCMK and (c) LGCMKLS.

**Appendix 5-B:** the ion concentrations in the pore solution at 90 days

Ion concentrations in the pore solution at 90 days of the investigated systems at different temperatures are given in Table 5-5. The  $\text{OH}^-$  concentration was calculated from charge balance

The ion concentrations of S and Al in the pore solution of the investigated systems cured at different temperatures at 90 days of hydration are shown in Fig. 5-27. A significant increase of sulfate concentration (Fig. 5-27a) in the pore solution is observed in the PC system at 60°C, while it does not change in the CSA system. This can be explained by the increase of solubility of ettringite at high temperature [45]. Ettringite is present in the CSA system, but not the PC. The aluminium concentration (Fig. 5-27b) in the CSA is low at 5°C compared to the other temperature where the aluminium concentration is significantly higher than the PC blends.

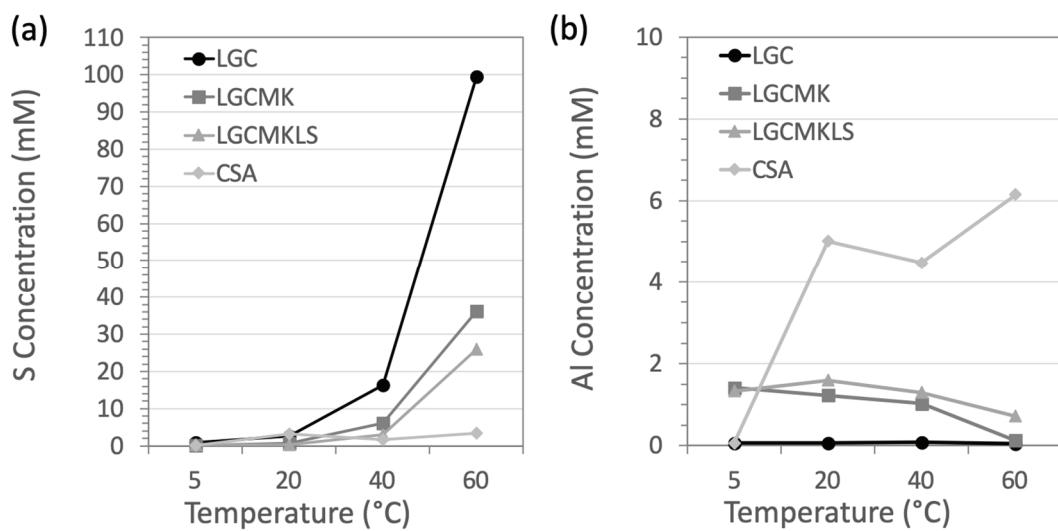


Fig. 5-27 The concentration of (a) S and (b) Al in the pore solution of the investigated systems at 5, 20, 40 and 60°C.

Table 5-5: Ion concentrations in the pore solution at 90 days of hydration of the investigated system at 5, 20, 40 and 60°C.

System	Temperature (°C)	Na (mM)	K (mM)	Ca (mM)	Si (mM)	S (mM)	Al (mM)	Cl (mM)	OH <sup>-</sup> (mM)
LGC	5	118.1	289.8	2.0	0.0	1.0	0.1	0.1	409.7
	20	124.1	281.0	1.8	0.0	2.6	0.1	0.1	403.5
	40	128.2	270.8	1.8	0.0	16.3	0.1	0.1	369.8
	60	136.1	278.7	3.5	0.0	99.4	0.0	0.1	222.8
LGCMK	5	67.4	109.0	1.3	0.2	0.2	1.4	0.1	177.0
	20	60.5	82.5	1.3	0.2	0.7	1.2	0.2	142.7
	40	42.7	60.3	1.0	0.3	6.1	1.0	2.3	89.3
	60	57.7	84.8	2.8	0.2	36.3	0.1	4.4	70.8
LGCMKLS	5	45.4	65.4	1.3	0.2	0.3	1.3	0.0	111.3
	20	41.0	53.1	1.1	0.2	0.4	1.6	0.1	93.6
	40	34.3	43.5	1.0	0.2	3.0	1.3	1.8	70.4
	60	46.5	64.5	1.0	0.2	25.9	0.7	3.8	56.6
CSA	5	37.4	0.6	7.1	0.0	0.1	0.1	0.7	51.1
	20	33.0	0.8	1.1	0.1	3.2	5.0	4.7	19.7
	40	27.4	0.2	0.8	0.1	1.7	4.5	4.8	16.4
	60	32.1	0.2	0.8	0.1	3.4	6.2	5.0	15.9

Fig. 5-28 exhibits the effective saturation indices of selected hydrates. It was calculated from the pore solution chemistry. The effective saturation indices globally agree well with the XRD result at 90 days. Some discrepancies are observed on the CSA systems. Strätlingite at 5°C is present in large quantities from the XRD data, while the effective saturation indices of strätlingite is in the range of undersaturation. Moreover, AH<sub>3</sub> at 60°C is at the equilibrium stage but no AH<sub>3</sub> is observed by XRD.

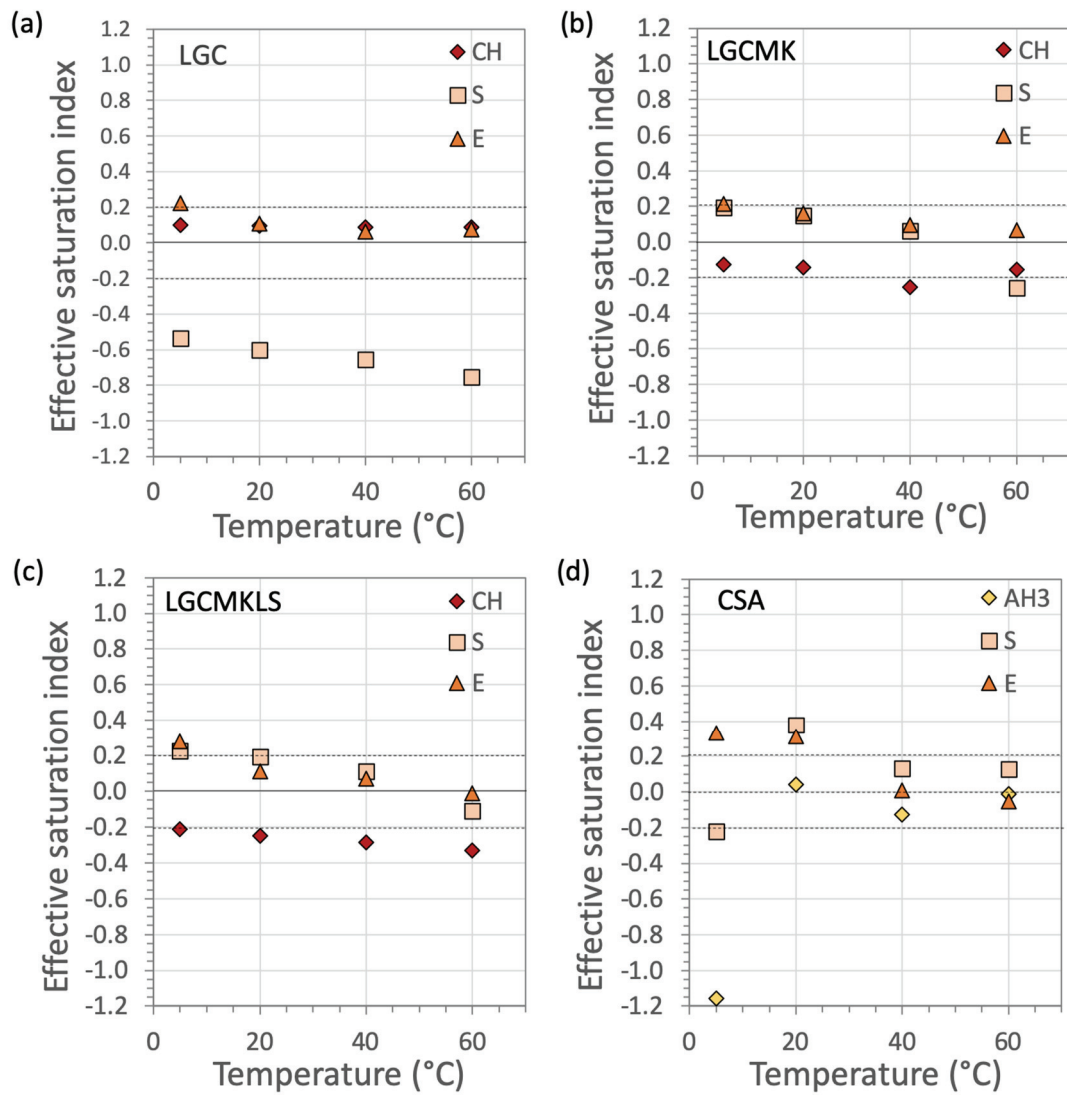


Fig. 5-28 Effective saturation indices of hydrate phases in (a) LGC, (b) LGCMK, (c) LGCMKLS and (d) CSA calculated from ion concentration of pore solution at 90 days: CH = portlandite, S = strätlingite, E = ettringite, AH<sub>3</sub> = aluminium hydroxide

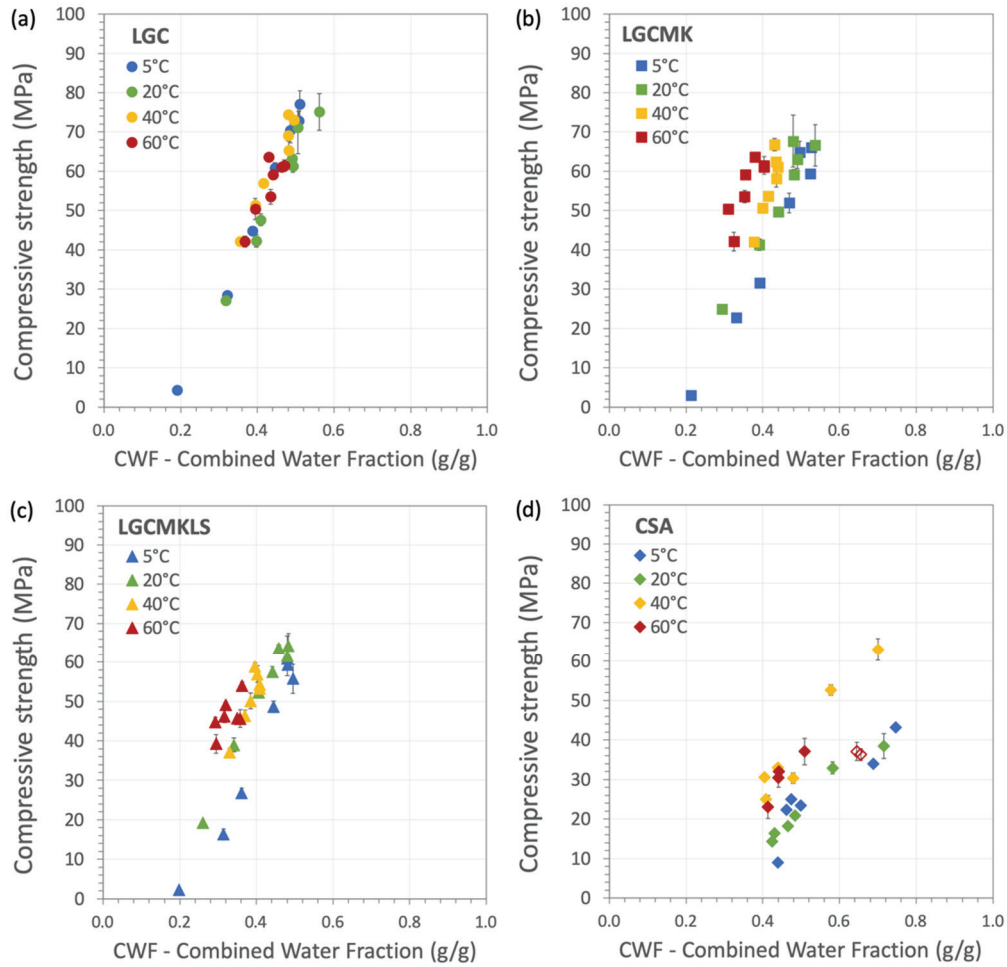
**Appendix 5-C: Relationship between combined water fraction (CWF) and compressive strength separated by the systems**

Fig. 5-29 Comparison of combined water fraction (CWF) and compressive strength calculated by TGA: (a) LGC, (b) LGCMK, (c) LGCMKLS and (d) CSA.

# Chapter 6 Transport properties

**Note:** This chapter is based on an article in preparation for submission to a peer reviewed journal.

Contribution of the doctoral candidate: Writing of the first manuscript draft, experimental design, conduction of the experiment.

## Abstract

The chloride ingress in cementitious systems with higher alumina content was studied by electro-migration and bulk diffusion. Two different higher alumina systems, Portland cement blended with metakaolin and calcium sulfoaluminate cement with high belite (CSA), were studied at different curing temperatures of 5, 20, 40 and 60°C. Durability indicators such as the pore solution conductivity, the porosity, and the effective conductivity are compared to the chloride ingress. The higher alumina system, with the presence of metakaolin, shows good resistivity of chloride ingress in the cement paste when compared to OPC. For PC-based cement, the mini migration method gives a good indication of performance in the bulk diffusion test which normally takes 6 months to 1 year. The setup for the CSA has to be developed to give conditions more representative to the bulk diffusion test and to be more reliable. The relation between the effective properties, and the durability indicators are non-trivial when comparing these systems.

**Keywords:** Metakaolin, Limestone, Calcium sulfoaluminate cement, Temperature, Chloride ingress, Chloride migration, Bulk conductivity, Pore solution conductivity, Porosity.



---

**CONTENTS**

---

<b>Chapter 6</b>	<b>Transport properties.....</b>	<b>133</b>
6.1	Introduction .....	135
6.2	Materials and methods .....	136
6.2.1	Raw materials characterization .....	136
6.2.2	Mix design and preparation.....	137
6.2.3	Methods.....	139
6.3	Results.....	144
6.3.1	Chloride penetration depth .....	144
6.3.2	Effective diffusion coefficient ( $D_{eff}$ ).....	147
6.3.3	Effective conductivity ( $\sigma_{eff}$ ) .....	147
6.3.4	Electrical conductivity and ion concentrations of pore solution .....	148
6.3.5	Formation factor and tortuosity .....	151
6.4	Discussion.....	153
6.4.1	Role of $OH^-$ concentrations in the sample .....	153
6.4.2	Effective conductivity in metakaolin blended systems.....	154
6.4.3	Relationship between effective conductivity and $D_{eff}$ .....	154
6.4.4	Relationship between effective conductivity at 180 days, $D_{eff}$ at 28 days and chloride penetration depth.....	155
6.5	Conclusions .....	157
6.6	References.....	158
6.7	Appendix .....	160

---

## 6.1 Introduction

Low CO<sub>2</sub> binders become more interesting in cement research [1]. One approach to lower embodied CO<sub>2</sub> is to blend Portland cement with supplementary cementitious materials (SCMs) [2] (PC based system). Another approach is an alternative binder called calcium sulfoaluminate cement (CSA) which contains ye'elimite as the main reactive clinker phase. A common feature of these new types of cement is that they have higher alumina content when compared to Portland cement. This impacts the hydration kinetics, phase assemblages and microstructure, as shown in Chapter 3-5. The pore solution chemistry, in particular the pH, is also affected which has a major effect for the transport properties [3]. This leads to a change of the resistance with respect to several durability issues which are important to be studied before using these new formulations as commercial products.

Chloride ingress is one of the main causes of the de-passivation and corrosion of steel reinforcement leading to degradation of concrete structures [4]. It is known that the use of SCMs improves the resistance to chloride ion transport in concrete; this is usually attributed to the porosity refinement. In addition, several studies have reported a high capacity of chloride binding in the metakaolin blends due to the chemical binding of Friedel's salt formation [5–7] and a physical binding of C-A-S-H [8]. CSA also forms the AFm phase as a main hydration product which can bind the free chlorides in the pore solution [9]. Moreover, the pH level in CSA (BYF type) was found to be sufficient to passivate carbon steel [10,11]. Therefore, these higher alumina systems potentially have good chloride resistance.

The determination of the chloride penetration in cement by the bulk diffusion test requires time, typically 6 months or more to obtain measurements. Recently, Wilson et. al proposed a mini migration method to estimate the effective diffusion coefficients at the cement paste scale which shorten the experimental time to 14 days [12]. Many types of binders, including metakaolin-limestone blends, were studied, but they were all Portland cement-based systems and were cured at the same temperature. A few studies on chloride ingress in CSA have been reported only at 20°C [13,14].

The objectives of this study are to compare the mini migration method to the bulk diffusion method and to verify the capability of these two approaches to assess the chloride ingress in cement paste. Different types of cement paste, PC-base and CSA-base cements, cured at different temperatures were studied. In addition, the correlation between different parameters: the effective diffusion coefficient, the chloride penetration depth, the effective conductivity, the pore solution conductivity, the ions concentrations, the pore connectivity were explored.

## 6.2 Materials and methods

### 6.2.1 Raw materials characterization

The raw materials used in the PC system are a light grey cement (LGC), metakaolin (MK), limestone (LS) and a chemical grade gypsum (GS). For the CSA system, a laboratory prepared belite-ye'elimite (BY) clinker, anhydrite and a laboratory prepared mayenite (MY) were used as raw materials. The synthesis of the clinker is described in Chapter 2. The chemical composition and particle size value of these materials determined by X-Ray fluorescence (XRF) and laser diffraction (Malvern MasterSizer S) are given in Table 6-1. The phase composition quantified by XRD is shown in Table 6-2.

Table 6-1: Chemical composition and particle size value of the raw materials

PSD	LGC	MK	LS	BY clinker	Anhydrite	MY
Dv,10	1.26	0.54	2.27	0.54	2.7	0.25
Dv,50	8.44	5.13	7.71	4.34	8.41	8.97
Dv,90	24.37	20.17	19.3	15.88	29.88	31.75
XRF (wt.%)						
SiO <sub>2</sub>	22.4	52.0	0.11	18.9	2.5	0.1
Al <sub>2</sub> O <sub>3</sub>	3.8	43.8	0.00	20.9	0.6	50.1
Fe <sub>2</sub> O <sub>3</sub>	1.2	0.3	0.04	0.0	0.3	0.1
CaO	65.6	0.0	56.2	53.1	38.7	47.6
MgO	0.8	0.0	0.15	0.1	1.9	-
SO <sub>3</sub>	3.3	0.1	0.03	6.4	52.2	0.1
K <sub>2</sub> O	0.7	0.1	0.01	-	0.2	-
Na <sub>2</sub> O	0.2	0.3	0.06	0.1	0.1	0.1
TiO <sub>2</sub>	0.2	1.5	0.01			
P <sub>2</sub> O <sub>5</sub>	0.1	0.2	0.00	0.0	0.0	0.0
Others	0.0	0.1	0.00	0.0	0.2	0.0
*LOI	1.1	1.5	43.4	0.6	3.4	1.2
Sum	99.6	100.0	100.0	100.0	100.2	99.4

\*LOI = Loss of ignition

Table 6-2: Phase composition of the raw materials

XRD (wt.%)	LGC	MK	LS	BY clinker	Anhydrite	MY
C <sub>3</sub> S	60.6	-	-	-	-	-
C <sub>2</sub> S	21.5	-	-	59.6	-	-
C <sub>3</sub> A	9.1	-	-	-	-	1.9
C <sub>4</sub> AF	1.4	-	-	-	-	-
C <sub>4</sub> A <sub>3</sub> \$	-	-	-	40.4	-	-
C <sub>12</sub> A <sub>7</sub>	-	-	-	-	-	97.5
CA	-	-	-	-	-	0.6
Dolomite	-	-	-	-	6.9	-
Portlandite	-	-	-	-	0.1	-
Calcite	1.5	-	99	-	-	-
Dolomite	0.7	-	0.7	-	-	-
Gypsum	0.2	-	-	-	2.5	-
Anhydrite	4.7	-	-	0.1	77.7	-
Quartz	0.3	-	0.3	-	2.3	-
Metakaolin	-	94.2	-	-	1.2	-
Rutile	-	-	-	-	8.5	-
Anatase	-	1.2	-	-	0.7	-
Mullite	-	4.6	-	-	-	-
Muscovite	-	-	-	-	-	-
Cristobalite	-	-	-	-	-	-
Sum	100.0	100.0	100.0	100.1	99.9	100.0

## 6.2.2 Mix design and preparation

The systems investigated in this study are divided in two main groups; the PC system and the CSA system. In the PC system, there are three subsystems; LGC, LGCMK and LGCMKLS. The LGC system is used as a reference system. The CSA system is composed of a BY clinker blended with anhydrite with anhydrite to ye'elinite molar ratio of 1:1. A small amount of mayenite was added to accelerate the ye'elinite reaction [15] to give the main reaction during 6 – 12 hours at 20°C. The water to binder ratio (w/b) in this study was fixed at 0.6. The mixed proportions are given in Table 6-3.

Table 6-3: Composition of the investigated systems (% mass).

Materials	LGC	LGCMK	LGCMKLS	CSA
LGC	97	76	66	0
MK	0	20	20	0
LS	0	0	10	0
GS	3	4	4	0
BY	0	0	0	89.1
Anhydrite	0	0	0	10.5
MY	0	0	0	0.4

The binders and deionized water were equilibrated overnight at the intended curing temperature before mixing. A small amount of admixture, polycarboxylate (PCE), was added into the distilled water before equilibration at the curing temperature to control the workability of the cement paste only for the PC based systems. The dry powders were blended with a laboratory benchtop mixer at 1200 rpm for 1 minute, then water added and mixed at 1600 rpm for 2 minutes. After the high-shear mixing, a vacuum mixing at 450 rpm was applied to remove the air bubble entrapped in the cement pastes. The cement pastes were gently transferred into 50 ml cylindrical polypropylene containers under sealed condition with a few drops of distilled water on top of the paste to keep saturated conditions during curing. The samples were stored at 5, 20, 40 and 60°C for at least 20h before demoulding. The samples cured at 5°C were demoulded at 48h due to the slow reaction and setting. Then, the samples were kept under saturated condition with some small pieces of the same paste added at the bottom of each container to prevent leaching and to obtain the curing condition of their own pore solution (see Fig. 6-1). The samples were then maintained at the original curing temperatures until testing.

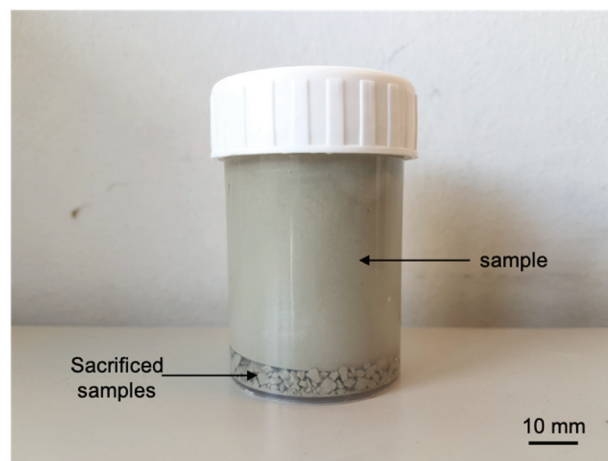


Fig. 6-1 Sample curing for transport property test.

## 6.2.3 Methods

### 6.2.3.1 Bulk diffusion test

After curing in the pore solution for 28 days, the sides of the cylindrical cement paste samples were abraded and allowed to surface dry for about 1 hour before coating. The rough surface was created to help epoxy attached to the surface of the sample. The samples were coated with epoxy resin (ARALDIT GY 250) and dried for 24 hours. About 2 mm of the bottom of the cylinder were cut off to open the cement paste surface and allow unidirectional penetration of chloride. The samples were fully immersed separately between the PC systems and the CSA systems in a plastic container with a 0.5M NaCl solution for 6 and 9 months. The samples were divided into two groups. The first group was exposed to the 0.5M NaCl solution at room temperature. The other group was exposed to the 0.5M NaCl solution at the same temperature as for curing (5, 40 and 60°C). In this study, the samples cured at 20°C and exposed at room temperature are noted as the 20°C data. The solutions were regularly changed every month, except in the 7<sup>th</sup> month due to the COVID restrictions (only the PC system).

The samples were taken out from the solution and cut with a dry blade in a longitudinal direction. The sample pieces were hand ground on silicon carbide paper with 150, 300 and 500 grits always moving parallel to the surface to maintain the chloride profile in the sample. After grinding, the freeze-drying method was used to stop the hydration. The samples were wrapped with a piece of tissue and kept in a zip lock bag before storing in the freezer at -85°C for at least 24 hours, then transferred to a freeze dryer for at least 48 hours.

A simple method of silver nitrate colorimetric indicator was used in this study to measure the free chloride penetration depth in cement paste. 0.1N AgNO<sub>3</sub> was sprayed on the surface of the sample. The boundary between white and brown areas could be well distinguished. The white area is a precipitation of silver chloride indicating the presence of free chloride in the sample. In the brown area, the silver ions react with the hydroxyl to form a brown precipitate which is assumed as the chloride free area. After 1 hour, the chloride penetration depth (d) was measured as shown in Fig. 6-2. The average value from 5 measurements at every 5 mm along with the chloride front is reported. In principle, micro-XRF should be used to obtain a better quantification. However, the equipment became unavailable due to failure and the COVID crisis. Therefore, this semi-quantitative approach was used as a practical replacement.

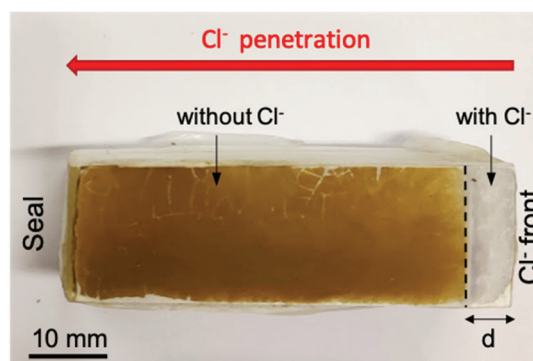


Fig. 6-2 The sample after applying 0.1N AgNO<sub>3</sub> on the surface. The chloride penetration depth (d) was measured at the white and brown boundary.

### 6.2.3.2 Mini-migration test

The setup of the mini-migration experiment and its justification are given in detail in [12]. The schematic of estimation of the effective chloride diffusion coefficient ( $D_{eff}$ ) from the mini-migration test is shown in Fig. 6-3.

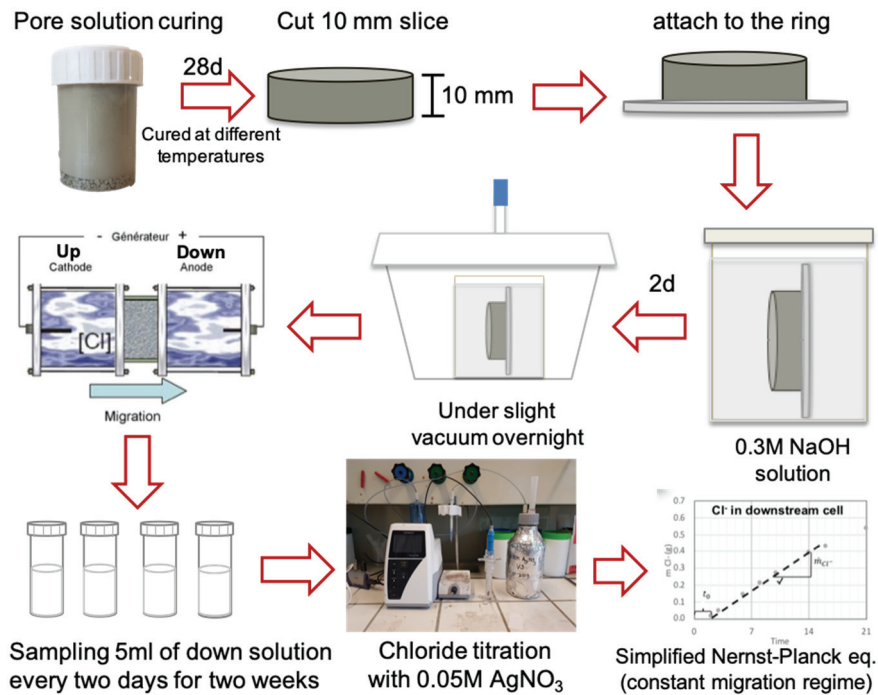


Fig. 6-3 Schematic of estimation of the effective chloride diffusion coefficient ( $D_{eff}$ ) from mini-migration test.

After curing for 28 days at 5, 20, 40 and 60°C of hydration in saturated condition, the samples were cut in a disc shape 10mm thick and 33mm diameter. They are kept in wet tissue to prevent surface drying. The two surfaces of the sample were lightly ground with some drops of water and the residue on the surface was removed by ultrasonic bath for 30 seconds. The samples were dried for 15 min before mounting in a plastic ring with silicone, as shown in Fig. 6-4. After coating the sides of the sample, the mounted sample was stored in a humidity chamber to prevent the surface drying of the samples. They were immersed in a 0.3M NaOH solution for 48 hours under slight vacuum. The two reservoirs were attached together with the mounted sample in the middle and the two rubber rings were held in between. A 0.5M NaCl and 0.3M NaOH solution was used in the upstream reservoir, while a 0.3M NaOH solution was used in the downstream reservoir to limit the leaching of alkalis. The upstream and downstream reservoirs were filled with the solution at the same time. The setup of the mini-migration cell is shown in Fig. 6-5.

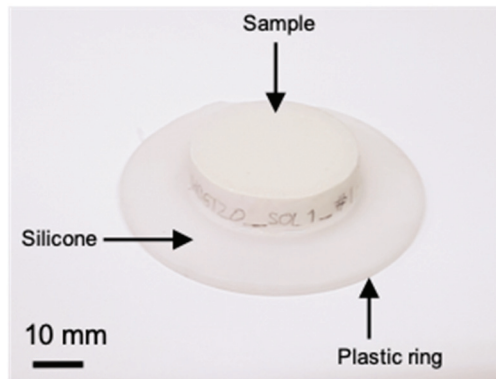


Fig. 6-4 A sample mounted with a plastic ring by silicone

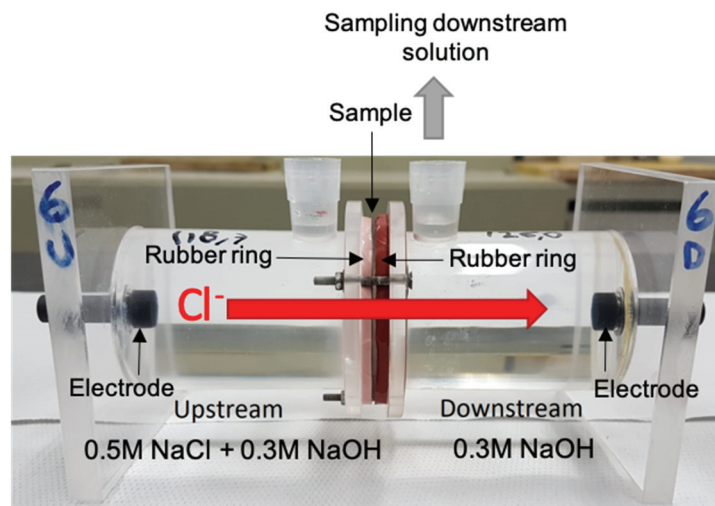


Fig. 6-5 The setup of mini-migration test

The applied voltage in each system is shown in Table 6-4. The voltage of each sample was adjusted to obtain an initial current between 5 – 25 mA. The applied voltage was then kept constant during 24h. The voltage used controls the time for the experiment. The actual voltage was measured in the solution across the sample at the beginning and the end of the test. It is lower by about 2.5V than the applied voltage due to a loss of potential at the electrodes. The actual voltage of each specimen is considered for the  $D_{\text{eff}}$  calculation (see Equation 6-1). The applied voltage for LGC and CSA was generally similar for the sample cured at the different temperatures and lower than for the blended systems. The voltage used for the blended systems varied depending on the curing temperature.



Table 6-4 The applied voltage (V) of each system for the mini migration test

Systems	Applied voltage (V)			
	5°C	20°C	40°C	60°C
LGC	4	5	4	4
LGCMK	8	13	12	20
LGCMKLS	8	13	12	20
CSA	4.5	3	3	4.5

The current curves (shown in Appendix A) during the mini migration tests were continuously monitored by the logging instrument (Squirrel Data Logger, Grant Instruments). The minimum of the current indicates the breakthrough time of chloride from the upstream to the downstream reservoir. Moreover, it can provide an estimation of the time of the end of the constant migration regime which is the region of interest for  $D_{\text{eff}}$  calculation.

These two parameters, the voltage and the current, are the main parameters that have to be monitored for the initial setup, and during the first 24 hours. The applied voltage can accelerate or slow down the flow of chloride which affects the total time of the experiment. The voltage needs to be chosen to ensure that the steady state migration regime can be captured by sampling every 1 – 2 days during the experimental time (14 days).

The  $D_{\text{eff}}$  was calculated from the evolution of chloride concentration in the downstream compartment. The 5 ml of the solution in the downstream reservoir was sampled every 2-4 days to analyse the flow of chlorides and a fresh 5ml of 0.3M NaOH solution was added to the downstream reservoir to balance the level of the solution. The sampling solutions from the downstream reservoir were titrated with a TitroLine® 5000 using 0.05M  $\text{AgNO}_3$  solution to obtain the chloride mass as a function of time as shown in Fig. 6-6. The standard solution of 0.1M NaCl was used for the calibration. The time that the chloride from the upstream reservoir breaks through the sample to the downstream reservoir is given as  $t_0$ . Only the points in the constant migration regime are considered. The slope indicates the chloride flow rate that is used for the  $D_{\text{eff}}$  calculation. After the constant migration regime, the chloride flow gradually reduced with time due to reaction at the electrodes.

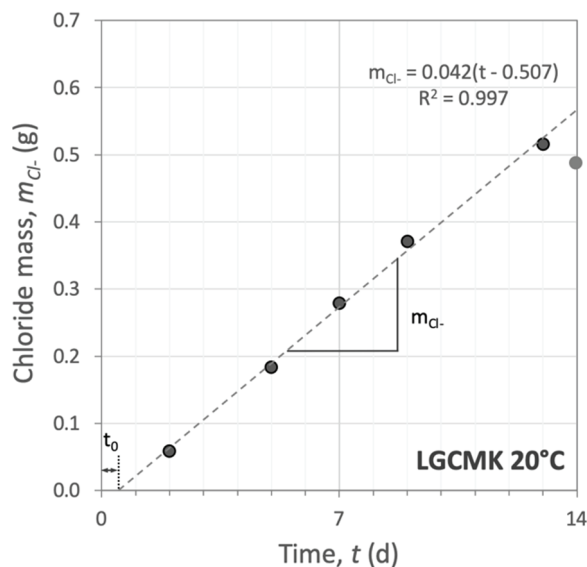


Fig. 6-6 A typical result of the evolution of chloride mass obtained by the chloride titration from the downstream sampling solution as a function of time.

The effective chloride diffusion coefficient ( $D_{\text{eff}}$ ) was estimated with a simplified Nernst-Planck equation for transport in solution:

Equation 6-1: 
$$D_{\text{eff}} = \frac{J_{\text{down}}}{c_{\text{up}}} \frac{RT}{F} \frac{l}{\Delta E}$$

where  $D_{\text{eff}}$  is the chloride effective diffusion coefficient,  $c_{\text{up}}$  is the chloride concentration in the upstream reservoir ( $\text{mol}/\text{m}^3$ ),  $R$  is the gas constant,  $T$  is the temperature (K),  $F$  is the Faraday constant,  $l$  is the specimen thickness (m),  $\Delta E$  is the voltage drop across the specimen (V) and  $J$  is the chloride flux through the sample ( $\text{mol}/\text{m}^2\text{s}$ ).  $J$  can be determined by the slope of chloride mass,  $\dot{m}_{\text{Cl}^-}$  (g/s) obtained from the chloride titration of the downstream reservoir solution as a function of time:

Equation 6-2: 
$$J_{\text{down}} = \frac{1}{S} \cdot \frac{\dot{m}_{\text{Cl}^-}}{M_{\text{w,Cl}^-}}$$

where  $S$  is the surface area of the sample ( $\text{m}^2$ ),  $M_{\text{w,Cl}^-}$  is the molar mass of chloride (g/mol).

The measure gives an effective diffusion coefficient. The “effective” means that it is a property of the material (solid skeleton, and pore network filled with the pore solution), in principle, independent of the boundary conditions and geometry of the sample.

### 6.2.3.3 Bulk resistivity measurement

The samples were cured at different temperatures in the pore solution until the test date. The same samples were measured with the bulk resistivity as a function of time. The samples were equilibrated at room temperature for 1 hour before the measurement. The bulk resistivity ( $\rho_b$ ) was measured with a method adapted from ASTM C1876 [16] for cement pastes cured in pore solution. A Giatec RCON2 instrument was used at 1 kHz on cylindrical cement paste samples with smaller electrodes fabricated as downscaled replicates of the RCON2 electrodes for concrete. After the measurement, the samples were kept in the same curing condition. The effective conductivity,  $\sigma_{\text{eff}}$ , was calculated using Equation 6-3.

Equation 6-3: 
$$\sigma_{\text{eff}} = \frac{1}{\rho_b} = \frac{l}{RA}$$

where  $l$  is the length of the specimen,  $R$  = electrical resistance of a uniform specimen and  $A$  is the cross-sectional area of the specimen.

#### 6.2.3.4 Analysis of pore solution

The pore solutions of the hardened samples were extracted by the steel die method [17] using pressures up to 250 N/mm<sup>2</sup>. The solutions were filtered immediately with nylon filters (0.45 $\mu$ m). The pH values and conductivity were measured directly after the extraction. The pH electrode was calibrated against KOH solutions with known concentrations. The conductivity was calibrated with a saturated NaCl solution. The concentrations of Na, K, Ca, Si, S, Al and Cl were determined with a Dionex DP ICS-3000 ion chromatography in samples diluted by a factor 10, 100 and 1000 depending on the ion concentration. Standards from 0.1 – 50 mg/L were used. The relative error of the measurements was < 10%. The hydroxide concentrations of the pore solutions were calculated from the charge balance of the ions

#### 6.2.3.5 Mercury intrusion porosimetry (MIP)

The critical pore diameter and the total porosity was measured by mercury intrusion porosimetry (Micromeritics AutoPore IV 9500 porosimeter). A slice of about 1 g of hardened paste samples at 90 days was polished on every side of the surface to remove the carbonated area and broken into 4 to 5 pieces. Then, the small pieces of sample were placed in a glass dilatometer. A pressure for the intrusion was applied up to 440 MPa. A contact angle of 140° was assumed between mercury and the cement paste.

### 6.3 Results

#### 6.3.1 Chloride penetration depth

The average chloride penetration depth obtained after 9-months (PC based systems) and 6-months (CSA) exposure time in the bulk diffusion test are shown in Fig. 6-7 and Table 6-5. Since the diffusion depends on temperature, two sets of exposure temperature in 0.5M NaCl solution (at room temperature and the same as the curing temperature) were analysed. The 20°C sample of LGCMKLS and the CSA exposed at 60°C cracked during the sample preparation. Therefore, these two samples could not be measured.

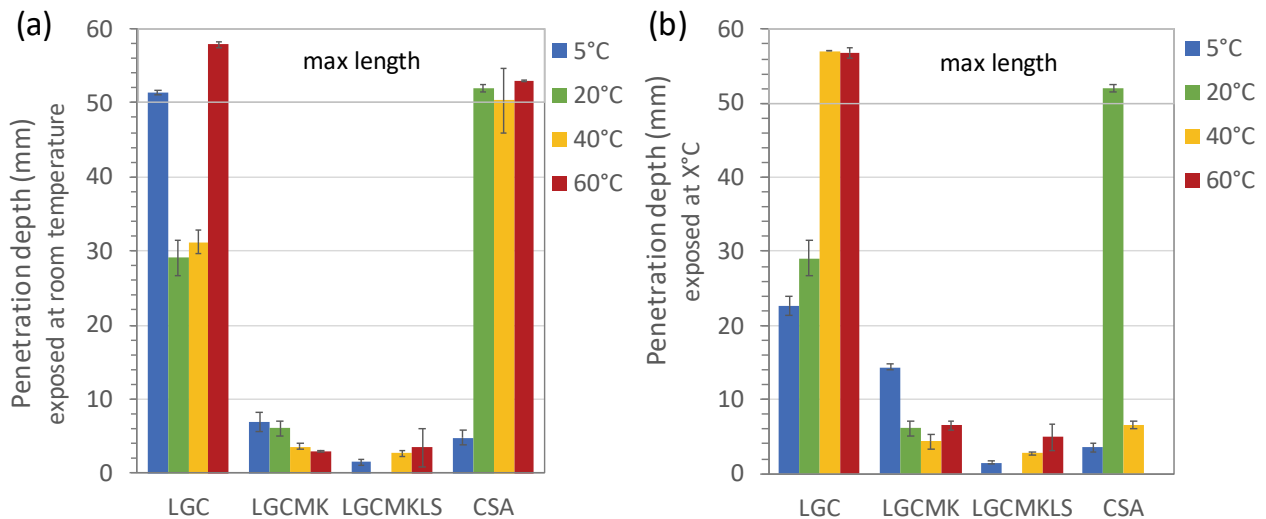


Fig. 6-7 Chloride penetration depth cured in a saturated condition for 28 days and exposed in 0.5M NaCl solution at (a) room temperature and (b) the same curing temperature of the investigated systems for 9 months for the PC system and 6 months for the CSA system.

Fig. 6-7 shows the chloride penetration depth for the systems tested at room temperature (Fig. 6-7a) and at the same curing temperature (Fig. 6-7b). The samples are not all the same maximum length, therefore the maximum depth considered here is 50 mm. In certain cases, the chloride penetrates through the samples. The blended systems are generally good resistance to chloride (low penetration depth). The LGC and CSA systems have much more chloride penetration. Temperature of the testing seems to have hardly differences for the blended systems. There is a lot of variation between the two sets of the experiment on the LGC system, but particularly in the CSA system. In the CSA system, it is clear that part of this variation was the tendency for cracking. For example, Fig. 6-8 shows the CSA sample cured and exposed at 60°C which has cracking and big heterogeneity. Even though chloride has penetrated through the sample, there are still some big areas where there is no chloride (the brown area). There is no visual crack in the other specimens.

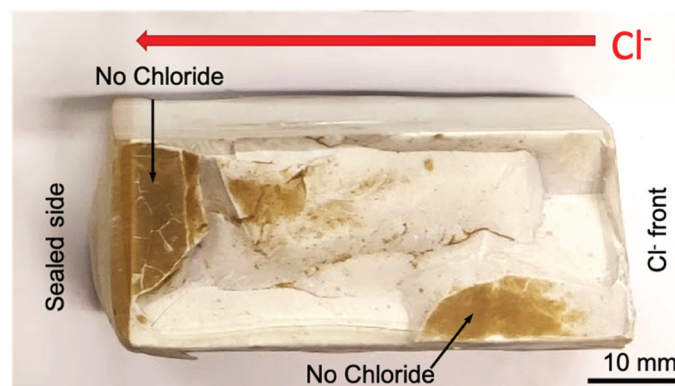


Fig. 6-8 The crack samples of the CSA system cured and exposed at 60°C after applied AgNO<sub>3</sub> on the surface of the sample. The area without chloride can be observed in some parts.

Table 6-5 Chloride penetration depth in the bulk diffusion test of the investigated systems

Curing temperature	Exposure temperature	Exposure time (m)	Systems	Average penetration depth (mm)	Standard deviation	Max length (mm)
5°C	5°C	9	LGC	22.7	1.3	57.0
		9	LGCMK	14.4	0.4	60.0
		9	LGCMKLS	1.5	0.2	59.0
		6	CSA	3.52	0.6	48.0
5°C	20°C	9	LGC	51.4	0.4	56.8
		9	LGCMK	6.9	1.3	60.0
		9	LGCMKLS	1.5	0.4	54.5
		6	CSA	4.8	1.1	55.0
20°C	20°C	9	LGC	29.1	2.4	58.0
		9	LGCMK	6.1	1.0	59.0
		9	LGCMKLS	n.d.	n.d.	n.d.
		6	CSA	51.9	0.5	51.9
40°C	40°C	9	LGC	57	0.0	57.0
		9	LGCMK	4.4	1.0	57.3
		9	LGCMKLS	2.8	0.2	59.0
		6	CSA	6.6	0.5	56.0
40°C	20°C	9	LGC	31.2	1.5	57.0
		9	LGCMK	3.6	0.4	56.3
		9	LGCMKLS	2.7	0.4	58.0
		6	CSA	50.3	4.3	54.0
60°C	60°C	9	LGC	56.9	0.7	58.0
		9	LGCMK	6.5	0.6	60.0
		9	LGCMKLS	4.9	1.8	57.0
		6	CSA	n.d.	n.d.	n.d.
60°C	20°C	9	LGC	57.8	0.3	57.8
		9	LGCMK	3	0.1	60.3
		9	LGCMKLS	3.5	2.6	52.5
		6	CSA	52.9	0.1	52.9

n.d. = not determined as cracked during sample preparation

### 6.3.2 Effective diffusion coefficient ( $D_{\text{eff}}$ )

The mini-migration method from [12] was applied in this study. It is a quasi-steady state electromigration method to measure the effective diffusion coefficient [12] calculated from the flux of chloride species according to Equation 6-2. The  $D_{\text{eff}}$  of the investigated systems cured at different temperatures with the same set up are compared.

After curing the sample for 28 days of hydration in the saturated condition at different temperatures, the mini migration test was carried out at room temperature. The average of the two duplicates of each sample is reported in Fig. 6-9. The presence of metakaolin in the blended systems significantly lowers  $D_{\text{eff}}$  when compared to LGC, especially for the samples cured at 60°C. Two types of behaviour are observed in the CSA system. The  $D_{\text{eff}}$  of the samples cured at 20 and 40°C is in the range of LGC, while the  $D_{\text{eff}}$  of the samples cured at 5 and 60°C are low similar to the blended systems. The significant scatter observed for the CSA system could be again related to the variation in the stable phases, in particular at 60°C (where monosulfate and C-S-H are dominant) compared to the mini-migration test carried out at room temperature where ettringite and strätlingite are stabilised, resulting in small cracks. How the microstructure and the pore network are developed are important for the  $D_{\text{eff}}$ . Temperature was found to have a higher influence on the microstructure of the CSA system than the LGCMK system as reported in Chapter 5.

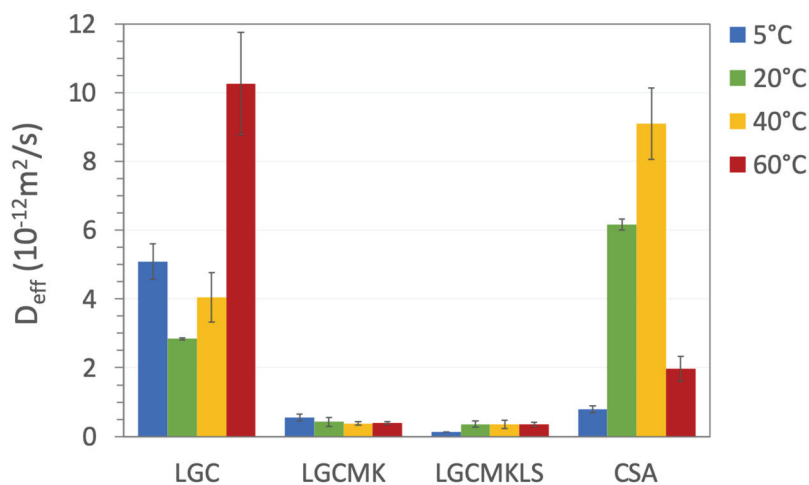


Fig. 6-9 Effective diffusion coefficient of the investigated systems cured in the saturated condition at 5, 20, 40 and 60°C for 28 days of hydration. The test was carried out at room temperature for all the sample.

### 6.3.3 Effective conductivity ( $\sigma_{\text{eff}}$ )

The effective conductivity was calculated from the bulk resistivity measurement. Fig. 6-10 illustrates the effective conductivity of the investigated systems cured at 5, 20, 40 and 60°C as a function of time. LGC shows a high range of effective conductivity at all temperatures compared to the higher alumina systems. The effective conductivity of LGC is in a similar range at all temperatures. Only the 40°C sample shows an increase of effective conductivity with time, while the 5 and 20°C sample show a decrease with time which could correspond to ongoing hydration in these samples. In the presence of metakaolin, the effective conductivity shows a dramatic drop after 7 days of hydration at 5°C, while the effective conductivity of the blended systems cured at 20°C decreases slightly after 7 days. The samples cured at 40 and 60°C present a very low range of effective conductivity over time compared to the other systems. A similar trend can be observed in the CSA system. However, the effective conductivity of CSA is slightly higher (almost double) than the LGCMK system at late age.

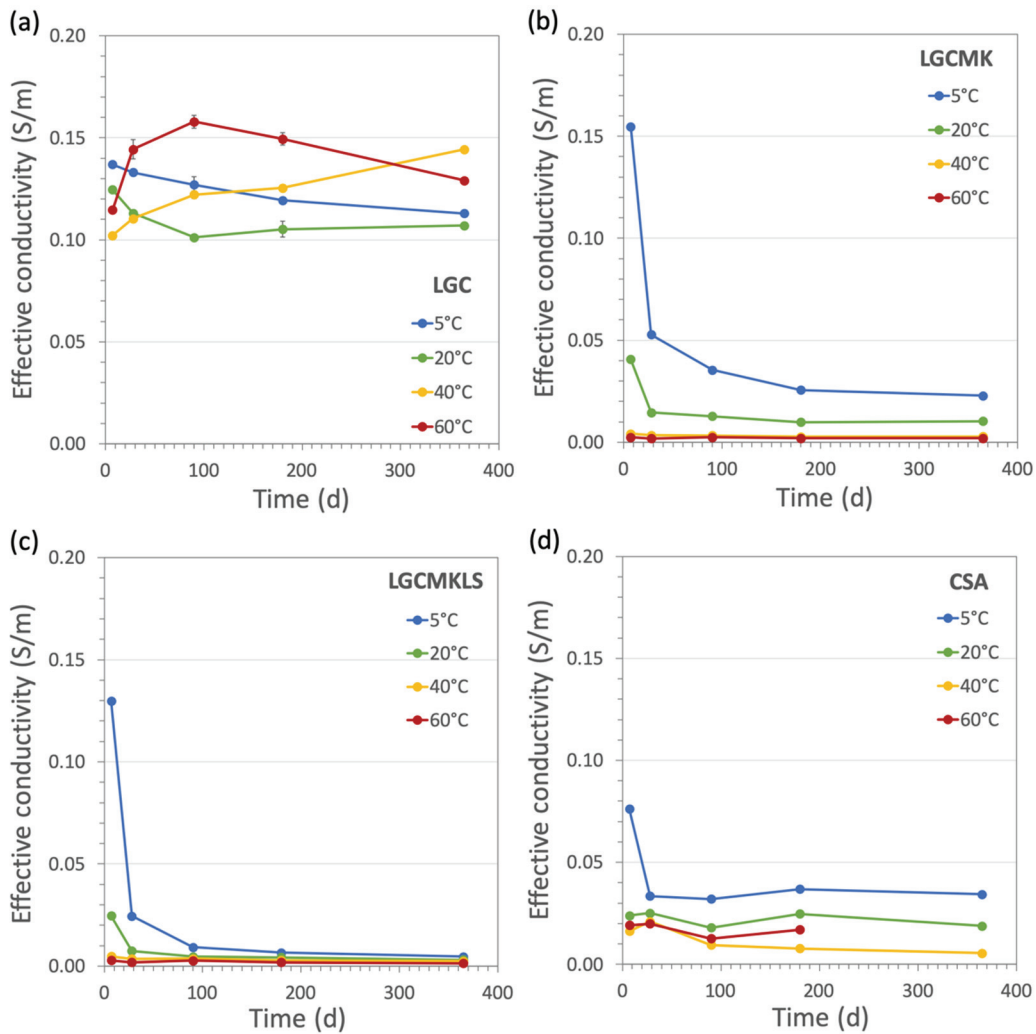


Fig. 6-10 Effective conductivity of (a) LGC, (b) LGCMK, (c) LGCMKLS and (d) CSA cured at 5, 20, 40 and 60°C as a function of time.

### 6.3.4 Electrical conductivity and ion concentrations of pore solution

Pore solutions of the investigated systems cured at different temperatures were analysed at 90 days of hydration. Number of ions in the pore solution controls the conductivity. It is dominated by the  $\text{OH}^-$  ions as shown in Fig. 6-11. In general, pore solution conductivity has a linear correlation to the  $\text{OH}^-$  concentration. A slight shift from the trend can be observed at 60°C due to the higher sulfate concentration, which is due to the higher solubility of ettringite at this temperature (see Chapter 5). Therefore, the pore solution conductivity can be roughly estimated from the  $\text{OH}^-$  concentration.

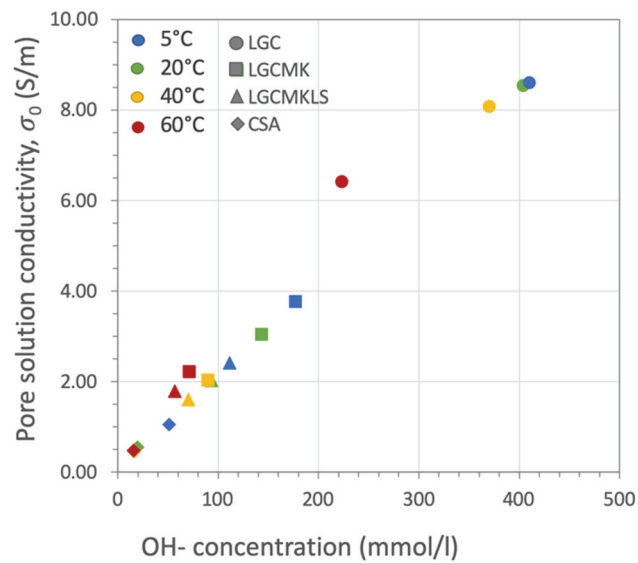


Fig. 6-11 Pore solution conductivity ( $\sigma_0$ ) as a function of OH<sup>-</sup> concentration of pore solution.

Fig. 6-12 shows that the electrical conductivity of pore solution in LGC is higher than the higher alumina systems. This indicates that the LGC system has more conductive ions such as alkalis (Na and K) and hydroxide (OH<sup>-</sup>) in the pore solution when compared to the higher alumina systems. The alkalis in the PC systems come mainly from the LGC cement. A small amount of alkalis is also found in metakaolin (Table 6-1). For the blended systems, the electrical conductivity of pore solution in LGCMKLS is slightly lower than LGCMK due to lower cement content in LGCMKLS. The difference between LGCMK and LGCMKLS is higher at low temperature. CSA shows the lowest range of electrical conductivity of pore solution. When temperature is increased, the electrical conductivity of the pore solution of the LGC system is decreased, significantly at 60°C. The higher alumina systems show the decrease of electrical conductivity of pore solution up to 40°C. It is slightly increased at 60°C.

The concentration of OH<sup>-</sup> in pore solution as a function of temperature is plotted in Fig. 6-12b. The OH<sup>-</sup> concentration is decreased when the temperature is increased, more significantly in the LGC system. CSA has much lower OH<sup>-</sup> concentration than the PC system leading to low effective conductivity and electrical conductivity of pore solution by default. For the LGC system, a strong decrease of OH<sup>-</sup> at 60°C may relate to sulfate release due to destabilization of ettringite.



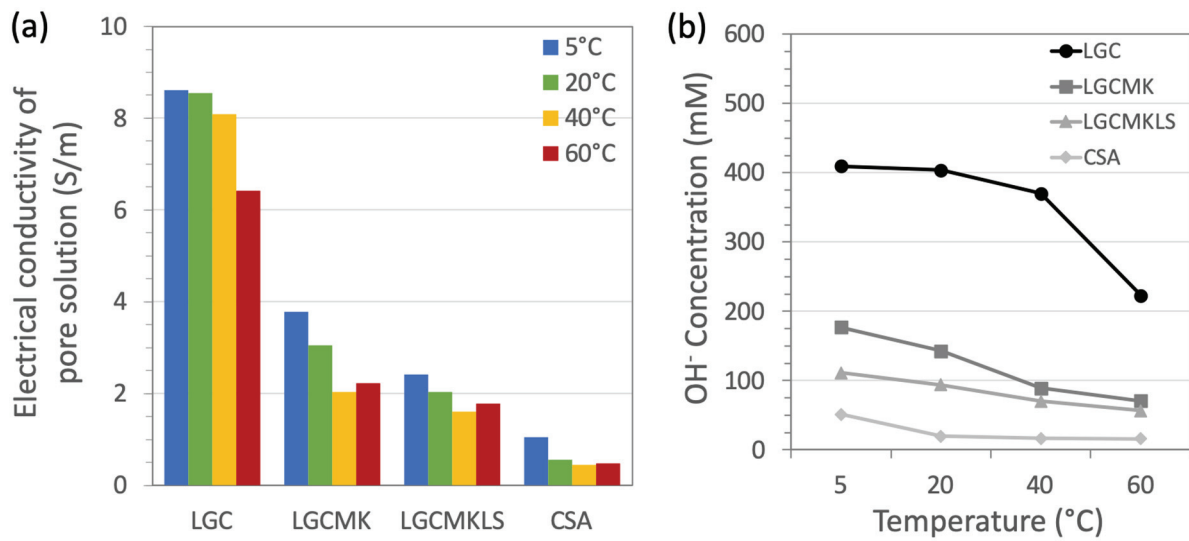


Fig. 6-12 (a) Electrical conductivity and (b) OH<sup>-</sup> concentration of pore solution of LGC, LGCMK, LGCMKLS and CSA cured at different temperatures.

Table 6-6 shows the measured ion concentrations of pore solution cured at different temperatures at 90 days of hydration. In LGC, the alkali ion concentrations (Na, K) in pore solution are slightly increased at elevated temperature. The higher alumina systems show a decrease in alkalis concentration in the pore solution when temperature is increased up to 40°C, but it is slightly increased at 60°C. This could potentially be related to the presence of more C-S-H, the main alkali binding phase [18], due to a higher MK reaction at higher temperature shown in Chapter 3. In contrast to the alkali concentrations, the OH<sup>-</sup> concentrations decrease in all systems with temperature as the sulfate and chloride concentrations increase with temperature.

Due to impurities in the raw materials used, some chloride is present in all cements. In the higher alumina systems, the chloride and sulfate concentrations in the pore solution before exposure are increased with increasing temperature indicating a destabilisation of Friedel's salt at higher temperature. In fact, the solubility of Friedel's salt (and ettringite) increases with temperature, while the solubility of monosulfate remains rather constant [6,19], such that less Friedel's salt and ettringite but more monosulfate is present at higher temperature (see Chapter 3 and 4). As a result, more chloride and sulfate are present in the pore solution at higher temperature. Friedel's salt is better stabilized in the system containing high calcium [7], thus lower chloride concentrations are observed in the LGC system.

Table 6-6 The ion concentrations in the pore solution of the PC and CSA systems cured at 5,20, 40 and 60°C at 90 days. OH<sup>-</sup> was estimated by charge balance.

Sample	Temp (°C)	Ion concentrations (mmol/l)					
		Na	K	Ca	Cl	SO <sub>4</sub>	OH <sup>-</sup>
LGC	5	118.1	289.8	2.0	0.1	1.0	409.7
	20	124.1	281.0	1.8	0.1	2.6	403.5
	40	128.2	270.8	1.8	0.1	16.3	369.8
	60	136.1	278.7	3.5	0.1	99.4	222.8
LGCMK	5	67.4	109.0	1.3	0.1	0.2	177.0
	20	60.5	82.5	1.3	0.2	0.7	142.7
	40	42.7	60.3	1.0	2.3	6.1	89.3
	60	57.7	84.8	2.8	4.4	36.3	70.8
LGCMKLS	5	45.4	65.4	1.3	0.0	0.3	111.3
	20	41.0	53.1	1.1	0.1	0.4	93.6
	40	34.3	43.5	1.0	1.8	3.0	70.4
	60	46.5	64.5	1.0	3.8	25.9	56.6
CSA	5	37.4	0.6	7.1	0.7	0.1	51.1
	20	33.0	0.8	1.1	4.7	3.2	19.7
	40	27.4	0.2	0.8	4.8	1.7	16.4
	60	32.1	0.2	0.8	5.0	3.4	15.9

### 6.3.5 Formation factor and tortuosity

To be able to decouple the effects of pore solution and pore structure, the formation factor was calculated [20]. The formation factor ( $F$ ) is defined as the resistivity of bulk ( $\rho_b$ ) cement paste divided by the resistivity of the pore solution ( $\rho_0$ ) [20]. The resistivity is the inverse,  $1/\sigma$ , of the conductivity ( $\sigma$ ).

Equation 6-4: 
$$F = \frac{\rho_b}{\rho_0}$$

This formation factor normalizes the influence of the pore solution on chloride transport. It was originally developed to represent only the geometrical constraints of pore networks in rocks. By assuming that the effect of the geometrical constraints and the pore solution are independent, the following can be assumed:

Equation 6-5: 
$$\frac{D_{eff}}{D_0} = \frac{\sigma_{eff}}{\sigma_0}$$

where  $D_0$  represents the diffusion coefficient in the pore solution. It can be written as

Equation 6-6:

$$D_{eff} = \frac{D_0}{F}$$

The inverse formation factor can therefore be directly related to the diffusion coefficient.

The blended systems have low inverse formation factors, especially at high temperature, see Fig. 6-13, while LGC and CSA present higher inverse formation factors, such that a high effective diffusivity can be expected for these two systems.

The formation factor ( $F$ ), is the “tortuosity” ( $\tau$ ) normalised by the porosity ( $\phi$ ) [12]:

Equation 6-7:

$$F \equiv \frac{\rho_b}{\rho_0} = \frac{\sigma_0}{\sigma_{eff}} \cong \frac{\tau}{\phi}$$

The “tortuosity” is considered to represent the geometrical constraint of the pore network on the diffusion path. However, its physical interpretation is difficult for non-trivial pore networks [12]. As a first approximation, it can be viewed as a multiplication factor, encompassing all other interactions between the pore solution and the solid. The porosity in this study is taken from the MIP porosity, which is used to measure the connected paths for transport property (in dried samples). Fig. 6-14 illustrates that the blended systems have higher tortuosity (hence lower estimated diffusivities) than the LGC and CSA systems. These increase as a function of temperature. Even though the blended systems have a low electrical conductivity of pore solution at 90 days, the difference of this factor between LGC and the blended systems is only 2-3 times, but the bulk conductivity of the blended system is lower than the LGC system by approximately 5 times. It means that the pore structure and its surface are the major factors governing the effective conductivity. From the MIP result in Chapter 5, the total porosity increases with temperature, but the “tortuosity” is also increased. Thus, the tortuosity of the blended system is a more important factor that lowers the effective conductivity.

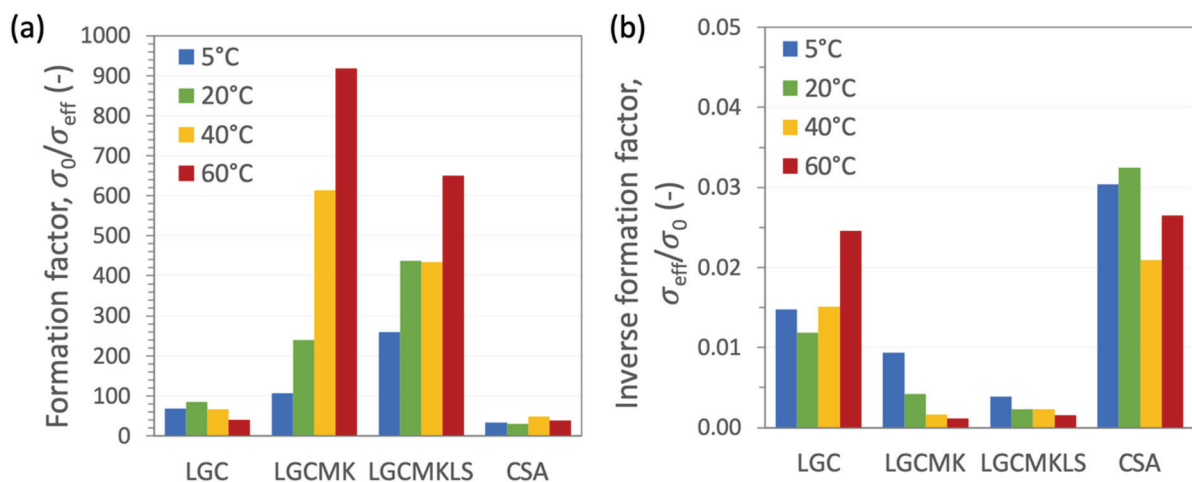


Fig. 6-13 (a) Formation factor and (b) inverse formation factor calculated by conductivity.

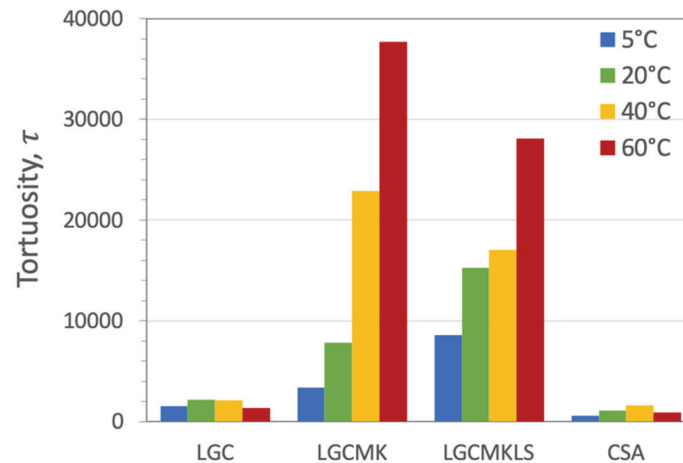


Fig. 6-14 Tortuosity (defined by Equation 6-7) of the investigated systems at different temperatures.

## 6.4 Discussion

The comparison of the higher alumina systems shows that the metakaolin blends have good chloride resistance compared to LGC and CSA, based on the penetration depth, mini migration and electrical conductivity. CSA provides some inconsistent data between the experiments compared to the PC based system, for example the penetration depth measurement can be good, as well as the diffusion coefficient measurement by mini-migration. However, the results of CSA vary dramatically with the temperature, and the presence of cracks. Therefore, some correlations of different parameters were explored to be able to discover the relationship between microstructure and properties and have a better understanding on the chloride ingress of different types of cement.

### 6.4.1 Role of OH<sup>-</sup> concentrations in the sample

CSA has a lower pH (~12 at 23°C) than the PC based systems (> 12.5 mainly due to their high alkali content). This effect is especially distinct here because of the use of laboratory prepared clinker with no added alkali. The concentration of OH<sup>-</sup> ions has a particularly strong effect on the high electrical conductivity.

For the bulk diffusion experiment, the samples were cured under conditions saturated with pore solution. Therefore, the effective conductivity of the CSA is low by default (see Fig. 6-10). To be able to evaluate the CSA system in a similar pH range to the PC system, a CSA sample was cast with the w/b ratio of 0.6 at 20°C, then cured in 0.3M NaOH solution after the first day of hydration. The effective conductivity was measured at 28 days of hydration. The effect of OH<sup>-</sup> ion on the effective conductivity is shown in Fig. 6-15 for the CSA system. The effective conductivity is dramatically increased when the sample is cured in the NaOH solution. This indicates that the OH<sup>-</sup> concentration is an important factor for the effective conductivity measurement. The effective conductivity is not a straightforward method to compare the different systems when the pH or the OH<sup>-</sup> concentration is very different. Similar curing conditions can be used in different pH systems but the effect of alkali on phase assemblage and hydration of the lower pH system should be considered [21–23].

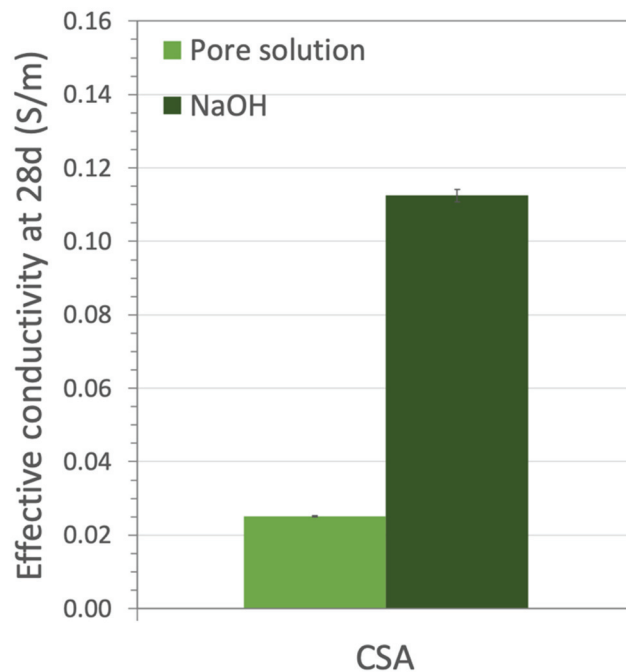


Fig. 6-15 The increase of effective conductivity value of CSA cured in 0.3M NaOH compared to pore solution curing measured at 28 days.

#### 6.4.2 Effective conductivity in metakaolin blended systems

The effective conductivity in the metakaolin blended systems show a drastic drop after 7 days of hydration at 5°C (see Fig. 6-10b and Fig. 6-10c). This probably corresponds to the metakaolin reaction. Moreover, the reaction degree of metakaolin increases with increasing temperature. The low effective conductivity at high temperature is probably related to the metakaolin contribution that may reduce critical pore entry as discussed in Chapter 5. Further investigation on metakaolin reaction and microstructure is needed to better understand the contribution of metakaolin to the transport properties [12,24].

#### 6.4.3 Relationship between effective conductivity and $D_{eff}$

Conductivity and diffusion are both related to the mobility of ions in the pore structure. The relationship between these two parameters are plotted shown in Fig. 6-16. W. Wilson et al. found a general relationship of the effective conductivity and the  $D_{eff}$  when the curing temperature was carried out at 20°C [12]. In this study, different curing temperatures were applied for 28 days and the mini-migration experiment was carried out at room temperature. Therefore, many parameters such as hydration kinetics, phase assemblages and microstructure development have to be considered because the hydration continues during the 14 days of the mini-migration experiment. The hydration of the sample cured at high or low temperature might follow a different hydration path during the mini migration at room temperature. From Fig. 6-16, three groups of the relationship can be observed: 1) the group of LGC shows high effective conductivity and high  $D_{eff}$ , 2) the blended systems have low diffusivity which tends to have good chloride resistance, in agreement with [7] and 3) the group of CSA all show a low effective conductivity but high  $D_{eff}$  as the measurements were carried out in the different conditions. In the effective conductivity measurement, the samples were measured in the pore solution curing which has low  $OH^-$  concentration. For the mini migration experiment,

the samples were immersed in high  $\text{OH}^-$  concentration (0.3M NaOH). In fact, the value of the effective conductivity of the CSA sample cured in 0.3M NaOH (the empty green diamond) is shifted towards higher effective conductivity. There is a general trend, however, there is not a clear relationship between the effective conductivity and the  $D_{\text{eff}}$  when the effect of temperature is involved.

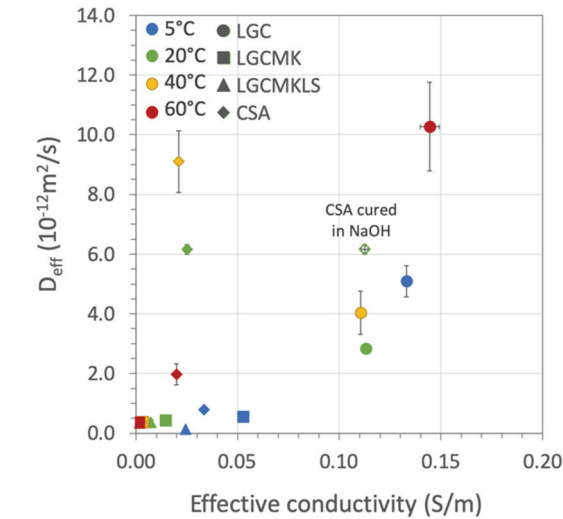


Fig. 6-16 The relationship between the effective conductivity and the effective diffusion coefficient,  $D_{\text{eff}}$ , from the mini migration test of the investigated systems at 28 days.

#### 6.4.4 Relationship between effective conductivity at 180 days, $D_{\text{eff}}$ at 28 days and chloride penetration depth

The effective conductivity samples were cured at different temperatures; hence they can be compared to the chloride penetration depths obtained from the samples exposed at different temperatures to compare similar microstructures. The relationship between effective conductivity after 180 days and the chloride penetration depth is shown in Fig. 6-17a. In the plot, the samples in the range of maximum length for penetration depth experiment are marked by a grey box. There are some correlations in the PC based systems between these two factors but there is a large scatter probably due to the low precision of chloride penetration depth measurement. No clear trends can be observed for the CSA cements.

Since the mini migration test was carried out at room temperature, the chloride penetration depth exposed at room temperature data are used for the comparison. Fig. 6-17b illustrates the relationship between  $D_{\text{eff}}$  and the chloride penetration depth. The data points in the max length region are not considered. From Fig. 6-17b, there is a correlation between the  $D_{\text{eff}}$  and the penetration depth which looks clearer than the relation between the effective conductivity and the penetration depth presented in Fig. 6-17a but the data points are quite scattered. Therefore, the  $D_{\text{eff}}$  can be used as a rough indicator of the real exposure condition at similar exposure temperature. However, due to the scarcity of the data, this relationship is ensured for the CSA system. It needs to be investigated more on samples more resistant to cracking.

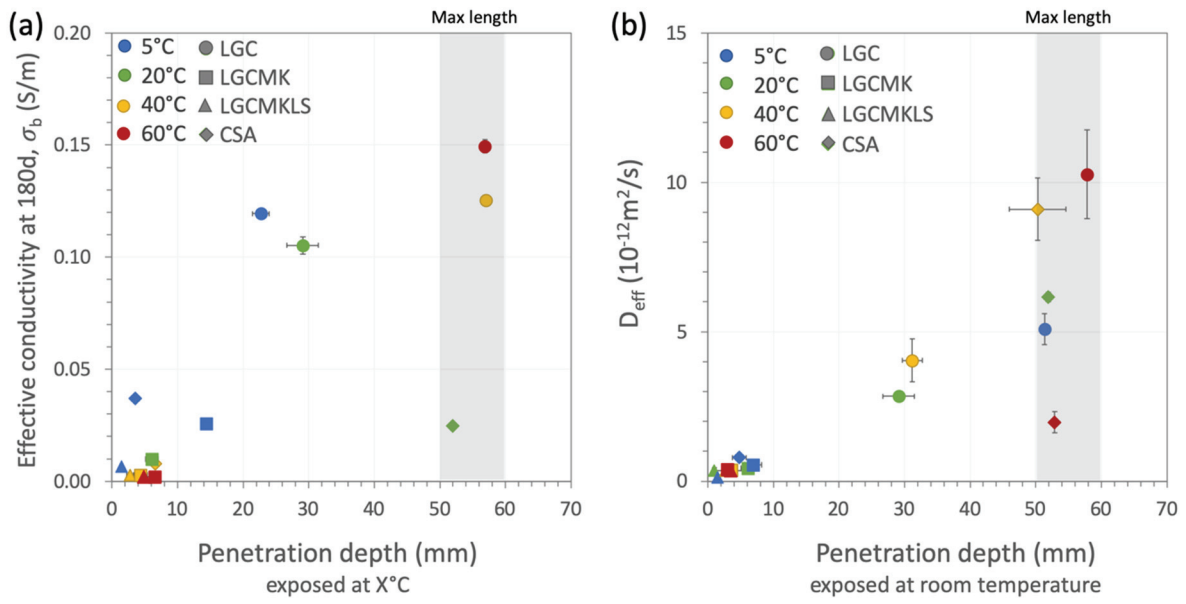


Fig. 6-17 Relationship between (a) the penetration depth (9 months for the PC systems, 6 months for the CSA system) exposed at different temperature and the effective conductivity at 180d and (b) the penetration depth and the effective diffusion coefficient ( $D_{eff}$ ) exposed at room temperature of the investigated systems.

## 6.5 Conclusions

The transport properties and chloride ingress in cement paste in different types of binders were investigated by effective conductivity measurement, mini migration test and the bulk diffusion methods at different curing temperatures. In this study, the relationships between bulk diffusion result, chloride ingress result and the microstructure features were explored. The main conclusions are summarized as follows:

- From bulk diffusion experiment, the higher alumina system shows good chloride ingress resistance when the temperature is kept constant, probably because they have a higher binding capacity due to the presence of more AFm phases. In those cases, where the samples were initially hydrated at 5, 40 or 60°C, but bulk diffusion was measured at room temperature, much higher chloride ingress was observed for the CSA systems, which could be related to phase changes and cracking. Further investigation is needed. The dimension stability of the CSA system should be optimized to avoid cracking during a long duration of testing.
- Temperature does not have a strong influence on the performance of metakaolin blended systems. However, a lot of variation is observed in LGC and, particularly in CSA which could be due to the cracking.
- Higher chloride concentrations in the pore solution at high temperature in the higher alumina systems is observed due to a higher solubility of Friedel's salt at high temperature. Therefore, low chloride resistance at high temperature could be related to the two factors: higher diffusivity and lower chloride binding capacity.
- The mini migration method can be used as a rough indicator on the chloride resistance, however, it is not well adapted to low pH clinker. The effective conductivity can be used to compare across the system which has a similar range of pH as effective conductivity depends strongly on the ionic strength and, especially on OH<sup>-</sup> which is a good charge carrier. To be able to compare between the different types of binder, it is more representative to use the bulk diffusion method, but the binders have to be resistant to shrinkage and expansion.
- To be able to relate the effective conductivity and the effective chloride diffusion coefficient ( $D_{eff}$ ), the curing conditions of the effective conductivity and the solution that use in the mini migration test should be similar, indicating that the mini migration setup for low pH range needs to be further refined (see Appendix 6C).
- The change of the temperature between the curing and the mini migration experiment complicates the decoupling of the parameters. Since the mini migration test is not instantaneous, the hydration continues at a different temperature than the curing state, leading to changes in phase assemblages and microstructure and possibly cracking. The PC based system has a slower phase evolution after 28 days. In the CSA system, a significant change on phase assemblage is observed after 28 days due to the late reaction of belite. Therefore, the test should be carried out when the phase is stable. In the case of CSA, the phase assemblage is stable at a much later age, probably at 180 days of hydration. Hence, the mini migration method at 28 days can only be a rough estimation.



## 6.6 References

- [1] E. Gartner, H. Hirao, A review of alternative approaches to the reduction of CO<sub>2</sub> emissions associated with the manufacture of the binder phase in concrete, *Cem. Concr. Res.* 78 (2015) 126–142. <https://doi.org/10.1016/j.cemconres.2015.04.012>.
- [2] B. Lothenbach, K. Scrivener, R.D. Hooton, Supplementary cementitious materials, *Cem. Concr. Res.* 41 (2011) 1244–1256. <https://doi.org/10.1016/j.cemconres.2010.12.001>.
- [3] Y. Elakneswaran, A. Iwasa, T. Nawa, T. Sato, K. Kurumisawa, Ion-cement hydrate interactions govern multi-ionic transport model for cementitious materials, *Cem. Concr. Res.* 40 (2010) 1756–1765. <https://doi.org/10.1016/j.cemconres.2010.08.019>.
- [4] I. Bertolini, B. Elsener, P. Pedeferri, E. Redaelli, R.B. Polder, *Corrosion of Steel in Concrete: Prevention, Diagnosis, Repair*, John Wiley & Sons, 2003. <https://doi.org/10.1002/3527603379>.
- [5] U.A. Birnin-Yauri, F.P. Glasser, Friedel's salt, Ca<sub>2</sub>Al(OH)<sub>6</sub>(Cl,OH)·2H<sub>2</sub>O: its solid solutions and their role in chloride binding, *Cem. Concr. Res.* 28 (1998) 1713–1723. [https://doi.org/10.1016/S0008-8846\(98\)00162-8](https://doi.org/10.1016/S0008-8846(98)00162-8).
- [6] M. Balonis, B. Lothenbach, G. Le Saout, F.P. Glasser, Impact of chloride on the mineralogy of hydrated Portland cement systems, *Cem. Concr. Res.* 40 (2010) 1009–1022. <https://doi.org/10.1016/j.cemconres.2010.03.002>.
- [7] Z. Shi, M.R. Geiker, K. De Weerd, T.A. Østnor, B. Lothenbach, F. Winnefeld, J. Skibsted, Role of calcium on chloride binding in hydrated Portland cement–metakaolin–limestone blends, *Cem. Concr. Res.* 95 (2017) 205–216. <https://doi.org/10.1016/j.cemconres.2017.02.003>.
- [8] H. Maraghechi, F. Avet, H. Wong, H. Kamyab, K. Scrivener, Performance of Limestone Calcined Clay Cement (LC3) with various kaolinite contents with respect to chloride transport, *Mater. Struct.* 51 (2018) 125. <https://doi.org/10.1617/s11527-018-1255-3>.
- [9] G. Paul, E. Boccaleri, L. Buzzi, F. Canonico, D. Gastaldi, Friedel's salt formation in sulfoaluminate cements: A combined XRD and 27 Al MAS NMR study, *Cem. Concr. Res.* 67 (2015) 93–102. <https://doi.org/10.1016/j.cemconres.2014.08.004>.
- [10] G.Y. Koga, B. Albert, V. Roche, R. Pereira Nogueira, On the intrinsic passivating ability of Belite-Ye'elimite-Ferrite towards carbon steel: A straightforward comparison with ordinary Portland cement, *Corros. Sci.* 147 (2019) 141–151. <https://doi.org/10.1016/j.corsci.2018.11.012>.
- [11] G.Y. Koga, P. Comperat, B. Albert, V. Roche, R.P. Nogueira, Effect of endogenous chloride contamination on the electrochemical and hydration responses of reinforced Belite-Ye'elimite-Ferrite (BYF) cement mortars, *Cem. Concr. Res.* 122 (2019) 212–226. <https://doi.org/10.1016/j.cemconres.2019.04.022>.
- [12] W. Wilson, F. Georget, K. Scrivener, Unravelling chloride transport/microstructure relationships for blended-cement pastes with the mini-migration method, *Cem. Concr. Res.* 140 (2021) 106264. <https://doi.org/10.1016/j.cemconres.2020.106264>.
- [13] G. Jen, N. Stompinis, R. Jones, Chloride ingress in a belite-calcium sulfoaluminate cement matrix, *Cem. Concr. Res.* 98 (2017) 130–135. <https://doi.org/10.1016/j.cemconres.2017.02.013>.
- [14] G.Y. Koga, P. Comperat, B. Albert, V. Roche, R.P. Nogueira, Electrochemical responses and chloride ingress in reinforced Belite-Ye'elimite-Ferrite (BYF) cement matrix exposed to exogenous salt sources, *Corros. Sci.* 166 (2020) 108469. <https://doi.org/10.1016/j.corsci.2020.108469>.

- [15] F. Bullerjahn, M. Zajac, M. Ben Haha, K.L. Scrivener, Factors influencing the hydration kinetics of ye'elinite; effect of mayenite, *Cem. Concr. Res.* 116 (2019) 113–119. <https://doi.org/10.1016/j.cemconres.2018.10.026>.
- [16] ASTM C1876-19, Standard Test Method for Bulk Electrical Resistivity or Bulk Conductivity of Concrete, (2019). <http://www.astm.org/cgi-bin/resolver.cgi?C1876-19>.
- [17] R.S. Barneyback, S. Diamond, Expression and analysis of pore fluids from hardened cement pastes and mortars, *Cem. Concr. Res.* 11 (1981) 279–285. [https://doi.org/10.1016/0008-8846\(81\)90069-7](https://doi.org/10.1016/0008-8846(81)90069-7).
- [18] H.J.H. Brouwers, R.J. vanEijk, Alkali concentrations of pore solution in hydrating OPC, *Cem. Concr. Res.* 33 (2003) 191–196. [https://doi.org/10.1016/S0008-8846\(02\)01022-0](https://doi.org/10.1016/S0008-8846(02)01022-0).
- [19] B. Lothenbach, D.A. Kulik, T. Matschei, M. Balonis, L. Baquerizo, B. Dilnesa, G.D. Miron, R.J. Myers, Cemdata18: A chemical thermodynamic database for hydrated Portland cements and alkali-activated materials, *Cem. Concr. Res.* 115 (2019) 472–506. <https://doi.org/10.1016/j.cemconres.2018.04.018>.
- [20] G.E. Archie, The Electrical Resistivity Log as an Aid in Determining Some Reservoir Characteristics, *Trans. AIME.* 146 (1942) 54–62. <https://doi.org/10.2118/942054-G>.
- [21] B. Mota Gassó, Impact of alkali salts on the kinetics and microstructural development of cementitious systems, 2015.
- [22] W. Hanpongpun, Investigation of the use of Limestone Calcined Clay Cement (LC<sup>3</sup>) applied to Thailand, 2019.
- [23] L.U.D. Tambara, M. Cheriaf, J.C. Rocha, A. Palomo, A. Fernández-Jiménez, Effect of alkalis content on calcium sulfoaluminate (CSA) cement hydration, *Cem. Concr. Res.* 128 (2020) 105953. <https://doi.org/10.1016/j.cemconres.2019.105953>.
- [24] S. Sui, F. Georget, H. Maraghechi, W. Sun, K. Scrivener, Towards a generic approach to durability: Factors affecting chloride transport in binary and ternary cementitious materials, *Cem. Concr. Res.* 124 (2019) 105783. <https://doi.org/10.1016/j.cemconres.2019.105783>.

## 6.7 Appendix

### Appendix 6-A: Current curves from mini migration test

From Fig. 6-18a, although the applied voltage is similar in LGC, the current curves show different characteristics. The specimen cured at 20°C does not show an increase of the current, while the specimens cured at the other temperatures show the increase of the current which can identify the flow of chloride through the sample. The specimen cured at 60°C has the shortest constant migration regime indicating the higher flow of chloride. For blended systems, the increase of applied voltage at 60°C causes the higher flow of chloride, extremely in the LGCMKLS system. CSA shows the high flow of chloride in the samples cured at 20 and 40°C in one day even if the applied voltage is lower than the sample cured at 5 and 60°C.

In the case of the blended system, the flow of chloride at high temperature curing is high due to the high voltage applied. This indicates that the applied voltage should be slightly lower to be able to decelerate the flow of chloride and gradually obtain increasing chloride in the downstream reservoir.

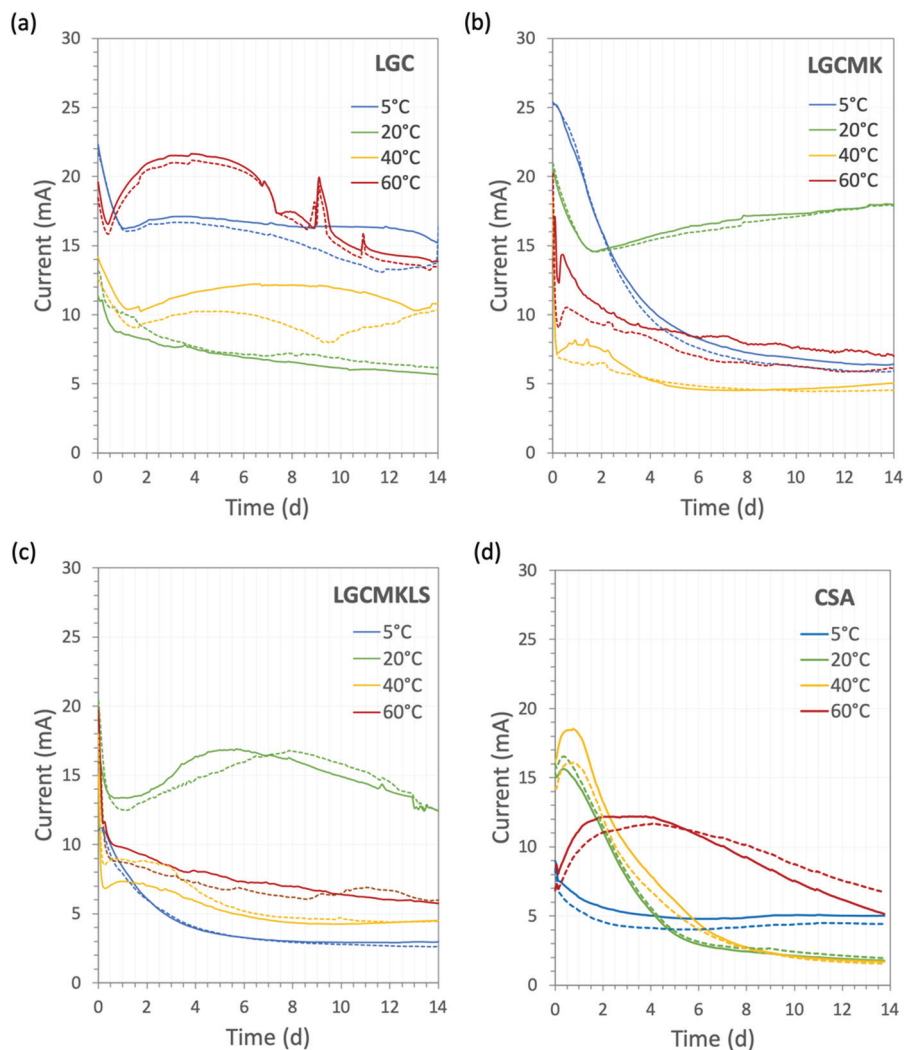


Fig. 6-18 Current curves during the mini migration test of (a) LGC, (b) LGCMK, (c) LGCMKLS and (d) CSA systems with two duplicates cured in the saturated condition for 28 days.

**Appendix 6-B:** Phase assemblages of CSA curing in a 0.3M NaOH solution

Fig. 6-19 shows the comparison of CSA phase assemblages at 28 days of hydration between pore solution curing and 0.3M NaOH curing. The result illustrates that high pH can slightly accelerate the reaction of ye'elimite [Ogawa and Roy (1982), F. Winnefeld (2010)]. However, the phases are the same but their content are slightly different between the two curing conditions.

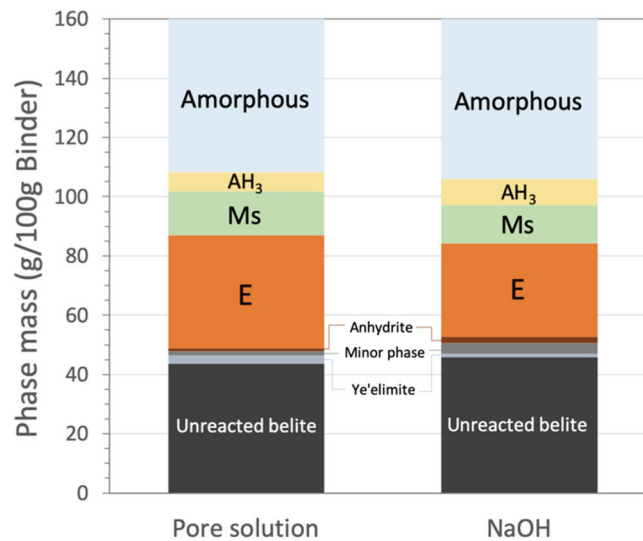


Fig. 6-19 Phase assemblages of CSA at 28 days of hydration compared between pore solution curing and 0.3M NaOH curing determined from XRD-Rietveld.

**Appendix 6-C:** Preliminary study of mini migration for CSA

The mini migration method uses a 0.3M NaOH solution in the downstream reservoir for the PC system which is quite similar to the pH in the pore solution. Therefore, the 0.3M NaOH solution can prevent leaching. However, CSA has lower pH compared to the PC system. The preliminary test of a mini migration experiment on the CSA system cured at 20°C using a low pH solution compared to a 0.3M NaOH solution was carried out. The solutions, pH and the applied voltage used in the preliminary test are shown in Table 6-7. The first solution is used as a reference which is the same as the PC system experiment. The second solution is corresponding to the low pH solution that is in the range of the pH in CSA. The last solution is the low pH solution with some ions for preventing the leaching of aluminate hydrates during the test. The applied voltage was set according to the range of the current between 5 – 20 mA, preferable around 15 mA. The mini migration test was carried out at the room temperature (~25°C).

Table 6-7 Parameters used in the preliminary study

	Solution 1	Solution 2	Solution 3
Downstream solution	0.3M NaOH	0.025M NaOH	0.025M NaOH + 0.01M $\text{Al}_2(\text{SO}_4)_3$
pH	13.5	12.5	12.3
Applied voltage	3	3.5	3.5

The surfaces facing upstream solution and downstream solution are shown in Fig. 6-20. A clean surface is observed only in the sample exposed in the reference solution. The surface facing downstream solution of the sample exposed in solution 2 and 3 were covered with a gel-like layer. When these samples are dried, it is clearly seen the damage of the sample facing downstream. This is probably due to the electro chemistry in a low ion concentration regime. Moreover, the color of the solution 2 and 3 becomes yellow after 1 day of the test with a strong smell of bleach, indicating the formation of the chlorine gas at the downstream electrode.

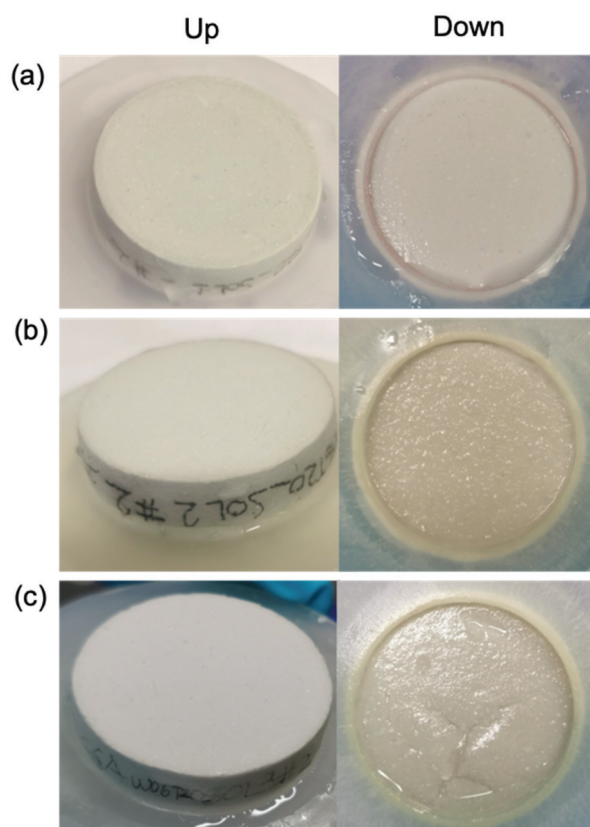


Fig. 6-20 The appearance of the up and down sample surface exposed in (a) 0.3M NaOH, (b) 0.025M NaOH and (c) 0.025M NaOH + 0.01  $\text{Al}_2(\text{SO}_4)_3$  after mini migration test.

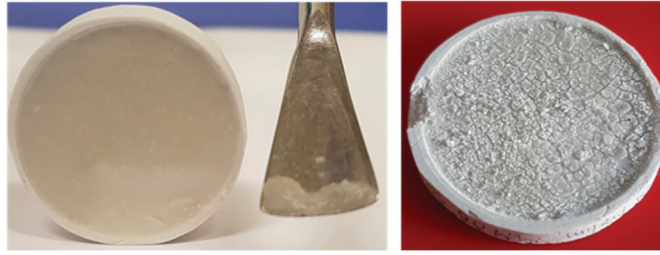


Fig. 6-21 The damage of the down surface when the solution 2 and 3 are used.

Furthermore, the current during the mini migration test was monitored shown in Fig. 6-22. The result shows that very fast ion transport occurs in the low pH solution (Fig. 6-22b) when compared to the reference (Fig. 6-22a). It cannot indicate the constant migration regime from the current curve of the low pH solution. Therefore, 0.3M NaOH solution was chosen to be used in the real mini migration test. Further investigation is needed to use compatible conditions with the CSA pore solution in the mini-migration setup.

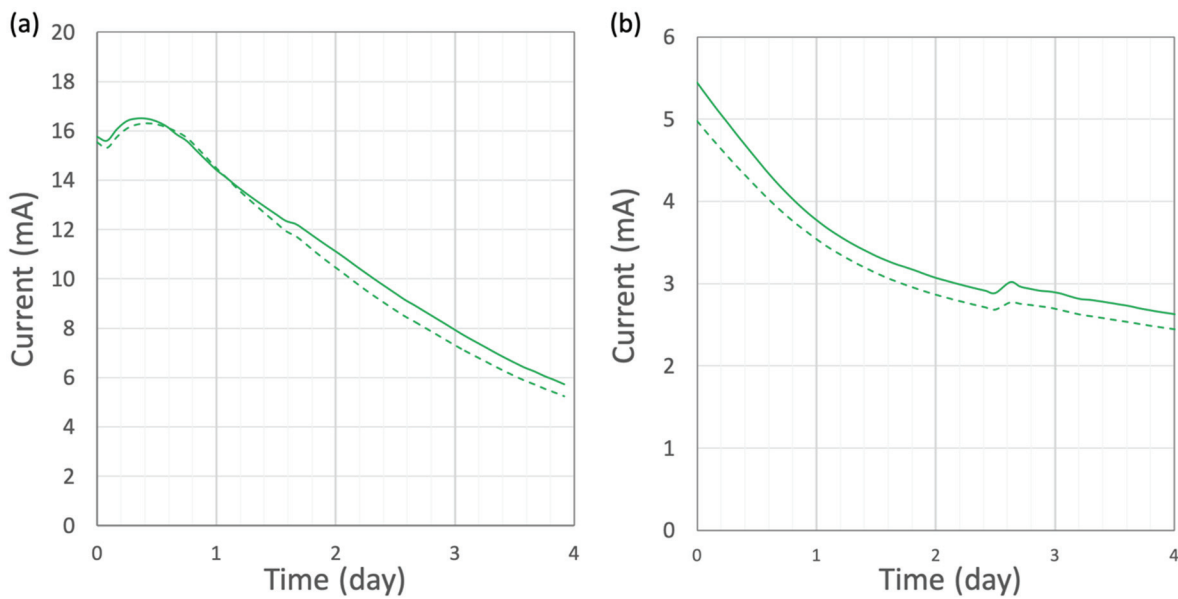


Fig. 6-22 Comparison of current monitored during the mini migration test: (a) 0.3M NaOH and (b) 0.025M NaOH.



# Chapter 7 Conclusions and perspectives

## CONTENTS

---

<b>Chapter 7</b>	<b>Conclusions and perspectives .....</b>	<b>165</b>
7.1	Accuracy of thermodynamic modelling .....	166
7.2	Portland cement systems.....	166
7.3	Calcium sulfoaluminate system .....	167
7.4	CO <sub>2</sub> emissions.....	168
7.5	Reference .....	170

---



In this study, binders with similar chemical composition were studied to explore the impact of the reactive phases and temperature on the hydrated phase assemblage, microstructure and properties.

## 7.1 Accuracy of thermodynamic modelling

Temperature has a major impact particularly on the aluminate phases. For example, ettringite and strätlingite are less stable at high temperature and various types of AFm are formed at different temperatures. Thermodynamic modelling is a good tool to predict the phase assemblages in the equilibrium state in the practical curing temperature range (5 to 60°C). Compared to experimental observations, the qualitative prediction is quite good but the quantitative prediction relies on the several factors.

- Thermodynamic modelling depends first on the accurate determination of the reacted phases as input, which determines the amounts of oxides available in the system. Measuring this degree of reaction is particularly challenging for metakaolin. Metakaolin is an amorphous phase which cannot be quantified by common techniques but it is important to use the degree of reaction of metakaolin as an input. <sup>29</sup>Si-NMR was used in this study with satisfactory results. The reactivity of metakaolin can be determined by portlandite consumption, combined with mass balance, but less accurate and precise with an approximate error of 20% of degree of reaction. This error comes from the accumulation from multiple techniques.
- At present the thermodynamic models cannot well predict the composition of the C-(A)-S-H phase, especially with respect to the incorporation of aluminium. Therefore, good thermodynamic prediction requires an input of the experimental composition of the C-S-H. As it is a major phase, even if the composition varies by a small amount, the impact on the prediction is large. However, it is quite difficult to determine the C-A-S-H composition precisely due to the scatter in the analyses due to intermixing. This is especially the case at the higher temperatures studied.

The phases that are difficult to detect by common techniques such as XRD, TGA and SEM could be identified by the new tool, edxia. It helps us to verify the presence of the phase in the microstructure such as strätlingite and C-S-H in CSA. The incorporation of minor elements in the hydrated phases can also be identified resulting in data on solid solution that can be later improved the thermodynamic database.

The co-existence of portlandite and strätlingite was observed in the blended system in non-equilibrium state because of the dense microstructure which may hinder ion transport.

To be able to improve the thermodynamic database, the solubility of some phases such as strätlingite, hydrotalcite and siliceous hydrogarnet needs to be verified as a function of temperature. The result from this study indicates that iron can possibly be in the strätlingite and C-S-H in higher alumina systems. This needs further investigations on both synthetic and real systems. Comparison with experiment, indicates that the stability of hemicarbonat and monocarbonat in thermodynamic modelling may be overestimated. Further study is needed to improve the thermodynamic data.

## 7.2 Portland cement systems

The reference Portland cement results shows that the temperature not only affects the phase formation but also the microstructure. It becomes much more heterogeneous at high temperature, with large voids, which have some negative impact on compressive strength, but a much larger negative impact on transport properties.

The blended systems have a more homogeneous microstructure even at high temperature. Therefore, the impact of temperature on transport properties is lower. On the negative side, the blended systems seem to inhibit the reaction of belite which may lower the compressive strength even though metakaolin reaction also contributes to the compressive strength. However, this study confirmed that they have a really good performance in terms of resistance to chloride ingress. The mini-migration test is a good method to get a rapid estimation of the resistance to chloride. Also, the effective conductivity which is a simple measurement can be used as a good indicator. The improvement of chloride resistance is often attributed to the “formation factor” or “tortuosity” but the high value of these parameters indicates more than a simple change in the pore geometry is involved.

In general, the strength of Portland cement-based systems correlates well with the combined water fraction, although there are some deviations in the blended systems, with different temperatures. Some global relations between the strength and porosity is also observed.

It is important to study the hydration and microstructure together with the cement properties because it provides a better understanding of the difference in properties. Higher alumina system shows a very good performance with respect to chloride resistance but slightly lower compressive strength compared to the Portland cement. Therefore, more information of the degree of reaction of metakaolin, the microstructure evolution and pore solution at different ages should be investigated to obtain a complete view.

### 7.3 Calcium sulfoaluminate system

The CSA system in this study has a similar chemical composition as the OPC blended system, but the final phase assemblages and microstructure are different. The main reason is the low reactivity of belite. This system is still evolving at late age, leading to the change between 90 and 180 days due to the late belite reaction. The reactivity of CSA is more sensitive to the temperature than the PC system. The hydrate phases formed are ettringite, monosulfate, strätlingite, aluminium hydroxide and C-S-H. Before the formation of C-S-H, the samples have a very open microstructure which does not perform well with respect to chloride ingress. Once the C-S-H starts forming, it reduces the pore entry radius. Hence, a better performance is seen with respect to chloride ingress but only at late ages. The bulk diffusion test can be a good method to compare the resistance of chloride ingress of different binders when the system has no cracks. The effective conductivity is not recommended to compare the systems that have different ranges of pH.

The overall strength of CSA is lower than the PC system. The contribution of C-S-H formation to the strength is lower than expected. The combined water fraction does not appear to relate well to the strength in this case. The strength seems to be limited at a late age.

#### **Perspectives:**

CSA could be investigated in more detail. The laboratory prepared clinker takes a lot of time to prepare the required materials for the whole study. However, it is a compromise to more easily compare the systems. It removed some components of a normal commercial CSA cement such as alkalis and iron. Better performance may be obtained from a properly optimized commercial CSA cement. In particular, better particle distribution, and admixtures might lead to a better microstructure. However, the approach of this study was useful to better understand the chemistry, and the phase assemblages of CSA cements.

The real mechanisms that govern belite reaction in CSA still need further investigations to prove whether it is because of the depletion of amorphous aluminium containing phase ( $AH_3$  and  $CAH_{10}$ ) or other factors. In particular, the pore solution concentrations as a function of time are required.

In addition, the hydration still continues after 90 days. The investigation of the durability test should be carried out at later ages to analyse the long-term performance. Some researchers have used boron to accelerate the belite reaction and obtain better performance earlier. However, this has an important impact on cost. The mini-migration setup for the CSA system should be modified either by adding some alkalis to the binder to be equivalent to the blended systems (and real CSA systems), or by adapting the setup. To be able to compare the effective conductivity to the effective diffusion coefficient ( $D_{eff}$ ), curing conditions between experiments should be similar.

For the durability test, the CSA system should be studied in mortar level to avoid cracks for a long curing experiment. The dimensional stability of CSA under realistic curing temperatures should be studied to understand the cracks development and how they relate to the durability properties, especially at high temperature. The mini migration test may not be practical when the temperature is changed because the hydration still carries on during the test but at different than the curing state.

## 7.4 CO<sub>2</sub> emissions

A comparison of CO<sub>2</sub> emission from the chemical composition of the investigated system in this study is shown in Table 7-1. The calculation is based on the stoichiometric clinker phases composed of Ca from Gartner's work [1]. The energy demand for the production of the clinker is not included in this calculation. The CO<sub>2</sub> emission of the higher alumina systems can be lower than the reference Portland cement by more than 20%, and more than 30% in the ternary blends. Because of the high belite content, the CSA system is similar to the LGCMK.

In Fig. 7-1, the chemical CO<sub>2</sub> emissions are normalized by the strength. This indicates that the blended systems have lower CO<sub>2</sub> emission per unit strength. Fig. 7-2 shows the strength normalized by the CO<sub>2</sub> emission at different temperatures as a function of time. It determines that the blended systems gain higher compressive strength per unit of CO<sub>2</sub> emission compared to Portland cement and CSA when metakaolin starts to react. On the other hand, this comparison does not indicate any environmental benefit of CSA. Of course, for a more complete analysis it would be necessary to also take into account the CO<sub>2</sub> emission associated with firing and grinding.

Table 7-1 CO<sub>2</sub> emission and % CO<sub>2</sub> reduction of the investigated system considering only the chemical contribution to CO<sub>2</sub> emission.

	LGC	LGCMK	LGCMKLS	CSA
CO <sub>2</sub> emission (kg/t clinker)	494	387	336	381
% CO <sub>2</sub> reduction	Reference	22	32	23

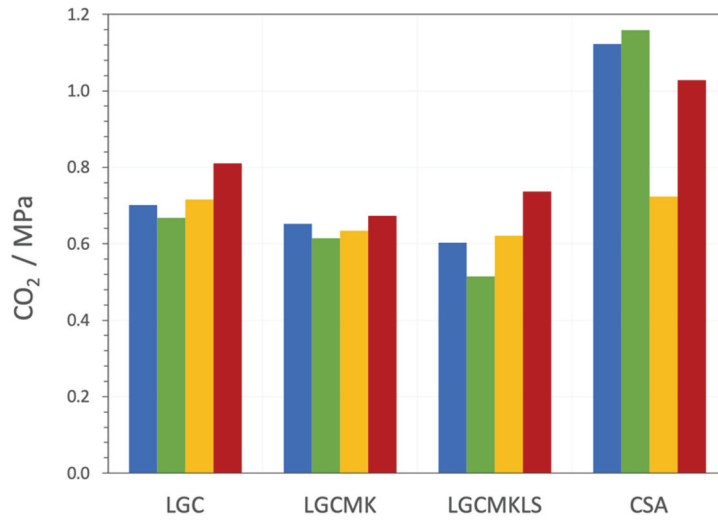


Fig. 7-1 Comparison of the raw materials CO<sub>2</sub> emission to the production of stoichiometric phases as given in [1] to the compressive strength at 90 days.

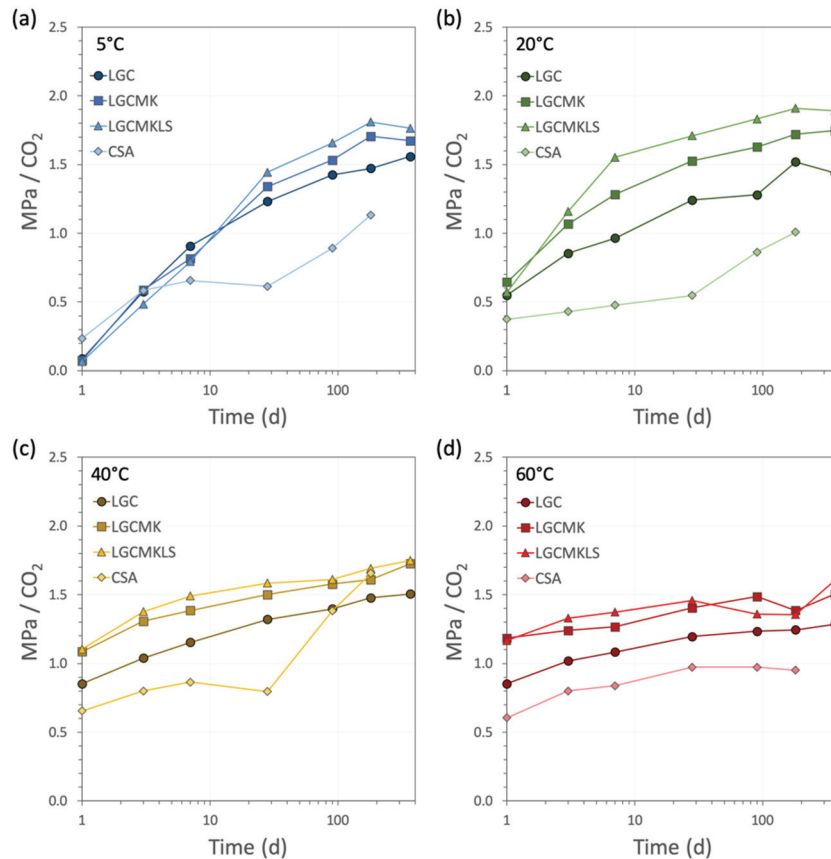


Fig. 7-2 Comparison of the raw materials CO<sub>2</sub> emission of the investigated systems according to the production of stoichiometric phases as given in [1] to the compressive strength at different temperatures.

Overall, the work presented here seems to indicate clear advantages of the PC blended systems, particularly the ternary blend with limestone. CO<sub>2</sub> emissions per unit strength are clearly lower and the transport properties with respect to chloride ingress much improved. In addition, the raw materials are abundant and widely distributed geographically as opposed to the comparative rarity and higher cost of minerals with Al<sub>2</sub>O<sub>3</sub> >> SiO<sub>2</sub> needed to produce CSA.

## 7.5 Reference

- [1] E. Gartner, Industrially interesting approaches to “low-CO<sub>2</sub>” cements, *Cem. Concr. Res.* 34 (2004) 1489–1498.  
<https://doi.org/10.1016/j.cemconres.2004.01.021>.

# Appendices

## Appendix A: Belite and ye'elimite clinker

The initial goal of this part was to synthesize belite clinker and ye'elimite clinker separately. Ye'elimite synthesis was accomplished. However, belite synthesis could not be reproduced on a large scale. The detail of the laboratory prepared belite and ye'elimite is described in this part.

### Belite clinker

The target of the composition of belite was  $\beta$ -belite > 90%, Rankinite < 5%, no alite, and no free lime. The raw meal was prepared by cylinder method. Belite clinker was synthesized in a static furnace at 1380°C with a heating rate of 7°C/min for 2 hours.  $\beta$ -belite content reached the target with a small amount of  $\gamma$ -belite and alite. Therefore, the second attempt was trying to reduce alite content in the clinker by lowering sintering temperature to 1300°C and changing stabilizers. However, it was not successful. High  $\gamma$ -belite content was observed with variations between batches. Many attempts were carried out by changing some parameters e.g. stabilizer, C/S, sintering temperature, cooling method but the clinker still contains high  $\gamma$ -belite content. A comparison between high  $\beta$ -belite and high  $\gamma$ -belite is shown in

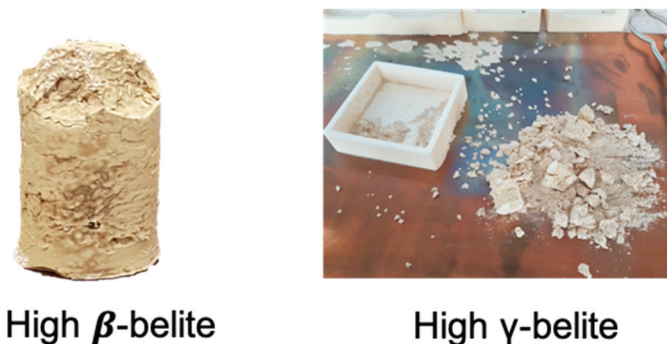


Figure 1 A visual comparison between high  $\beta$ -belite and high  $\gamma$ -belite.

The reactivity of high  $\beta$ -belite was investigated by isothermal calorimetry at 20°C. The microstructure of hydrated high  $\beta$ -belite was analyzed by SEM. From Figure 1, no reaction was observed during 96 hours of hydration at 20°C. No hydration products are detected after 28 days of hydration.

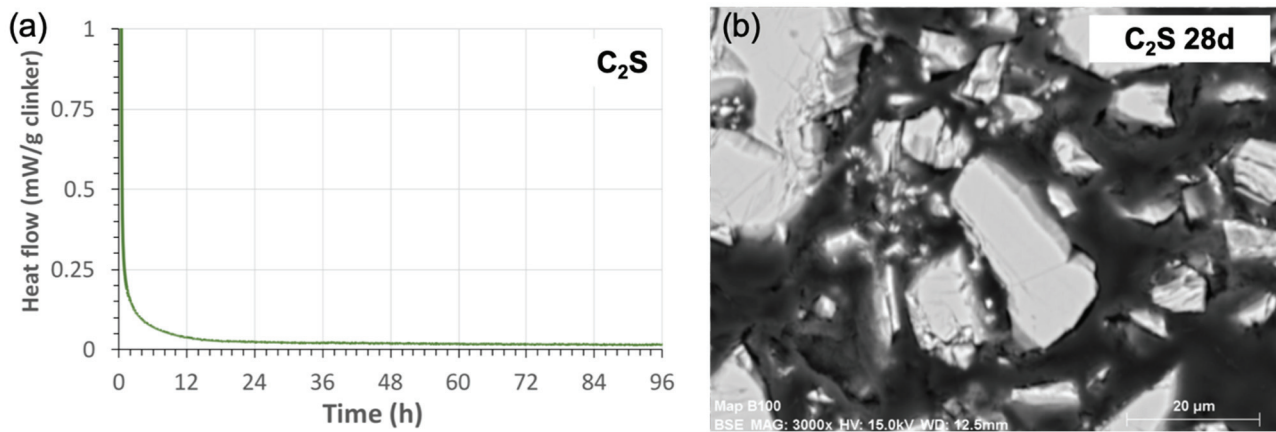


Figure 2 (a) The reaction of high  $\beta$ -belite and (b) the microstructure at 28 days of hydration cured at 20°C.

### Ye'elimite clinker

The raw meal of ye'elimite was prepared by HeidelbergCement Technology. High purity clinker synthesis in lab scale generally uses pressing disc, nodulizing method or compacted materials in the crucible, where only a relatively low amount of clinker can be produced at once. The cylinder method was also applied to compare the quality of ye'elimite clinker prepared by pressing disc method (in Figure 3) and cylinder method (in Figure 4) using the same heating profile and the same furnace for the synthesis.

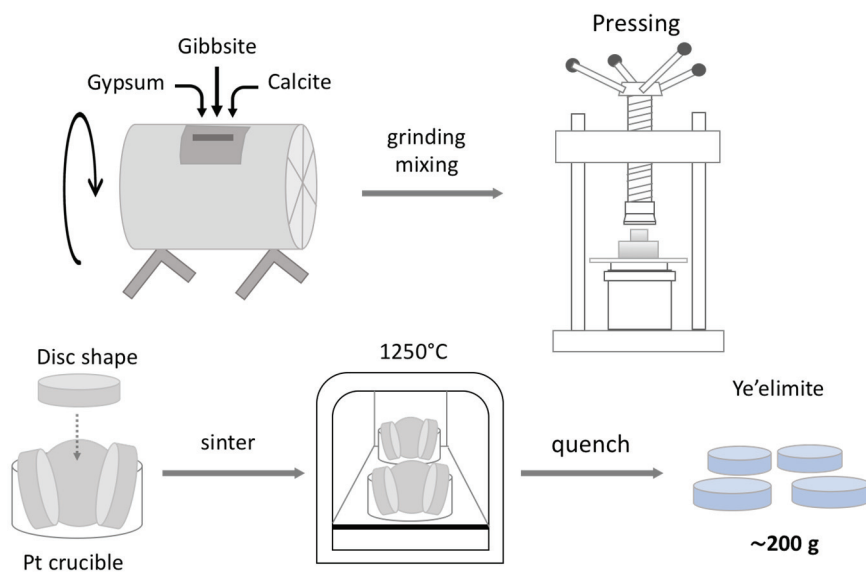


Figure 3 Pressing disc method



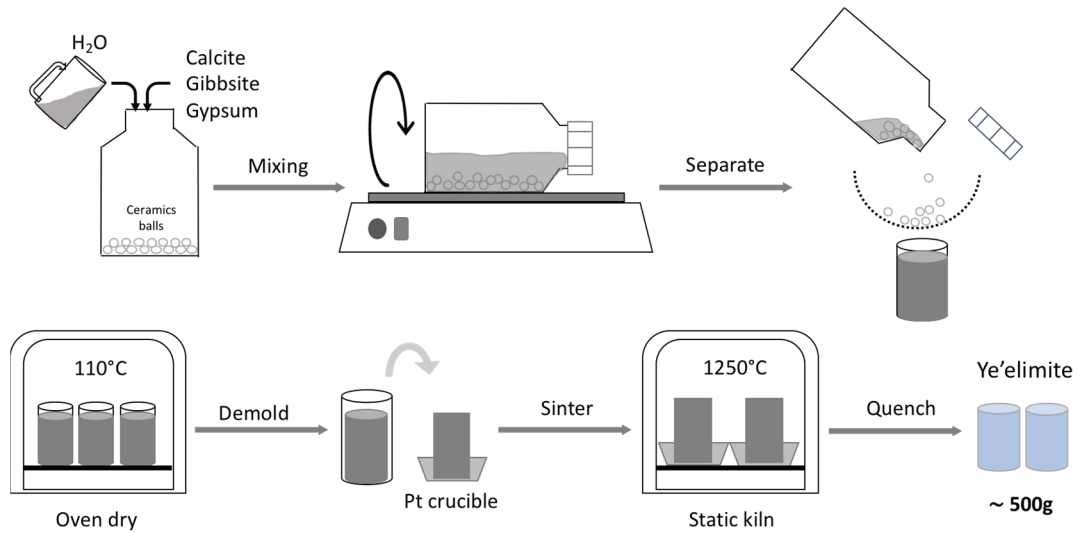


Figure 4 Cylinder method

For the cylinder method clinker, the composition of the clinker was analysed from different parts of the clinker (top, middle and bottom). Figure 5 shows similar major phase content between the two methods, but it shows slightly different content for the minor phases.

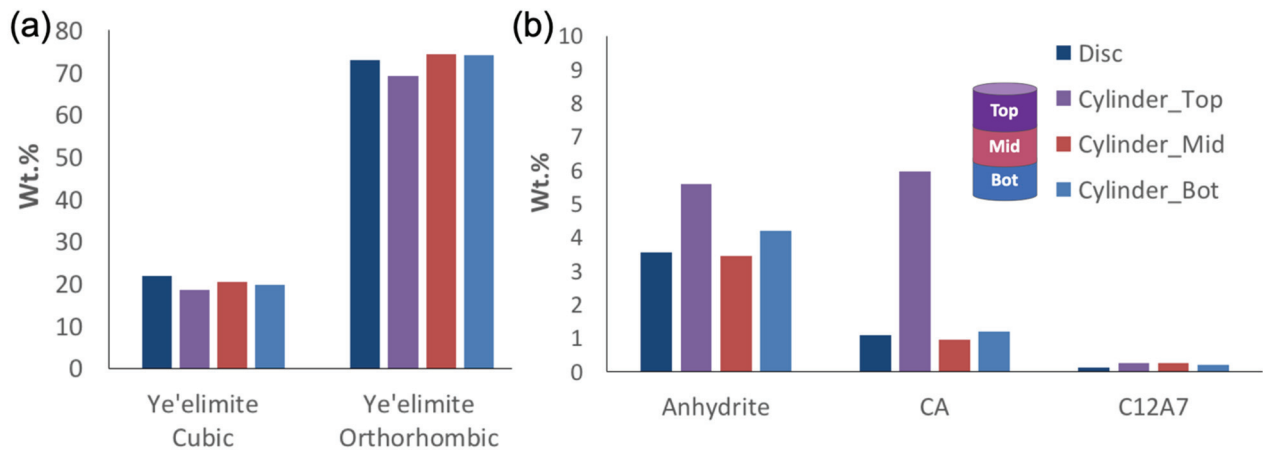


Figure 5 The composition of ye'elimite clinker (a) major phases and (b) minor phases from different parts of the cylinder.

The average phase content between the two methods is shown in Figure 6. It illustrates that there is no effect of two different raw meal preparations on the phase composition of ye'elimite clinker. Therefore, the cylinder method can be applied to have higher productivity without changing the phase composition.

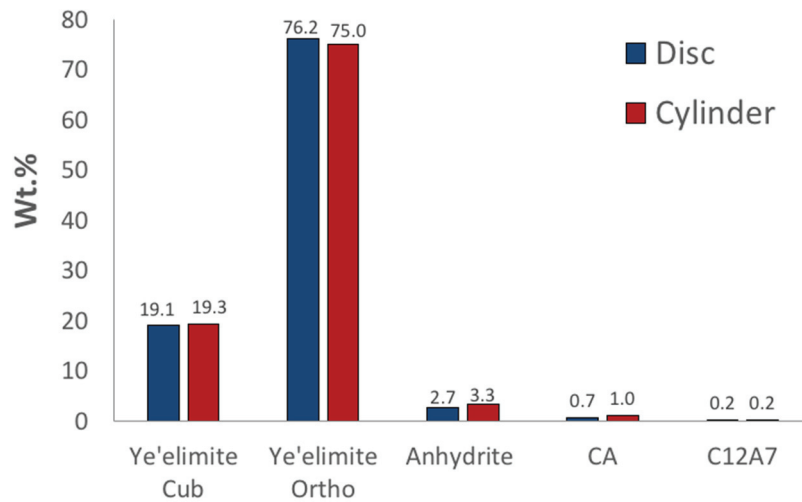


Figure 6 The average phase content of ye'elimitite clinker prepared with the disc method and the cylinder method.

The clinker prepared by the cylinder method was characterized by the structure of ye'elimitite (orthorhombic) by  $^{27}\text{Al}$  NMR. The spectra acquired at 9.4T with a spinning frequency of 20.0 kHz. Figure 7 shows that there are no significant differences between the middle and the bottom parts of the cylinder and less ordered crystallinity compared to the pure orthorhombic ye'elimitite.

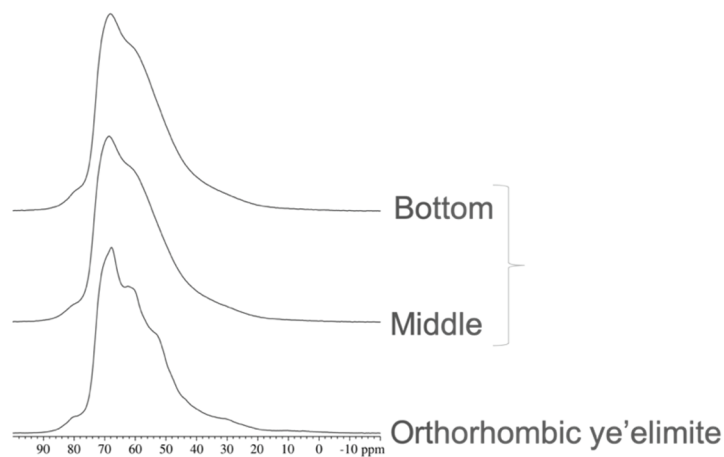


Figure 7 Structure of ye'elimitite of the clinker prepared by cylinder method compared to a pure orthorhombic ye'elimitite analysed by  $^{27}\text{Al}$  NMR.

The reactivity between these two methods of preparation was investigated, as shown in Figure 8. The ye'elimitite prepared by disc method has a slightly slower reaction than the cylinder method, probably due to the coarser particles. The raw meal prepared by the cylinder method is well homogenized and the particle size is also slightly reduced.

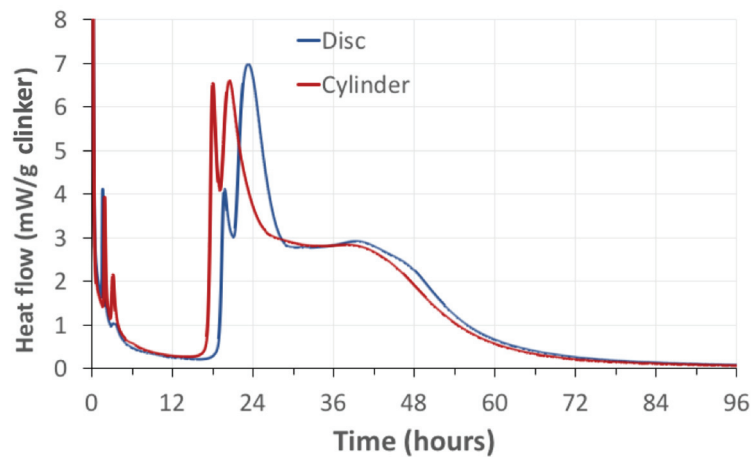


Figure 8 Reactivity of ye'elimite between the two methods

In summary, the cylinder method can be used for ye'elimite synthesis, but the top part of the clinker cylinder contains slightly higher minor phases. The reactivity between the two protocols is quite similar. From  $^{27}\text{Al}$  MAS NMR, the ye'elimite from cylinder method is homogenized but it has less crystallinity compared to the synthetic pure orthorhombic ye'elimite.

## Appendix B: Effect of mayenite at 60°C

According to Chapter 5, faster reaction was obtained at high temperature investigated by isothermal calorimetry. The microstructure of CSA with mayenite at 60°C shows heterogeneous microstructure. The aim of this part is to investigate the effect of mayenite on CSA hydration and microstructure at 60°C.

Figure 9a shows a slightly slower reaction of the sample without mayenite compared to the sample with mayenite. The cumulative heat of the sample without mayenite is slightly higher.

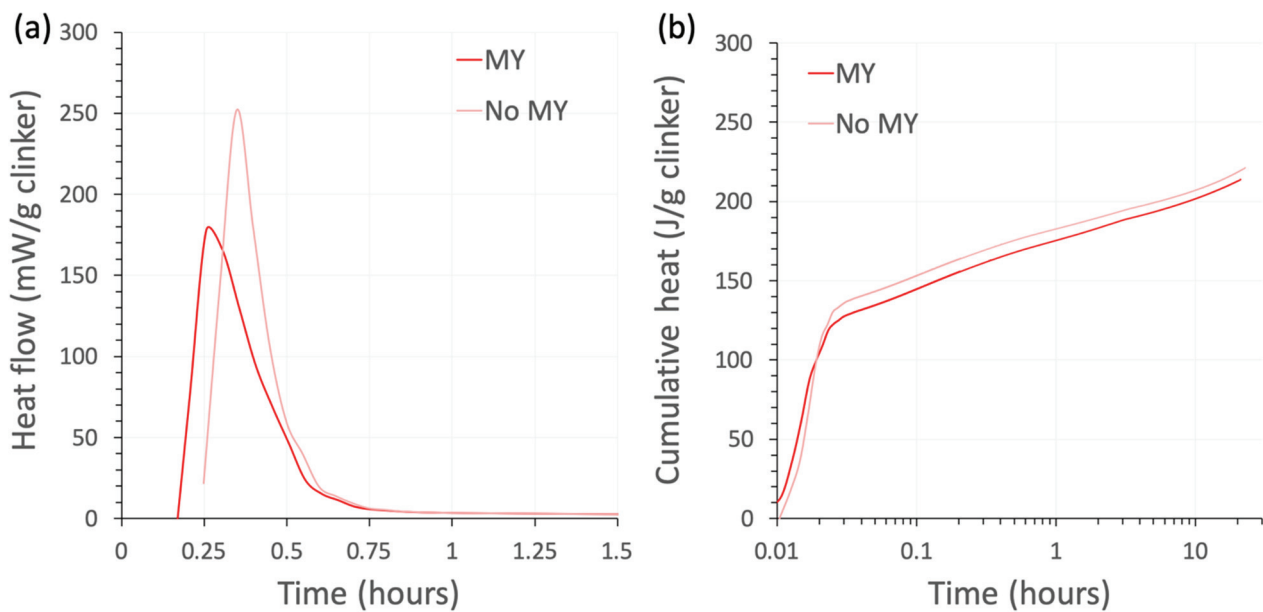


Figure 9 A comparison of heat of hydration between with and without mayenite at 60°C (a) heat flow and (b) cumulative heat.

Phase assemblages at 7 and 28 days of hydration of CSA with and without mayenite cured at 60°C are shown in Figure 10. At 7 days of hydration, the formation of hydrated phases is similar between with and without mayenite. Since mayenite can accelerate the reaction of ye'elinite, the remaining ye'elinite is higher when no mayenite is added in the CSA system. At 28 days of hydration, the ettringite content of the sample with mayenite is higher than the sample without mayenite. The microstructure of the sample with mayenite addition (in Figure 11) is more heterogeneous than the microstructure of the sample without mayenite, obviously seen at 28 days of hydration. Therefore, the reaction of the CSA system with mayenite addition cured at 60 °C is accelerated, resulting in slight changes of phase assemblage at late age, especially ettringite and monosulfate causing, and causing an heterogeneous microstructure.

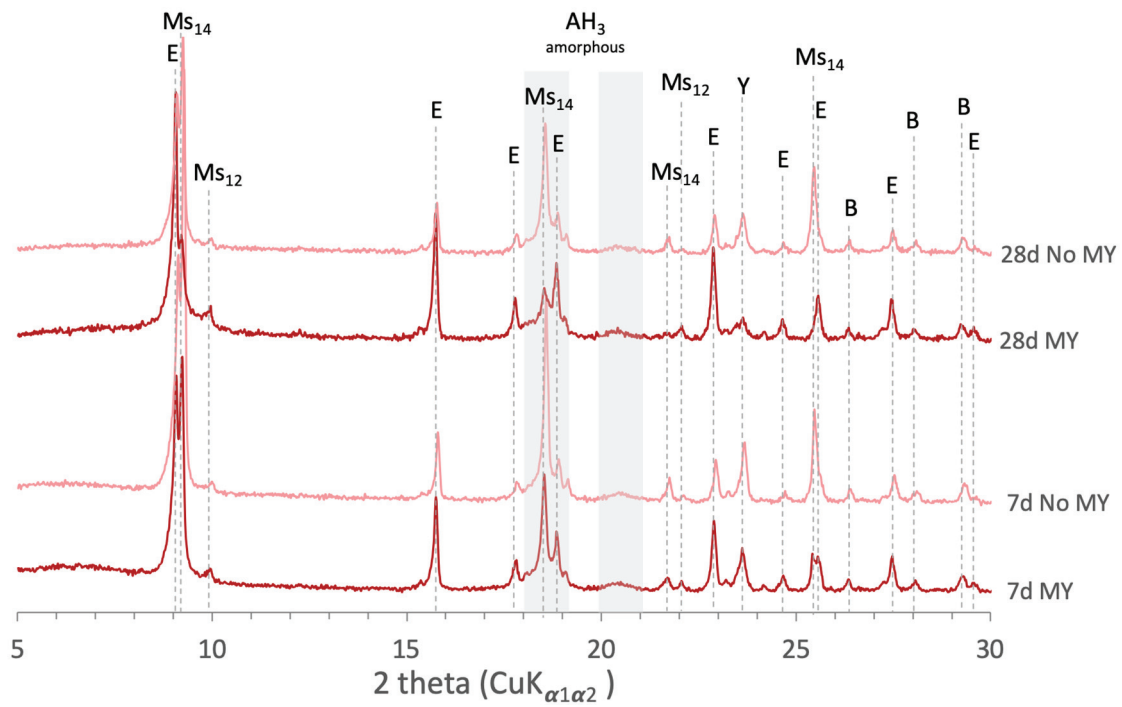


Figure 10 Comparison of phase assemblages between with and without mayenite cured at 60°C at 7 and 28 days of hydration: E = ettringite, CH = Portlandite, Ms = monosulfate, B = belite, Y = ye'elimite, AH<sub>3</sub> = aluminium hydroxide.

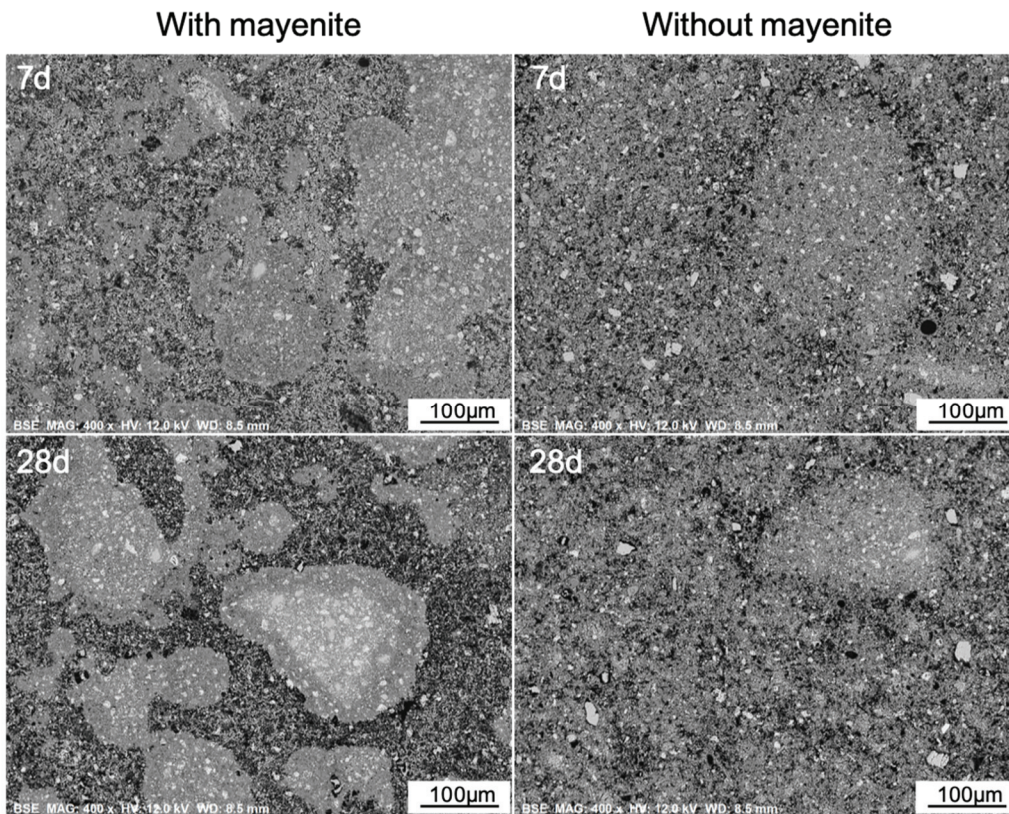


Figure 11 Microstructures of CSA with and without mayenite cured at 60°C at 7 and 28 days of hydration.



## Appendix C: EDS point analysis of C-(A)-S-H of the PC systems

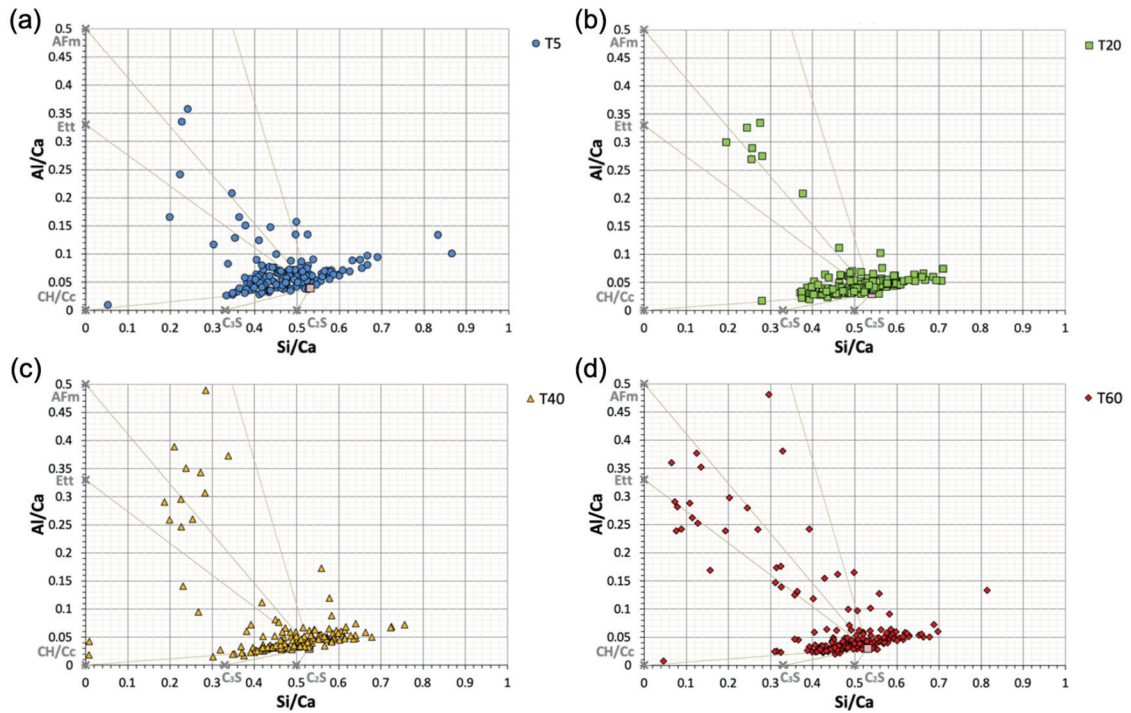


Figure 12 The ratio plots of Si/Ca and Al/Ca analysed by EDS point analysis of C-S-H composition of LGC at (a) 5°C, (b) 20°C, (c) 40°C and (d) 60°C.

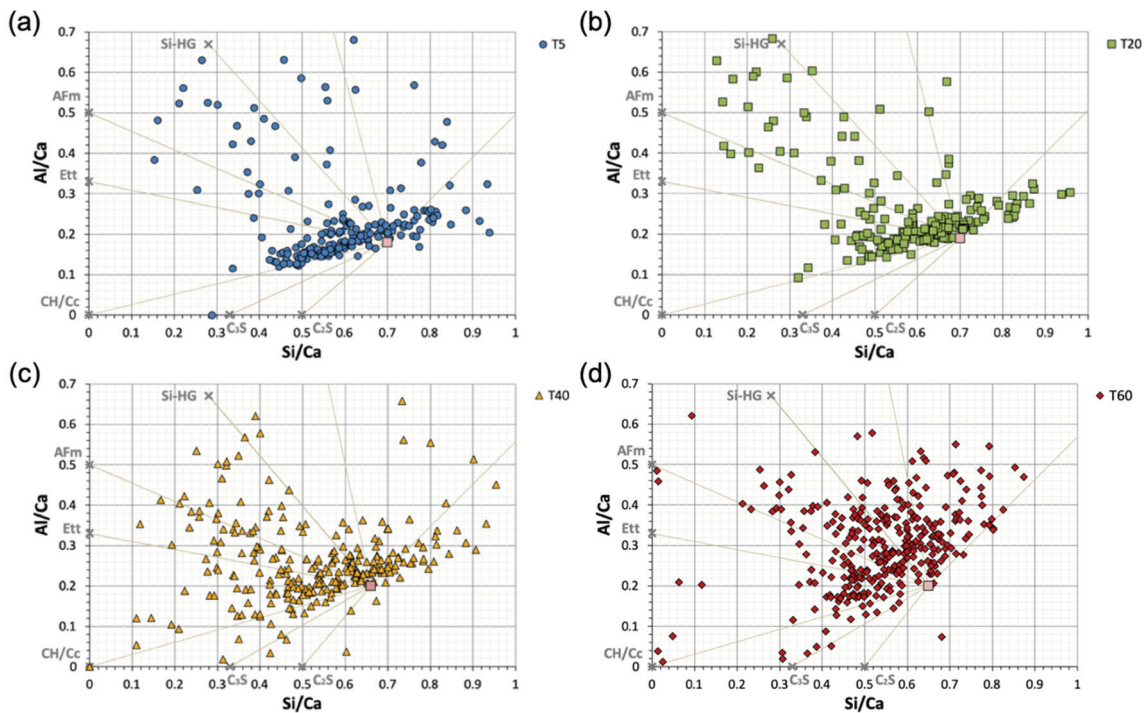


Figure 13 The ratio plots of Si/Ca and Al/Ca analysed by EDS point analysis of C-S-H composition of LGCMK at (a) 5°C, (b) 20°C, (c) 40°C and (d) 60°C.

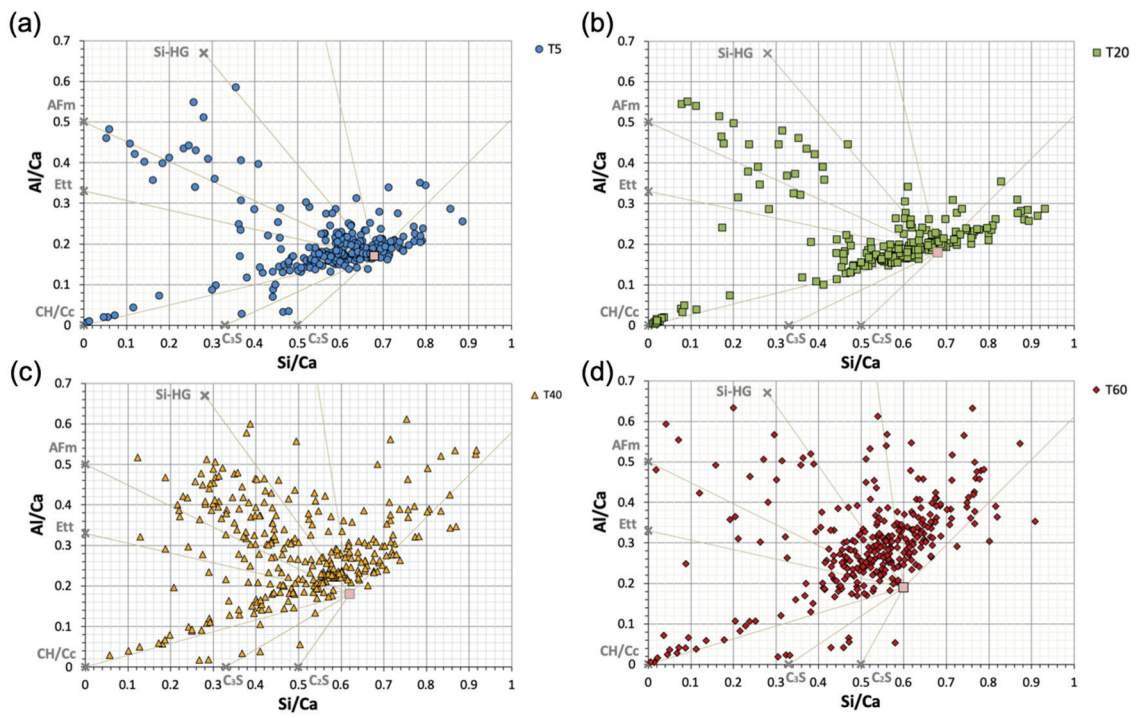


Figure 14 The ratio plots of Si/Ca and Al/Ca analysed by EDS point analysis of C-S-H composition of LGCMKLS at (a) 5°C, (b) 20°C, (c) 40°C and (d) 60°C.

## Appendix D: Activation energy (Ea)

Activation energy (Ea) is the least amount of energy required to activate atoms or molecules to a state in which they can undergo a chemical reaction. From Arrhenius's law, the relation to the activation energy and the rate of reaction indicates the sensitivity of the reaction rate to temperature. The cumulative heat in Chapter 5 of the PC systems was used for the Ea calculation by method of rates. Figure 15 shows that Ea can be calculated up to a certain point due to different competing reactions. Thus, it cannot be captured by Arrhenius's law. However, the Ea of the silicate reaction is about 40 kJ/mol which is similar to literature.

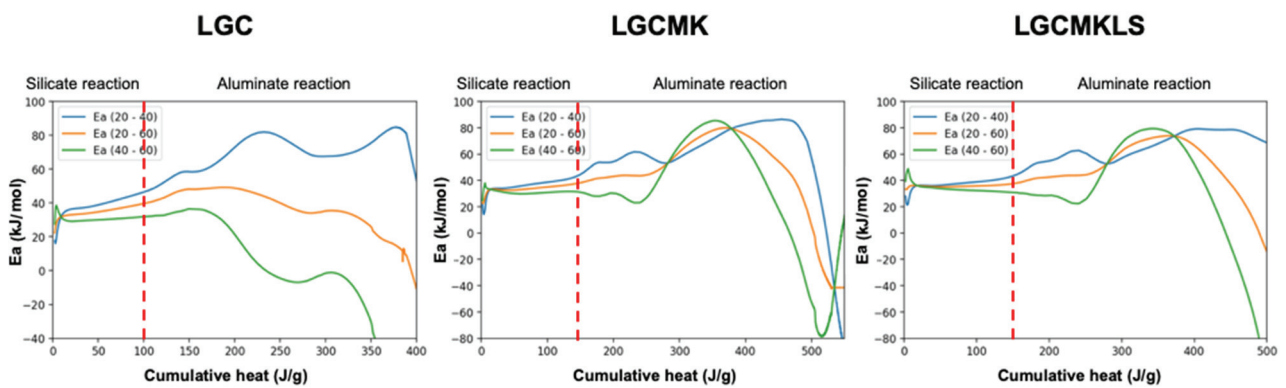


Figure 15 Activation energy (Ea) calculated by method of rates of LGC, LGCMK and LGCMKLS.



# Appendix E: Bulk diffusion test – AgNO<sub>3</sub> spraying – Chloride penetration depth

Schematic of bulk diffusion test, AgNO<sub>3</sub> spraying and chloride penetration depth are shown in Figure 16 - Figure 19.

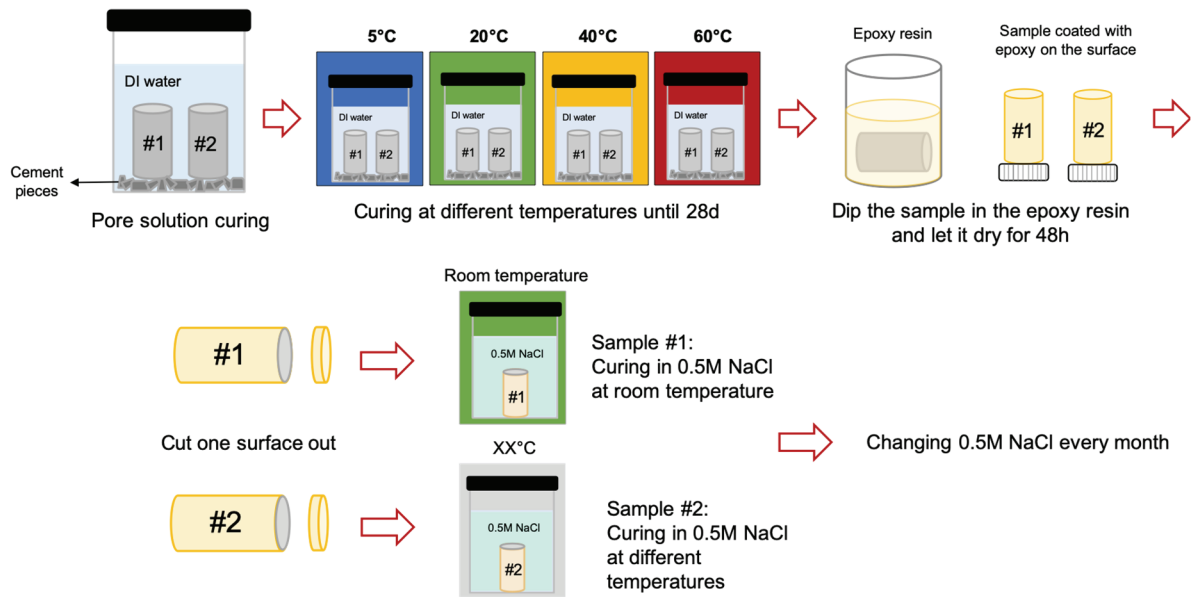


Figure 16 Step 1: Curing method for mini bulk diffusion test.

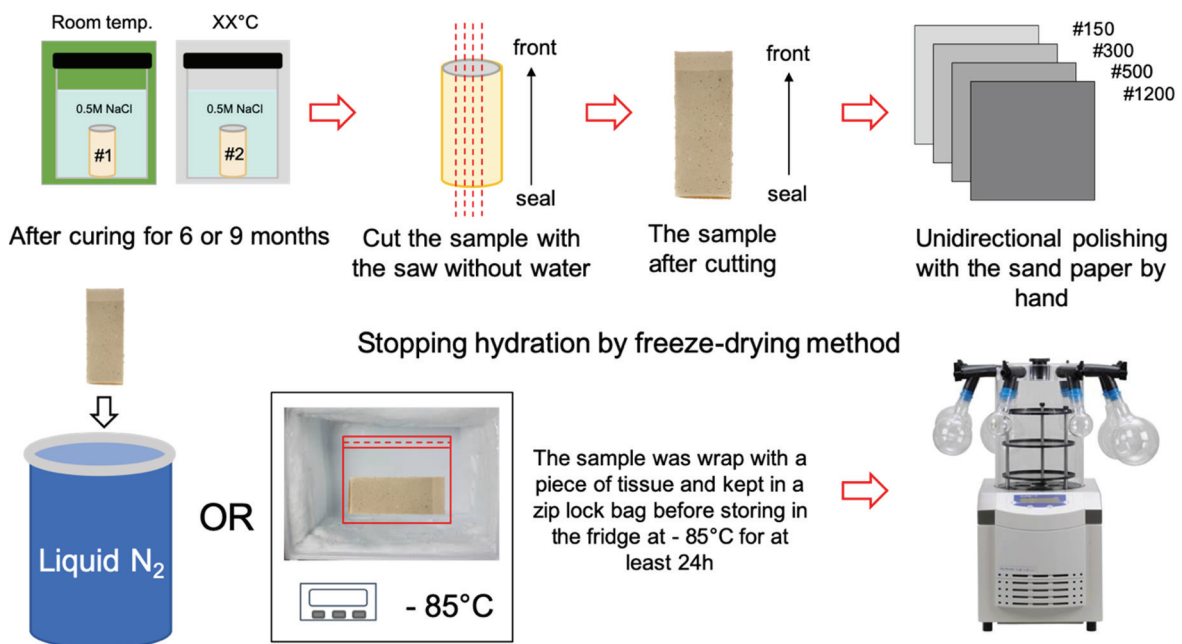


Figure 17 Step 2: Sample preparation and hydration stoppage.

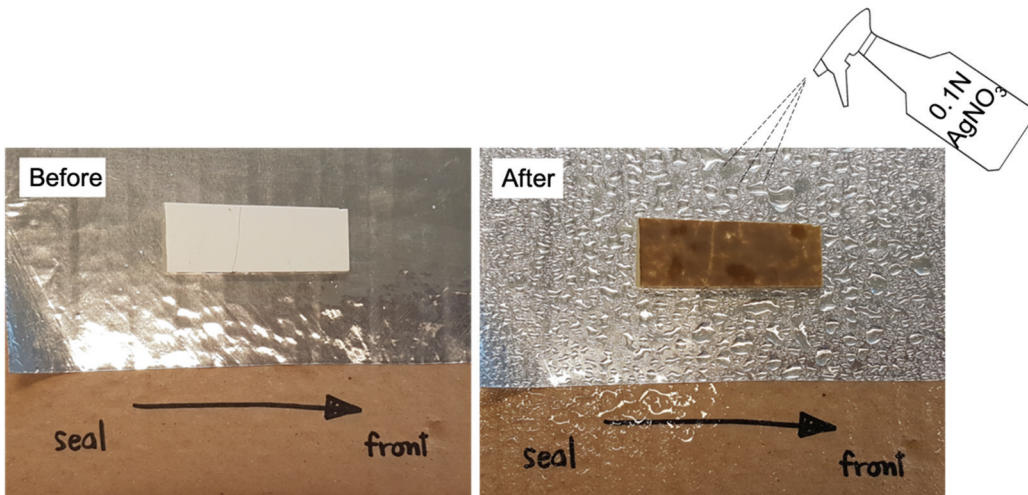


Figure 18 Step 3: Applying 0.1N AgNO<sub>3</sub> spraying on the sample

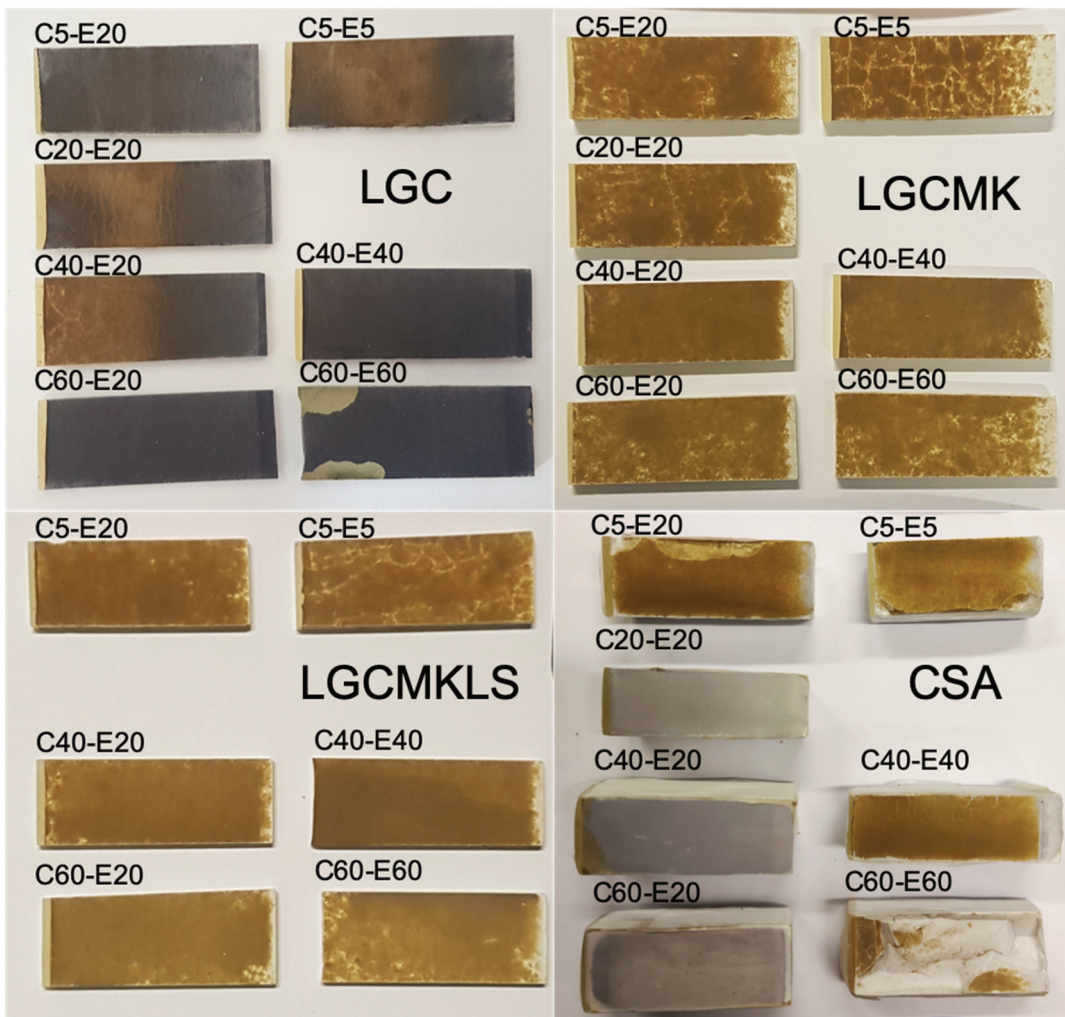


Figure 19 Investigated samples after applying AgNO<sub>3</sub> for 1 hour: C = Curing temperature, E = Exposure temperature.



# Curriculum Vitae

## NATECHANOK CHITVORANUND

### CONTACT INFORMATION

E-mail: natechanok.chitvoranund@epfl.ch / natechach@gmail.com

### PERSONAL INFORMATION

Date of birth: 18.01.1986

Gender: Female

Nationality: Thai

### PROFESSIONAL EXPERIENCES

---

2012 – 2017

Researcher, Cement and Cementitious Research Group,  
Siam Research and innovation Co., Ltd., SCG cement, Saraburi Thailand

#### Research topics

- Clinker and cement hydration: working on the development of calcium sulfoaluminate base and the improvement of existing clinker quality at laboratory and pilot scale
- Supplementary cementitious materials: working on the combination of calcined clay and limestone as clinker substitute
- Cementitious materials: working on fast setting cement (water plug) and internal curing using bottom ash

### EDUCATION

---

2017 – PRESENT

Ph.D. candidates, Laboratory of Construction Materials (LMC)  
EDMX Materials Science and Engineering  
École Polytechnique Fédérale de Lausanne (EPFL), Lausanne, Switzerland  
Thesis: Stability and properties of hydrate phase assemblages with higher alumina content in real microstructure

2009 – 2011

M.Sc. (Ceramic Technology), Faculty of Science  
Chulalongkorn University, Bangkok, Thailand  
Thesis: Coating of Ag particles on glass surface by electroless plating

2005 – 2008

B.Sc. (Material Science), Faculty of Science  
Chulalongkorn University, Bangkok, Thailand  
Thesis: Enhancing the antibacterial activities on stoneware ceramic by silver and derivative

---

**PUBLICATIONS**

---

- 2021 **N. Chitvoranund**, B. Lothenbach, J. Skibsted and K. Scrivener, Effect of temperature on the hydration of Portland cement blended with metakaolin, 11<sup>th</sup> ACI/RILEM International Conference on Cementitious Materials and Alternative Binders for Sustainable Concrete, online conference (Postponed date from June 2020 to 7<sup>th</sup> – 9<sup>th</sup> June 2021) (Proceeding publication)
- 2018 **N. Chitvoranund**, B. Lothenbach, J. Skibsted and K. Scrivener, Effect of temperature on C-A-S-H composition of white Portland cement blended with metakaolin, 38<sup>th</sup> Cement and Concrete Science Conference, 9<sup>th</sup> – 11<sup>th</sup> September 2018, Coventry, UK (Proceeding publication)
- 2017 **N. Chitvoranund**, F. Winnefeld, C.W. Hargis, S. Sinthupinyo and B. Lothenbach, Synthesis and hydration of alite-calcium sulfoaluminate cement, *Advances in Cement Research*, 29 (3), 101 – 111.
- 2016 M. Wyrzykowski, S. Ghourchian, S. Sinthupinyo, **N. Chitvoranund**, T. Chintana and P. Lura, Internal curing of high performance mortars with bottom ash, *Cement and Concrete Composites*, 71, 1 – 9.
- 2015 **N. Chitvoranund**, F. Winnefeld, S. Sinthupinyo and B. Lothenbach, Phase assemblage study of alite-calcium sulfoaluminate cement blended with supplementary cementitious materials, the 14<sup>th</sup> International Congress on the Chemistry of Cement (ICCC 2015), 13<sup>th</sup> – 16<sup>th</sup> October 2015, Beijing, China (Proceeding publication).
- N. Chitvoranund**, B. Lothenbach, S. Sinthupinyo and F. Winnefeld, Reactivity of calcined clay in alite-calcium sulfoaluminate cement hydration, 1<sup>st</sup> International Conference on calcined clays for sustainable concrete, 23<sup>rd</sup> – 25<sup>th</sup> June 2015, Lausanne, Switzerland (Proceeding publication, page 373-379).
- 2013 **N. Chitvoranund**, S. Jiemsirilers and D. Pongkao Kashima, Effect of surface treatments on adhesion of silver film on glass substrate fabricated by electroless plating, *Advanced Materials Research*, 664, 566 – 573.